UNIVERSITÀ
DEGLI STUDI
DI PADOVA

Sede amministrativa: Università degli studi di Padova

Dipartimento di Ingegneria Industriale

SCUOLA DI DOTTORATO DI RICERCA IN INGEGNERIA INDUSTRIALE
INDIRIZZO: INGEGNERIA CHIMICA, DEI MATERIALI E DELLA PRODUZIONE
CICLO XXVII

MODELLING AND EXPERIMENTAL INVESTIGATION OF MICROKINETICS IN HETEROGENEOUS CATALYSIS: HYDROGEN COMBUSTION AND PRODUCTION

Direttore della scuola: Ch.mo Prof. Paolo Colombo
Coordinatore d'indirizzo: Ch.mo Prof. Enrico Savio
Supervisore: Ch.mo Prof. Paolo Canu

Dottorando: Nicola Michelon

PhD thesis

Nicola Michelon

February 2, 2015

Foreword

The realisation of the present work of thesis involved the intellectual and financial support of many people and institutions to whom the author is very grateful. Most of the research activity described in this dissertation has been carried out at the Departments of Industrial Engineering and Department, at the University of Padua (Italy), under the supervision of Prof. Paolo Canu. Support from prof. Marta Maria Natile and prof. Antonella Glisenti, Chemical Science Department-University of Padua, on XRD surface characterisation and experimental hydrogen combustion has to be mentioned as well. Prof. Alessandro Trovarelli, Chemical Science and Technology Department-University of Udine, provided help in characterization of NI-based supported catalyst for H_2 production by steam reforming. Part of the work was carried out at the Combustion Fundamental Group at the Paul Scherrer Institut (PSI), Villingen - Switzerland (CH), during a residential period under the supervision of prof. Ioannis Mantzaras. During this period, significant and novel numerical results were obtained on fundamental of hydrogen combustion. 2-D transient simulation led to insights on combustion managing with particular attention on start up processes. Financial support to this study has been provided by the University of Padua, CreLab research group (Prof. Paolo Canu) of University of Padua and, in part, by the Combustion Fundamental Group of the PSI.

Abstract

This thesis investigates both hydrogen combustion and production, focusing on fundamentals of Pt-catalysed oxidation and steam methane reforming on nickel-based catalysts.

On the first aspect, we started reporting and investigating discrepancies on the structure and predictions of detail surface kinetic models from Literature, for H_2-O_2 reaction on Pt. Quantitative comparisons have been carried out through a closed-vessel, well-stirred reactor model with catalytic internal surface. Discrepancies in the predictions of the microkinetic models apparently comes from disagreement in the experimental date they are based on. Differences in experimental set-ups and Pt surface structure prompted us to develop own data, using plane Pt surface in suitable reactors. A novel laboratory reactor to investigate hydrogen oxidation on Pt surfaces has been designed, based on modelling, and built.

Experimental catalytic activity test proved that Pt activity can vary dramatically. Catalyst pretreatments with H_2 and O_2 revealed the mechanism of competition for surface sites as well as restructuring of the surface. Significantly long transformation was measured, particularly after catalyst O_2 pretreatment, that are not included in the elementary chemistry models from Literature. Reaction light-off at H_2 lean compositions have been measured and compared with Literature experimental data, providing explanations for the differences among published data.

Subsequently, transient simulation of hydrogen combustion in platinum-coated channel has been adopted to evaluate the behavior under heterogeneous and hetero-/homogeneous chemistries. Effects of catalyst support material properties, FeCr-alloy and cordierite, have been compared. Implication for the operation of various practical catalytic reactors are finally drawn.

Concerning H_2 production, we investigated the catalytic reforming of natural gas, by steam, both theoretically and experimentally. We identified relevant ranges of operative variables to study the catalyst at industrially relevant conditions. We designed by scaling down from industrial plants an original set-up to investigate the reaction kinetics at high-pressure (10 bars). We compared three nickel-based

catalysts at low steam-to-carbon conditions, approaching S/C = 1, to collect activity and coking data for validation and development of detailed surface chemistry model.

Riassunto

Questa tesi investiga sia la combustion che la produzione di idrogeno, con particolare attenzione verso aspetti fondamentali della ossidazione catalizzata da platino e la reazione di steam reforming del metano su catalizzatori a base di nickel.

Per quanto riguarda il primo aspetto, siamo partiti dall'osservare ed approfondire discrepanze sulla struttura e sui risultati di modelli cinetici di reazioni superficiali presenti in Letteratura, per la reazione di H_2 e O_2 su Pt. I confronti quantitativi sono stati fatti utilizzando un Modello di reattore chiuso ben mescolato con le superfici interne catalitiche. Le differenze nelle perizie dei diversi modelli sembrano discendere da differenze nei dati sperimentali su cui sono stati calibrati. Il fatto che se non stati utilizzate diverse configurazioni sperimentali, e probabilmente strutture delle superfici di Pt , ci ha stimolato a intraprendere una campagna sperimentale per ottenere dati propri, utilizzando superfici di platino planari in opportuni reattori. Un nuovo reattore di laboratorio, a flusso stagnante, per indagare reazioni su Pt in forma di dischi è stato progettato sulla base di una modellazione dettagliata e realizzato in laboratorio.

I risultati sperimentali hanno dimostrato che l'attività del Pt può variare enormemente. Pretrattamenti con H_2 o O_2 Hanno chiarito il meccanismo della competizione per siti superficiali e la possibilità di ristrutturazione la superficie. Sono state misurate trasformazioni di lunga durata, soprattutto dopo pretrattamenti con O_2, che non trova una spiegazione in nessuno dei modelli cinetici dettagliati di letteratura. Mediante misure in rampa di temperatura si è studiato l'innesco di miscele povere di H_2 in aria. Il confronto con dati di letteratura suggerisce una plausibile interpretazione della discrepanza dei dati riportati.

Successivamente simulazioni transitorie della combustione di idrogeno in canali rivestiti di platino è stato utilizzato per valutare il comportamento della reazione eterogenea con e senza reazione omogenea. L'effetto delle proprietà del supporto del catalizzatore sono stati confrontati, considerando leghe Fe-Cr e cordierite. Le implicazioni pratiche per l'operatività di questi reattori sono state delineate.

Per quanto riguarda la produzione di idrogeno abbiamo studiato sia dal punto di vista teorico che sperimentale la reazione di reforming di gas naturale mediante

vapore. Abbiamo identificato intervalli significativi da un punto di vista industriale per le variabili operative, per studiare la cinetica dei catalizzatori. Abbiamo progettato un reattore di laboratorio mediante regole di scala rispetto a un impianto modello industriale di riferimento, con l'obiettivo di studiare la reazione a pressioni elevate (10bars). Abbiamo confrontato tre catalizzatori basati su Nickel con formulazioni diverse, modificando rapporto vapore/carbonio in alimentazione, per avvicinarsi alle condizioni stechiometriche. Si sono raccolti numerosi ,dati sia di attività cataliticha che di formazione di carbone, utili per uno sviluppo di modelli cinetici dettagliati della reazione superficiale.

Contents

Chapter 1

Introduction

World energy economy is everyday focused on more efficient technologies, renewable energies, optimization process and continuous efforts are required to convert fossil fuel based technologies in more sustainable and environment friendly ones. Hydrogen has been identified as a potential zero-emission energy carrier, primarily for the transportation sector. It is relevant also for energy storage. H_2 use in industrial processes lead to an annual world demand of 50 million tonnes [1]. The overall framework strongly push on the hydrogen world demand, whose annual growth has been estimated to be of 3.4% in the period 2008-2013, see Fig. 1.1. It has to be highlighted that the increasing trend is mostly related to the North American market and even more to the Asiatic one whose demand has been doubled from the 2003 to the 2013 [2].

The combustion of hydrogen and hydrogen-rich fuels has attracted increased attention in many practical applications, ranging from industrial plants to microreactors for portable power generation units. That is due to its high energy density per unit mass, as comparatively reported in Tab. 1.1.

Recent approaches in large power plants aim at mitigating greenhouse gas emissions with pre-combustion CO_2 capture, which is achieved by decarbonising the fossil fuel and thus producing a hydrogen rich reactive mixture [3, 4, 5]. Moreover, hydrogen rich fuels are of great interest for the latest post-combustion CO_2 capture strategies. Therein, the fuel/air mixture is diluted with large fuel gas-recycle (CO_2 and H_2O), so as to increase the CO_2 content in the exhaust gas and thus facilitate its capture [6, 7].

An option to enhance the combustion stability of such highly diluted reactive mixtures is to inject H_2 (typically produced via reforming a fraction of the gaseous fuel) into the fuel stream [8]. Apart from large power plants, hydrogen and H_2-containing fuels are also of interest in microreactors of small scale ($\approx$100 We) power generation devices [9, 10, 11]. In such devices H_2 can be produced in appropriate microreformers from methane [12, 13, 14] or heavy hydro-

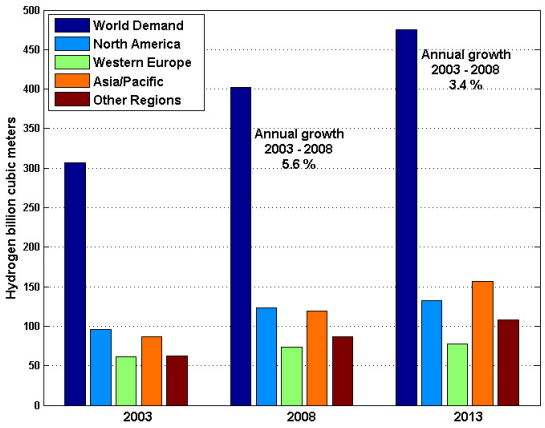

Figure 1.1: *H_2 world demand. Real estimations for the period 2003-2008 and forecasts for 2008-2013 are reported.*

Species	**HHV** MJ/kg	**LHV** MJ/kg	**HHL/LHV ratio** -
Hydrogen	142	121	1.17
Methane	56	50	1.12
Gasoline	47	44	1.07
Coal	27	27	1.00
Wood	15	15	1.00

Table 1.1: *Higher and lower heat of combustion of the most common fuels.*

carbons [15, 16]. In modern power generation systems there is renewed interest for hybrid combustion methodologies, which combine catalytic (heterogeneous) and gas phase (homogeneous) combustion. Hybrid techniques not only reduce NO_x emissions [17] but also improve combustion stability in the latest pre- and post-combustion CO2 capture approaches. One such hybrid technique is the catalytically stabilized thermal combustion (CST) [18], whereby part of the fuel is converted catalytically in a honeycomb reactor and the remaining is combusted in a following gas phase burner, with both combustion modules operating at fuel lean stoichiometries. In pre-combustion CO_2 capture methods, the large hydrogen content in the fuel accentuates the risk of flame flashback. However, the CST hybrid technique largely mitigates flashback by hindering upstream flame propagation inside the catalytic module due to the inhibiting effect of heterogeneous reactions on homogeneous combustion [19]. On the other hand, for post-combustion CO_2 capture methods, inclusion of an upstream catalytic reactor enhances the combustion stability of the less reactive diluted fuel mixtures by lowering the effective ignition activation energy [20]. Even though hybrid hetero-/homogeneous combustion is one possibility for large scale power generation, it is the favored method for microreactors. This is due to the particularly large surface to volume ratios of microreactors, the existence of a multitude of flame instabilities in tight geometrical confinements [21, 22, 23, 24, 25] and the effective suppression of such instabilities by coating the microreactor walls with a catalyst [26, 27].

The kinetics of hydrogen oxidation on noble metals has been extensively investigated in the last years and detailed mean field reaction mechanisms have been constructed [28, 29, 30, 31, 32]. Moreover, experimental and numerical studies have assessed the impact of homogeneous kinetics and of the hetero-/homogeneous chemistry coupling in the combustion of hydrogen or hydrogen containing fuels over noble metals [33, 34, 35, 36, 37, 38].

Experiments over a heated platinum foil with hydrogen/air mixtures at fuel lean stoichiometry have shown that hydrogen self inhibits its catalytic ignition [39, 40], a result of the higher sticking coefficient of H_2 compared to that of O_2. Self inhibition in hydrogen catalytic ignition at lean stoichiometries is also attested over palladium, albeit with a resulting higher reactivity than that of platinum [39, 29]. On the other hand, rhodium catalysts exhibits an opposite behavior [41, 42] (i.e. promotion of ignition with increasing H_2 content), an outcome of its higher oxygen to hydrogen sticking coefficient ratio compared to that of Pt or Pd. Catalytic ignition and reactor start up are key processes for industrial systems. The operating conditions necessary for achieving catalytic ignition (light off) dictate the design complexity of practical hybrid CST systems, e.g. in gas turbine burners the inability of fuel lean methane/air (and largely of natural gas/air mixtures) to ignite at partial loading compressor discharge temperatures (ca. 700 K), necessitates the addition of a pre-burner to raise the reactive mixture temperature [18].

Moreover, the time required to reach steady state controls the overall emissions of unburned fuel during the operation of a catalytic reactor [11].

The start up of hydrogen combustion over Pt surfaces is quite complex, not only due to the aforementioned self inhibition of hydrogen catalytic ignition (light off temperatures are in the range 340-380 K at atmospheric pressure and lean stoichiometries [39, 40]), but also due to the diffusional imbalance of hydrogen. The lower than unity Lewis number of hydrogen ($LeH_2 \approx 0.3$ in fuel lean H_2/air mixtures) leads to superadiabatic surface temperatures [43, 34, 20] that endanger the reactor and catalyst integrity and further promote the onset of homogeneous ignition.

Catalyst exposure at high temperatures and reactive mixtures does not only deal with mechanical consequences, as the honeycomb washcoat crumbling, but also involves the catalyst surface in a possible radical restructuring. Platinum dynamic is one of the most widely studied, both theoretically with ab-initio approaches related to model crystalline structures (i.e. Density Functional theory, DFT) and experimentally, mostly at *Ultra High Vacuum* conditions.

Evolutions from smooth surface to widespread "*roofs*" connected by sharply defined edges [44, 45] have been confirmed by Scanning Electron Microscopy analysis. Despite the extensive researches, to the best of the author's knowledge, there is still a lack of macroscopic evidences of a possible relation between catalytic activity and surface evolutions.

Interactions with reactive species have been found fundamental for the Pt structural changes, thus underling the importance of operative conditions managing and reaction heat effects, especially at the start up where temperature runaways may easily occur.

Hydrogen world demand is not only fully based on the energy business but its role as chemical is widely consolidated. Syngas (H_2 and CO) play a crucial role in several chemical processes as methanol synthesis, Fischer-Tropsch process for hydrocarbons production, ammonia synthesis as well as processes that require reactant hydrogenation [2, 46].

Being hydrogen gas not directly available in nature, mostly limited to traces, large scale production, both on-demand and just-in-time, is required. The main industrially consolidated processes are:

- **Carbonaceous fossil fuels cracking**: methane and low hydrocarbons (C2, C3, C4, C5) are the most common fuels but coal gasification has also been used;

- **Biomass gasification**: it is the most interesting, being CO2-neutral, but has not been tested at the large plant scale and laboratory researches are still developing;

- **Water splitting**: the main advantage is that carbonaceous species are avoided. Electrolysis is nowadays the most promising alternative that has been adopted on the industrial scale, but thermal energy recovery optimisation is needed to further reduce the operative costs.

At the present, H_2 is almost exclusively produced from hydrocarbons (HC), and particularly from natural gas, which is widely available and easily transportable: 95% of the produced hydrogen comes from HC, whose 50% is obtained by steam reforming of natural gas [47]. Since it allows for very high yields in hydrogen, usually approaching thermodynamic equilibrium [48], steam reforming of natural gas (mainly composed of methane), is currently the more industrially exploited process for syngas production. The overall reaction set is endothermic with increasing number of moles, thus H_2 formation is thermodynamically favoured at low pressure and high temperature (1073 K). However, real operative conditions are forced to 10 bar both because of the natural gas pressure, usually available at 5 bar, and the pressure drops caused by the catalytic bed and pumping necessities for downstream processes.

The key component of the process is certainly the catalyst and the ensuing possible operative conditions. Notwithstanding the catalyst composition is not usually related to the most expensive metals, being primarily based on nickel. A price comparison is summarized in Tab. 1.2. Catalyst properties strongly determine the range of possible operative conditions, and maintenance costs. The catalyst lifetime is mainly affected by its resistance to carbon deposition produced by the cracking of hydrocarbons, which progressively reduces its activity. The increasing catalyst deactivation which further promotes carbon deposition requires suitable programmed plant shut downs to prevent catalyst packing. In order to reduce economic risks and safety issues, industrial plant operative conditions are currently based on large steam excess, commonly defined as the molar ratio between water and C inlet fluxes,steam to carbon ratio (SC), whose typically range is SC = 2-4.

Since the energy costs of producing steam, the separation of its excess from the syngas by condensation, and the recycling/pumping of water, industries are promoting process optimisation and even more specifically new catalytic technologies. The operative costs relative to steam production are approximately two-thirds of the total costs. Actually steam reformer reactors are mostly equipped with different fixed beds catalytic layers, one upstream, more carbon resistant but less active and another one, downstream, more catalytically efficient but sensible to C deposition. R&D industrial departments are mainly focusing the attention on the first catalytic layer which, being in the coolest part of the reactor, usually far from equilibrium, and exposed to high HC concentrations, at which carbon deposition is favoured, especially for high HC mixtures.

Metal	Price $Euro/g$
Gold (Au)	32.313
Silver (Ag)	0.438
Platinum (Pt)	33.240
Palladium (Pd)	22.120
Rhodium (Rh)	34.450
Ruthenium (Ru)	3.860
Nickel (Ni)	0.012

Table 1.2: *Precious metal prices, 01/2015 [49].*

Alternative processes to the steam reforming are offered by autothermal reforming, whose advantage consist in the fuel partial oxidation, which exothermically sustain the endothermic reforming reaction, and the partial hydrocarbons oxidation, which only involve oxygen lean HC mixtures, thus completely removing water/steam costs. However, the lower syngas production and safety hazard limit their industrial application mainly to a coupling with steam reforming sections or small production plants. Large scale reforming plants are intensively adopted for the upstream production of syngas for iron oxide reduction which requires hydrogen reach syngas mixture, with a H_2/CO ratio = 4 [50].

In this thesis, hydrogen combustion and production have been investigated both experimentally and numerically.

In Chapter 2, microkinetics mechanisms of hydrogen Pt-catalysed oxidation, collected from the Literature, are discussed. Elementary chemistry has been qualitatively and quantitatively compared, first studying the competitive hydrogen and oxygen adsorption kinetics, later evaluating the reaction light-off profiles in a closed-vessel, well-stirred catalytic reactor assuming different kinetic mechanisms from Literature. By the same numerical model, initial platinum coverages composition effects have been studied comparing the adsorbed species dynamics on the basis of the Deutschmann elementary chemistry. Pt surface rearrangement has been invoked, leading to experimental and numerical studies which qualitatively distinguish the platinum active sites distribution. Finally, the discrepancies evidenced in the previous analysis have led to an experimental campaign in order to validate Literature kinetic models.

In Chapter 3, a novel laboratory reator and experimental methodologies by which hydrogen Pt catalysed oxidation has been investigated are discussed. Particular attention has been focused on the reactor design: a Stagnation Point Flow Reactor configuration has been numerical studied with parametric analysis of the

key dimensions and operating variables, through a CFD model. Isothermal assumption has been validated by nonreactive preliminary tests.

In Chapter 4, experimental catalytic activity measurements are reported. Significant activity evolution has been reported, also related to surface pre-treatments. Platinum surface restructuring and crystalline structure reorganisation have been evidenced by SEM and XRD analysis. Reaction light-off at hydrogen fuel lean compositions have been measured, thus evaluating the ignition temperatures trend at increasing hydrogen partial pressure. Finally, comparison with literature experimental data is proposed.

In Chapter 5, a numerical study on the competition between hydrogen active sites inhibition and thermal promotion, in the range ϕ=0.10-0.28 at operative pressures P=1 and 5 bar, is proposed. Transient simulation of hydrogen combustion in platinum-coated channel has been adopted to evaluate the behaviour under heterogeneous and hetero-/homogeneous chemistries. Time to reach the steady state, steady wall channel temperatures, hydrogen conversion have been considered as terms of comparison. Effects of catalyst support material properties, FeCr-alloy and cordierite have been also compared. Implications of the above findings for the operation of various practical catalytic reactors are finally drawn.

In Chapter 6, Literature overview on steam methane reforming kinetics is discussed. The complexity of the chemical pattern is still not represented by an unique commonly accepted elementary kinetic, moreover carbon deposition rate modelling is still demanding. Thermodynamic analysis has been proposed in order to evaluate the impact of temperature, pressure, steam-to-carbon ratio at reaction equilibrium. High pressure experimental set-up and methodologies are subsequently discussed. In agreement with the Literature, irrespective scaling rules have been discussed, particularly focusing on the flow regime and heat transfer. Catalytic activity for three commercial catalysts have been experimentally evidenced, also defining critical steam-to-carbon operative conditions. Attention has been given to correctly compare catalyst activities also considering active metal loading and surface active areas. Insights for a kinetic study has been proposed.

Chapter 2

The mechanism of H2 oxidation on platinum

Catalytically assisted combustion have progressed significantly in the last years both for large and small scale energy production applications (> 150 MW and $\approx$ 1.5 MW respectively), whereby honeycomb reactors allow for a multitude of catalytically coated channels, as well as for microreactors, whose technology is particularly growing, mainly oriented to portable power generation units. The great advancing in numerical tools has further promoted the studying and optimisation of chemical reactive system. Multidimensional fluid dynamic and solid phase modelling coupled with heterogeneous and homogeneous elementary chemistries, which have made radical and intermediate species accessible, have allowed for studying gas-phase and catalytic kinetics interactions, also including heat conduction effects in the catalyst support. The inclusion of heat transfer in the solid phase has strongly promoted reactor modelling especially concerning the start up dynamics. Reacting environment models can be very predictive but micro-kinetic information are required to be accurately representative for an efficient scale-up. Several reaction mechanisms are presented in literature but their validation is often questionable as they refer to catalysts in quite different forms (supported, structured, with different shapes, like foils, wires); also, reactor configurations and operating conditions frequently are not well explained. Simplified systems are needed to investigate reproducible phenomena that enhance reagents-catalyst's structure interaction and reaction intermediates [51], however kinetic approach is still prohibitive for large scale simulations. Hydrogen platinum catalysed oxidation is one of the most studied gas-solid reactive systems from the early '80s, both for the interesting applications of the gas as combustion stabiliser or energy carrier, as well as the high catalyst activity which promotes reaction ignition at relatively low temperatures. The coupling of the hydrogen properties together with the platinum ones has made this reaction a model for kinetic investigation

methodologies as well as a fundamental component of more complex chemical patterns: i.e. high hydrocarbons combustion, in which HCs cracking produces H_2 which is consequently involved in the downstream oxidation processes.

2.1 The mechanism on the Pt surface

H_2/Pt kinetic model have been developed on the basis of several studies which range from the macroscopic measurement of heterogeneous and homogeneous reaction ignitions at ambient pressure [52, 53, 54, 55, 30], mainly related to the temperature derivative as consequence of the strong reaction exothermicity, to low pressure experimental setups (10^{-3}-10 Torr) in which intermediate species, particularly the precursors of homogeneous ignition, i.e. OH radicals, were directly measured [56, 57, 58, 59]. The interplay between homogeneous and heterogeneous chemistry has been further experimentally and numerically confirmed with ambient pressure optically accessible reactors in which Planar Laser Induced Fluorescence (PLIF) technique has been adopted for spatially resolved intermediate species concentrations mapping [34, 60]. Parallel to the gas phase species dynamic, platinum surface physics has been investigated by typical surface science analysis (XPS, LEED, STM, HRSEM, XRD) and theoretical techniques as Density Functional Theory (DFT) and Unity Bond Index-Quadratic Exponential Potential (UBI-QEP) [61, 62, 63], by which metal surface reaction energetics, heat of desorption and activation energy barriers, can be determined with a typical accuracy of 1-3 kcal/mol. Despite the wide range of studies, there is still debate on the elementary mechanism, especially for the heterogeneous chemistry, which is affected by different interpretations of the activation energy barriers dynamics dependency on adsorbed species. Moreover, being the catalytic chemistry strongly related to surface science studies which are mainly carried out at UHV conditions and on different single-crystal platinum surface structures, the collage of elementary kinetic steps (i.e. [64]) is questionable both because of the pressure gap, that makes objectionable the parameters validity at high pressure, and for the effects of different catalyst surface structures. The following discussion attempt to develop a critical analysis of the H_2/O_2/Pt kinetic mechanisms available in the Literature, based on their quantitative predictions. The main H_2/Air/Pt heterogeneous elementary kinetics are reported in Tab. 2.1.

A comparative example of the structure of detailed surface mechanisms is reported in 2.2. Full details of the mechanisms considered in the following calculation are reported in the Appendix. The mechanism allow to calculate the reaction rates for each step as

Table 2.1: *Main surface microkinetic mechanisms for platinum catalysed oxidation.*

Author	Year	Notes
Schmidt	1993	
Kasemo	1994	
Deutschmann	1995	first to introduce coverage dependent activation energy
Vlachos	1999	introduced double coverage dependent activation energy
Forsth	2002	coverage dependent sticking coefficients
Aghalayam	2003	subsection of the CH_4 oxidation kinetic

Table 2.2: *Surface mechanism of H_2/O_2 interactions on Pt. Surface specie are denoted by (s.)*

	Deutschmann[b]			Kasemo[c]			Schmidt[d]		
Adsorption Reactions	A (γ)	b	E	A(γ)	b	E	A (γ)	b	E
1. $H_2 + 2Pt(s) \rightarrow 2H(s)$	0.046	—	—	0.046	—	—	0.05	—	—
2. $H + Pt(s) \rightarrow H(s)$	1.0	—	—	1.0	—	—	1.0	—	—
3. $O_2 + 2Pt(s) \rightarrow 2O(s)$	0.07	—	—	0.023	—	—	0.003	—	—
4. $O + Pt(s) \rightarrow O(s)$	1.0	—	—	1.0	—	—	1.0	—	—
5. $H_2O + Pt(s) \rightarrow H_2O(s)$	0.75	—	—	0.7	—	—	0.1	—	—
6. $OH + Pt(s) \rightarrow OH(s)$	1.0	—	—	1.0	—	—	1.0	—	—
Surface Reactions									
7. $H(s) + O(s) \rightarrow OH(s) + Pt(s)$	3.7×10^{21}	0.0	11.5	3.7×10^{21}	0.0	11.5	3.7×10^{23}	0.0	10.5
8. $OH(s) + Pt(s) \rightarrow H(s) + O(s)$	from k_7 and $K_{c,7}$			3.7×10^{21}	0.0	24.5	3.7×10^{16}	0.0	21.0
9. $H(s) + OH(s) \rightarrow H_2O(s) + Pt(s)$	3.7×10^{21}	0.0	17.5	3.7×10^{21}	0.0	17.5	3.3×10^{25}	0.0	62.8
10. $H_2O(s) + Pt(s) \rightarrow H(s) + OH(s)$	from k_9 and $K_{c,9}$			3.7×10^{21}	0.0	113.5	6.7×10^{21}	0.0	155.0
11. $OH(s) + OH(s) \rightarrow H_2O(s) + O(s)$	3.7×10^{21}	0.0	48.2	3.7×10^{21}	0.0	48.2	3.7×10^{23}	0.0	51.5
12. $H_2O(s) + O(s) \rightarrow OH(s) + OH(s)$	from k_{11} and $K_{c,11}$			3.7×10^{21}	0.0	131.4		—	
Desorption Reactions									
13. $2H(s) \rightarrow H_2 + 2Pt(s)$	3.7×10^{21}	0.0	$67.4–6\Theta_H$	3.7×10^{21}	0.0	67.4	5.0×10^{12}	0.0	75.4
14. $2O(s) \rightarrow O_2 + 2Pt(s)$	3.7×10^{21}	0.0	$213.2–60\Theta_O$	3.7×10^{21}	0.0	213.2	5.0×10^{12}	0.0	218.0
15. $H_2O(s) \rightarrow H_2O + Pt(s)$	1.0×10^{13}	0.0	40.3	1.0×10^{13}	0.0	42.3	1.0×10^{13}	0.0	45.2
16. $OH(s) \rightarrow OH + Pt(s)$	1.0×10^{13}	0.0	192.8	1.0×10^{13}	0.0	192.8	1.5×10^{13}	0.0	201.1

$$R'' = \vec{R}'' - \overleftarrow{R}'' = \vec{k}'' \prod_{i}^{N_{reag}} C_i^{\alpha_i} - \overleftarrow{k}\, 2 \prod_{i}^{N_{prod}} C_i^{\alpha_i} \tag{2.1}$$

where the symbol '' specifies *per unit surface*, and concentration involved may be volumetric (i.e. in the gas phase facing the surface) or surface concentrations, if referred to surface species (i.e. surface sites or adsorbed species). Often the latter are expressed as surface molar fraction, called *coverages*, defined as:

$$\theta_i = \frac{\text{adsorbed molecules of } i}{\text{total active sites}} \tag{2.2}$$

From Rs the species production rates on the surface can be obtained through the steps stoichiometry.

$$r''_i = \sum_{j=1}^{N_R} \nu_{ij} R''_j \tag{2.3}$$

The production rate enter directly the pertinent material balances.

The reaction rate coefficient k is normally expressed by the Arrhenius expression:

$$k = A \cdot T^b \cdot \exp(E/RT) \tag{2.4}$$

or alternatively by the a sticking coefficient γ which can be modified by temperature through a power law or an exponential function.

2.1.1 Adsorption steps

The common structure of the mechanism involves adsorbed species for a reaction taking place only on the catalyst surface. Solid-gas phase interactions are restricted to adsorption and desorption phenomena. In addition, adsorption interactions proved to be the rate determining step in parametric calculations. For this reason, they deserve a critical discussion. Earlier mechanisms were based only on classical Arrhenius k_s or constant sticking coefficients [65, 59]. Subsequently, to further evolve the model including the adsorbed species effects, coverage dependency for activation energies and sticking coefficients have been implemented [29, 64, 66]. The key concept can be better expressed considering the model proposed by Forsth, in which the sticking coefficient, which represents the probability that a molecule colliding with the surface will adsorb without bouncing back to the gas phase, has a corrective factor. Increasing the number of adsorbed molecules on the surface, the sites available for a new molecules to adsorb will be reduced. Given the coverage fraction definition as reported in Eqn. 2.2, the corrective factor for hydrogen sticking $s_H(\theta)$ is expressed by the linear dependency in

$$\gamma_H(\theta_H) = \gamma_H \cdot f_H(\theta_H) = \gamma_H^o(1 - \theta_H) \tag{2.5}$$

In the case of oxygen, a second order correction, Eqn. 2.6, has been adopted to consider the dissociative adsorption which requires a free active site for each mono-atomic oxygen.

$$\gamma_O(\theta_O) = \gamma_O^o f_O(\theta_O) = \gamma_O^o(1 - \theta_O)^2 \tag{2.6}$$

In some kinetic mechanism proposed (e.g. [29]), the adsorption step is numerically described by a constant sticking coefficients, prevalent at low temperatures, without the coverage corrective correction, plus a parallel Arrhenius equation which is first order with respect to the active sites concentration, whose contribute mainly emerges at high temperatures. Irrespective of the form, both mechanisms reproduced the hydrogen self inhibition on platinum (i.e. the total occupation by H of the surface sites) which is reflected by the first order corrective factor in Eqn. 2.5 and on the platinum concentration in the Deutschmann kinetic. On the contrary, coverage dependent activation energies for the desorption steps of H(S) and O(S), whose corrections have been neglected in the Forsth elementary kinetic, have been invoked by Deutschmann, thus promoting the desorption rate, by lowering the energy barrier, at increasing coverages. It is well known that in the hydrogen Pt-catalysed oxidation the fundamental kinetic steps are the adsorption and desorption dynamics, which have to be representative of the hydrogen self-inhibition that waste the platinum active sites thus limiting the oxygen adsorption and requiring higher temperature for competitive oxygen adsorption. At low hydrogen partial pressures, the surface occupation by H is smaller, and the catalytic activity inhibition is reduced. Even though the oxygen adsorption is kinetically not as favored as H-adsorption, the higher O_2 concentration overcomes the gap, subsequently igniting the reaction at relative low temperatures. At higher hydrogen partial pressure, the strong catalyst inhibition promoted by the higher hydrogen adsorption rate with respect to the oxygen one, requires to increase the temperature to increase the hydrogen desorption providing more platinum active sites available for reaction. Indeed, on the opposite of the competitive adsorption kinetic previously discussed, hydrogen desorption rate is significantly higher with respect to the oxygen one, which sticks on the platinum surface even at high temperatures. A comparison of the rate of progress of the hydrogen and oxygen adsorption rates, calculated with the kinetic mechanisms of Deutschamann and Forsth, are shown in Figs. 2.1. Calculation have been carried out by implementing the kinetic mechanisms through Cantera [67], a free suite of object-oriented software tools for problems involving chemical kinetics, thermodynamics, and/or transport processes. Rates of progress have been calculated by the *rop* function of

Table 2.3: *Operative conditions for adsorption rate of progress calculations reported in Fig. 2.1.*

Pressure	**Temperature**	ϕ	θ_i
[bar]	[K]		
1	295 - 700	0.1, 0.5, 1.0	Pt(S)=1

Table 2.4: *Operative conditions for oxygen adsorption rate of progress calculation reported in Fig. 2.2.*

Pressure	**Temperature**	ϕ	θ
[bar]	[K]		
1	295 - 700	0.5	Pt(S)=1

Cantera, yielding the forward and reverse rates of progress of a given reaction at the conditions reported in Tabs. 2.3.

Adsorption rate of progress have been evaluated at temperatures varying in the range 295-700 K and three equivalence ratios, from 0.10 to 1, representative of the increasing in hydrogen partial pressure. Platinum surface has been considered initially free of any adsorbed species, thus imposing the coverage mole fraction θ_{Pt} = 1. Observing the results in Fig. 2.1, it is evident that both kinetic mechanisms follow the rule of the chemical inhibition at increasing hydrogen partial pressure. Very good agreement between the two kinetic models has been observed in H_2 adsorption rate. The adsorption rate of progress varied by nearly an order of magnitude when the equivalence ratio was increased from 0.10 to 1.0 (blue lines).

On the opposite, O_2 adsorption rates (green lines) predicted by the two models sensibly disagree, especially at lower temperatures. For example, at 300 K and ϕ = 0.10, the rate of progress are 8.5E-2 and 1E-2 kmol/m^3 s, respectively to Deutschmann and Forsth's mechanisms. That means a factor of 8.5! Being the adsorption of H_2 mostly equivalent for the two kinetic considered, the discrepancy highlighted in Fig. 2.1 has strong influences when predicting the catalytic reaction ignition. Indeed, the higher oxygen adsorption rate predicted by the Deutschmann catalytic elementary chemistry, compared to the competitive hydrogen one, further promotes the oxygen sticking at lower temperatures thus favoring a reaction ignition at lower temperature. Further discussion of the mentioned effects on reaction ignition is postponed.
Considering the numerical analysis in [34], heterogeneous elementary chemistries proposed by Schmidt, Kasemo e Deutschmann show significantly different O_2 sticking coefficients. They range from γ = 0.003 (Schmidt et al.) to 0.07(T_0/T)

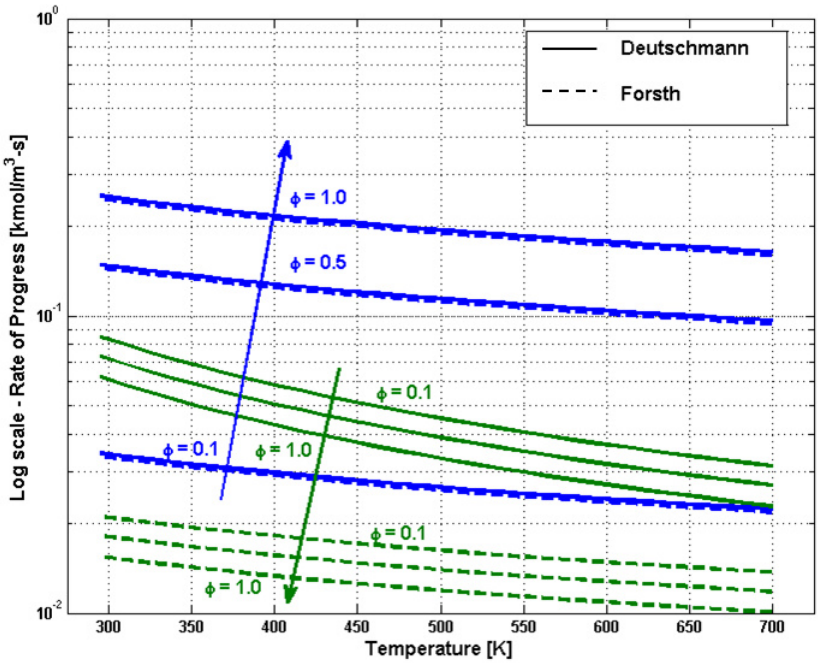

Figure 2.1: *Rate of progress for hydrogen (blue) and oxygen (green) adsorption reactions on platinum, at different equivalence ratio values. Predictions by two kinetic mechanisms are reported: Deutschmann (solid line), with the no-coverage dependent sticking coefficient, and Forsth, with the coverage dependency correction.*

(Deutschmann et al.); an average value was suggested by Kasemo et al. with γ = 0.023. Because of the importance of the oxygen sticking in catalytic reaction ignition with a competitive H_2 inhibited adsorption, the gap evidenced in the three sticking coefficients cannot be overlooked. Deutschmann's mechanism is again confirmed to be more reactive, with an oxygen sticking coefficients more than twenty time higher, at 300 K, with respect to the Schmidt's one. Comparison of the oxygen adsorption (Eqn. 2.7) rate of progress, at the operative conditions reported in Tab. 2.4, is reported in Fig. 2.2.

$$O_2 + Pt(S) \rightarrow 2O(S) \tag{2.7}$$

Equal reactants mole fractions, corresponding to $\phi = 0.5$ and completely free platinum active sites were imposed. Results clearly show that O_2 adsorption rates differ in order of magnitude when considering the two extreme sticking coefficient values $\gamma = 0.003$ and $\gamma = 0.07(T_0/T)$.

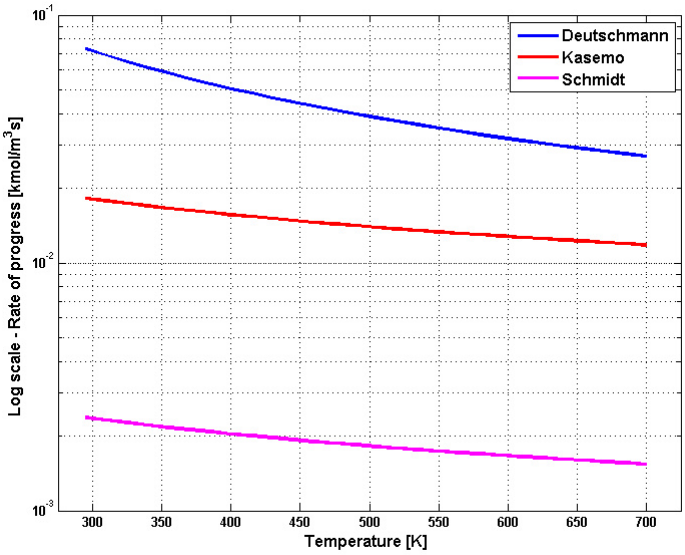

Figure 2.2: *Rate of progress for oxygen adsorption rate on platinum, in the temperature range 295-700 K, calculated with the kinetic mechanism proposed by Deutschmann, Kasemo and Schmidt.*

2.1.2 Desorption steps

As expected, opposite behavior has been obtained for the reactants desorption rates. However, very good agreement has been found for the two kinetic paths considered, both for H_2 and for O_2. Desorption rate have been estimated considering a gas mixture composition with equivalence ratio $\phi = 0.5$, thus equal reactants mole fractions, in order to avoid gas phase composition effects thus without preferentially promoting any species. Surface coverages have been varied according to the operative conditions reported in Tab. 2.6 in order to highlight coverage effects on the activation energy as defined in the Deutschmann's kinetic. Both kinetics propose a significantly higher H_2 desorption rate with respect to the O_2 one, differing of 9 orders of magnitude even at 700 K, as shown in Fig. 2.3. Comparatively small deviations between the 2 models are observed in the oxygen desorption rate calculated. The Deutschmann's kinetics at higher O(S) coverages predicts a lowering of the energy barrier at increasing mono-atomic oxygen adsorbed, as previously reported in Tab. 2.5. The large gap in species desorption rate, with H_2 desorbing much more easily, gives a chance to O_2 to react with the adsorbed hydrogen even at high hydrogen partial pressure. Increasing the temperature from 300 K to 500 K, the H_2 desorption rate grows by five orders of magnitude and, even if O_2 desorption rate is strongly increased as well, it re-

Table 2.5: *Coverage dependent activation energies for H(S) and O(S) desorption reaction proposed in Deutschmann's elementary mechanism.*

Desorption reactions	**Activation energy**
	kJ/mol
$2H(S) \rightarrow H_2 + 2Pt(S)$	$67.4\text{-}6\theta_H$
$2O(S) \rightarrow O_2 + 2Pt(S)$	$213.2\text{-}60\theta_O$

Table 2.6: *Operative conditions for desorption rate of progress calculations*

Pressure	**Temperature**	ϕ	θ_i
[bar]	[K]		
1	295 - 700	0.5	Pt(S)=0.2, O(S)=0.2, H(S)=0.6
1	295 - 700	0.5	Pt(S)=0.2, O(S)=0.6, H(S)=0.2

mains negligible compared to H_2. Platinum active sites starts to be available to O_2 molecules that can adsorb significantly on the surface then igniting the catalytic reaction at sufficient θ_O coverages. The competitive reactants-platinum interaction are thus balanced by a more efficient hydrogen sticking and its easier desorption at relative low temperatures.

On the basis of these considerations and on the gap evidenced in Fig. 2.1, it is expected that the Deutschmann mechanism is more reactive.

Despite the not only qualitative but mostly quantitative discrepancies, it has been proved in [34] that, even though the heterogeneous schemes had significant differences in the surface coverage and radical fluxes obtained, those variations had practically no impact on homogeneous ignition, thus ascribing the main effects to the gas-phase chemistry. It has to be clarified that those consideration are strongly related to the homogeneous reactive regime which mainly deals with radical species (H, O, OH) propagation from the catalytic wall to the gas phase. More over the operative conditions adopted make the energy balance being not negligible thus involving very high wall temperatures, over 750 K, at which hydrogen self-inhibition is overtaken and the system is in fully reactive catalytic regime. In order to quantitatively compare the kinetic mechanisms previously mentioned, an isothermal batch reactor model has been developed.

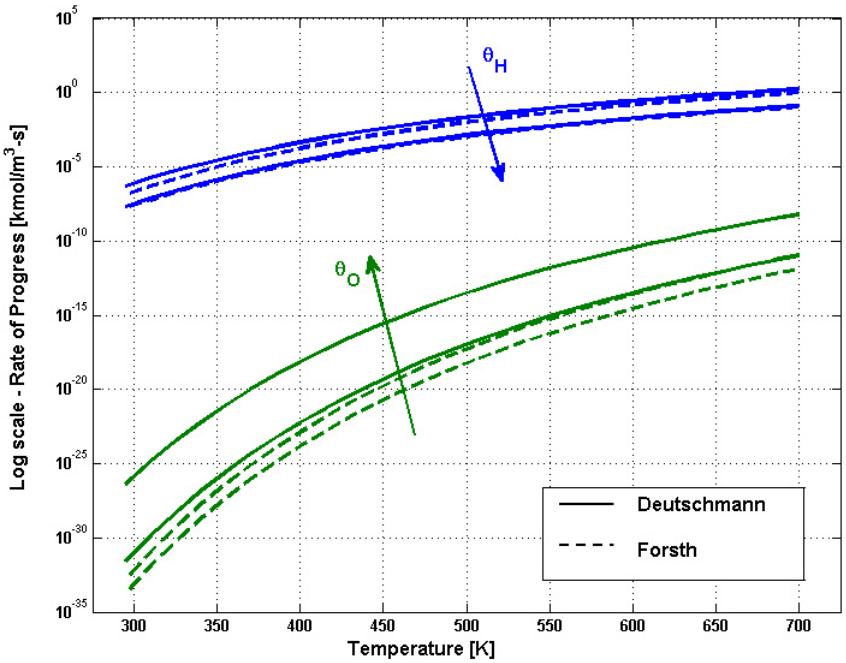

Figure 2.3: *Rate of progress for hydrogen (blue) and oxygen (green) desorption reactions on platinum, at increasing oxygen coverages. Predictions by two kinetic mechanisms are reported: Deutschmann (solid line), with the coverage dependent activation energy, and Forsth (dashed), without any coverage based correction.*

2.2 Comparison of mechanisms in a closed-vessel, well-stirred catalytic reactor

A batch reactor model has been selected for the numerical analysis of the hydrogen Pt-catalysed oxidation surface chemistry models listed in Tab. 2.1. It assumes that a gas mixture is allowed to react a constant temperature in a well-stirred closed vessel, with constant volume. The given catalytic surface per unit volume is assigned. The mixture is diluted enough to neglect pressure variations determined by the mole number variation, given the constraint on the volume. The simplified, well-mixed reactor model allows for a mere evaluation of the kinetic effects, thus avoiding mass and heat transfer distortions. Isothermal assumption, ambient operative pressure and surface-to-volume ratio S/V = 33.3 m^{-1}, value representative of micro channel reactor [68], have been considered. The gas phase material balance with the assumptions above is:

$$\frac{dY_i^g}{dt} = \frac{S\,V * r_i^g * MW_i}{\rho_{mix}} \tag{2.8}$$

where r_i^g is the molar rate of production of the i-th species of the gas phase due to the surface reactions. The material balance for the adsorbed species on the surface is:

$$\frac{d\theta_j^s}{dt} = \frac{r_j^s}{\Gamma} \tag{2.9}$$

Now r_i^s is the molar rate of production of the j-th species on the surface (including Pt(S)) due to the surface reactions. Other symbols are explained in the Nomenclature at the end of the Thesis. According to the Eqns. 2.8,2.9, gas and surface species balances have been coupled thus allowing the evaluation of both the gas and the solid species production rates at each time step. Such coupling does not correspond to the common assumption in numerical modelling of gas solid-catalysed reactions because. Being the surface evolution sensibly faster with respect to the gas phase one, the two equation sets are usually decoupled in an ODE set for the gas phase and an algebraic set for the steady solution of the surface species, Eqn. 2.10.

$$\sigma_m \frac{\dot{s}_m}{\Gamma} = 0 \qquad m = 1, ..., Ms. \tag{2.10}$$

It implies that at each time step, on the basis of the given gas phase concentration facing the solids, the surface species are calculated to new steady state values. The gas species production rates are calculated according to the new coverages. This is a common time-saving assumption which reduces the computational costs

Table 2.7: *Simulated species considered for the gas and the solid phases.*

Phase	Species
gas	H_2, O_2, H_2O, OH, H, O, HO_2, H_2O_2, N2
solid	Pt(S), H(S), H_2O(S), OH(S), O(S)

which is thought to be affected by the additional solution of the differential surface species balances. With the fully coupled model, it has been possible to follow both the gas and the solid dynamics at each time step. Simulations have been carried out in Matlab environment, coupled with the Cantera toolbox. The advantage of Cantera is that thermodynamic libraries, kinetics and physical properties are easily accessible directly from the Matlab interface by specific functions. All the elementary chemistries proposed in Tab. 2.1 have been translated in the Cantera input format (*.cti). Transcriptions are reported in Appendix A, which includes name of the species, thermodynamic database, chemical reactions pattern and the corresponding kinetic parameters. It has to be anticipated that Vlachos's kinetic mechanism has been considered both in his original version (named Vlachos), which includes the coverage dependent activation energies, and in a simplified one (named Vlachos_mod), with constant E_a. For each simulation, gas and solid phases have been defined including the species reported in Tab. 2.7, platinum surface site density Γ = 2.7 x 10^{-9} mol/cm^2 was assumed. The homogeneous reactions in the gas phase have always been ignore, due to the low temperature considered [34, 69]

2.2.1 Comparison of reaction light-off

Catalytic reaction light off is defined as the sudden increase of conversion achieved at a given temperature, during heating. Light-off of H_2 on Pt has been studied in the temperature range T = 293-493 K, with a resolution of 10 K, at different hydrogen-in-air compositions from 1 to 28 $\%_{vol}$. The batch reactor model (Eqn. 2.8,2.9) was solved at each temperature by simulating an overall reaction time of 2s. Such a time interval has been chosen as representative of the gas residence time in a microreactor of interest. It is expected that at very large reaction time all the kinetics achieve the equilibrium, also at a low temperature. The total reaction time considered here allows for realistic reaction light-off. Moreover, the comparison of the kinetics is valid because it is related to the same operative conditions. Results are reported as hydrogen conversion after 2s, at different temperature and initial mixture composition, for Vlachos and Forth's kinetics, in Figs. 2.4 and 2.5.

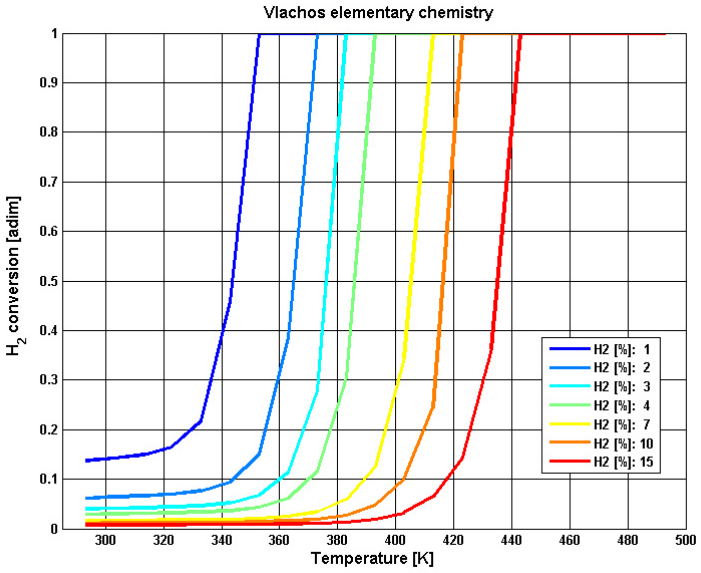

Figure 2.4: *Hydrogen Pt-catalysed reaction light-off obtained with the kinetics proposed by Vlachos.*

Neglecting the possible shifting to higher or lower temperatures, reaction light-off profiles obtained with the elementary chemistry proposed by Vlachos are qualitatively representative of the global trend evidenced also for the other kinetics. We can see the hydrogen self-inhibition effect, that rises the temperature required to ignite the mixture when larger amount of H_2 is present. Results must be compared to those obtained using the Forth's kinetic, Fig. 2.5. Now the hydrogen self-inhibition effect is not evident, and all the calculated conversion profiles are essentially unaffected by the hydrogen partial pressure, Moreover, crossing profiles indicate that the same reactant conversion occurs at a lower temperature with a higher H_2 initial concentration (i.e. x_{H_2} = 15 %).

With the exception of the Forth's kinetics, all the mechanisms were qualitatively in good agreement on the hydrogen inhibition effect according to which, at increasing H_2 mole fraction, catalytic ignition was progressively delayed to higher temperatures. Ignition is predicted even at ambient temperature for very low x_{H_2} = 1-2 %, rising to approximately 450 K for x_{H_2} = 28 %. It is also interesting to underline that, as expected by the previous considerations, the Deutschmann kinetic mechanism is the most reactive one (see Fig. 2.6). Full hydrogen conversion was obtained already at ambient temperature for H_2 mole fractions up to x_{H_2} = 4%.

A qualitative comparison of Figs. 2.4 and 2.6 (i.e. Vlachos and Deutschmann mechanisms) immediately highlights the gap in the catalytic activity predicted by the two Authors. In Fig. 2.4, for x_{H_2} = 7% reaction ignited approximately at 390

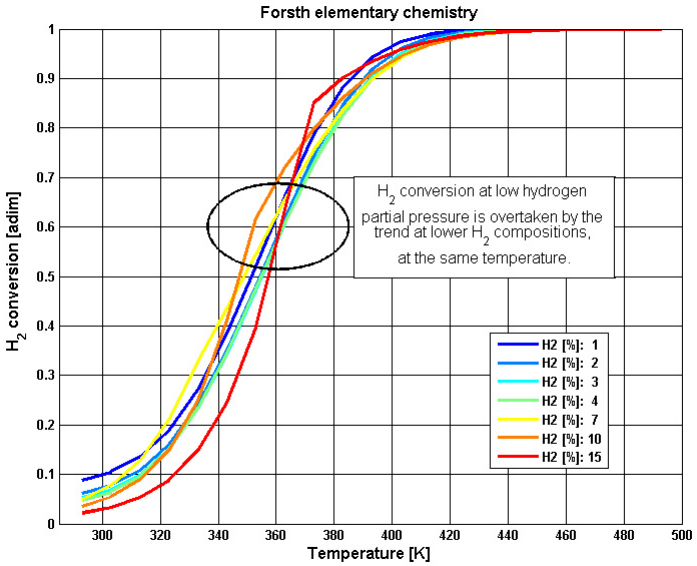

Figure 2.5: *Hydrogen Pt-catalysed reaction light-off obtained with the kinetics proposed by Forsth.*

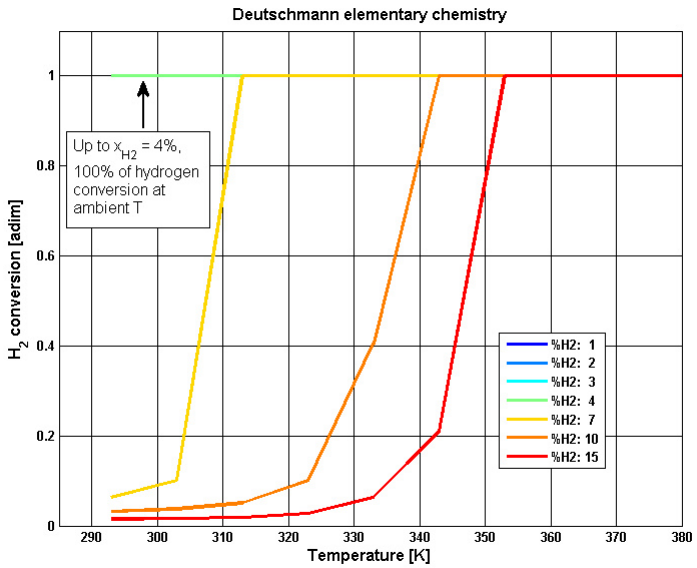

Figure 2.6: *Hydrogen Pt-catalysed reaction light-off obtained with the kinetics proposed by Deutschmann.*

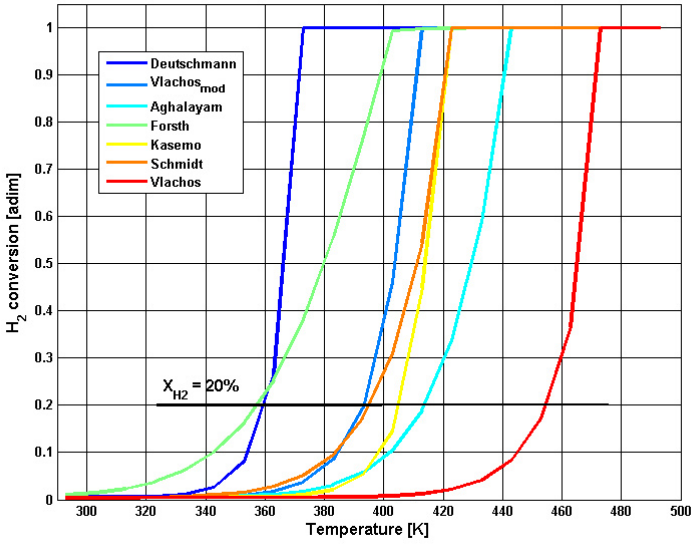

Figure 2.7: *Comparison of reaction light-off preditions by different surface mechanism.* $x_{H_2}(t = 0) = 28\%$. *Vlachos's mechanism has been considered both with (Vlachos) and without (Vlachos$_{mod}$) coverage dependent activation energies.*

K while in Fig. 2.6 70% of conversion was already achieved at 310 K, i.e. 80 K below. Moreover, a comparison of the reaction light-off at high hydrogen partial pressure appears crucial. At high p_{H2} inhibition and coverage influences should sensibly affect the kinetics, evidencing discrepancies among the mechanisms considered. This is shown in Fig. 2.7 where all the mechanism are compare at the same initial H_2 concentration. The wide distribution of H_2 conversion profiles reported in Fig. 2.7 defines a range of approximately 100 K of ignition temperature predictions, from 360 K (Forsth, Deutschmann) to 460 K (Vlachos) considering the $X_{H_2} = 20\%$ as a reference (evidenced in Fig. 2.7).

The numerical results in Fig. 2.7 explain the introduction of a simplified Vlachos's mechanism: the double coverage dependency, both from θ_H and from θ_O for some surface elementary steps (more detail in [66]), delayed the reaction ignition to significantly higher temperatures with respect to the trend observed for the other kinetic models. Neglecting that correction and conserving the normal parameter set, with single coverage dependent activation energies, the reaction light-off was shifted by 50 K, now in good agreement with Kasemo and Schmidt trends. The discrepancies among the different Literature mechanisms one used in the same well-stirred, close, isothermal reactor, at the same conditions are very large. That led us to check the experimental data they were supposed to be calibrated on. The experimental ignition temperatures from Literature are reported in

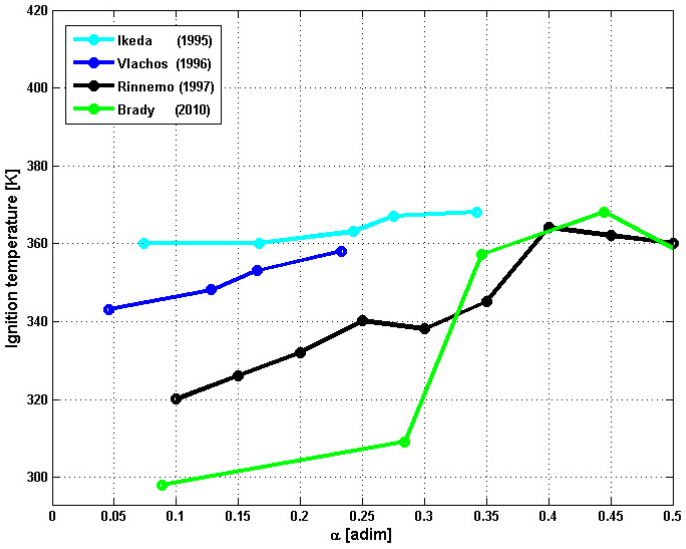

Figure 2.8: *Experimental ignition temperatures in the H_2 Pt-catalysed oxidation. Data from the Literature reported as a function of $\alpha = p_{H2}/(p_{H2} + p_{O2})$*

.

Fig. 2.8. The Figure clearly evidences the disagreements that may significantly affects the kinetic parameter tuning. At low α values, ϕ = 0.05-0.28,the gap between Brady and Ikeda is about 60 K. It is also quite interesting to notice that the gap between the experimental data is nearly constant until α = 0.25, value at which both Rinnemo and Brady trends jump to temperatures approaching the Ikeda's trend. At the same time, the sudden increase of 50 K for the ignition temperature measured by Brady when α crosses the value of 0.3 is quite surprising. Fairly naturally, some doubt about the experimental techniques or procedure arises. Accurate measurements of temperature in the presence of a localized, very fast, exothermic reaction, possibly interested by radiation could be difficult. However, the original paper does not allow to precisely understand these details. At the same time, the sudden jump observed in 5.9 also suggest some bifurcation behavior, with a switch to an ignited state that is history-dependent. Likely, the ignited branch can persist at lower α values by operating in different order. All these intriguing possibilities call for an independent experimental work, aiming at understanding the subtle interplay between kinetics, heat- and mass-transfer in reaction that was supposed to be characterized enough. That is the subject of Chap. 3.

2.2.2 Effects of the initial platinum surface coverage

Coverage evolution have been widely investigated, Bui et al. (1997) [70] carried out numerical studies to predict the surface concentration variations, at different gas inlet compositions. In particular, two main coverage rearrangements have been observed before and after the catalytic ignition. Seen through the hydrogen molar fraction, x_{H_2}, before the ignition, oxygen appeared the dominant surface component in case x_{H_2} <0.15, while hydrogen prevails for x_{H_2} >0.15. Fernandes et al. (1999) [45] performed similar calculations to study the critical surface concentration by varying the inlet reagents molar ratio x_{H_2}/x_{O_2}) in a 88% N_2 diluted mixture. Two completely different configurations have been predicted, around x_{H_2}/x_{O_2}) = 0.9. For 0< x_{H_2}/x_{O_2}) <0.9, oxygen is the dominant surface component while, for x_{H_2}/x_{O_2})>0.9 hydrogen prevails on the surface. Based on these evidences, we planned further investigations of coverage effects through the closed vessel reactor model of Eqs. 2.8 and 2.9, i.e. mass and molar balances for the gas and the solid phases respectively. The aim of this simple analysis is to highlight macroscopic phenomena, thus in the gas phase composition, that are univocally related to the platinum surface coverage. In particular, three initial surface conditions have been considered, as reported in Tab. 2.8:

1. totally free platinum active sites, i.e. all the sites are available for adsorption; $\theta_{Pt} = 1$,
2. surface fully covered by adsorbed H atoms; $\theta_H = 1$
3. surface fully covered by adsorbed O atoms; $\theta_O = 1$

Table 2.8: *Reactor conditions to investigate the surface coverage effects on reaction light-off.*

Kinetic	$\mathbf{x}_{H_2}$ [%]	$\mathbf{x}_{O_2}$ [%]	$\theta(t = 0)$	**Temperature** [K]	**Pressure** [bar]
Deutschmann	5	2.5	Pt(S) = 1	370	1
Deutschmann	5	2.5	H(S) = 1	370	1
Deutschmann	5	2.5	O(S) = 1	370	1

Reactor temperature was set to 370 K to promote catalytic ignition also at high $H(S)$ coverage, still allowing sensible evaluation of the surface composition variations up to the steady state. Platinum total site density, Γ, was set assumed equal to 2.7x10^{-9} mol/cm^2.

Deutschmann's elementary chemistry has been adopted for the following analysis. It is the most recently validated surface mechanism for hydrogen Pt-catalysed heterogeneous combustion, particularly for operative conditions that involve gas phase reaction [34]. Results are summarized in Figs.2.9, 2.10 and 2.11. All share the same structure, reporting the gas phase composition (H_2, O_2 and H_2O) in the upper panel, and the corresponding surface composition (coverages) in the panel below, for the species Pt(S), H(S), H_2O(S), OH(S), O(S). Each case will be individually presented and discussed below.

Totally free Pt-sites available

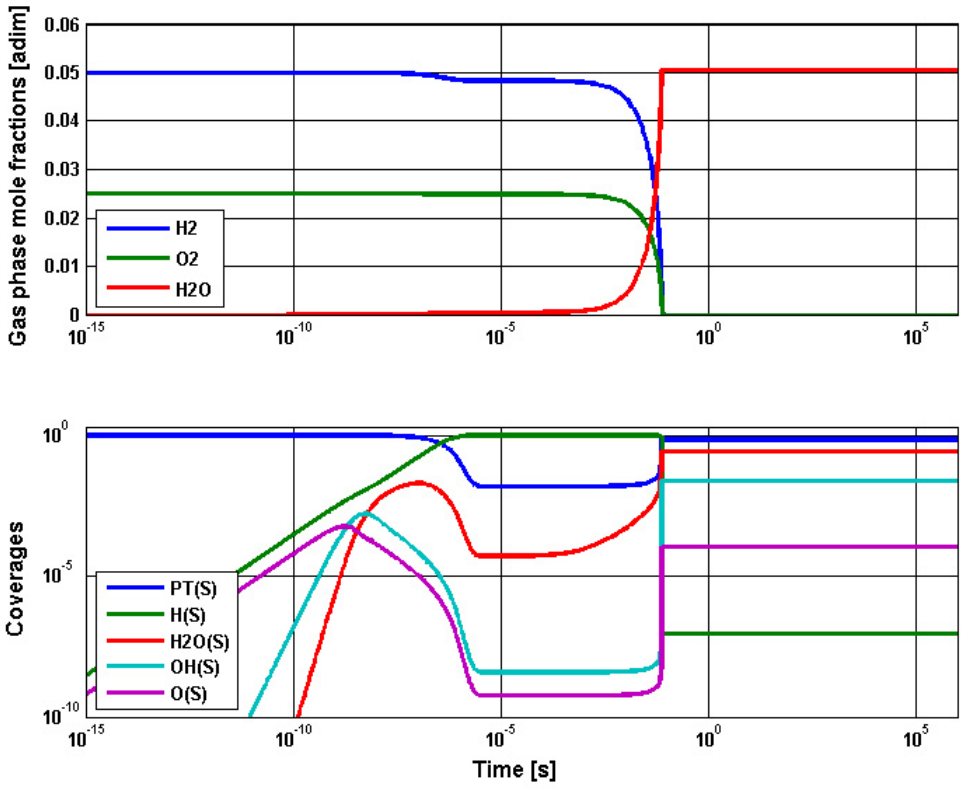

Figure 2.9: *Gas (above) and surface (below) mole fractions evolution (note that the time coordinate is logarithmic). Initial condition:* θ_{Pt}*=1,* x_{H2} = 5%, x_{O2} = 2.5%. *T=460 K. P=1 bar.*

The first configuration to be investigated is a clean surface, without any species adsorbed. The gas phase composition is 5% H_2, with O_2 stoichiometric for the

total combustion, as reported in Tab.2.8. Results of Fig. 2.9 clearly show that surface has a complex evolution, extremely fast. The surface Pt sites are rapidly populated by adsorbed H and O atoms first, thanks to the dissociative adsorption path. H(S) is preferred over O(S). Surface intermediate, OH(S), and products, H_2O(S), appear later, as expected. But it is matter of very short time intervals, in the order of 10^-10s. Evidences of the significant surface H_2 uptake have been confirmed by the lowering of its gas phase mole fraction thus leading to intermediate quasi-steady state, between 1e-6-1e-3 s, in which H(S) and Pt(S) prevailed. During this intermediate steady-state period, lasting less than 1 ms, the actual ignition is gained, exploding abruptly at approx. 0.1s In this latency interval, the surface reaction proceeds gradually with a very low O adsorbed. The gradually increase of H_2O(S) coverages confirms that catalytic reaction was progressing, thanks to OH(S) in addition to O(S). Approaching 0.1s, the reactants consumption evolves quickly, on a ms time-scale, to the full combustion, with an exponential trends in the gas phase mole fractions. After ignition and total reactants consumption, the surface remains predominantly made of free Pt(S), with some H_2O(S) and OH(S).

Fully H-covered Pt surface

More realistically, the extreme affinity of H_2 for Pt suggests that as soon as a Pt surface get in contact with a mixture containing some H_2, H-adsorption is immediately triggered, soon leading to an extensive, if not total, site occupancy. The evolution of such a surface, as predicted by the Deutschmann' mechanism a fixed T, V, and P, is shown in fig.2.10. The coverages evolves with a gradual increase of platinum free active sites Pt(S), that result from the desorption of H(S). Interestingly, really a few O(S) is required (off scale) to trigger the water production, indicated by the growing amount of H_2O(S). The intermediate steady state regime already observed with the Pt(S) = 1 initial condition stabilized also in this case, between approx. 10^{-7} and 10^{-4}s. After that, the same exponential evolution to the explosive ignition seen in 2.9 for $\theta_{Pt}(t = 0) = 1$ is predicted in this case, as well. The actual ignition is predicted at approx. 0.1 s as in the previous case. The moles of H(S) initially adsorbed on the surface cause an excess H_2 in the reactor, so that hydrogen did not reach the full conversion. After oxygen consumption, H_2 surplus equilibrated in the two phases leading to prevalent H(S), Pt(S) and H_2O(S) coverages in the solid, while in the gas phase, in addition to the prevalent H_2O produced, traces of H_2 could be appreciated (on a different scale).

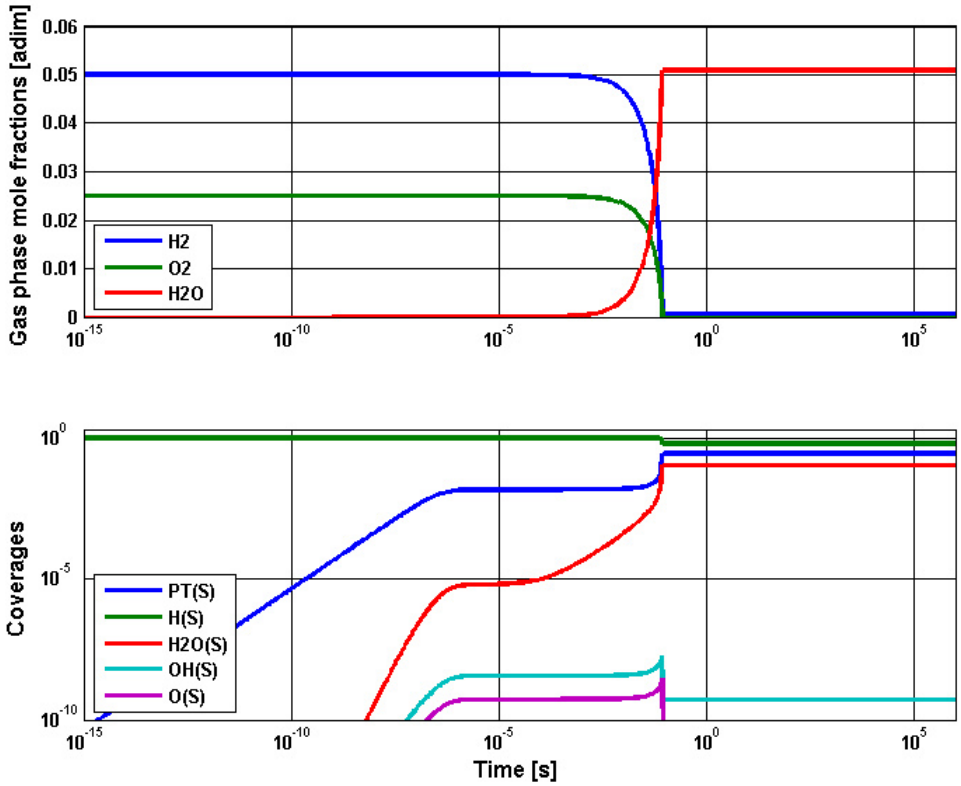

Figure 2.10: *Gas (above) and surface (below) mole fractions evolution (note that the time coordinate is logarithmic). Initial condition:* θ_H*=1,* x_{H2} *= 5%,* x_{O2} *= 2.5%. T=460 K. P=1 bar.*

Fully O-covered Pt surface

Starting from a complete O(S) covered Pt surface, the evolution predicted by the simulation was significantly different from the previous ones. Results are shown in Fig.2.11. According to the discussion on the desorption step above, the O(S) remains on the surface quite longer than H(S). Surface evolution was significantly reduced to the time interval between 10^{-2} and 10^{-1}s. At t = 10^{-2}, adsorbed oxygen dropped all in a sudden and some H_2 adsorption can break through. Consequently, a first step of H_2 conversion was observed in the gas phase, both because of its adsorption on platinum and for the reaction with the O(S), as evidenced by the H_2O produced. As confirmed by the lack of neither an increment of O_2 mole fractions in the gas phase due to O(S) desorption from the catalyst, nor a reduction of O_2 as a consequence of adsorption/reaction in the solid, we can state that the first reacting step did not involve O_2 from the gas phase, but it completely consumed the

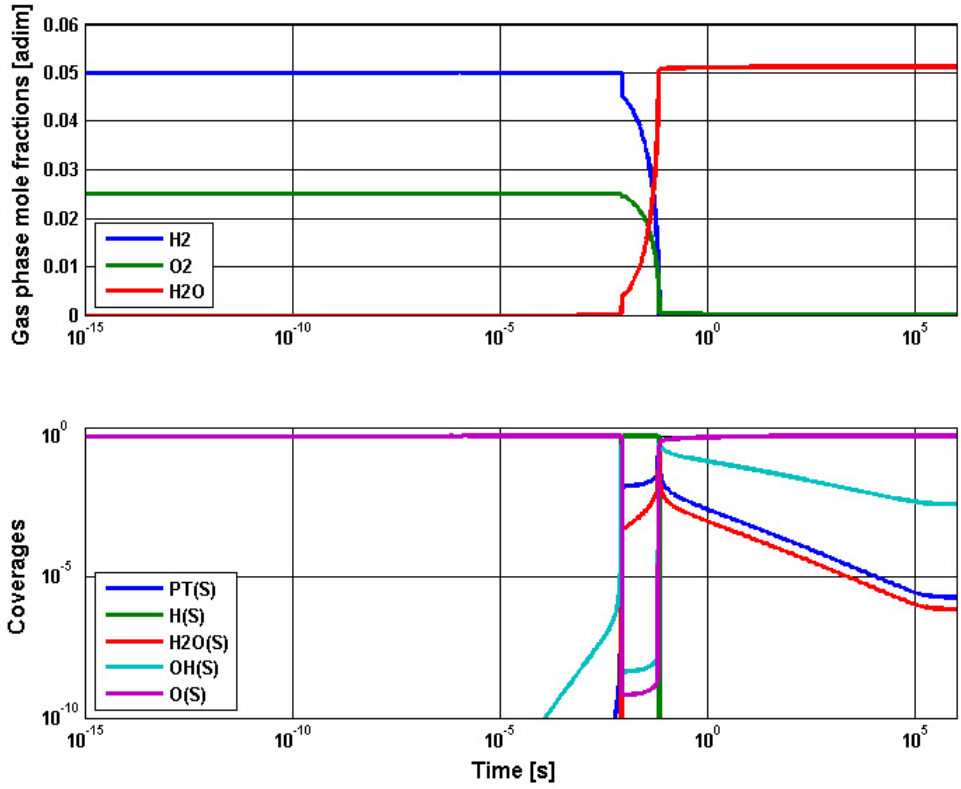

Figure 2.11: *Gas (above) and surface (below) mole fractions evolution (note that the time coordinate is logarithmic). Initial condition:* θ_O*=1,* x_{H2} *= 5%,* x_{O2} *= 2.5%. T=460 K. P=1 bar.*

initially adsorbed O(S). Subsequently, the gradual increment of Pt(S) followed by the H_2O(S) increase led to a second step of reactants consumption. This double step reaction, that has been appointed as Two-Step Ignition (TSI), will be reconsidered in the experimental results discussion, however it has to be underlined that the characteristic time-scale of the transformations, as predicted by the numerical analysis in the closed, well-mixed reactor, is in the order of milliseconds. After the complete hydrogen consumption, the surface coverage became mostly O(S) and OH(S).

2.3 Surface restructuring

A surface mechanism that aims at describing the actual reaction path at the molecular level must account for the surface structure in a more detailed picture, well be-

yond the simple surface site density account, Γ. With this respect, there are experimental studies that proved that the catalytic surface is not even a static structure. The great advancing of surface analysis capabilities and in situ technologies have revealed the intimate relationship between catalyst structure and turnover rates, under reaction conditions [71]. It means that catalytic activity is strongly related not only to the bulk material properties, but mostly to the surface structure that determines the specific Pt site density, thus how many atoms are available for the gas-solid interaction, and the low-coordination sites, representative of the quality of the active sites. Heterogeneous catalysts usually involves a large amount of low coordination sites such as steps, ridges, kinks, and vacancies, which have long been considered as the active sites during catalytic reactions. Surface defects are thus responsible of the catalyst activity and selectivity, because they strongly bind with reactants and readily break chemical bonds. Moreover, high concentration of unsaturated surface sites can promote substrate rearrangements as a consequence of molecule adsorption, also leading to microfaceting and cluster formation. Platinum is one of the most versatile catalysts: it is both used for reducing conditions, as for isomerisation processes, and as an oxidation catalyst for hydrogen, ammonia or carbon monoxide oxidations. Its chemical stability in both oxidising and reducing conditions makes this metal an ideal catalyst in many applications. Because different reactions are sensitive to specific structural features of the catalyst surface, it is important to consider the possible effects of the surface structures. The previous considerations justify the efforts by surface scientists in studying structure-activity relation on model catalysts having a uniform crystalline structure (single crystals), which allows for specific and well known structural defects, which are particularly interesting for the catalysis. The great advantage in ideal surfaces is the possible support offered by mathematical models by which they can be reproduced: numerical techniques as DFT, UBI-QEP and Potential Energy Surface (PES) allow for studying specific interactions of the reactive molecule with several surface structures. However, modern elementary kinetics are quite far from including details of surface restructuring and from defining a specific activity related to the quality of each active site. The common approach is based on the Main Field Theory which approximates the overall platinum surface to an uniform distribution of single-type active sites, generically named Pt(S) in the mechanisms used for platinum, and an average active sites surface density, whose commonly accepted values is $\Gamma = 2.7 \times 10^{-9}$ mol/cm^2, representative of polycrystalline platinum structures. In the specific case of platinum, different catalyst configurations (foils, wire, gauze) have been studied under reactive conditions and significant surface rearrangements have been confirmed. Kraehnert and Baerns [44, 72] suggested that thermal treatments on the catalytic surface in inert atmosphere, even for very long operative time (30 hours at 650 K), do not induce any structural changes. On the opposite, the exposure of the catalyst to reactive conditions, as

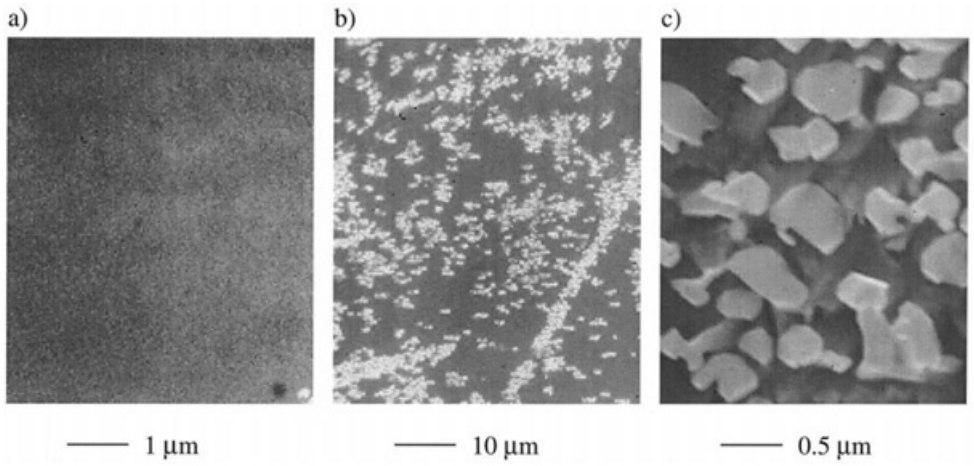

Figure 2.12: *SEM of platinum foil before(a) and after (b,c) 10 hr of catalytic oxidation at 873 K, $H_2/O_2 = 0.5$, and 88 % N_2 dilution at two different magnifications. Results are from [45]*

hydrogen oxidation [45, 73] and ammonia oxidation [44], clearly evidenced morphological evolutions of the catalyst. Example of SEM analysis from [45] and [44] are reported in Figs. 2.12 and 2.13.

In Imbihl et al. [73] it has been suggested that the main mechanism for the surface restructuring is the great mobility of the Pt-X_{ads} compound, where X is the adsorbed molecule. It also distinguished the possible surface evolution for catalyst exposed to H_2 and O_2: hydrogen adsorption appears significant only below 723 K and leads to bi-dimensional facets while oxygen promotes Pt atom surface diffusion only at higher temperatures, around 1000 K, involving three-dimensional restructuring.

Horch et al. [74] analysed the effect of hydrogen adsorption on platinum and they underlined that Pt-H compounds displacement, at room temperature, is up to 500 times higher the displacement of simple Pt atoms, because of the lower energy barrier. Water effects have been also investigated by Nielsen et al.[75] who concluded that steam pretreatment was able to gradually reset the surface by reducing the sharp edges of facets leading to a smooth surface, as a consequence of the lowering of the total free energy. During reactive conditions Pt-catalysed ammonia oxidation, water desorption has been found to be enhanced by the new sharp edged structure of the platinum thus increasing the turn over frequency. On the basis of the experiences previously discussed, platinum pretreatment effects at oxidative or reducing conditions have been experimentally planned, to better elucidate macroscopic effects on catalyst activity.

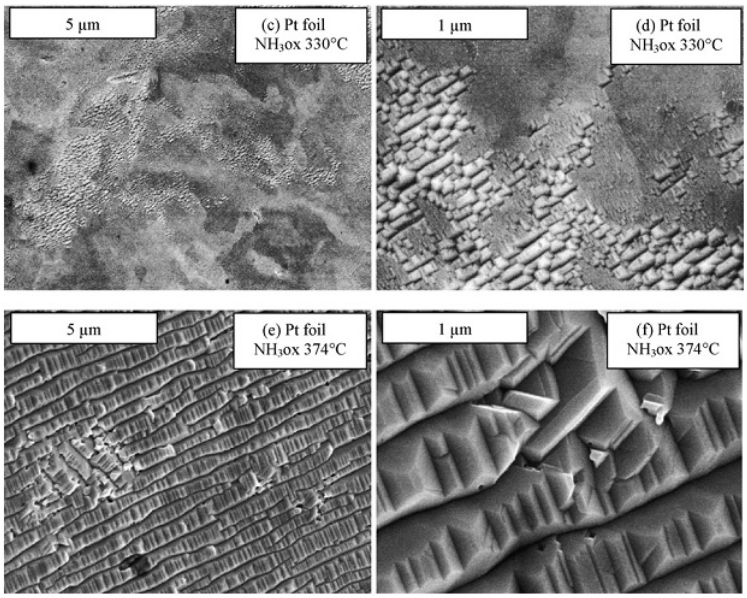

Figure 2.13: *SEM of Pt foil exposed to ammonia oxidation at 330 °C and 374 °C. Two different magnifications are reported: 5 µm (left) and 1 µm (right). Results are from [44].*

2.4 Conclusions

Detailed mean field based elementary chemistries of hydrogen Pt-catalysed oxidation have been published, see Tab. 2.1. They speculate about the elementary surface chemistry and their quantitative treatment, in terms of reaction rates. In this Chapter a quantitative comparison has been carried out, with particular attention on hydrogen and oxygen competitive adsorption kinetics, highlighting significant discrepancies among mechanisms. Deutschmann and Forsth kinetics, who proposed two different surface coverage corrective functions, predict quite different O_2 adsorption rates. Further comparison of the Deutschmann kinetic with the Kasemo and Schmidt ones, has confirmed the higher reactivity predicted by the Deutschmann's kinetics, apparently determined by the higher oxygen adsorption rate, Fig. 2.1. An isothermal heterogeneous reactor model, in the form of a closed-vessel with a well-stirred gas phase has been implemented to compare Literature mechanisms of Tab. 2.1 in terms of light-off, at different reactant compositions. The numeric comparison has highlighted incongruities in reaction light-off profiles, especially at high hydrogen partial pressure at which catalytic activity inhibition by H(S) prevails. For x_{H_2} = 28%, reaction ignition, determined at 20% of reactant conversion (Fig. 2.7), has been calculated to vary from 360 K to 460 K. Further investigation of the experimental ignition temperature collected

in the Literature, by which kinetic parameters have been tuned, have been reported thus evidencing particular discrepancies at low hydrogen concentration relative to O_2. Being the elementary chemistries mainly obtained from a collage of single kinetic step studies which underlines the importance of the catalyst surface structure, evidences of platinum surface rearrangement have been reported from the Literature. SEM analysis on platinum foils exposed to hydrogen or ammonia oxidation confirmed that the catalyst is not a static phase and surface evolves quite easily, affecting the gas-solid interaction both in terms of specific surface area as well as in the local activation energy barrier. Considering the discrepancies previously evidenced, an experimental campaign of hydrogen Pt-catalysed oxidation has been planned to evaluate both ignition temperatures at varying hydrogen partial pressure and catalyst pre-treatment effects on kinetics.

Chapter 3

Design and setup of a novel stagnation point flow reactor

Despite the apparently simple chemistry, in the previous chapter 2 discrepancies have been identified in the predictions of hydrogen oxidation on Pt by the detailed kinetic models reported in the Literature. Also the experimental measurements, compared by the ignition temperature, are not consistent, reporting differences up to 100 K. Likewise, the experiments have been carried out on different configurations, having flow and catalyst geometry, and possibly catalyst surface structure quite different one from the other. Mechanisms have been developed and tuned on different experimental data set, thus reflecting the differences in the measurements. Unfortunately, fine details in the experiments that could affect the results are seldom reported in the original papers. Based on previous experience in our laboratory, briefly reported in chapter 4, we expect that even the simplest samples of bulk Pt in the form of a single crystal with a unique crystal domain lead to unexpected results, that can vary from test to test. The discussion anticipated in section 2.3, about surface modifications that may evolve during the reaction, lead us to design a new reactor. It goal is the investigation of the H_2-O_2 chemistry on Pt, using single crystals or polycrystals bulk Pt, in the form of disk that is usually adopted for Surface Science studies. That would allow us to consistently plan parallel UHV experiments as well as characterization in UHV instrumentation, typical of Surface Science community. In this chapter we describe the reactor conceptual design and its construction, together with the details of the testing ring.

3.1 The stagnation point flow reactor (SPFR)

Given the decision to investigate pure Pt, as single crystal of polycrystalline form, a further choice concerns the shape of the surface. The commercially available

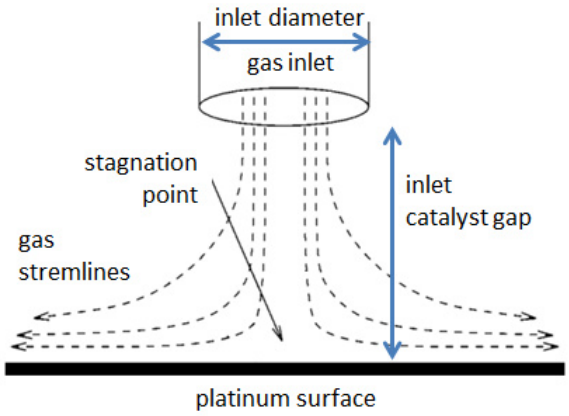

Figure 3.1: *Conceptual scheme of the stagnation point flow reactor.*

forms of pure Pt are foils, wires, and slabs, usually as disks. In a perspective of investigating also single crystals, the disk is the preferred shape.

The optimal flow configuration to study a fluid-solid, catalytic reaction on a disk-shaped surface is the Stagnation Point Flow. Its concept is shown in Fig.3.1: the gas from the inlet flows and impinges orthogonally onto the catalyst surface, reacting and spreading radially towards the surface periphery. We call such a flow configuration to a catalytic surface a *Stagnation Point Flow Reactor*, referred to as SPFR in the following.

The advantage of this configuration consists in its relatively simple geometry and uniform contact time between the gas and the solid phase. In addition, it can be described by a simple 2D model by a suitable change of independent variables [76]. Implementations that allow for detailed surface chemistry are also available both in the CHEMKIN-II [77] and Cantera [67] environments.

The contact between the fluid and the circular surface is expected to be effectively uniform, for any portion of the fluid coming from the inlet, only if it is in the form of a jet of very small diameter, compared with the catalyst surface. On the contrary, actual realizations of the SPF concept use a distributed inlet, through a porous surface having an extension comparable with the target surface (the catalyst). This is shown in Fig. 3.2, from [78] where the flow now enters from below. Although widely used, we expect the geometry of Fig. 3.2 to cause quite an extensive amount of bypass to occur, i.e. fluid that never contacts the catalyst.

Given that such a configuration can be easily reproduced by standard, flexible and widely validated CFD implementations, we used *COMSOL Multiphysics* to investigate the effective role of the inlet size, as well as other design criteria, preliminary to the reactor construction. Note that *COMSOL Multiphysics* could be interfaced with Cantera, in case detailed surface chemistry is involved.

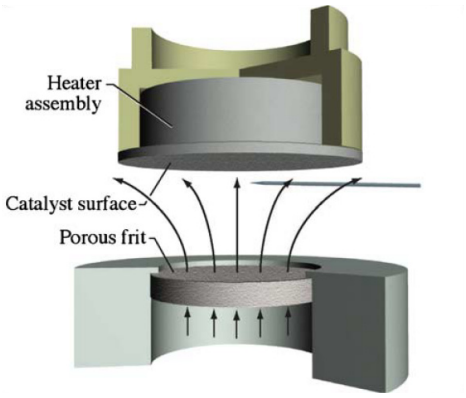

Figure 3.2: *Example of a stagnation point flow arragement from the Literature, [78].*

3.2 A model of reactive, stagnation point flow

3.2.1 Geometry

The SPFR concept shown in Fig. 3.1 has been implemented in a real geometry, as shown in Fig. 3.3, that schematically reproduce the gas phase domain within the solid boundaries. We take advantage of the 2D axial symmetry, so that Fig. 3.3 just shows a semi-section of the SPFR. The model has been implemented in a way that allows to easily modify the most relevant lengths. These include the radius of the central inlet pipe, the gap between the bottom surface, that includes the Pt disk, and its ceiling, constraining the radial flow, and the disk radius. These are the most crucial dimensions in the design. The reference values are reported in 3.1.

With the purpose of understanding the effect of design parameters (mainly dimensions) on the effectiveness of the SPFR, we will carry out a parametric sweep analysis on reactor geometry (the inlet radius and the gap above the catalyst) at different operative conditions (inlet flow rate and temperature, and reaction rate), to appreciate disguising effects due to poor catalyst contacting efficiency.

- Inlet-catalyst gap = 1, 3, 5 mm
- inlet radius = 1, 5 mm
- Inlet flow rates = 50, 75, 100, 200, 250 mL/min
- Temperature between 200 and 750 K
- kinetic constant = 10^4 - 10^6 m/s

The sizing of the gas phase flow sections was selected to be consistent with the mechanical feasibility, assuming stainless steel as the reactor material. Also,

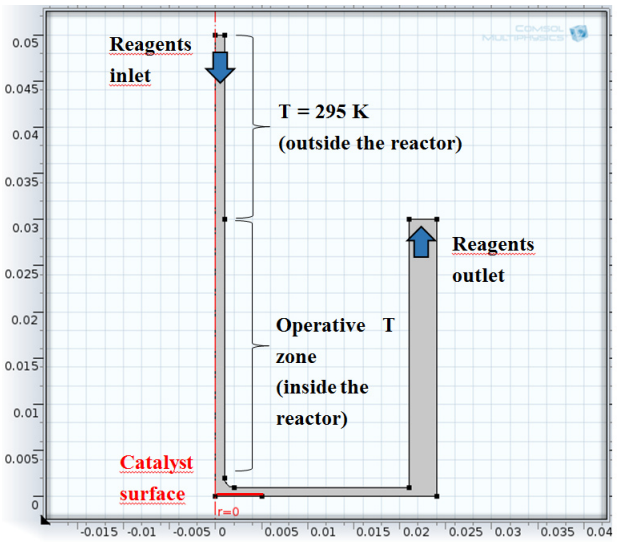

Figure 3.3: *Schematic representation of the gas phase flux in the stagnation point flow reactor model. Dimensions are in meters.*

dimensions are selected to minimize the gas residence time after the catalys, to prevent secondary reactions in the gas phase. Assuming inert and impervious walls, the solid domain has been neglected.

3.2.2 Equations solved

Within the fluid domain we solved the following equations

1. Stationary, compressible Navier-Stokes equations:

Table 3.1: *Default values for the main SPFR features, as used in the simulations.*

Parameter name	Expression	Units	Description
R_{in}	1	mm	inlet radius
d	1	mm	inlet-catalyst gap
H	50	mm	reactor height
R_{cat}	5	mm	catalyst radius
R_{react}	24	mm	reactor radius
R_{out}	3	mm	exit gap
$\dot{V}$	50	mL/min	total inlet flow rate

$$\begin{aligned} \nabla \cdot (\rho u) &= 0 \\ \rho(\mathbf{u} \cdot \nabla)\mathbf{u} &= \nabla \cdot \left[-p\mathbf{I} + \mu \left(\nabla \mathbf{u} + (\nabla \mathbf{u})^T \right) - \frac{2}{3}\mu(\nabla \cdot \mathbf{u})\mathbf{I} \right] + \mathbf{F} \end{aligned} \tag{3.1}$$

that are the total mass conservation (continuity) and the momentum conservation equations. They provide the $\mathbf{u}$ and P fields;

2. Stationary, species conservation equations:

$$\rho(\mathbf{u} \cdot \nabla)Y_i = \nabla \cdot \left[\rho D_i \nabla Y_i + \rho D_i^T \frac{\nabla T}{T} \right] \tag{3.2}$$

Note that it does not account for any reaction in the gas phase. It is assumed that the heterogeneous reaction on the catalytic surface prevails. However, this is not apparent in the gas phase conservation equation, but it is a boundary condition for it. Solution of these equation provided that spatial distribution of mass fractions $\mathbf{Y}$.

The whole set of eqs. 3.1 and 3.2 are solved by the *COMSOL Multiphysics* application mode called *Reacting Flow, Concentrated Species*. Note that the maximum value of the Re number is achieved in the inlet pipe for the larger size, the higher temperature, and maximum flow rate consider. Re ranges between tens and a few hundreds, suggesting that laminar flow prevails everywhere.

3. Stationary, energy conservation equation

$$\rho C_p(\mathbf{u} \cdot \nabla)T = \nabla \cdot (\lambda \nabla T) \tag{3.3}$$

Similarly to eq. 3.2, there is no generation/dissipation of heat within the gas phase. It may occur at the boundaries, depending on their configuration. The energy equation is solved unless isothermal conditions are assumed, providing the T distribution within the gas domain. The energy equation 3.3 is solved by the *COMSOL Multiphysics* application mode called *Heat Transfer in Fluids*.

Being the reactants very diluted (typically 1% H_2 in air), nitrogen properties have been assumed for the gas phase. Transport properties have been defined as functions of the temperature through the COMSOL database.

3.2.3 Kinetics

With the purpose of investigating the geometry of the SPFR for its final construction, we assumed that the H_2 oxidation occurs on the surface as its global reaction, with partial reaction orders like an elementary reaction. That leads to the following expression for the rate of reaction (per unit surface):

$$R" = k"(T)\rho_{H_2}\rho_{O_2}^{0.5} \quad (3.4)$$

$$r"_i = \nu_i R" \quad (3.5)$$

$$k"(T) = k^o \exp\left(\frac{-Ea}{RT}\right) \quad (3.6)$$

where $k"(T)$ is the kinetic constant (for a surface reaction), expressed in the form of the Arrhenius equation Eqn. 3.6, ν is the stoichiometric coefficient and ρ_i [kg/m^3] is the mass concentration of the i-species.

Although the reactive species are H_2 and O_2, simulations where O_2 is much more that the stoichiometric value assume that ρ_{O2} is constant.

3.2.4 Boundary conditions

Boundary conditions are classified according to the pertinent equations:

1. Compressible Navier-Stokes equations.

   Each internal solid surface is assumed to behave like a wall, i.e. **u**=0. The normal velocity is assigned an the beginning of the inlet pipe, depending on the assigned flow rate. Zero relative pressure and zero viscous stress were set at the reactor outlet.

2. Species conservation equations.

   On each internal solid surface, except for the catalyst, a zero normal flux was imposed. The composition was set at the inlet and zero normal gradients of mass fraction at the outlet (i.e purely convective flow). On the platinum disk surface, exposed to reactants flow (the red line in Fig. 3.3), a *Reacting boundary* condition was applied. Mass inflow of H_2 and O_2 are calculated exactly as $r"_i$ through the simple global kinetic of Eqn. 3.5. The production of i, i.e. $r"_i > 0$ implies an inlet in the flow domain.

3. Stationary, energy conservation equation.

   Inlet volumetric flow rates have been considered at ambient conditions. Thus temperatures in the inlet boundary and the first portion of inlet wall were set to 298 K, as reported in Fig. 3.3.

Two cases have been considered:

- **Isothermal**

  it was implemented by fixing the wall temperature of solid surfaces (including the catalyst). If it differs from the inlet temperature, some preheating will be evident

- **Adiabatic**

  that requires a zero heat flux across any solid boundary. It was used to estimate the temperature increment due to the reaction and the effect on the velocity. The heat of reaction is applied as heat source on the catalyst surface.

3.2.5 Meshing

A user controlled mesh has been built. Starting from an *extra fine* mesh (according to COMSOL classification) for the whole flow domain, at any boundary the mesh has been refined (*extremely fine*). Being thermal and concentrations gradient enhanced in proximity of the reactive surface, mesh has been further refined at the catalyst wall. The *extremely fine* mesh as a maximum element size decreased from 1.6110^{-1} to 610^{-2} mm. Finally, a structured mesh composed by three rectangles in each boundary, before the unstructured triangular mesh, was set. With this settings, approximately 18000 elements have been created, thus obtaining a final distribution as represented in Fig. 3.4. In an ordinary simulation, this mesh solves approx. 70000 variables (i.e.

3.2.6 Analysis of the simulation results

The simulations provide very detailed information about the flow structure, the pressure, temperature and composition distribution. Unfortunately, most of these prediction cannot be confirmed by similarly accurate measurements. The analytic instruments determine the residual amount of H_2 in the outlet stream, assumed totally mixed over the exit section. Accordingly, the most effective and interesting information is the reagent conversions. It can be calculated from the simulations as

$$X_i = 1 - \frac{W_i^{OUT}}{W_i^{IN}} \tag{3.7}$$

where W is the mass flow rate, (kg/s). While the inlet flow rate is known, the calculation of the outlet one is not obvious. For a given i species it results from

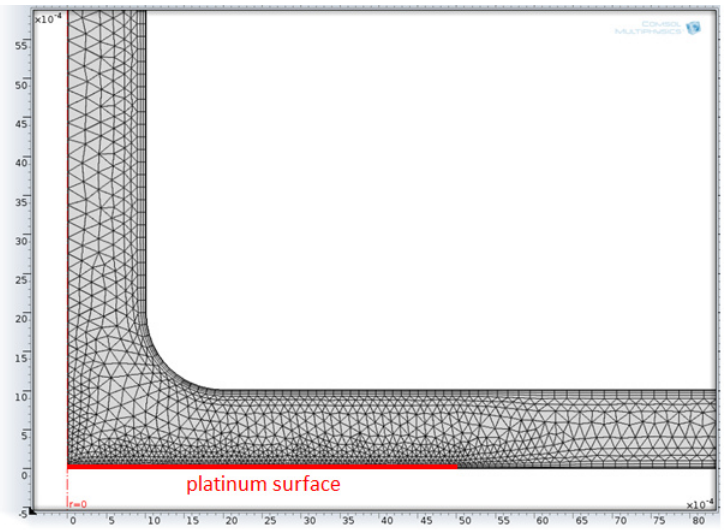

Figure 3.4: *Mesh structure adopted in the simulations. Dimensions are in meters and the figure is zoomed on the reactive area. Improved refinement close to the catalyst surface and structured mesh on the boundaries can be distinguished.*

the integral of the total flux $\mathbf{m}_i$ (kg/s/m2) over the outlet section times $2r\pi dr$, where r is the distance from the axis of symmetry:

$$W_i = \int_S m_i^N 2\pi r \, dr \tag{3.8}$$

where m_i^N is the normal flux of i and S the outlet section.

3.3 Simulation results

In the following the results obtained by solving the SPFR model described above will be presented and design indications formulated. We will first describe common feature of the reacting flow; then we will carry out a parametric study to investigate the role of the design parameters.

3.3.1 Base case

The detailed features of the results will be discussed on a reference set of parameters. These are: R_i=1 mm, d=1 mm, $k^o = 10^4$ m/s, $\dot{V}$=100 ml/min (= 1.6710^{-6} m^3/s). These are the inlet channel radius, the gap above the catalyst, the pre-exponential factor, and the inlet volumetric flow rate (at ambient conditions). In addition, the reactor temperature has been investigated form 25°C up to 500°C.

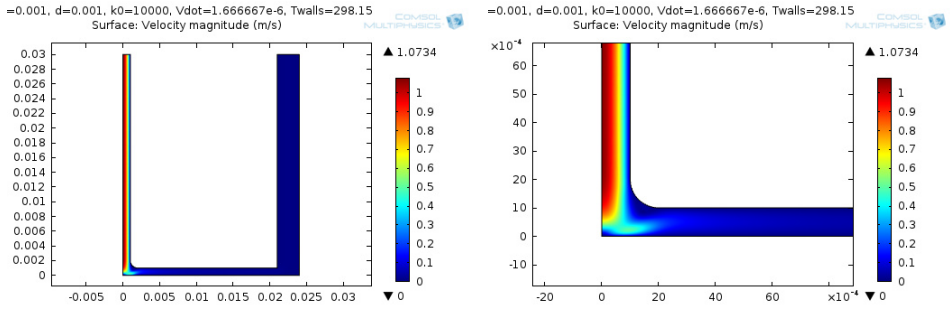

Figure 3.5: *Velocity ($= \sqrt{u_r^2 + u_z^2}$) distribution in the flow domain. R_i=1 mm, d=1 mm, $k^o = 10^4$ m/s, $\dot{V}$=100 ml/min, T=25°C. Axes report lengths, as m.*

With the purpose of understanding the efficiency of contact between the flowing mixture and the reactive Pt surface, we assumed that the gas is rich enough in O_2 to consider constant its concentration. Consistently, the simplified surface reaction rate is

$$R" = k'(T)\rho_{H_2} \qquad k' = k^o \cdot \exp(-Ea/RT) = k"\rho_{O_2}^{0.5} \tag{3.9}$$

where the pre-exponential factor is assigned arbitrary values to force a fast or slow reaction rate. The activation energy was kept constant to a value of $E_a/R =$ 6000 [K]. With the reference set of parameters, the flow field is quite obvious; it is shown in Fig. 3.5. The parabolic velocity profile rapidly develops in the inlet channel. The velocity magnitude drops dramatically when the flow diverges, in a geometry that expands the cross section by progressing from the center. This could be a concern for secondary homogeneous reactions that may evolve after the catalyst, at the higher temperature. Fig. 3.5, in its enlargement of the stagnation point, shows some unexpected velocity distribution close to the catalyst. We can investigate that region in more detail.

Fig. 3.6 shows the streamlines at 25 and 500°C. In both cases it is evident that some fluid has a path that never touches the catalyst. That was not unexpected; the flow domain has to be full of fluid that gradually flows to the periphery. The crucial issue is its velocity, if it allow the H_2 and O_2 to diffuse to the reactive surface, even from the fathers streamlines. That can be assessed by observing the H_2 flux distribution in the flow domain, as will soon be shown. From Fig. 3.6 we can also note a non obvious result. At the lowest temperature (25°C) a recirculation region stabilized near the turning corner. At higher temperature the gas flow around the corner is more uniform, notwithstanding the higher velocity. Apparently, the much lower density affects the convective transport of momentum, decreasing its inertia.

The fate of the reactant H_2 is well described by Fig. 3.7, where its total flux

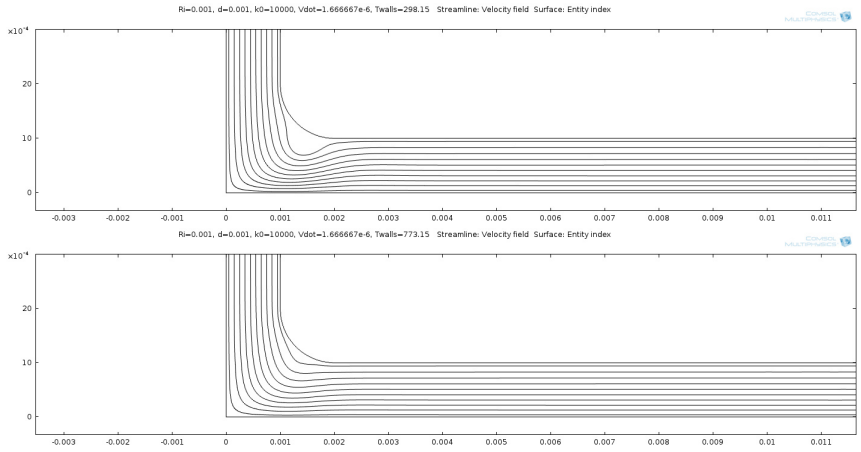

Figure 3.6: *Streamlines in the flow domain. R_i=1 mm, d=1 mm, k^o = 10^4 m/s, $\dot{V}$=100 ml/min, T=25°C (above) and 500°C (below). Axes report lengths, as m.*

(which is a vector field) is represented by arrows. At the lower temperature (panel above) the H_2 follows the convective field; H_2 reaches the surface almost entirely; it does not enter the wake beside the corner; the flux drops as the flow diverges; the surface uptake is very low, because of the low temperature that does not trigger the surface activity. At higher temperature (panel below), the sink by the reactive surface is dominant and H_2 flux after the catalyst is vanishing. Note that at the small flow rate of 100 mL/min the catalyst can determine some transfer of H_2 against the convective flow, as observed at the catalyst rightmost edge, in Fig. 3.8.

The strength of the reaction has always to compete with convection, that keeps H_2 flowing in the bulk of the gas, reducing its catalyst contact time and chances to diffuse across the main flow to reach the surface. That is investigated by rising the inlet flow rate to 300 mL/min and the results are shown in Fig. 3.9. There is a much larger H_2 flux that reaches the catalyst (note that arrows had to be rescaled for clarity, but they would be 12 times the equivalent in Fig. 3.7). Yet, the H_2 uptake by the catalyst apparently matches the larger flux, resulting in a consumption of H_2 that approaches a total conversion, as indicated by the disappearance of the flux vectors.

However, this is a semiquantitative representation, and the actual impact on the overall H_2 conversion between inlet and outlet must be evaluated, using eqs. 3.7 and 3.8. That would be consistent with the experimental practice of catalyst testing, were H_2 conversion is measured by scanning the reactor temperature. In the simulations, we collect the results (in terms of X_i) of a sequence of steady state calculations, by varying the reactor temperature (at isothermal conditions) or the inlet temperature (in adiabatic conditions). Eventually, all the results are shown a $X_{H2}(T)$ curves.

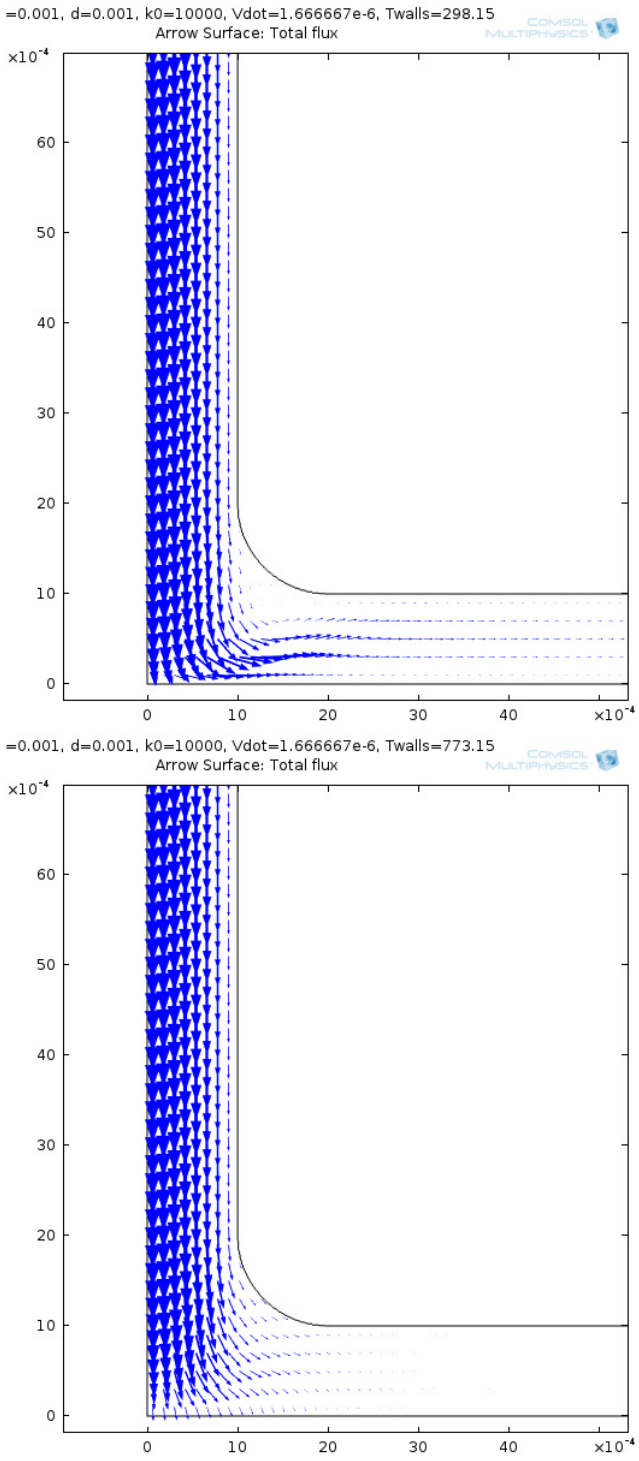

Figure 3.7: *Total (convective and diffusive) flow of H_2 in the flow domain close to the reactive surface. R_i=1 mm, d=1 mm, k^o = 10^4 m/s, $\dot{V}$=100 ml/min, T=25°C (above) and 500°C (below). Axes report lengths, as m.*

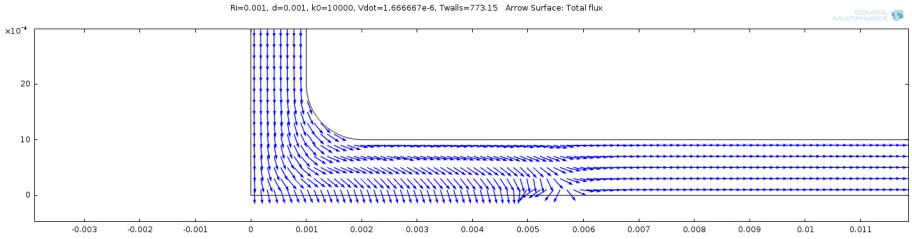

Figure 3.8: *Total (convective and diffusive) flow of H_2 in the flow domain close to the reactive surface. R_i=1 mm, d=1 mm, k^o = 10^4 m/s, $\dot{V}$=100 ml/min, T=500°C (below). Axes report lengths, as m. Arrows length is normalized (not proportional to the flux intensity).*

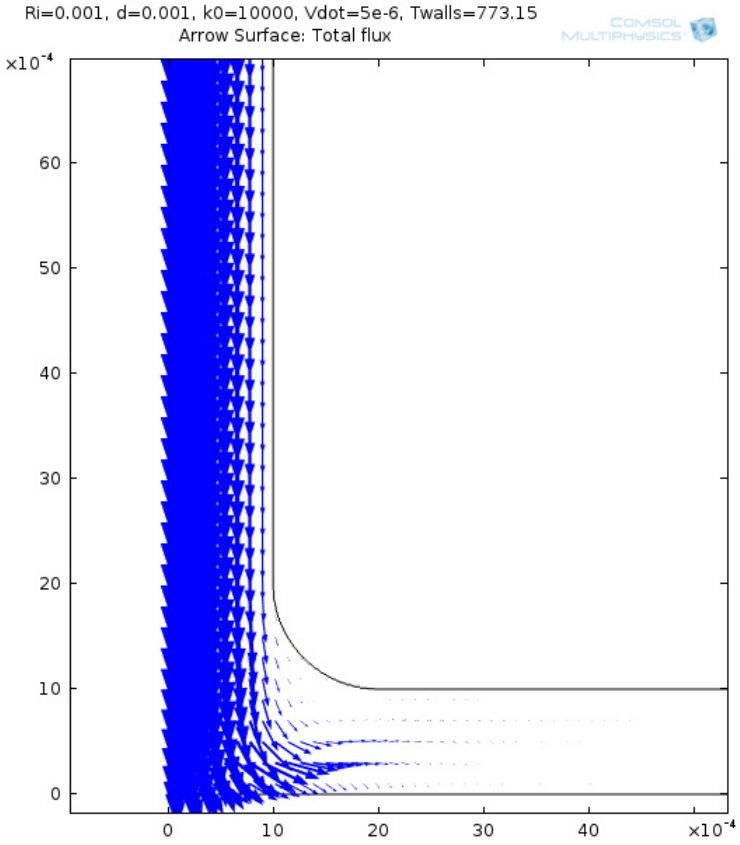

Figure 3.9: *Total (convective and diffusive) flow of H_2 in the flow domain close to the reactive surface. R_i=1 mm, d=1 mm, k^o = 10^4 m/s, $\dot{V}$=300 ml/min, T= 500°C. Axes report lengths, as m. Arrows length is scaled to 1/12 the length used in 3.7, for clarity.*

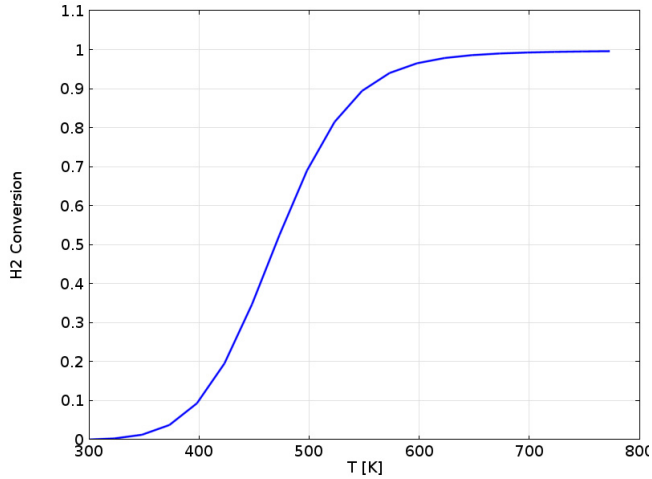

Figure 3.10: *H_2 conversion across the reactor. R_i=1 mm, d=1 mm, k^o = 10^4 m/s, $\dot{V}$=100 ml/min.*

Table 3.2: *Ranges of the conditions and lengths for the parametric analysis.*

$\dot{V}$.[mL$_{STP}$/min]	R$_i$ [mm]	d [mm]	k^o [m/s]	T [°C]
100 to 300	1 to 5	1 to 3	10^4 to 10^6	25 to 500

The $X_{H2}(T)$ results for the base case parameters, scanning reactor temperatures from ambient to 500°C, is shown in Fig. 3.10. We can conclude that in the reference conditions, total conversion can be achieved above approx. 700 K. This value is not significant per sè, because it depends on the suface reaction rate which in turn is determined by the mechanism selected and the kinetics parameters. The values of the pre-exponential factor and activation energy are indicative, simply inspired to values that are likely for Pt-catalysis. The absolute significance of the kinetics and involved parameters is not relevant at the this stage, where relative comparisons are carried out. Quite naturally, the results above call for a thorough investigation of the effect of the parameters involved, and particularly those related to the geometry. The proper identification of the dimensions is a requirement for the subsequent realization of the laboratory reactor for testing disk-shaped catalysts.

3.3.2 Parametric studies

In this section we investigate several parameters, listed in Tab. 3.2, together with the space investigated. Their meaning is: the inlet total flow rate, $\dot{V}$, the radius of the inlet channel, R_i , the gap above the catalyst, i.e. the height of the diverging section, d, the pre-exponential factor in eq. 3.9, k^o, and the reactor temperature, T, assuming isothermal operations.

Contact time

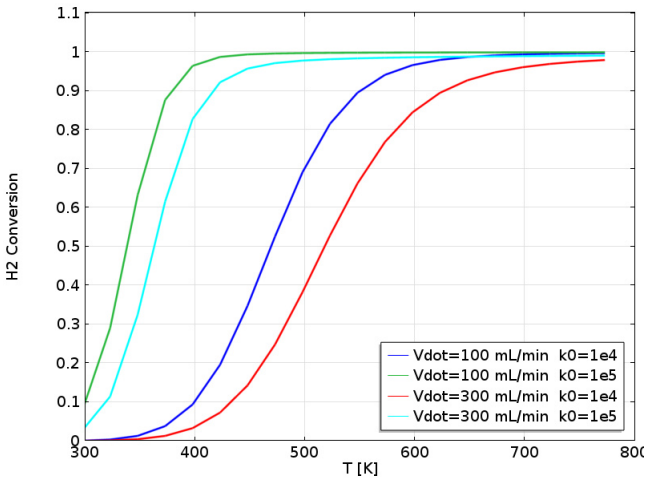

Figure 3.11: *H_2 conversion across the reactor as a function of temperature, parametric in the flow and reactions rates. R_i=1 mm, d=1 mm.*

It has already been observed that the flow and the reaction rates can affect the flow structure and consequently the final conversion of H_2. Keeping the base geometry, we explore the parameter space of Tab. 3.2 for $\dot{V}$ and k^o. In practice, the contact time of the gas with the catalytic surface is investigated, and compared to the activity of the catalyst. Results are shown in Fig. 3.11.

Total conversion can be always achieved, at sufficiently high temperature. As expected, the lower the flow rate, the lower the temperature required for total conversion. At higher reaction rate, the conversion increases significantly also at quite high flow rate. Eventually, we could formulate a criteria of equivalence in terms of a Damkhöler-type number k^o/v, to be developed further.

Interestingly, at high gas velocity (because of the flow rate and the temperature), some diffusion limitation may play a role. The temperature appears less effective in advancing the conversion, as evident by the profiles being smoother, with a smaller derivative with respect to temperature. In order to double check this

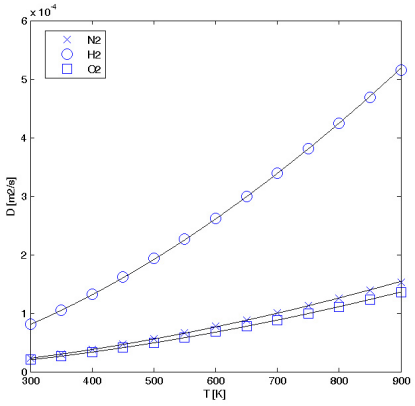

Figure 3.12: *Mixture average diffusion coefficients of H_2, O_2, and N_2, in a mixture of 1/20/79 %vol, respectively. Data calculated from CHEMKIN-II. Lines are approximations along eq. 3.10.*

intuition, we varied the diffusion coefficient of H_2, either by artificially reducing its value (using a scale factor) or including/excluding its temperature dependency, according to the formulation:

$$D_{H_2,air} = \alpha \cdot D_{H_2,air}(300K)\left(\frac{T}{300K}\right)^{\beta} \tag{3.10}$$

The approximation above has been tuned on mixture-average values calculated through the CHEMKIN-II code, using its property database. The approximation of eq. 3.10 is accurate enough, as shown in Fig. 3.12, for $D_{H_2,air}$= 8.12 10^{-5} m^2/s and β=1.692

For the parametric study, the scale factor α has been changed from 1 to 1/5 and the exponent β from 0 (=constant diffusion coefficient) to 1.692. The results for two values of the gas flow rate (100 and 300 mL/min) are shown in Fig. 3.13.

The first important observation is the large effect of the diffusion coefficient, which suggests that H_2 flux is predominantly diffusive, and not convective. The second important indication is that the assumption of constant D_{H_2} (i.e. β=0) predicts a maximum in conversion, with lower values at the highest temperature. This is not surprising, because the higher temperature determines higher velocity and then shorter contact time. Even though the reaction rate increases as well, because of the higher temperature, the conversion cannot take advantage of a faster reaction, because of the bottleneck of a limiting diffusion, unless the diffusion coefficient increases with temperature, as expected. In fact, in the high temperature region, the reaction rate is already very fast and the increase of conversion is actually controlled by the diffusion coefficient. The effect is magnified by the artificial reduction of the diffusion coefficient through the scale factor α=1/5.

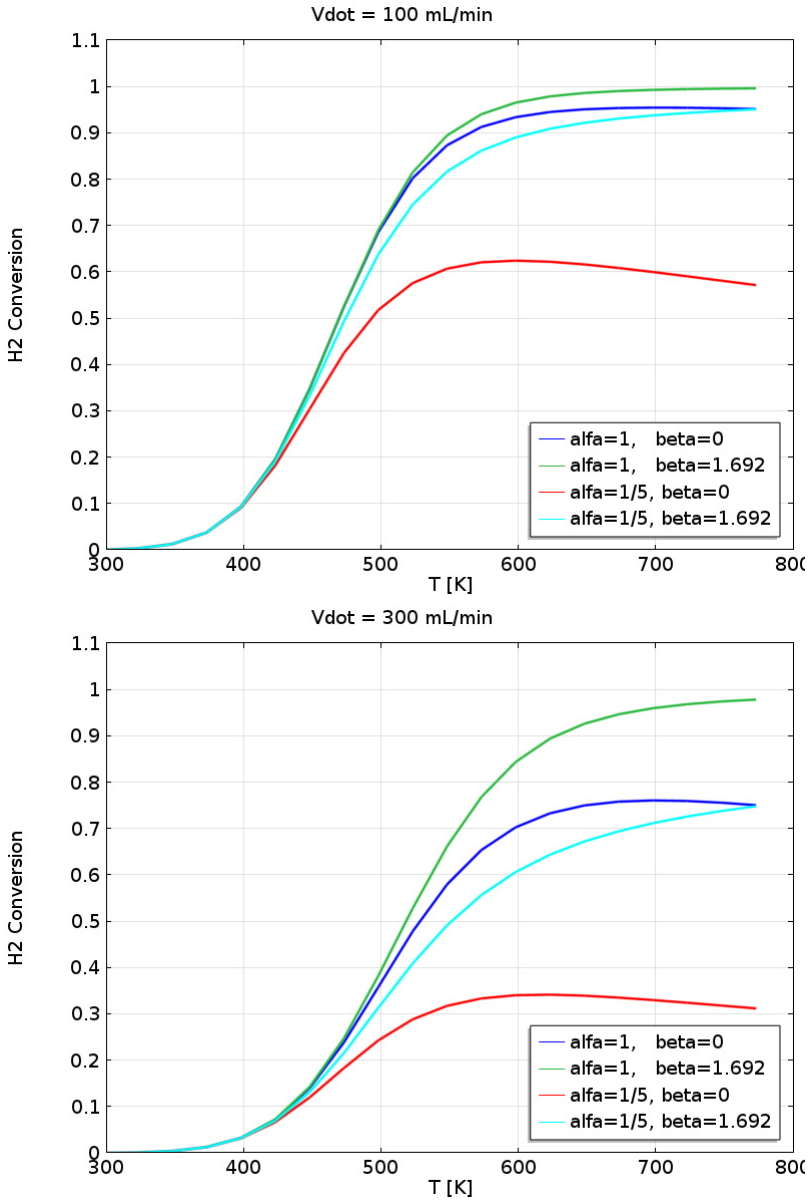

Figure 3.13: *H_2 conversion across the reactor as a function of temperature, for different modifications of the H_2 diffusion coefficient, following eq. 3.10. R_i=1 mm, d=1 mm, $k^o = 10^4$. $\dot{V}$ = 100 mL/min (left) and 300 mL/min (right)*

It must be recalled that the diffusion coefficient of H_2 is large compared with that of O_2, as already apparent from Fig. 3.12. The diffusional limitations here observed with H_2 alone, are expected to be even larger with O_2. That can be relevant for reactions approaching stoichiometric (or sub-stoichiometric) O_2.

The results of Fig. 3.13 clearly indicate that any kinetic study in this geometry, possibly with large, confined reaction rates, requires an appropriate model of the fluid mechanics and mass transfer in the reactor flow domain, that can predict accurately the interference (and limitations) that have to be ascribed to physical, and not chemical processes.

A further indication of the limitations connected with the diffusion process is that also the heat transfer rate can play a role. Of course, that is not evident in isothermal flow simulations. However, as far as the Lewis number, $Le = \lambda/\rho c_p D$, is close (or less) than unity for the limiting reagent, we can expect the oxidation process to be limited by the rate of heat conduction in proximity of the catalyst. This aspect deserves a more detailed analysis, given that the local temperature can dramatically affect the surface reaction.

Geometry

In the next section we allow for different width of the inlet channel and the gap above the catalyst, to identify the best dimensions for the final construction.

Enlarging the gap above the catalyst, d, from 1 to 3 mm causes an extension of the wake behind the corner, as clear from Fig. 3.14 at $\dot{V}$=100 mL/min. The recirculation zone is reduced at higher temperature, as already seen in the base case (Fig. 3.6). The stagnant zone grows even larger at higher inlet velocities, as shown in Fig. 3.15.

The larger section in the diverging, horizontal path, causes the velocity to drop much more than in the base case. The H_2 sink on the catalyst now prevails markedly over the convective flux, triggering an upstream flux of H_2 near the catalyst edge, as clearly shown in Fig. 3.16

On the contrary, an inlet channel as large as the catalyst, appears to take advantage of the whole reactive surface, according to Fig. 3.17. However, there is clearly a bypass through the restriction, where a jet is formed, with a high local velocity (see Fig. 3.18). The large convection caused by the jet is apparent in the H_2 flux escaping the catalyst region, very clearly marked in Fig. 3.17. The effect on the H_2 conversion is well described by Fig. 3.19. Even increasing dramatically the rate of reaction, the ignition can be anticipated, but the upper limit due to diffusive effects is evident. The maximum conversion also decreases with larger flow rate, when the jet shown in Fig. 3.18 is faster and the mass transfer to the catalytic surface, that is mostly orthogonal to the main stream, is diffusion limited. The lower panel in Fig. 3.19 clearly shows how weak is the increase of

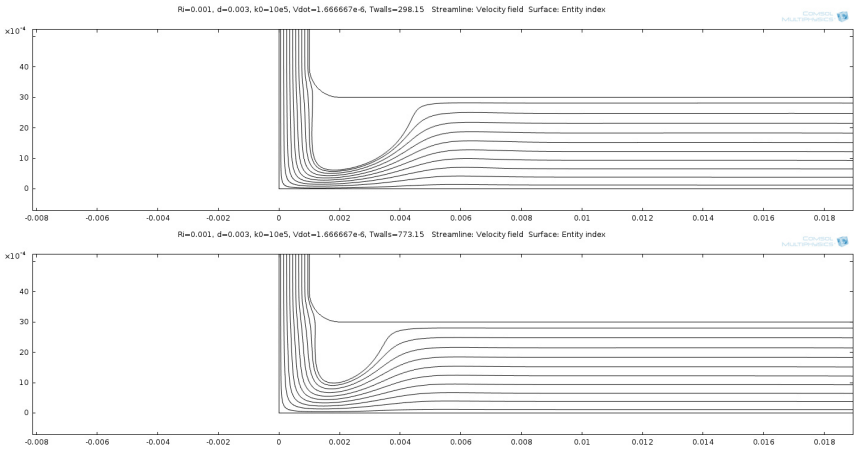

Figure 3.14: *Streamlines in the flow domain. R_i=1 mm, d=3 mm, k^o = 10^4 m/s, $\dot{V}$=100 ml/min, T=25°C (above) and 500°C (below). Axes report lengths, as m.*

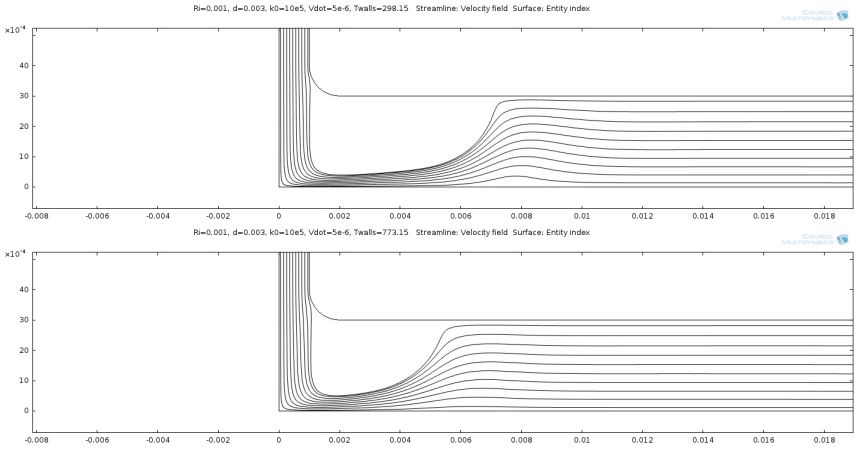

Figure 3.15: *Streamlines in the flow domain. R_i=1 mm, d=3 mm, k^o = 10^4 m/s, $\dot{V}$=300 ml/min, T=25°C (above) and 500°C (below). Axes report lengths, as m.*

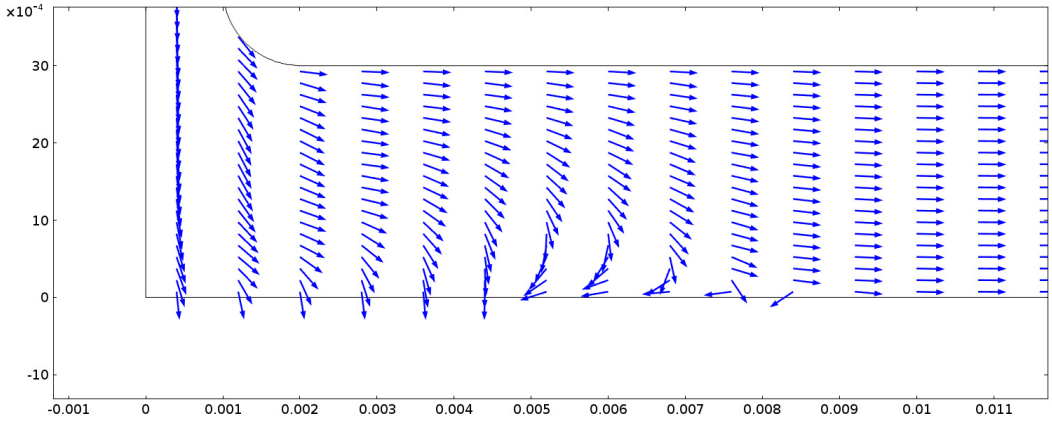

Figure 3.16: *Total (convective and diffusive) flow of H_2 in the flow domain close to the reactive surface. R_i=1 mm, d=3 mm, k^o = 10^4 m/s, $\dot{V}$=100 ml/min, T=500°C. Axes report lengths, as m. Arrows length is normalized (not proportional to the flux intensity).*

conversion with temperature, when the diffusion is controlling.

Eventually, the combined effect on the global conversion of H_2 determined by the two critical dimensions, R_i and d, is summarized in Fig. 3.20. The common consequence of enlarging the flow passages is always a loss of conversion and a larger control by diffusion, which is evident by the damping of the temperature positive effect on conversion, above a level of temperature, that shifts progressively to lower values, as the flow cross sections increase. The larger flow passages amplify the effect of larger flow rates, that are clearly even more affected by the diffusive control (conversion increases more gradually with temperature).

The parametric studies at isothermal conditions allows to conclude that the SPFR has to be built with the smallest possible diameter for the inlet channel and minimum gap that can be reproducibly achieved above the catalyst. Accordingly, given the mechanical tolerances and the approximation in the disk positioning in its seat, we concluded that the best configuration is R_i=1 mm and d =1 mm.

In order to promote the validity of the isothermal assumption, gas phase heat transfer has been studied as a function of the inlet flow rate. The SPFR model has been expanded by including the energy balance to evaluate fed gas preheating from ambient temperature to the reactor one. It must be underlined that the heat of reaction was still neglected. The gas-phase temperature map reported in Fig. 3.21 evidenced that, at low gas inlet flow rate, heat transfer from reactor body to the gas phase thoroughly pre-heated the gas phase up to the reactor operative temperature. On the opposite, at high inlet flow rate, heat transfer was limited by the prevailing convective flux. 400 K are not exceeded in the gas phase approaching the catalyst in the central area. Being the isothermal assumption fundamental for the following

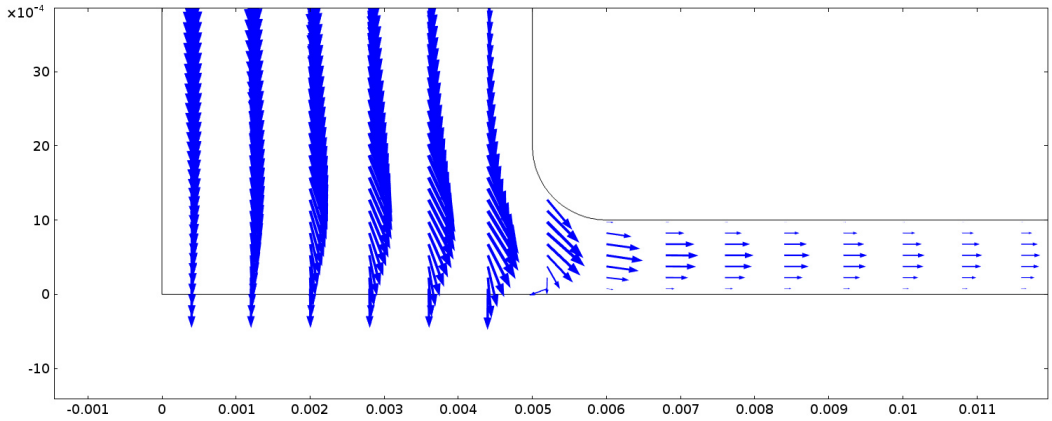

Figure 3.17: *Total (convective and diffusive) flow of H_2 in the flow domain close to the reactive surface. R_i=5 mm, d=1 mm, $k^o = 10^4$ m/s, $\dot{V}$=300 ml/min, T=500°C. Axes report lengths, as m.*

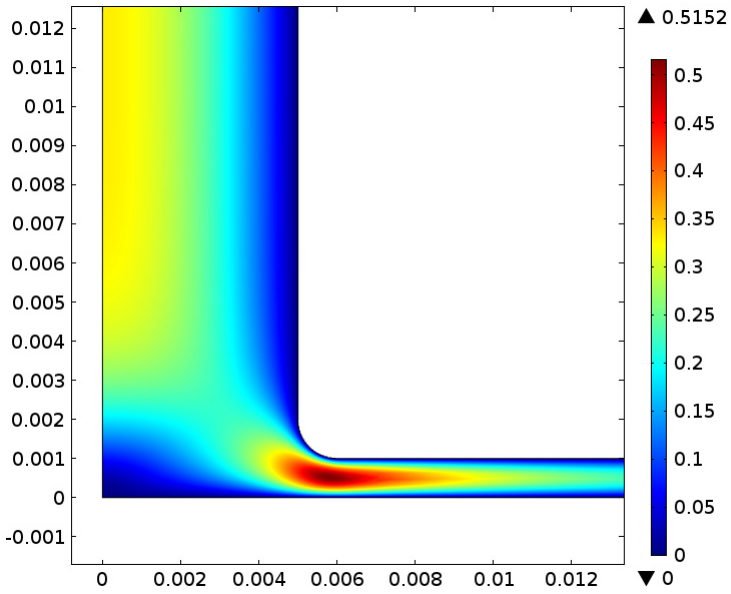

Figure 3.18: *Velocity ($= \sqrt{u_r^2 + u_z^2}$) distribution in the flow domain near the catalyst. R_i=5 mm, d=1 mm, $k^o = 10^4$ m/s, $\dot{V}$=300 ml/min, T=500°C. Axes report lengths, as m.*

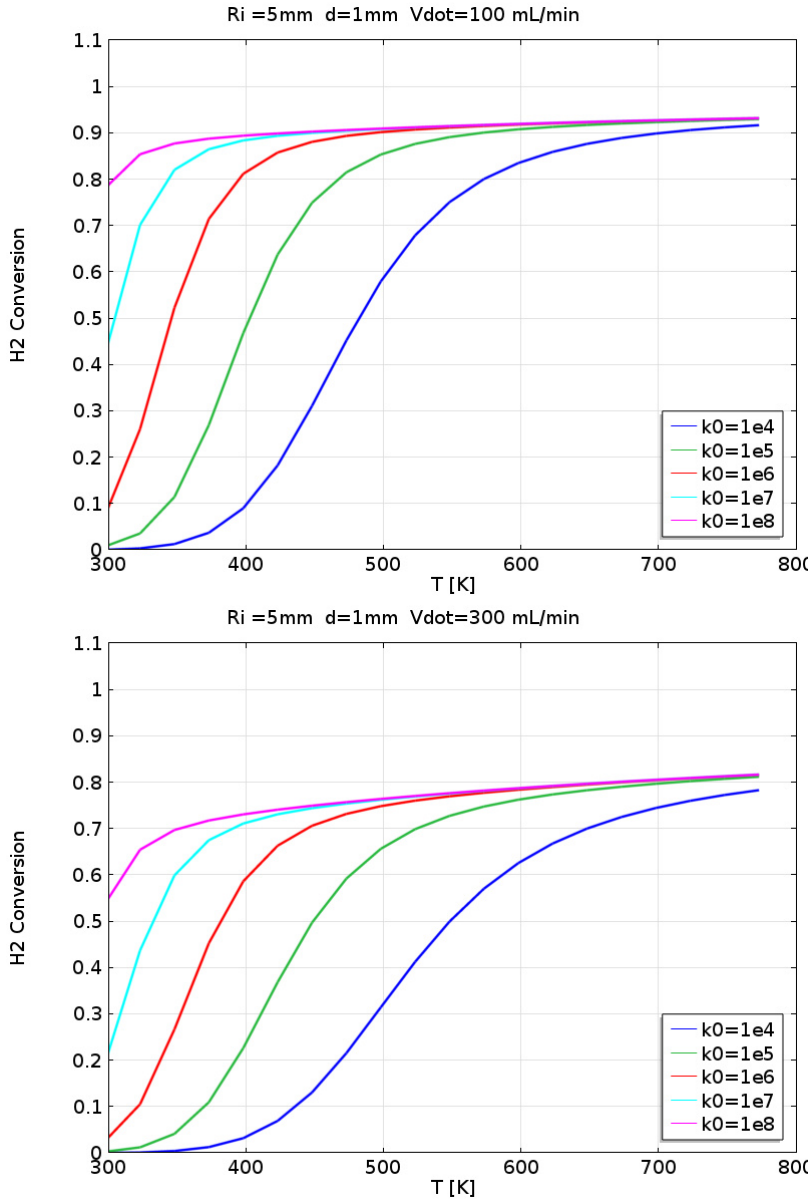

Figure 3.19: *H_2 conversion across the reactor as a function of temperature, at increasing reaction rate. R_i=5 mm, d=1 mm, $\dot{V}$ = 100 mL/min (above) and 300 mL/min (below).*

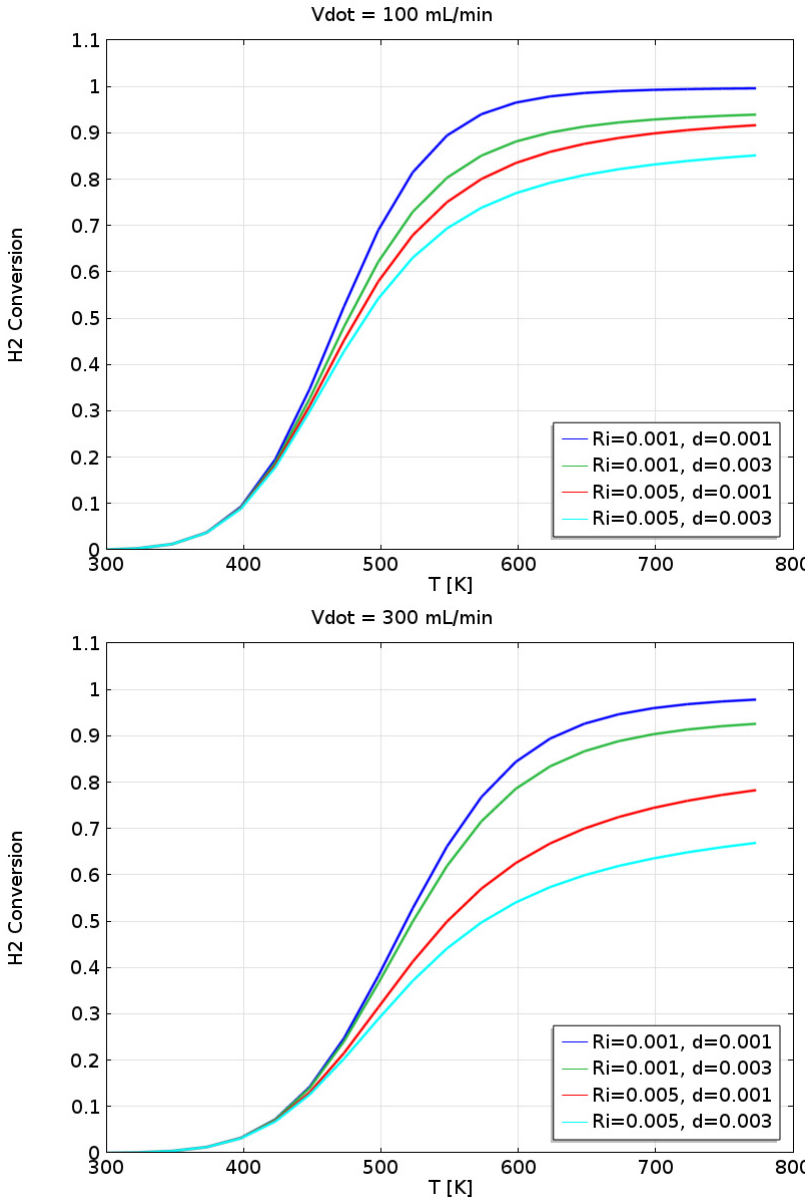

Figure 3.20: *H_2 conversion across the reactor as a function of temperature, for different modifications of the critical reactor dimensions, R_i and d=1 mm. k^o= 10^4m/s $\dot{V}$ = 100 mL/min (above) and 300 mL/min (below).*

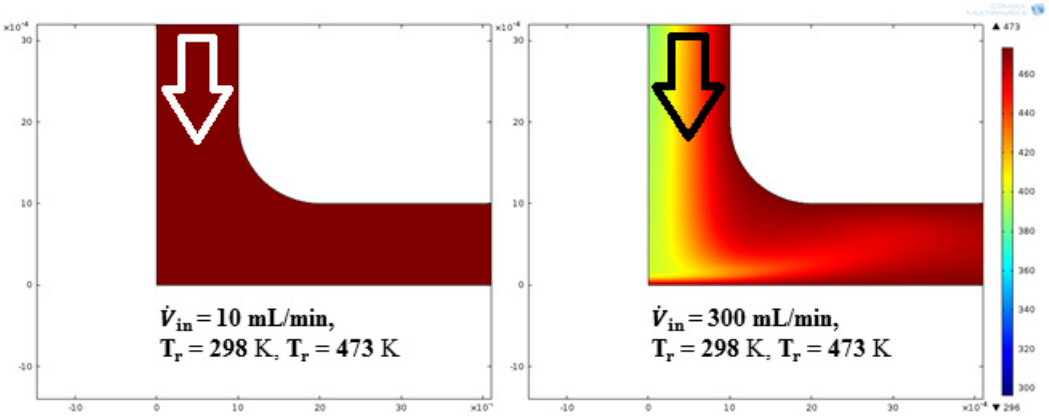

Figure 3.21: *2D temperature colour map of the stagnation point flow reactive area. Gas inlets and direction are shown by the arrows. Homogeneous temperature has been evidenced for 10 mL/min inlet flow rate, on the opposite isotropic temperature distribution was not achieved for the 300 mL/min case.*

tests, gas inlet flow rates should not exceed 100 mL/min in order to guarantee complete gas pre-heating.

3.4 Laboratory testing unit

After the previous design investigation, the final reactor has been built as shown in the following section 3.4.1. Through this prototype, the H_2 oxidation on Pt disks has been carried out in a laboratory testing rig schematically shown in Fig. 3.22.

Along the gas flow we can see the mass flow controllers (Bronkhorst), a T-junction/static mixer, the reactor with the catalyst inside, the analytic instruments. Reaction products were monitored both with a mass-spectrometer (HIDEN HPR-20), for high frequency, semi-quantitative analysis, and with a gas chromatographer (Agilent 7820), for quantitative measurements, but at lower sampling frequency. Each part is connected to one or more computers and specifically: i) the mass flow controller's set points are imposed through a manufacturer program that communicates with the flow meters through a serial connection; ii) the oven is controlled by an Omron temperature controlled, whose setting and monitoring is based on CX-Thermo software (Omron); ii) each analytic instrument is controlled by proprietary software of the instrument supplier, each one based on a different computer.

According to the total flow rate and the desired mixture compositions, three mass flow controller have been used to assemble the feed mixture,one for H_2, one

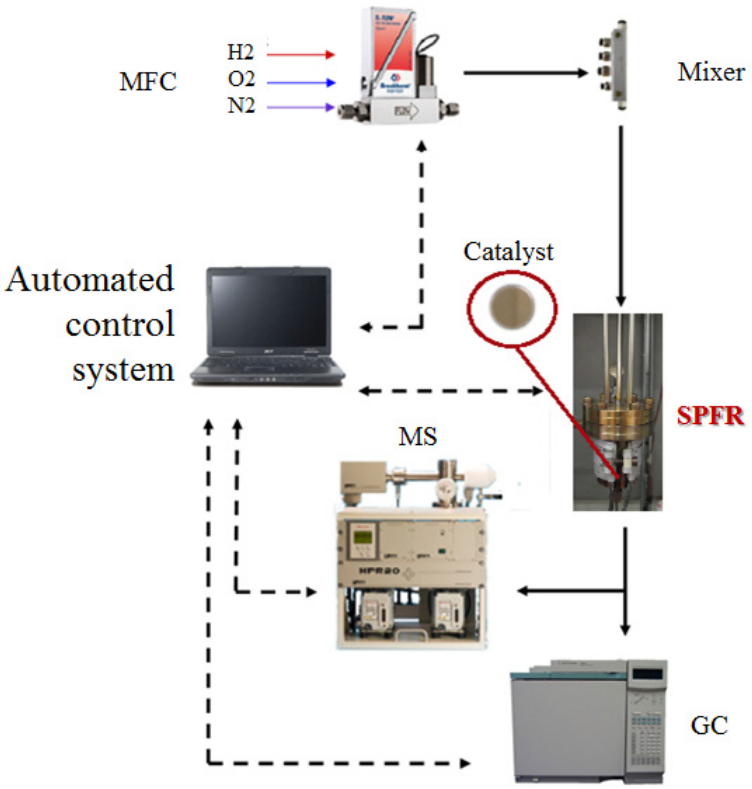

Figure 3.22: *Pictorial view of the laboratory testing rig. Gas flow (solid lines) and control connections (dashed lines).*

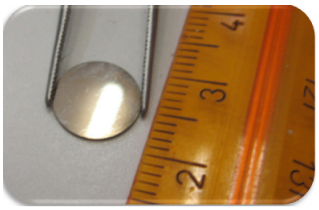

Figure 3.23: *Bulk platinum disk used to study H_2 catalysed oxidation in the SPFR.*

for O_2, and another for the inert gas. A static mixer was introduced upstream of the reactor. Details on reactor configuration, gas ans surface analyses are discussed in the following section.

3.4.1 SPFR final design

On the basis of the previous parametric studies, an actual stagnation point flow reactor prototype has been built. It has been conceived to test disk shaped catalyst, mainly precious metals, with a diameter of 11 mm and thickness of 1 mm as shown in Fig. 3.23.

The easiest building strategy is made clear in in Fig. 3.24. The reactor was obtained from two stainless steel bodies. These are the blue and the red parts in 3.24, left. They are coupled and hold together by screws, as shown in the same Figure, right. The internal body has the inlet channel drilled at its center. Once coupled,the two bodied allow for some space between them, then collect the gas after the contact with the catalyst.

The gas flows in through the central channel, it impinges orthogonally on the catalyst surface, then it flows radially from the center to the periphery of the internal body, escaping through the gap between bodies, up to the two collecting pipes on the top.

The reactor build as shown in 3.24 keeps some design parameters free to be adjusted while others had to be fixed. The gap above the catalyst can be modified through suitably thick spacers, positioned between the two flanges where the two reactor's parts are coupled. Most of the measurements have been carried out using a value of 1 mm, for this gap. The total flow rate and the reactor temperature can be clearly set quite easily over sufficiently large ranges. Unfortunately, the inlet channel radius cannot be easily modified. It has been set at 1 mm. In principle, it can be modified as well, by inserting a liner in the channel that reduces its opening section, but that has never been attempted

A coating with Titanium nitride has been applied by chemical vapour deposition (CVD) to limit the interaction between the reactants and the metals (Cr, Ni,..) and their oxides contained in the stainless steel of the reactor body.

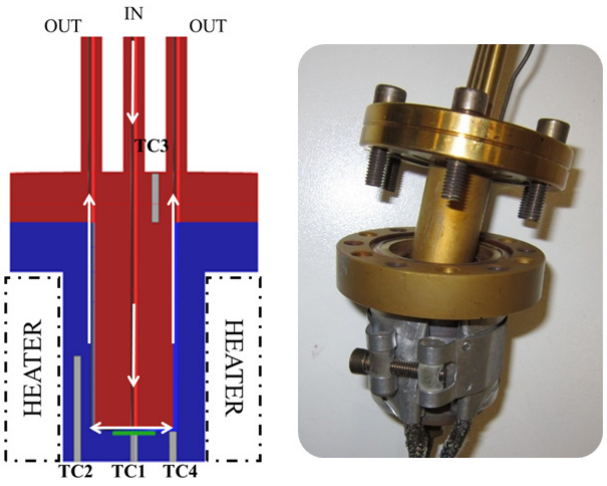

Figure 3.24: *Schematic representation of the SPFR (left) and a picture of the actual SPFR as built (without external insulation). The Pt disk, highlighted in green, is set on the bottom of internal part of the external body.*

Reactor heating was provided by a 275 W band heater clearly visible in the picture 3.24. It operates at 220V and it is controlled by a suitable designed controller which directly modulates the current. The set point is compared with the catalyst temperature, that is assumed as representative of the whole reactor. This assumption is further discussed below.

External insulation was obtained with a high density 30 mm thick quartz wool layer, enveloping the whole reactor body and part of the piping.

3.4.2 Temperature distribution

The reactor has been equipped with four K-type thermocouples for measuring the temperature of the catalyst, of the gas phase, in the reactor lower body and in the flange. Following the previous sequence, TCs have been named TC1, TC2, TC3 and TC4 respectively. Their actual position is shown in 3.24, left.

Considering the small thickness (1 mm) and the high thermal conductivity of the platinum disk (71.6 W/m K at 300 K), the temperature measured by TC1, on the lower side of the Pt disk, has been assumed representative of the upper side as well, the one directly exposed to the reactive mixture.

The catalyst thermocouple is connected to the temperature controlle, whereas the other three were simply measured and recorded.

The assumption that the reactor is isothermal, i.e. the temperature is the same in each part of it, has been validated by comparing the measured temperatures in a

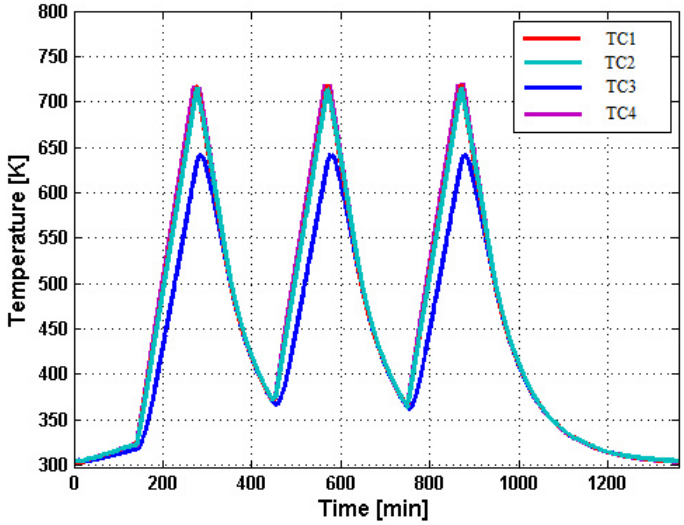

Figure 3.25: *Temperature measured by the 4 thermocouples during heating and cooling cycles. No reaction (pure N_2). Gas flow rate = 75 mL/min.*

preliminary test, using an in inert gas (N_2, inlet total flow rate $\dot{V}$ = 75 mL/min, with heating and cooling cycles. Results are summarized in Fig. 3.25 for 3 sequential cycles.

Temperature profiles reported in Fig. 3.25 clearly show that all the temperature profiles are very close, except for the thermocouple positioned on the top of the flange, which is much colder. Measurements suggested to extend the thermal insulation around the reactor, above and below it. In any case, we believe that the measurements validate the isothermal assumption.

3.4.3 Gas analysis section and configuration

Hydrogen oxidation is an extremely fast reaction in which stable gas species H_2 and O_2 (reactants) and H_2O (product) are involved. Semi-quantitative and quantitative analysis have been adopted for catalytic activity measurements. The advantage of this configuration consist in the coupling of continuous real-time analysis (mass-spectrometer), which are suitable for fairly fast transient studies, with discontinuous, quantitative measurements (gas-chromatograph) by which uncertainties in semi-quantitative results may be adjusts.

Being the mixture fairly simple, we attempted using a direct access mass spectrometer. Mass-spectrometry is an analysis technique based on samples ionization. The instrument used in the present work is the Hiden HPR-20 QIC (0-200 amu) It is mainly composed by three parts: the ionizing system, the quadrupole

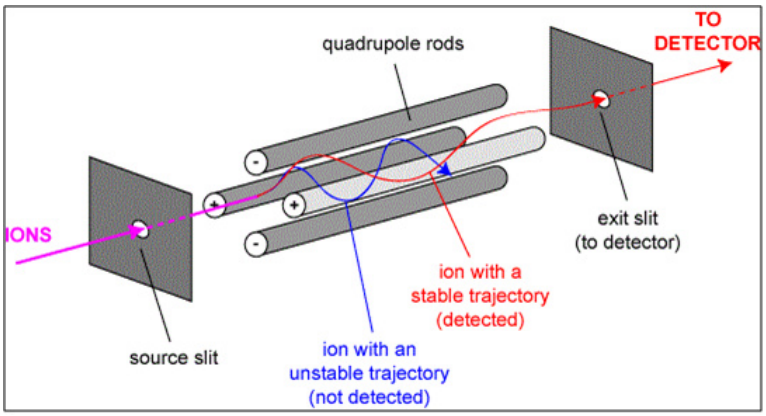

Figure 3.26: *Schematic representation of the quadrupole filter and ions paths through it.*

mass analyzer and the detectors. Inside the first section, an electron beam hits the sample and splits the components into ionized fragments. These fragments form a characteristic pattern that varies according to the ionization energy. The quadrupole, which is composed by four cylindrical metal rods, selects a specific ion according to its mass(m)/charge (z) ratio. Rods are coupled and connected electrically, thus a radio frequency voltage (RF) is applied between a pair of rods and the other one. A direct current voltage is then imposed on the radio frequency voltage. All fragments obtained from the first part are further accelerated by an electric potential and force to cross the space between the rods. Because of the direct current and radio frequency voltage, fragments undertake a sinusoidal trajectory according to their m/z ratio. Only the fragments with the given m/z ratio have a stable path through the quadrupole and they only reach the detector, as shown schematically in Fig. 3.26.

The detector provides measurements expressed in terms of species partial pressures. Once scaled to the signal of the total pressure, they approximate molar fractions. Data are affected by signal interference from molecule fragments with similar m/z characteristic ratio. Moreover, the instrument operates in high vacuum (10^{-7} Torr), thus pumping fluctuations destabilize the signals, showing fake dynamics.

In order to overcome the intrinsic uncertainties of the mass-spectrometer analysis, a gaschromatograph (Agilent GC-7820) has been used as well. The instrument in the configuration that we used is principally composed by three main parts, shown in Fig. 3.27: two valves, two columns (Porapak-Q and Mole Sieve 5A) and one detector (TCD). The two valves configuration allows for i) one sampling valve, in which the sampling loop (consisting in a calibrated volume of 250 μL) entraps the outflow gas mixture and allows for its injection, and ii) a switching

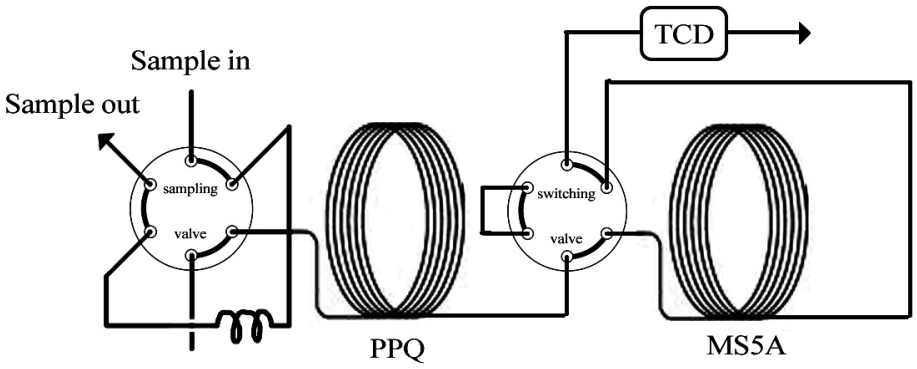

Figure 3.27: *GC7820 valves, columns and detector configuration.*

valve, which can be programmed, on the basis of specific gas residence times, to exclude one column. Thermal Conductivity Detector (TCD) was installed, nitrogen was fed as carried.

In ready-mode, GC sampling valve was heated up to 390 K, in order to avoid water condensation, while columns temperature was set at 330 K. After sample injection in the first column (PPQ), H_2 and O_2 were allow to flow in the second one (MS-5A). As a consequence of the significant low residence time, permanent gases can elute to the detector before that water reaches the MS-5A column, which may be damaged by H_2O adsorption. By switching the second valve and heating the columns to 390 K, water was directly sent to the TCD. Instrument has been calibrated for the gas species involved in the reaction, in order to unequivocally determine the relationship between peak magnitudes and the amount of analyte. Experimental data post-processing was carried out with a Matlab code, which also checks for mass balances and determine the reactants conversion profiles, representative of the reaction kinetic, were obtained.

The water produced that reaches the GC is quantified but the transfer line in not traced, being quite long, so that condensation along the lines cannot be excluded, even if very diluted mixtures are used.

3.4.4 Platinum surface analysis

Platinum surface evolution at reactive conditions has been investigated. In order to determine macro restructuring of the surface, developing some indentation that may affect the specific surface area of the platinum disk, Environmental Scanning Electron Microscopy (ESEM) has been applied before and after catalyst exposure to reactive mixture.

In a typical SEM, an electrons beam is thermionically emitted from an elec-

tron gun fitted with a tungsten filament cathode. When the primary electrons beam interacts with the sample, the electrons lose energy by repeated random scattering and absorption within a teardrop-shaped volume of the specimen, known as the interaction volume, which extends from less than 100 nm to approximately 5 μm into the surface. The size of the interaction volume depends on the electron's landing energy, the atomic number of the specimen and the specimen's density. The energy exchange between the electron beam and the sample results in the reflection of high-energy electrons by elastic scattering, emission of secondary electrons by inelastic scattering and the emission of electromagnetic radiation, each of which can be detected by specialized detectors. The resulting image is therefore a distribution map of the intensity of the signal being emitted from the scanned area of the specimen by which sample's surface topography and composition can be observed. A wide range of magnifications is possible, from about 10 times (equivalent to that of a powerful hand-lens) to more than 500000 times, about 250 times the magnification limit of the best microscope in the visible light. Surface analysis has been carried in collaboration with Centro Universitario Grandi Apparecchiature Scientifiche (CUGAS), equipped with an FEI Quanta 200 ESEM, at University of Padua.

In addition, investigation of the possible rearrangement of the surface crystalline structure has been carried out in collaboration with dott. Marta Maria Natile from the Department of Chemical Science at University of Padua. X-ray crystallography allow for identifying the atomic structure of crystalline surfaces. A finely focused monochromatic beam of X-ray is directed to the crystal surface, producing a diffraction pattern of regularly spaced spots known as reflections. By measuring the angles and intensities of these diffracted beams, three-dimensional pictures of the electron densities within the crystal can be reproduced. Diffraction can be modulated to better highlight the surface characteristics, instead of the solid volume ones adopting the grazing incidence X-ray configuration. That reduces the beam penetration into the bulk material and focuses on few atomic superficial layers.

Chapter 4

Experimental studies of H_2-O_2 reactivity on Pt surfaces

In the previous chapters we saw that detailed surface mechanisms are not fully consistent among each other. They predict quite different behaviors, particularly for the critical adsorption/desorption steps (chapter 2). However, each one is consistent with a given set of experiments, which in turn are not fully comparable. To progress the understanding of these differences in the experimental results of Pt as a catalyst, we endeavored to collect data on bare Pt surfaces, either single crystals or polycrystalline ones. For that purpose, we designed and built a novel stagnation point flow reactor (Chap. 3), whose results are presented in this Chapter.

We attempt to highlight the origin of macroscopic effects, like the different ignition temperatures. We wish to identify the causes of such differences and then develop the ability to reproduce them. We anticipate causes like i) uneven temperature distribution in the catalyst area 2) local gas velocity, including its shearing rate 3) some catalyst surface structure rearrangement, at reactive conditions.

Platinum catalysed hydrogen oxidation has been reproduced in the SPF reactor described in Chap. 3, operated at different conditions. Inlet composition, flow rate and heating policies were adjusted according to the different goals. Tests can be grouped in the following sections:

- reactor and catalyst preliminary tests;
- catalyst activation;
- catalyst pre-treatments effects;
- ignition temperature screening.

Catalytic inactivity of the stainless steel components of the reactor bodies, has been initially verified. Subsequently, platinum bulk disk was introduced in the reactor to test the catalytic hydrogen oxidation starting from ”virgin” conditions.

The initial catalytic activity was found to be quite lower than expected, with the new catalyst. Platinum activation strategies have been carried out, investigating the platinum surface evolution. Scanning Electron Microscopy (SEM) and X-Ray Diffraction (XRD) analysis confirmed significant surface restructuring and surface crystalline evolution after platinum exposure to reactive conditions. The effects of catalyst pre-treatment by oxidizing or reducing mixtures have been later investigated. Finally, the ignition temperature at different hydrogen partial pressure has been systematically measured and compared to Literature data.

4.1 Preliminary tests

At the beginning of the experimental campaign, some tests have been carried out to asses the measurements reproducibility, the lack of misleading factors in the reactor and setup, the reference activity of the Pt disk.

Reactor blank tests

The first concern in any experimental investigation should be spotting any misleading factor. Catalytic activity of the reactor body itself, made of stainless steel, had to be verified, before the introduction of the platinum bulk disk. Earlier experiments on surfaces different from Pt, namely microporous alumina, revealed by post-run XPS measurements, the unexpected presence of Ni on the surface. It was attributed to some release from the stainless steel exposed to the H_2+O_2 mixture, at temperatures in excess of 723 K.

The SPFR reactor has been subsequently coated with titanium nitride, TiN, to avoid interference in the catalytic activity caused by the metallic components of the stainless steel surfaces. The thin TiN film has been deposited by Physical Vapour Deposition on the whole reactor surface, including the most internal ones. The surface layer deposited is estimated thinner that 3 μm, which does not modify the reactor design. Blank tests were carried out to experimentally validate the chemical inertia of the reactor internal surfaces. Results for temperatures up to 455 K, with reactant inlet mole fractions x_{H_2} = 5 % and x_{O_2} = 5 % and inlet flow rate 50 mL/min, are reported in Fig. 4.1.

MS profiles clearly confirmed that the measured species partial pressure remained sufficiently constant during heating, with the same composition measured at ambient temperature. We concluded that no reaction occurred. Some noise has to be noticed in partial pressure profiles. However, the logarithmic scale emphasizes the small signal fluctuations. The standard deviation of the measured profiles, if related to the average as reported in Eqn. 4.1, was estimated around 2%, sufficiently small to be neglected.

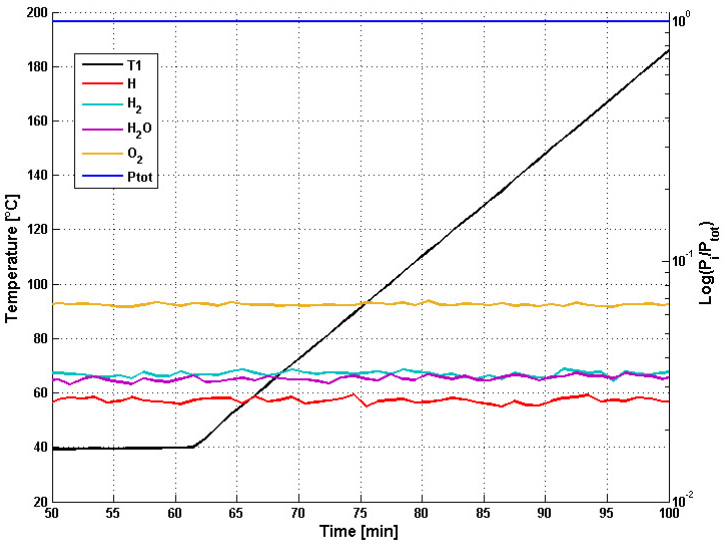

Figure 4.1: *Outlet composition from the empty SPFR, as given by MS in terms of partial pressures. Ramp heating policy has been adopted up to 455 K.*

$$C.V. = \frac{\sigma}{\bar{x}} = \frac{\sqrt{\frac{1}{n-1}\sum_{i=1}^{n}(x_i - \bar{x})^2}}{\bar{x}} \tag{4.1}$$

Results substantially underline the quality and stability of the mass-spectrometer signal, which has been adopted for most of the following tests.

The original platinum catalytic activity

As already mentioned, there are reasons to believe that the Pt activity in the H_2-O_2 reaction is depends on the Pt disk history. That would lead to a search for a procedure to reset the Pt history to a reproducible *initial state*. That would be discussed later in this Chapter.

At the time of the preliminary tests, and the *original* disk was used. This conventional initial state is the result of the disk remaining for a period of more than 1 year in a box, at ambient conditions.

The initial Pt disk catalytic activity was measured at fuel lean conditions (x_{H_2} = 2 % and x_{O_2} = 20.5 %), to limit the hydrogen inhibition and to promote reaction ignition at low temperature. Results are reported in Fig. 4.2. Despite the low hydrogen inlet concentration and the relatively high temperature achieved, the H_2 conversion measured was extremely small. The activity begins at approx. 400 K and the maximum hydrogen conversion measured was 8% at 473 K.

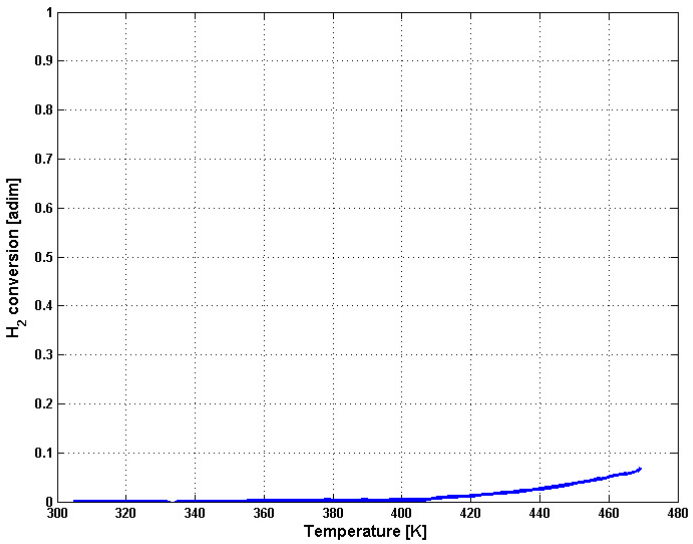

Figure 4.2: *H_2 conversion as a function of reactor temperature at fuel lean conditions (H_2=2%m, O_2 = 20.5%). Heating rate = 2 K/min. Initial disk state.*

Compared to the experimental data collected in Fig. 2.8, such a low Pt catalytic activity is surprising small. Fig. 2.8 suggests that the ignition temperature for very small α values (here is approx. 0.1), with $\alpha = p_{H_2}/(p_{H_2} + p_{O_2})$, should be below 360 K. That is much lower that the result reported in Fig. 4.2. We conclude that the disk in its initial state is not as active as expected from Literature data.

4.2 Catalyst activation

On the basis of previous experimental experiences in the Literature [44, 73, 79, 45], catalyst activation can be achieved by suitable pretreatments.

Catalyst surface restructuring is a known phenomena, widely discussed in literature both for bulk metals [44, 74, 80] and for supported or composites configurations [81]. As demonstrated in [74], STM analysis confirmed that H_2 is a candidate to enhance the diffusion rate of Pt atoms, on a Pt(110) surface, up to 500 times at room temperature. Moreover, catalytic etching in H_2/O_2 mixture at reactive conditions has been attributed to the interaction of radicals, most likely HO_2, and the catalyst surface atoms which evaporate as metastable platinum-containing species.

Despite the amount of experimental evidences of the solids transformations, when exposed to reactants, to the best of the Author's knowledge, there is not a

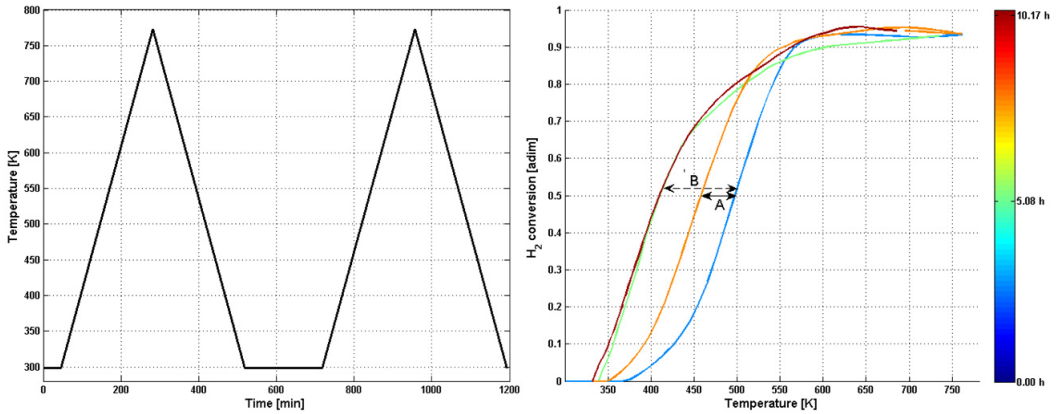

Figure 4.3: *Temperature set-point profile (left). Heating/cooling rate = 2 K/min. H_2 conversion as a function of reactor temperature at H_2 richer conditions (H_2 =5%, O_2 = 5%, α = 0.5). $\dot{V}$=50 mL/min. Disk after catalyst pre-treatment at 973 K in H_2 diluted mixture (right). The time scale is represented by the progressive changing of the colour line, from blue (t = 0) to dark red (end of the test =10.17 h in this case).*

well defined relation between platinum restructuring and catalytic activity.

4.2.1 H_2 pretreatments

With the aim of triggering some activity, Pt disk was exposed to H_2 diluted mixture (10% in nitrogen) at 973 K for 8 hours. Afterwards, activity tests have been carried out. When not involved in pre-treatments or activity test, catalyst was kept under flowing inert atmosphere (Ar) to avoid adsorption of contaminants on the platinum surface.

We applied a thermal policy based on two similar cycles, each one composed by heating and cooling phases in the range 323-773 K, at constant rates, as represented in Fig. 4.3 (left). Again, we planned to measure the reaction light-off. With respect to the preliminary tests, reactant mixture composition has been modified to $\alpha = 0.5$, with $x_{H_2} = x_{O_2} = 5\%$. Note that O_2 is twice the the stoichiometric value. The initial aim was improving the analytic sensibility to hydrogen partial pressure variations. Later we understood that the ignition behavior is strongly affected by α.

Results are shown in Fig. 4.3 (right). Time is described by the color: from blue to dark red, respectively to the initial and final instant of the test. With this logic, blue and orange lines refer to the two heating phases. Both lag behind the cooling branch, suggesting that ignition is more difficult than extinction.

It is well clear that catalyst pretreatment significantly improved the catalytic activity. There is a very good reproducibility of the measured activity during the cooling paths, at significantly higher catalytic activity with respect to the heating paths, where the conversion is significantly different for the two cycles. At 400 K, the H_2 conversion during the heating branch was 5% in the first cycle and 13 % in the second, while it was approx. 45% during both cooling branches.

The activation occurred despite (or perhaps supported by) the quite high temperature achieved, as compared to the preliminary test. The onset of activity is now estimated at about 370 K for the first cycle after the H_2 pretreatment. It grows to 50% of H_2 conversion at 500 K, up to a maximum of 95%, which is lower than 100% for the limitations discussed in Chap. 3.

As said, the activity during the heating cycles is quite different from the one measured during cooling. It also changes from the first to the second cycle. Apparently, there is some hysteresis then. Comparing the two heating trends, hysteresis can be quantified at $T_{50\%}$. The same conversion is achieved at different temperature during heating or cooling cycles. As evidenced on Fig. 4.3 by arrows A and B, the same conversion can be referred to 500K (first heating), 460K (second heating), 400 K (both cooling). Overall, a difference as high as 100 K can be observed.

This is a very significant results, if reported on the ignition plot like the one of Fig. 2.8. We can easily speculate about one of the reasons for the Literature experimental data from different experiments to be as different as 100 K. It would be enough to report the activity measured during heating (the largely prevailing practice), instead of the one during cooling, seldom considered. However, Fig. 4.3 shows that the activity during heating can vary from one experiment to its replica, immediately following it. Accordingly, the unequivocal identification of ignition temperature is an open issue.

Now the question is to what extent these changes can occur and whether and asymptotic behavior exists. If the changes are due to modifications of the surface, there will be a direct impact on the microkinetics model that could explain that. Clearly, the *active site* concept must be revised, to some extent. Either their number or their nature is changing. Apparently, the $X(T)$ profiles during the heating cycles shown in Fig. 4.3 are progressively shifting to the profiles measured during cooling.

The simplest explanation is non-chemical. It assumes that the differences arise from temperature difference in the reactor. During heating the reactor could be less uniform in temperature with respect to cooling, because the heating rate is excessively large. To clarify this intuition, we modified the heating policy, turning to a sequence of constant temperature steps, each one lasting 2 hours. Each step is achieved with a slow, 1 K/min heating rate, to avoid thermal instability (overshoots) and to facilitate a tighter temperature control. The new heating policy is

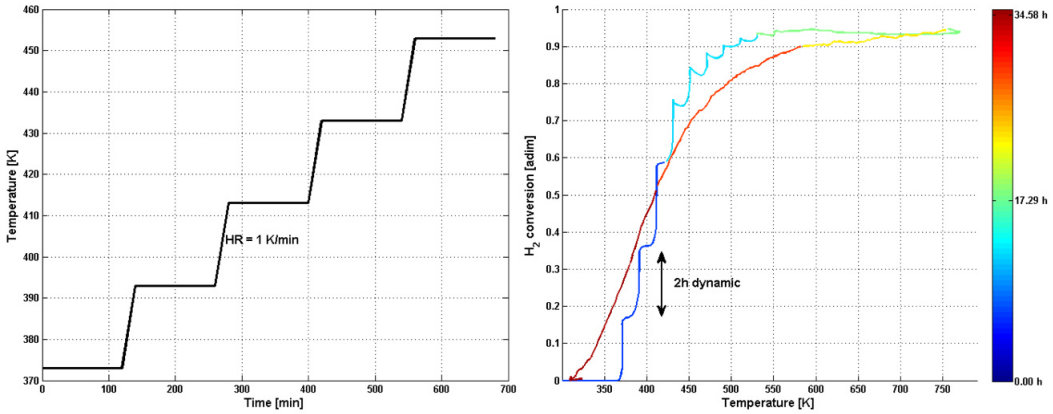

Figure 4.4: *Temperature set-point profile for stepwise heating (left); magnification of a few intermediate steps of the whole sequence, applied between 323K and 773K. Heating rate between steps = 1 K/min. Cooling rate = -2 K/min. H_2 conversion as a function of reactor temperature at H_2 =5%, O_2 = 5% (α = 0.5)(right). $\dot{V}$=50 mL/min. The time scale is represented by the progressive changing of the color line, from blue (t = 0) to dark red (end of the test = 35.58 h in this case).*

shown in Fig. 4.4, together with the results achieved.

The first impressive result is the evolution of conversion at constant temperature, almost at any temperature. At 373 K, H_2 conversion was apparently zero at the onset, but keeping this temperature for a longer time, caused a dramatic increase of conversion, up to 16%. Note that this value approaches the one measured during the cooling phase. The same happens with the second step, at 393 K, at which conversion raised up to 35% while it was less than 15% in the second heating cycle reported in Fig. 4.3. At 393 K the stepwise heating leads to a conversion very close to the one measured during cooling. At higher temperature steps, we always measured an increase of activity during the isothermal operations, but gradually decreasing the gain of conversion achieved over the 2h duration of each step. Oddly enough, increasing the temperature after an isothermal step, leads to a drop of conversion, at higher temperatures. That is very clear about 450 K. It means that activity decreases as the temperature rises, which is quite astonishing.

Overall, Fig. 4.4 shows an almost completely reduced hysteresis between heating and cooling cycles, if heating is carried out stepwise, with quite long lasting isothermal steps. In addition, the very long stepwise heating leads to activity in excess of the one measured during the cooling branch, expected to be the upper boundary to the measurable activity, and apparently the asymptotic value. Indeed, the $X(T)$ profile during cooling measured after the stepwise heating, is exactly the same at the one measured twice in Fig. 4.3. Impressive reproducibility is

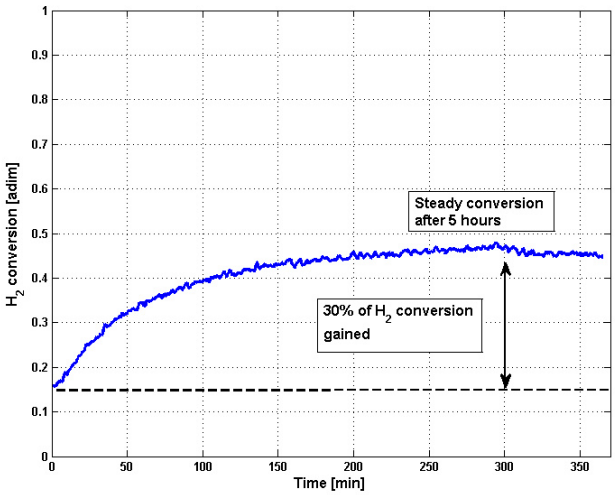

Figure 4.5: *H_2 conversion as a function of time. Reactor temperature = 393K. H_2 =5%, O_2 = 5% (α = 0.5). $\dot{V}$=50 mL/min. The time scale is represented by the progressive changing of the color line, from blue (t = 0) to dark red (end of the test = 35.58 h in this case).*

observed during cooling. Still, a fairly long permanence at increasingly constant temperature somehow *superactivates* the Pt disk.

All these evidences suggest that some evolution of activity takes place over time scales that are much larger than the one expected for thermal transients in a very small, stainless steal reactor. It is not even clear if the 2h steps, apparently quite long, allowed to complete the activation process, or additional evolution could take place. To further investigate the surprising catalytic activity evolution, H_2 oxidation has been carried out at constant temperature until a steady state was reached. Results at T = 393 K are shown in Fig. 4.5.

Unexpectedly long evolution of activity has been measured, to finally reach the steady state. The initial H_2 conversion was estimated about 15%, but it progressively increased, achieving 45% steady conversion, after approx. 5 hours. The steady state conversion was actually in excess of the one achieved after 2h, confirming that the evolution shown in Fig. 4.4 was not complete. Note also that after 120min=2h, the activity measured in Fig. 4.5 is higher than the one achieved at 393 K, after 2h at that temperature, and a previous stepwise heating from 323K. Apparently, the Pt disk is continuously evolving, after the initial H_2 pretreatment, becoming progressively more active.

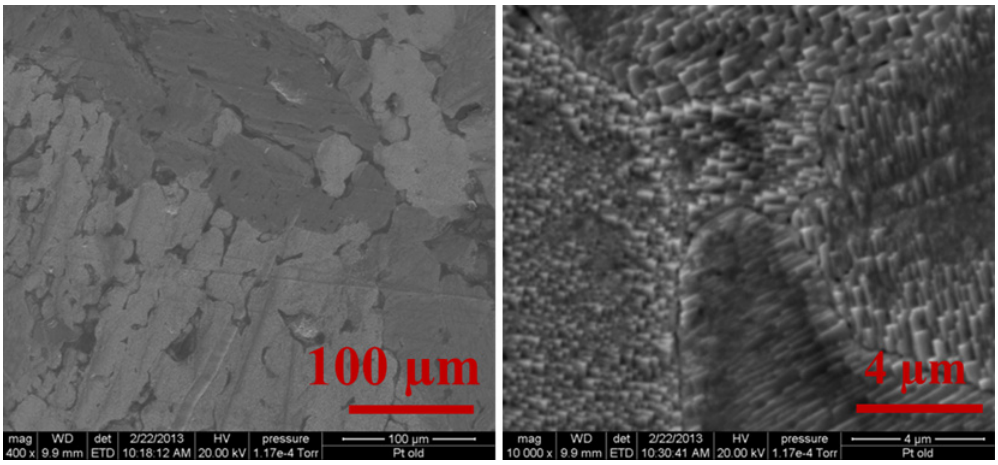

Figure 4.6: *SEM analysis of the Pt surface after H_2 pretreatment and the preliminary reactivity tests.*

4.2.2 Intermediate Surface Characterization

After these preliminary tests that saw a dramatic improvement of activity, following an initial exposure to H_2 and repeated H_2 oxidation reactions, the status of the catalyst surface has been checked. At this stage, simply SEM analysis was used, aiming at verifying morphology changes after the exposure to reactive atmosphere. As shown in Fig. 4.6, at two magnification ratios, surprising surface restructuring occurred. At the smallest magnification we can identify uneven grains, with a size distribution having characteristic length of approx. 100 μm. At a higher magnification, pillared structures can be clearly observed on the grain boundaries, protruding from the surface, up to an estimated height of 1 μm. Unfortunately, this is the outcome of several treatments, not allowing to retrace which one mostly contributed to the surface transformation. However experimental results confirmed that the temperature-activity relationship is not so obvious and that catalyst is a living structure which evolves when exposed to the reactive mixture.

The reaction rate increase was apparently related to the surface reorganisation; two main aspects have to be invoked to explain it:

- **specific surface area**: the number of platinum active sites directly exposed to the reactive mixture may be significantly increased by the observed roughness, enhancing the hydrogen conversion rate. In this sense, surface evolution at reactive conditions is promoted by the platinum atoms diffusivity;

- **crystalline structure**: despite the specific surface area evolution, local crys-

talline structure changes should be involved as responsible of the different interaction with the reactive molecules. As reported in the Literature [61, 82, 83], adsorption and desorption mechanism are strongly related to the crystalline orientation thus influencing the overall apparent kinetics. The platinum appears to self-restructure towards a preferential and more reactive crystalline orientation. Experimental evidences will be provided later in this Chapter.

4.2.3 Reducing/oxidising pretreatments

Reactants have been found to interact with the catalyst surface, not only in terms of intermediates towards reactive species, offering a lower activation energy path, but also being directly involved in surface morphology evolution.

In this section we present and discuss the effects of exposure of the catalyst surface to single reactive species, in diluted mixture. Species selected are the individual reagents, i.e. H_2 and O_2, diluted in N_2. Each single gas pretreatment was carried out at a constant temperature, for a given time (60 min). Then the initial activity in H_2+O_2 reaction was measured, at a conventional temperature of 120 ^{o}C (393 K). The pretreatment is applied a second time, increasing the temperature by 50 degrees each time.

The initial activity tests at the end of each pretreatment cycle were carried out at stoichiometric composition (5% H_2, 2.5% O_2) to preclude the prevailing of the most abundant reagent in the the solid/gas phase interaction.

Before additional tests to measure the evolution of the activity, the Pt disk was lapped in an attempt to return its surface (thus its activity) to the original state, by removing the observed roughness.

H_2 pretreatments

The first sequence of pretreatements was based on H_2 exposure, to confirm and develop the results discussed in Section 4.2.1. The sequence of pretreatments-reaction, at increasing pretreatment temperature, is sketched in Fig. 4.7). The temperature is lowered to 393K after each pretreatment cycle at higher temperature, to measure the activity at stoichiometric conditions.

The activity was measured at a relatively mild temperature, to reproduce conditions where homogeneous reaction can be completely excluded, surfaces other than Pt will not interact, nor release any trace elements. The H_2 feed composition was kept constant at 5% during the entire test, whereas O_2 feed was activated only in correspondence of the activity test at 393 K, once temperature has been dropped to 393K, as represented in Fig. 4.7. The H_2 conversion during the low temperature phases is shown in Fig. 4.8.

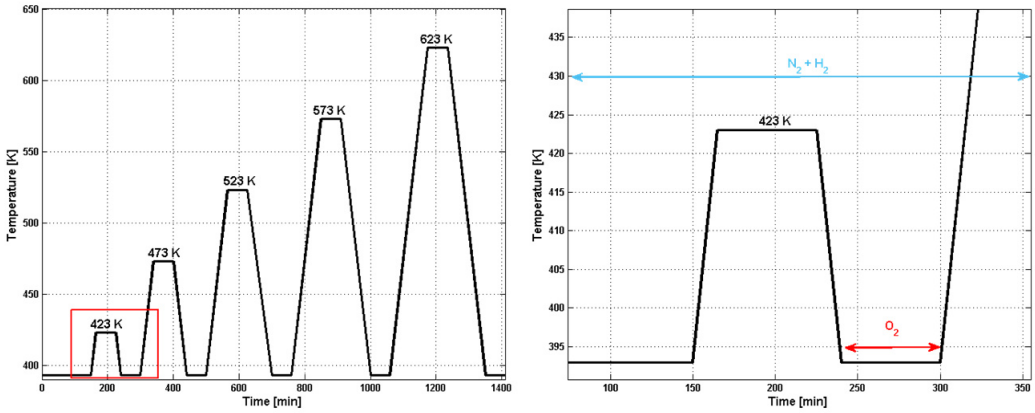

Figure 4.7: *Temperature profile (left) alternating pretreatments and reaction at 393K, and gas feeding scheme (right), switching on and off the O_2 feed.*

The initial activity, after the first pretreatment, is quite scarce, which confirms that lapping is an effective procedure to reset the surface. The initial H_2 conversion, as soon as O_2 is fed, is very low, something like 2%, but it rapidly rises up to approx. 5%. This result is consistent with Fig. 4.2, reporting what was called the *original* activity. In that case the activity measured at 393K was even lower, but the experiment was totally different. There, the temperature was constantly rising, at 2K/min, without any pretreatement before testing the activity. Results of Section 4.2.1 clearly pointed out that the activity may increase simply remaining at a given temperature where reaction is active. In this respect, the constant rate of heating interferes with the activation time scale; if the HR is too high, experiments will report lower activities than actually achievable.

The H_2 conversion measured after each additional pretreatment step, Fig. 4.8, was constantly increasing. Despite the relative low temperatures during pretreatments, gradual improvement of the catalyst activity was noticed after each pre-treatment, from 5% up to 60%, after 5 cycles (Fig. 4.8. Interestingly, the higher the temperature of the pretreatment, the higher the initial reactivity, at the first O_2 contact. Considering the test after H_2 pretreatment at the highest temperature, 623 K, the initial conversion was 65% and it progressively decreased, settling at 60%. Once again, that was interpreted as an indication that surface reactivity can change during the exposure to the reactants, i.e. along the course of the reaction.

Overall, the results of this experiment, summarized in Fig. 4.8, clearly show that catalytic activity is not an intrinsic properties of the metal, as apparent from the classification of microkinetics mechanism available in the Literature. These are classified as detailed mechanisme for a given chemistry on a generically spec-

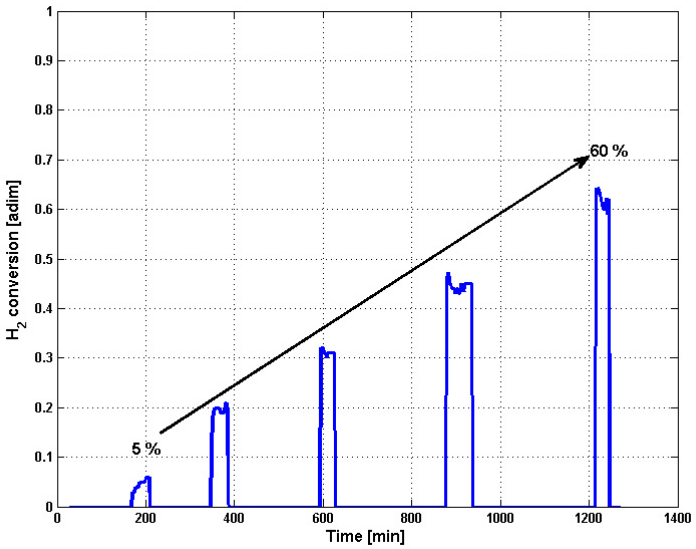

Figure 4.8: *H_2 conversion as a function of time in periods at 393K, between H_2 pretreatments at increasing temperature. H_2 =5%, O_2 = 2.5% (α = 0.67). $\dot{V}$=75 mL/min.*

ified metal, without further detail, except for a generic, constant surface site density. The catalyst activity strongly depends on the interaction with the reactive species and it can evolve enormously.

SEM and XRD surface characterization were carried out after the activity test sequence of Fig. 4.8. The surface morphology, according to SEM is shown in Fig. 4.9. Despite the large magnification, larger than Fig. 4.6, Pt surface appears very uniform and no grains boundaries are evident. Simply the unavoidable scratches from the lapping procedure are clear from the analysis.

In contrast with the SEM results, XRD reported a dramatic change in surface crystal structure, as a consequence of the H_2 preatreatments and activity tests sequence, as shown in Fig. 4.10. The preferential surface crystalline orientation on the Pt disk surface before the H_2 preatreatments and activity tests sequence was found predominantly Pt(111), typical of a poly-crystalline Pt, with a smaller fraction of Pt(200) domains. After H_2 treatments and reaction, the surface structure appears reversed, with a Pt(200) crystals arrangement largely prevailing on the Pt(111). Rearrangement has been clearly induced by the pretreatments and reaction cycles We attribute to the Pt(200) phase the largely enhanced activity of the Pd disk, once more suggesting that any comparison among activity of Pt surface requires a thorough understanding of the detailed surface structure, at least in terms of prevailing crystal domains.

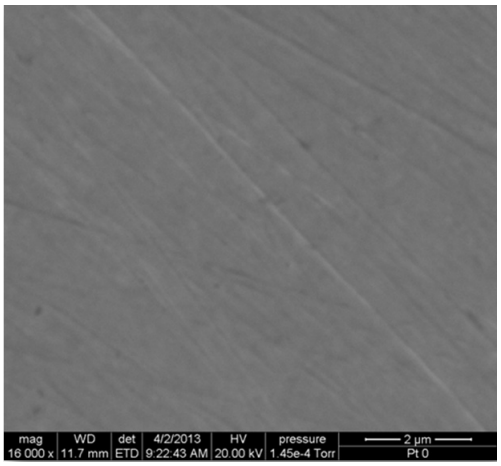

Figure 4.9: *SEM analysis of the Pt surface after the sequence of H_2 pretreatments and activity tests.*

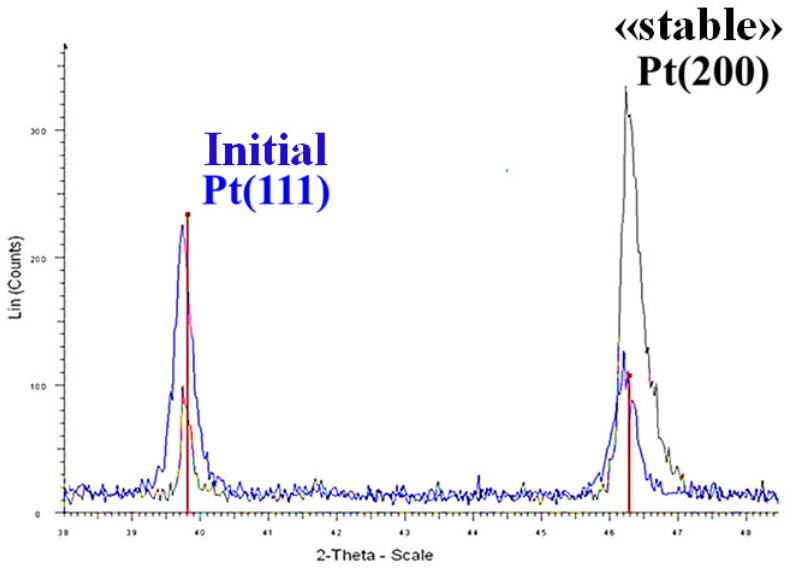

Figure 4.10: *XRD analysis of the Pt surface before (blue) and after (black) the sequence of H_2 pretreatments and activity tests.*

H_2/O_2/thermal pretreatments

Similarly to the previous tests, further investigation on the effects of different pretreatments has been carried out. Now we designed a series of pre-exposure and reactions cycles. Always keeping N_2 flowing at a constant flow rate of 75 mL/min STP, we applied:

1. 5% H_2, at a temperature of 575K, for 1h; the temperature is reached by heating at 3K/min and cooling at the same rate took place, down to 393 K; accordingly, the total duration of the heating interval is approx. 4h, with just 1h at the maximum of 573K. Afterwards, the activity is measured at 393K, with ϕ=1.

2. Pure N_2, at a temperature of 575K, for 1h; the temperature is reached and released with the same policy described for the step 1; this is a simple thermal treatment. Then, the activity is measured at 393K, with ϕ=1.

3. 5% O_2, at a temperature of 575K, for 1h; again, the same T(t) described for the step 1 was used; Again, the activity is measured at 393K, with ϕ=1.

Note that the maximum pretreatment temperature was limited to 573 K, 50 K lower than the previous test of Fig. 4.7. Also, pure N_2 was fed during heating and cooling phases, before and after each 1h pretreatment, respectively, to desorb reactant traces from the platinum surface. Finally, the sequence was applied to the disk as it results from the testing described in Section 4.2.3. Accordingly, we expect an H_2 conversion of approx. 60% at 393K, with the same stoichiometric mixture (5%H_2, 2.5% O_2) used in Sec. 4.2.3.

For a simpler exposition of the results, we reported in Fig. 4.11 the 3 cycles overlapped, on the same time scale. The standard heating policy used for all the 3 cycles is shown just once, to clarify its description above. Then, the H_2 conversion following each different pretreatment is shown, sharing the same time scale.

The first common observation is the initial activity drop. Immediately after any pretreatment, the activity is always the highest. Afterwards, within the 1h testing interval, activity always drops markedly, by about 20%. The loss of activity is already in progress after 1h, indicating that a stationary condition is far to reached. That will be the subject of a subsequent investigation, reported below.

H_2 and purely thermal pretreatments did not affect the quite high activity achieved after the H_2 exposure campaign reported in Sec. 4.2.3. The initial H_2 conversion is always about 60%, as expected (Fig. 4.8). However, the activity is rapidly lost, progressively reducing to 45%.

On the opposite, catalyst exposure to O_2 led to a surprisingly high initial activity, peaking at 85%. Also in this case, the exceptional activity degrades rapidly, down to 65%.

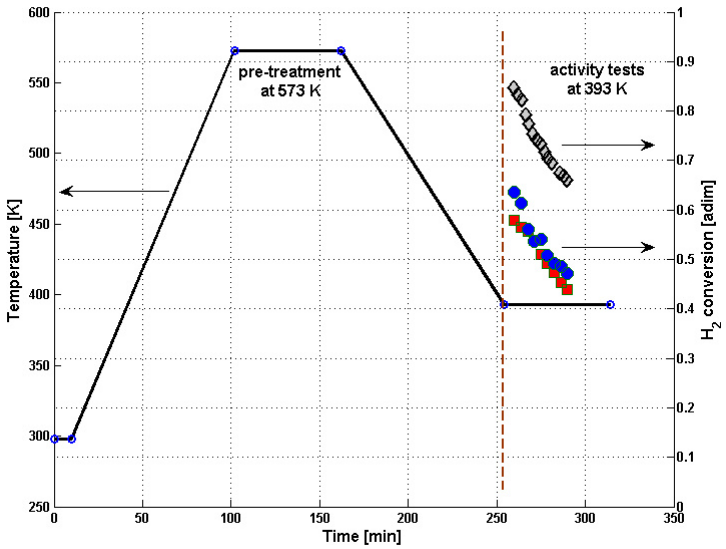

Figure 4.11: *Temperature set-point profile (solid line) and H_2 conversion measured after H_2 (•), thermal (■) and O_2 (◇) pretreatments. Reaction conditions: H_2 =5%, O_2 = 2.5% (α = 0.67). $\dot{V}$=75 mL/min.*

On the basis of the common knowledge about the affinity for Pt of H_2 and O_2, also discussed in Chapter 2, and reflected in the microkinetics available, the progressive loss of activity can be ascribed to the hydrogen self-inhibition.

Being the temperature 393 K quite too low for a competitive O_2 adsorption rate, H_2 tends to exclusively adsorb on the Pt surface, reducing Pt sites availability an then the global reaction rate. That explains also the higher activity after O_2 pretreatment. Despite the N_2 flow during cooling, aiming at desorbing any O_2 left, the high activity is consistent with a large initial availability of adsorbed O_2. Afterwards, H_2 is evidently able to displace it, depressing the surface activity.

Quite naturally, the question now is where the activity will end up, calling for longer intervals of activity testing. The disk has been reset by lapping, as described above, to remove the previous history of treatments. Then, the same experiments reported in Fig. 4.11 have been repeated, with a longer phase of activity testing, up to a steady value. That required 5h after H_2 and up to 9h after O_2 pretreatments. The results are shown in Fig. 4.12.

First observe that the actual reacting mixture is fed 1h after the stabilization of the testing temperature of 393K. It has been done to single out the possibility that the initial activity could be higher because the local temperature on the catalyst surface, after cooling, could have been higher that the 393K expected and

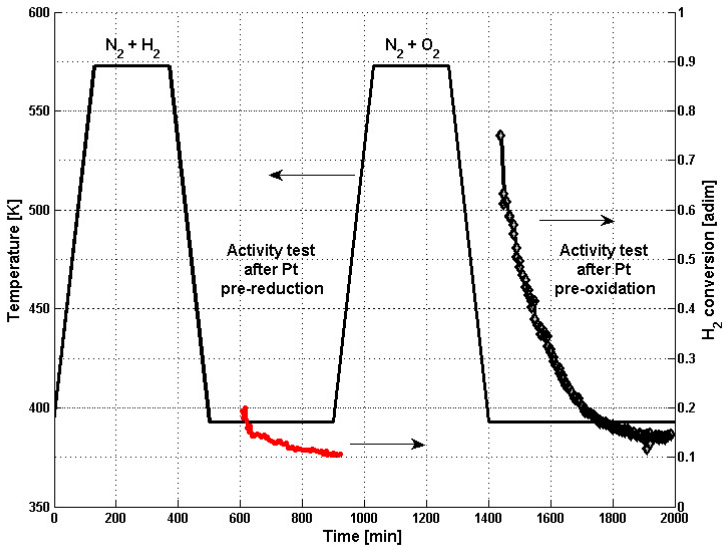

Figure 4.12: *Temperature set-point profile (solid line) and H_2 conversion measured after H_2 (red symbols) and O_2 (dark symbols) pretreatments. Reaction conditions: H_2 =5%, O_2 = 2.5% (α = 0.67). $\dot{V}$=75 mL/min.*

measured on the bottom side of the Pt disk. Results clearly indicate that the initial activity is always the highest, excluding the thermal disequilibrium hypothesis.

The second observation is that the initial activity after H_2 pretreatment is much lower than observed in Fig. 4.11, when the disk was activated by several cycles of H_2 pre-exposure. The results confirms that i) lapping is effective in resetting the activity ii) a 1h H_2 pretreatment is not sufficient to rise the Pt disk reactivity, despite the fairly high temperature of the pretreatment. Re-analysing in this perspective the results of Fig. 4.8, we conclude that the activation of the Pt disk requires a suitable combination of temperature and contact time, which must last sufficiently.

Again, per-exposure to O_2 give the surface a very high initial activity. Unfortunately, it drops dramatically as soon as H_2 can displace surface oxygen.

However, the most noticeable result is the achievement of a common asymptotic level of activity, whatever pretreatment has been applied. The evolution requires a significantly long interval of time after both pretreatments, i.e. 5 hours after the H_2 pretreatment and 9 hours after the O_2 one. The results show that the gas phase/solid interactions force the Pt to a lower activity when exposed to the full reactive mixture, which does not depend on the initial conditions.

4.3 The catalytic ignition temperature

The previous experiments suggest that the amount of O_2 in reacting mixture could substantially affect the Pt surface reactivity. All the evidences have been collected at constant temperature, with the same stoichiometric H_2-O_2 mixture. In this section we explore a larger range of temperature and mixture composition, always in the O_2-rich ($\alpha < 0.5$) range, down to very lean ($\alpha = 0.019$) mixtures. These have been achieved by varying the H_2 mole fraction in the feed in the range 0.4% to 15%, in synthetic air. The total inlet flow rate was set at 200 mL/min to explore very different H_2/O_2 ratio.

The temperature has been scanned from 313 K to 473 K, with heating rate of 0.5 K/min, with the purpose of identifying the light-off temperature. The heating rate is kept low, resulting in very long tests, to allow for sensible measuring of surface temperature deviations from the set-point, as a possible consequence of the heat of reaction at high H_2 partial pressure.

The ease with which the surface has shown to rearrange in the previous experiments prompted us to validate the new setting, with replicated experiments, at a fixed α value. Results with 2% H_2 in air of 3 replicated experiments are shown in Fig. 4.13. They prove that the reproducibility is excellent, including the details of an earlier increase of activity at 340K, before the sharp ignition at 380K takes place. The large O_2 excess proves to be a condition for stable activity compared to the stoichiometric conditions discussed in Section 4.2.3.

Reassured by the very stable activity shown by the replicas of Fig. 4.13, the large range of H_2/O_2 ratios described above has been explored, by increasing the H_2 partial pressure. The results are shown in Fig. 4.14. Stable conversion was observed at each T, unequivocally coupling the conversion to a well defined temperature.

According to the Literature, the H_2 inhibition has a major role. The higher the H_2 partial pressure, the higher the temperature required to ignite the mixture. At very low H_2 concentration (0.4-1%), i.e. with a large amount of O_2, ignition temperature as low as 70°C has been measured. However, the increase of H_2 conversion is not very large, though concentrated in a very narrow temperature range (it is step-like). The larger increase of H_2 conversion takes place fairly rapidly, about 370K. At still higher temperature, the rise of H_2 conversion with temperature is more gradual, apparently diffusion controlled, as predicted in Fig. 3.13 and consistent with a small H_2 concentration in the bulk. The $X(T)$ profile of the leaner mixture suggests a two steps ignition. Less evident 2-steps ignitions can be noticed at higher equivalence ratios (x_{H_2} = 2-4%), while they definitively disappear at higher H_2 content.

From the results of Fig. 4.14, we identified the ignition temperature as a function of α. We defined the ignition temperature as the one at which 10% of H_2 has

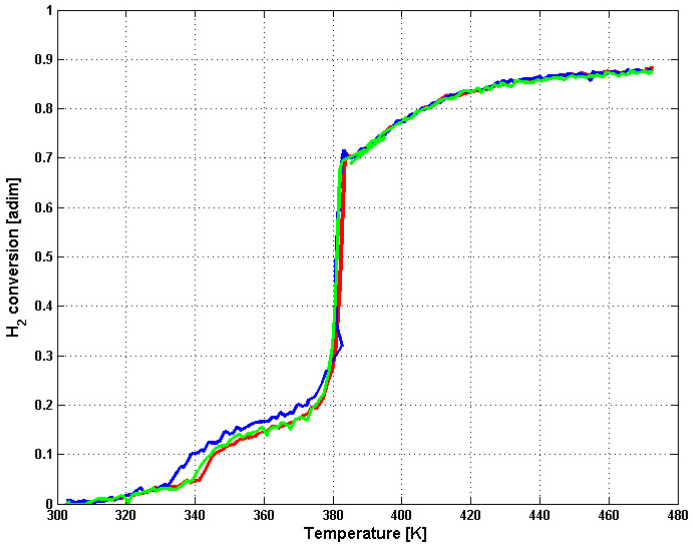

Figure 4.13: *H_2 conversion as a function of reactor temperature at O_2 rich conditions (H_2 =2% in air, α = 0.088). $\dot{V}$=200 mL/min. Three replicas at the same conditions.*

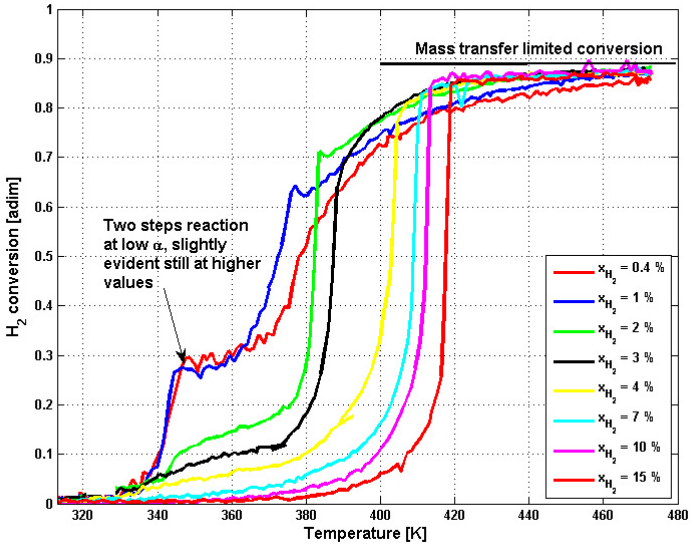

Figure 4.14: *H_2 conversion as a function of reactor temperature at O_2 rich conditions. $\dot{V}$=200 mL/min.*

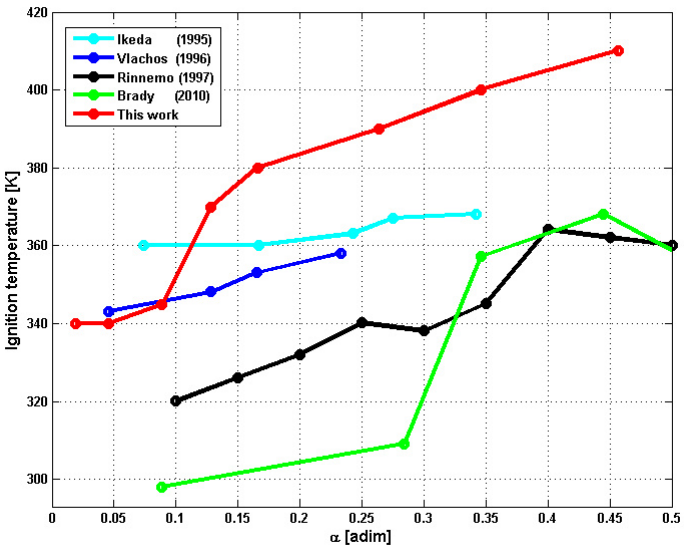

Figure 4.15: *Reaction ignition temperatures comparison between Literature values and the experimental measurements here obtained.*

reacted. Comparison of the ignition temperatures proposed in the Literature and those experimentally measured in the present research is reported in Fig. 4.15. Data are widely scattered, especially at high hydrogen concentration (α = 0.1-0.3), where a gap of 70 K with respect the Brady's dataset and of 50 K with respect to the Rinnemo's one can be observed. Note also that our results indicate a linear increase of T_{ign} with α, at H_2-rich conditions (high α values). The trend has a discontinuity about $\alpha = 0.1$, switching to much lower temperature with lean mixtures. That resemble a bifurcation behavior, also evident in Brady's measurements. In our case, that is connected to the 2-steps ignition highlighted above. Two indications can be drawn from that. i) Below a given threshold of the H_2 concentration the temperature required for ignition drops dramatically; ii)at very lean mixtures, the ignition stabilizes at a unique value of temperature, and is not affected by the amount of H_2 in the mixture. We believe that the bifurcation observed, together with the evolution of the Pt surface structure, provide sufficient explanation to the dispersion of ignition temperature data in the Literature.

4.4 Conclusions

Hydrogen Pt catalysed oxidation has been reproduced in a suitable designed Stagnation Point Flow Reactor. Catalyst activity has been found to be sensitive to sur-

face history. Pretreatments in H_2-rich mixtures develop a higher reactivity of the surface. The evolution has its own kinetics, affected by temperature, and pretreatment duration has a role. After catalyst pretreatment in H_2 at high temperature, almost complete H_2 consumption by O_2 can be achieved. Hysteresis, Fig. 4.3, has been measured and reproduced, as well as extensive surface evolution, Fig. 4.4, at constant temperature, lasting up to 6 h, Fig. 4.5.

Surface structure rearrangements were observed after intensive H_2 pretreatment and reaction, confirming that the catalyst has a living structure, also in the case of bulk metals.

Resetting the catalyst activity by lapping, we could prove that H_2 has an activating role, that was explained in terms of a shift of platinum surface crystalline structure, from a preferential Pt(111) to a more stable and evidently more reactive Pt(200).

Catalyst exposure to O_2 alone leads to an extremely high activity that gradually drops to an asymptotic value, independent of the previous history. The same asymptote is achieved after thermal of H_2 pretreatments. The very high initial activity after O_2 pretreatment was connected to the competition of O_2 and H_2 for active sites. The larger affinity of Pt for H_2 leads to the H_2-inhibition effect, which is very detrimental to the surface activity. Exposing the surface to O_2 can artificially unbalance a competition where H_2 is favored, resulting in a transient of very high activity, that vanishes as H_2 regain control of the surface.

Catalytic reaction light-off studies summarize all these observations. Reducing enough the H_2 concentration leads to a much higher activity, that results in a very low, apparently unique ignition temperature. As H_2 increases, reaction becomes progressively inhibited, passing through a bifurcation region, where 2-steps ignition appears to occur. That provides enough explanation to the discrepancies between our experimental ignition temperatures and the ones collected from the Literature, and among them.

Modern microkinetics mechanisms must be developed to account for these surface rearrangements that have been experimentally proved to dramatically affect the reactivity, especially in the range of operative conditions at which only catalytic reaction are active.

Chapter 5

Hydrogen self inhibition and thermal promotion

The present study undertakes a numerical investigation of the start up of a hydrogen fueled, Pt coated planar channel with a length of 10 mm and a height of 1 mm. A transient code is used, which includes 2-D elliptic gas phase description, 1-D heat transfer in the solid phase, surface radiation heat transfer, and detailed hetero-/homogeneous chemistry. The quasisteady state assumption (QSS) is invoked for the gas phase to negate the high computational cost of a fully transient simulation [84]. Most literature transient QSS models have employed 1-D description for both the solid and gas phases [85, 86, 87]. We have recently developed transient numerical models under the QSS assumption with 2-D gas phase description and detailed chemistry, and applied them to investigate the start up processes of methane or syngas catalytic reactors [84, 68, 88]. For the present hydrogen investigations the need for 2-D gas phase modeling is of paramount importance to correctly capture homogeneous combustion, which cannot be neglected in the catalytic oxidation of H_2/air mixtures due to the attained superadiabatic surface temperatures. Gaseous combustion, in turn, strongly depends on the boundary layer profiles of species and temperature [89, 19] that can only be captured by a 2-D model. Moreover, the 2-D description removes the need of empirical transport coefficients for interphase diffusion [90]. Till now, there has been no detailed study of transient hydrogen hetero-/homogeneous combustion in practical catalytic channel configurations. A possible exception is our recent [91] 2-D DNS (direct numerical simulation, without invoking the QSS assumption) investigation of hydrogen catalytic channel flow combustion. However, the prohibitive cost of DNS, originating from the stiffness of the catalytic reaction mechanism, limited the investigations to inlet temperatures 450-650 K, well above the light off temperatures of lean H_2/air mixtures over Pt (up to 380 K at atmospheric pressure [39, 40]). Furthermore, the total integration time was restricted to 200-400 ms in

[91], which was insufficient to reach steady state. Main objective of this work is to investigate the interplay of heterogeneous kinetics, reaction exothermicity, transport and homogeneous kinetics, and their impact on the light-off times and the steady state times in H_2 fueled catalytic channel geometries relevant to power generation. While the hydrogen chemical inhibition suggests shorter light-off times for the leaner mixtures, thermal effects due to the reaction exothermicity may overtake the chemical inhibition and thus reduce the steady state times in practical geometries. In addition, it will be shown that the catalytic reactivity of hydrogen exhibits a quite rich behavior, shifting from H_2 inhibiting to H_2 promoting above a critical temperature that depends on pressure, thus greatly affecting the steady state times. Simulations are carried out with a 2-D QSS code at lean stoichiometries (H_2/air equivalence ratio ϕ=0.10 to 0.45), two pressures (1 and 5 bar) and two different solid wall materials (cordierite and FeCr-alloy). Implications for the operation of various practical catalytic reactors are finally drawn.

5.1 Numerical model

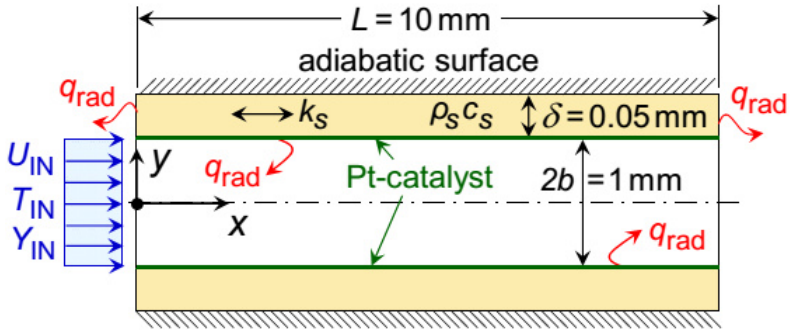

Figure 5.1: *Catalytic microreactor geometry.*

A two dimensional steady laminar elliptic code [84, 68, 88] is used to simulate the flow domain in a plane channel with length L = 10 mm, height 2b = 1 mm and wall thickness δ = 50 μm (see Fig. 5.1). The adopted 1 mm geometrical confinement is typical to either catalytic honeycomb reactors for large scale power generation [92] or to single channel microreactors for portable power generation [9]. Platinum coating is applied to the inner channel surfaces (y = $\pm$b), whereas the outer horizontal surfaces y = $\pm$(b + δ) are adiabatic. The temperatures, velocities and species profiles are uniform at the inlet. Fuel lean H_2/air mixtures (equivalence ratios ϕ = 0.10-0.28) are considered, with inlet temperatures in the range T_{IN} = 380-400 K and two different inlet pressures P = 1 and 5 bar (the latter

being of particular interest to microturbine based microreactors [93]). The lower inlet temperatures are selected so as to clearly demonstrate the impact of hydrogen catalytic chemical inhibition on the reactor start up. The initial temperature of the solid wall is spatially uniform and equal to the incoming mixture temperature, $T_w(x,t=0) = T_{IN}$.

The nominal inlet velocity is U_{IN} = 50 m/s at P = 1 bar and U_{IN} = 10 m/s at P = 5 bar, thus yielding the same mass flux throughputs ($\rho_{IN}U_{IN}$) for the two investigated pressures. The inlet velocities are sufficiently large to ensure kinetically controlled or mixed kinetically/transport controlled rather than pure transport controlled controlled hydrogen conversion even after catalyst light off, while guaranteeing at the same time laminar flow conditions (Reynolds numbers based on the inlet properties and the channel height, are Re_{IN} = 730-1650). Such velocities are also typical to honeycomb catalytic reactors of large gas turbines [92]. The quasisteady assumption necessitates gas phase convective and diffusive time scales shorter than the solid heat conduction time scale, such that the gaseous flow can equilibrate to the channel wall temperature at any time during the transient start up process [84, 94]. The 2-D steady flow solver is coupled to a 1-D transient model for the solid heat conduction (the choice of 1-D model for the solid will be elaborated in Section 5.1.2). Two solid materials relevant to industrial catalytic reactors, cordierite (ceramic) and FeCr-alloy (metallic), are investigated (Table 5.1 provides their properties [95]).

Table 5.1: *Properties for cordierite and FeCr-alloy channel wall materials*[a].

Material	$\mathbf{k}_s$ W/mK	ρ_s kg/m^3	$\mathbf{c}_s$ J/kgK	$\rho_s c_s$ kJ/m^{3}K
Cordierite	2	2600	1464	3806
FeCr-alloy	16	7200	700	5040

Due to symmetry, half of the channel domain ($0 \leq y \leq b+\delta$) is solved. For a steady gaseous flow with homogeneous reactions, the following governing equations are solved:

Continuity equation:

$$\frac{\partial(\rho u)}{\partial x} + \frac{\partial(\rho v)}{\partial y} \tag{5.1}$$

Momentum equations:

$$\frac{\partial(\rho uu)}{\partial x} + \frac{\partial(\rho vu)}{\partial y} + \frac{\partial P}{\partial x} - \frac{\partial}{\partial x}\left[2\mu\frac{\partial u}{\partial x} - \frac{2}{3}\mu(\frac{\partial u}{\partial x} + \frac{\partial v}{\partial y})\right] - \frac{\partial}{\partial y}\left[\mu(\frac{\partial u}{\partial y} + \frac{\partial v}{\partial x})\right] = 0 \tag{5.2}$$

$$\frac{\partial(\rho uv)}{\partial x}+\frac{\partial(\rho vv)}{\partial y}+\frac{\partial P}{\partial y}-\frac{\partial}{\partial x}\left[\mu(\frac{\partial v}{\partial x}+\frac{\partial u}{\partial y})\right]-\frac{\partial}{\partial y}\left[2\mu\frac{\partial v}{\partial y}-\frac{2}{3}\mu(\frac{\partial u}{\partial x}+\frac{\partial v}{\partial y})\right]=0 \quad (5.3)$$

Energy equation:

$$\frac{\partial(\rho uh)}{\partial x}+\frac{\partial(\rho vh)}{\partial y}+\frac{\partial}{\partial x}(\rho\sum_{k=1}^{K_g}Y_k h_k V_{k,x}-\lambda_g\frac{\partial T}{\partial x})+\frac{\partial}{\partial y}(\rho\sum_{k=1}^{K_g}Y_k h_k V_{k,y}-\lambda_g\frac{\partial T}{\partial y})=0 \quad (5.4)$$

Gas-phase species equations:

$$\frac{\partial(\rho uY_k)}{\partial x}+\frac{\partial(\rho vY_k)}{\partial y}+\frac{\partial}{\partial x}(\rho Y_k V_{k,x})+\frac{\partial}{\partial y}(\rho Y_k V_{k,y})-\dot{\omega}_k W_k=0, k=1,2,...,K_g \quad (5.5)$$

Surface species coverage equations:

$$\sigma_m\frac{\dot{s}_m}{\Gamma}=0, \quad m=1,2,...,M_s \quad (5.6)$$

The surface reaction rates are given by:

$$\sigma_m=\sum_{l=1}^{N_s}\nu_{ml}k_{fl}\prod_{j=1}^{K_g+K_s}C_j^{\nu_{jl}^{'}} \quad (5.7)$$

with Ns the number of surface reactions and ν_{ml} the stoichiometric coefficient of species m in surface reaction λ. For the gas phase species j = 1, 2, .. K_g the concentrations are $C_j=\rho Y_j/W_j$ (mol/cm^3), while for the surface species j = 1, 2, .. K_s the corresponding surface concentrations are $C_j=\Gamma\theta_j/\sigma_j$ (mol/cm^2). The reaction rate coefficients in Eqn. 5.7 are:

$$k_{fl}=A_l T^{\beta_l}exp\left(\frac{-E_l}{RT}\right)\prod_{i=1}^{K_s}\theta_l^{\mu_{i_l}}exp\left(\frac{\epsilon_{il}\theta_l}{RT}\right) \quad (5.8)$$

$$\overset{to}{V}_k=-D_{km}\nabla\left[ln(Y_k\bar{W}/W_k)\right]-\left[D_k^T W_k/(\rho Y_k\bar{W})\right]\nabla(lnT) \quad (5.9)$$

The ideal gas and caloric state laws were finally used:

$$P=\frac{\rho RT}{\bar{W}} \quad and \quad h_k=h_k^O(T_O)+\int_{T_O}^{T}C_{p,k}dT \quad (5.10)$$

For the solid, a transient 1 D heat balance equation was solved:

$$\left(\rho_s c_s \frac{\partial T_w}{\partial t} - k_s \frac{\partial^2 T_w}{\partial x^2}\right)\delta - \left(\dot{q} - \lambda_g \frac{\partial T}{\partial y}|_{y=b+} + \sum_{k=1}^{K_g}(\dot{s}_k\ h_k W_k)\right) = 0 \tag{5.11}$$

Radiation exchange between the discretised catalytic surface elements and between each wall element and the inlet and outlet channel enclosures was modelled with the net radiation method for diffuse gray areas [96]. For the kth catalytic surface element, the radiation balance yields:

$$\frac{1}{\epsilon_k} q_k = \sum_{j=1}^{N+2} F_{k-j}\sigma(T_k^4 - T_j^4) + \sum_{j=1}^{N+2}\left(\frac{1-\epsilon_j}{\epsilon_j}\right) F_{k-j} q_j \tag{5.12}$$

with the index j running over the N catalytic surface elements as well as the inlet (j = N + 1) and outlet (j = N + 2). All catalyst elements have a constant emissivity $\epsilon_j = \epsilon = 0.6$, j=1,2, .. N, while the inlet and outlet sections of the radiation enclosure are treated as black bodies ($\epsilon_{N+1} = \epsilon_{N+2}$=1). Details of the surface radiation heat transfer model have been provided elsewhere [68]. The interfacial boundary conditions for the gas phase species become:

$$(\rho Y_k V_k)_{y=b+}\ \dot{s}_k\ W_k = 0 \quad k = 1, 2, ..., K_g \tag{5.13}$$

Implicit in Eqn. 5.13 is the consideration of a geometrical surface area equal to the catalytically active area. Radiative boundary conditions are finally applied to the vertical front and rear solid wall faces:

$$k_s \frac{\partial T_w}{\partial x}|_{x=0^+} = \epsilon\sigma\left[T_w^4(x=0) - T_{IN}^4\right] \tag{5.14}$$

$$-k_s \frac{\partial T_w}{\partial x}|_{x=L-} = \epsilon\sigma\left[T_w^4(x=L) - T_{OUT}^4\right] \tag{5.15}$$

with the inlet and outlet radiation exchange temperatures set equal to the inlet gas mixture temperature and the outlet average gas temperature, respectively.

5.1.1 Chemical reaction mechanisms and solution procedure

The oxidation of hydrogen on platinum is described by the detailed mean field heterogeneous reaction scheme from Deutschmann et al. [31] (14 reactions involving 5 surface and 6 gaseous species). Simulations with this scheme have reproduced catalytic ignition experiments of fuel lean $H_2/O_2/N_2$ mixtures over stagnation point flow platinum surfaces [39]. The surface site density is $\Gamma = 2.7\text{x}10^{-9}$ mol/cm^2. For homogeneous combustion, the elementary gas phase mechanism from Li et al. [97] (21 reactions and 9 species) is used, which has been validated against autoignition and laminar flame speed measurements at pressures up to 87 bar. Moreover, the coupled hetero-/homogeneous reaction mechanisms have reproduced measurements of homogeneous ignition and of hetero-/homogeneous hydrogen consumption in a Pt coated channel, at fuel lean H_2/air stoichiometries and pressures up to 15 bar [35, 98, 4]. Surface and gas phase reaction rates are evaluated using Surface CHEMKIN [99] and CHEMKIN [100], respectively, while transport properties are calculated using the CHEMKIN database [101]. The flow domain ($0 \leq y \leq b$) is discretised using orthogonal staggered mesh with 100x24 grid points (in x and y, respectively, with finer spacing towards the wall and inlet), which are sufficient to produce a grid independent solution. One hundred grid points are also used to discretise the solid wall in the axial direction. Uniform profiles of species, temperature and axial velocity are applied to the inlet, while zero Neumann conditions are set at the outlet (x = L) and the plane of symmetry (y = 0). No slip is used for both velocity components at the gas wall catalytic interface (y = b). The flow equations are discretised by a finite volume approach and solution was obtained with a SIMPLER method for the pressure velocity field [34]. The transient solid energy equation is solved with a second order accurate, fully implicit scheme and a quadratic backward time discretisation [102]. Solution for the coupled flow and solid phase is obtained at each time step iteratively: convergence is reached when the solid temperature at all axial positions does not vary between successive iterations by more than 10-5 K. This results in up to 3000 iterations per time step.

5.2 Time scale analysis

The integration time step was selected to satisfy the QSS approximation, entailing convection, diffusion and characteristic chemical reaction times shorter than the corresponding solid heat conduction times. When such criteria are satisfied, the QSS approximation yields very good agreement with full DNS, as recently reported in [91]. Axial convective characteristic times were $t_{g,x} \approx L/U_{IN}$ = 0.2-1 ms for the selected velocities U_{IN} = 10 and 50 m/s. Transverse diffusive time

scales were computed as $t_{g,y} \approx b^2/a_g$, with $a_g = \lambda_g/(\rho c_p)$ the gas thermal diffusivity. Using the CHEMKIN transport and thermodynamic libraries [101, 103] for fuel-lean H_2/air mixtures, the computed $t_{g,y}$ ranged from 5 ms (P = 1 bar) to 24 ms (P = 5 bar). Characteristic chemical time scales are subsequently assessed. To this direction, catalytic ignition simulations are performed in a constant pressure isothermal batch reactor. The governing equations for the gas phase and surface species, respectively, for a batch reactor are:

$$\rho \frac{dY_k}{dt} = \dot{\omega}_k W_k + \frac{S}{V} \dot{s}_k W_k \quad k = 1,2,...,K_g$$

$$\frac{d\theta_m}{dt} = \sigma_m \frac{\dot{s_m}}{\Gamma} \quad m=1,2,...,K_s \tag{5.16}$$

As the slowest catalytic reaction rates (longest chemical times) in the channel reactor of Fig. 5.1 were associated with the lowest catalyst surface temperature (i.e. T_{IN} at t = 0, before appreciable reactor heat up), the most stringent estimates for catalytic reaction times were obtained at batch reactor temperatures $T_{batch}(t) = T_{IN}$. Calculations were performed in a batch reactor with a surface to volume ratio S/V = 20 cm^{-1} (equal to the S/V of the channel in Fig. 5.1). Characteristic chemical time scales were defined as:

$$\tau_{chem,k} = \frac{1}{t_{k,50}} \int_0^{t_{k,50}} \frac{C_k(t) - C_k(t=0)}{\dot{s}_k (S/V) + \dot{\omega}_k} dt,$$

$$\tau_{chem,m} = \frac{1}{t_{m,50}} \int_0^{t_{m,50}} \frac{\Gamma\theta_m(t) - \Gamma\theta_m(t=0)}{\dot{s}_m} dt \tag{5.17}$$

In Eqn. 5.17 $t_{k,50}$ ($t_{m,50}$) were the times at which a gaseous species k (surface species m) reached concentration equal to 50% of the difference between its initial and steady state values: $C_k(t = t_{k,50}) = 0.5$—$C_k(t = 0)$-$C_{k,st}$— ($\Gamma\theta_m(t = t_{m,50}) = 0.5$—$\Gamma\theta_m(t = 0)$-$\Gamma\theta_{m,st}$—). Gas phase reactions were frozen at the low initial temperatures for which light off was herein investigated (380 K at 1 bar and 400 K at 5 bar) and hence the terms $\dot{\omega}_k$ in Eqn. 5.17 did not affect the computed times. The isothermal batch reactor simulations were performed with an initial surface coverage θ_H (t = 0)= 0.99, as H(S) was the dominant surface species before light off [29]. Catalytic chemical times for gaseous and surface species are plotted in Fig. 5.2 for pressures of 1 and 5 bar and three equivalence ratios ϕ = 0.10, 0.20, and 0.28. Chemical times at P = 1 bar and 380 K were as long as 12 ms (5.2a).

The catalytic self inhibition of ignition [40] was evident from the longer H_2 chemical times at higher equivalence ratios. At P = 5 bar and 400 K (Fig. 5.2c)

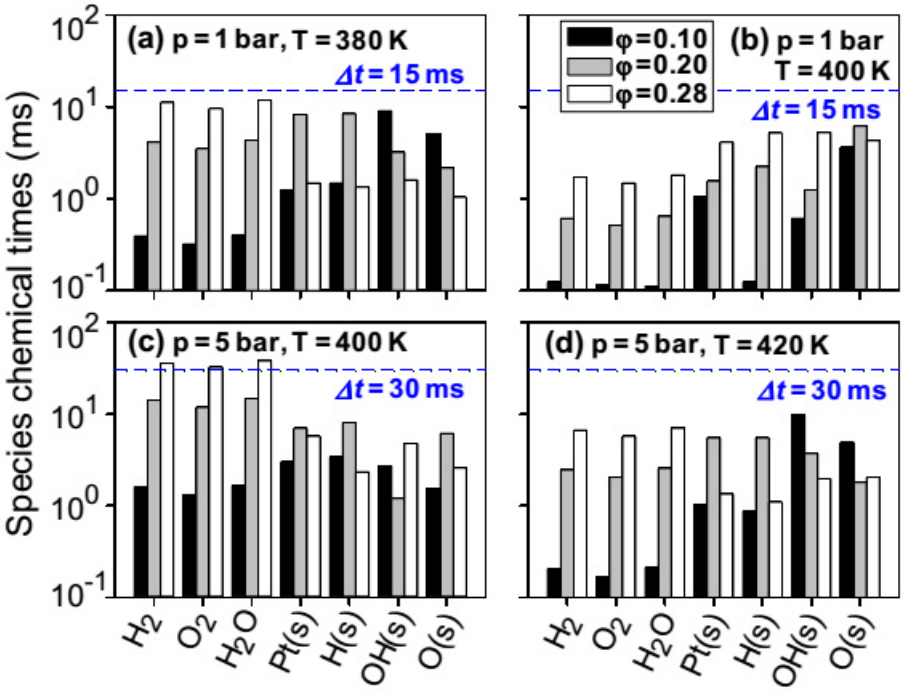

Figure 5.2: *Characteristic species chemical times during light-off of H_2/air mixtures at three equivalence ratios, computed in an isothermal batch reactor: (a) P = 1 bar, T = 380 K, (b) P = 1 bar, T = 400 K, (c) P = 5 bar, T = 400 K, (d) P = 5 bar, T = 420 K. Only species with characteristic times greater than 10^{-1} ms are shown.*

the characteristic times were as long as 36 ms. These times were longer compared to those at P = 1 bar, despite the higher reactor temperature at 5 bar, a result of the increased H_2 self inhibition due to the higher partial pressure of hydrogen. It is emphasized that the time analysis in Fig. 5.2 was quite strict when applied to the channel in Fig. 5.1, since as the solid started heating above the initial temperatures $T_w(x, t = 0) = 380$ or 400 K, the chemical time scales dropped substantially (see Fig. 5.2b at P = 1 bar and 400 K, and Fig. 5.2d at P = 5 bar and 420 K). It is finally noted that at temperatures above 600 K there was no hydrogen self inhibition but a promotion of light off with increasing equivalence ratio, and this result was irrespective of the initial coverage (H(S)(t = 0) = 0.99 or 0.01). For hydrogen catalytic combustion in Pt coated channels, gas phase chemistry becomes important only at wall temperatures in excess of 1250 K for the present geometrical confinements (1 mm channel gap) inlet temperatures and pressures, as discussed in Ghermay et al. [104]. Batch reactor time scale analysis carried out at a constant temperature of 1100 K with inclusion of combined hetero-/homogeneous chem-

istry in Eqn. 5.14 indicated that the characteristic reaction times for all species were shorter than 1.3 ms at 1 bar and 1.2 ms at 5 bar (see Fig. 5.3).

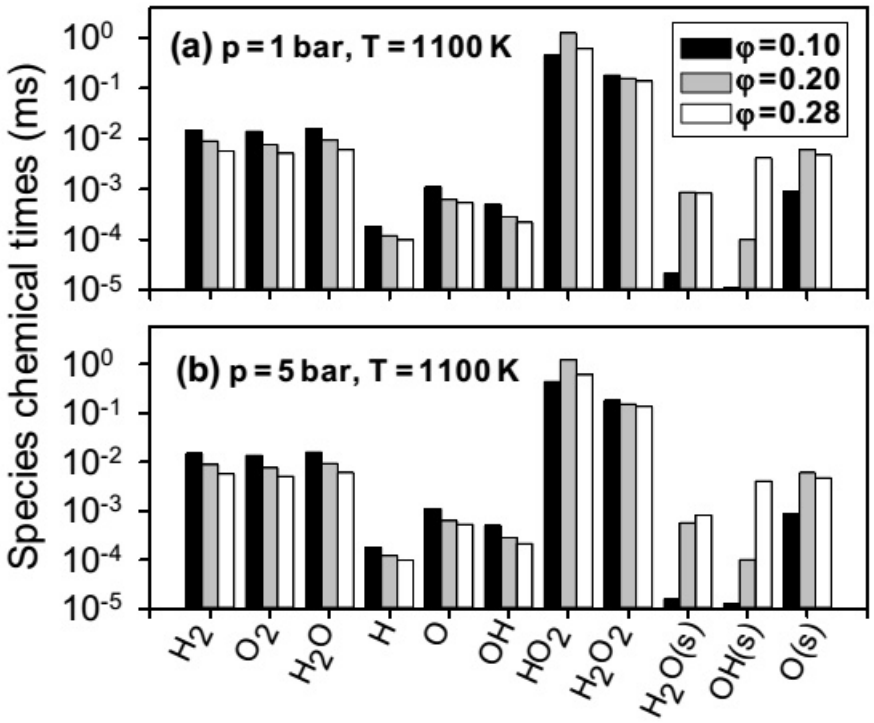

Figure 5.3: *Characteristic species chemical times in H_2/air hetero-/homogeneous combustion at three equivalence ratios, computed in an isothermal batch reactor: (a) P = 1 bar, T = 1100 K, (b) P = 5 bar, T = 1100 K. Only species with characteristic times greater than 10^{-4} ms are shown.*

The characteristic axial heat conduction time in the solid was $t_{s,x} \approx L^2/a_s$, with $a_s = k_s/\rho_s c_s$ the solid thermal diffusivity. Using properties from Tab. 5.1, computed axial heat conduction times for FeCr-alloy and cordierite were 32 s and 190 s, respectively. Since $t_{s,x} >> t_{g,x}$, $t_{g,x}$, $t_{chem,k}$, for both materials, the quasisteady assumption could be safely invoked within an axial solid heat conduction model. However, as the transverse heat conduction times in the solid $t_{s,y} \approx \delta^2/a_s$ were 3.2 ms for FeCr-alloy and 19 ms for cordierite, a 2-D solid heat conduction model was incompatible with the QSS approximation at least for the FeCr-alloy ($t_{s,y} <$ $t_{g,x}$, $t_{g,x}$). Therefore, a 1-D axial heat energy model was used for the solid wall, and for consistency this approach was adopted for both wall materials. According to the foregoing time scale analysis, two different integration time steps were used: Δt = 15 ms for P = 1 bar and δt = 30 ms for P = 5 bar. These time steps were sufficiently short to resolve the axial heat conduction in the solid and at the same

time long enough to allow for equilibration of the gas phase transport and chemical processes.

5.3 Numerical results and discussion

Computations in the channel of Fig. 5.1 were performed for five fuel lean H2/air equivalence ratios (ϕ = 0.10, 0.15, 0.20, 0.25 and 0.28) and two pressures (1 and 5 bar). The inlet temperatures are T_{IN} = 380 K and 400 K at 1 bar and 5 bar, respectively, to satisfy the QSS assumption as discussed in Section 1.2. Inlet velocities are U_{IN} = 50 m/s and 10 m/s at 1 bar and 5 bar, respectively, thus practically maintaining the same mass flux throughput at the two different pressures. The small difference in inlet temperatures (T_{IN} = 380 K at 1 bar and T_{IN} = 400 K at 5 bar) due to the requirements of the QSS assumption lead to small differences in the mass flux throughputs ($\rho_{IN}U_{IN}$) at the two different pressures which, however, do not affect the subsequent discussions. Finally, the bulk of the simulations pertain to FeCr-alloy channel wall material; cordierite wall material simulations will mainly be used for comparison purposes with the FeCr-alloy.

5.3.1 Impact of equivalence ratio and pressure on catalytic kinetics

To assist the understanding of the forthcoming 2-D transient channel simulations, an analysis of the catalytic reactivity and its dependence on the equivalence ratio and pressure is initially presented. Numerical platform for such kinetic studies is the steady state Surface Perfectly Stirred Reactor (SPSR) [105]. Simulations are carried out at a fixed reactor temperature in order to decouple thermal from chemical effects. The gas phase species governing equations in an SPSR are:

$$\frac{\rho}{\tau}(Y_{k,OUT} - Y_{k,IN}) = \frac{S}{V}\,\dot{s}_k\,W_k, \quad \text{k=1,2,...,K}_g \tag{5.18}$$

where τ is the residence time. In all computations, S/V = 20 cm^{-1}. To expose the dependence of the catalytic reactivity $\dot{s}_k$ on pressure, the ratio (ρ/τ) is kept constant in Eqn. 5.18 when changing the pressure. To further facilitate the interpretation of the detailed chemistry simulations, a global catalytic step of the following type is considered:

$$\dot{s}_{H_2} = (P/P_0)^n A C_{H_2}^b exp(-E/RT) \tag{5.19}$$

where the hydrogen concentration in the SPSR is $C_{H_2} = \rho Y_{H_2,OUT}/W_{H_2} = P\bar{W}$ $Y_{H_2,OUT}/(RTW_{H_2})$. The term $(P/P_0)^n$ in Eqn. 5.19, with P_0 = 1 bar, modifies the reaction pre-exponential A for reasons discussed next. The fractional hydrogen conversion Z is defined as:

$$Z = 1 - \frac{Y_{H_2,OUT}}{Y_{H_2,IN}} = \tag{5.20}$$

An expression for Z is derived from Eqns. 5.18 and 5.19:

$$Z(1-Z)^{-b} = \Omega \tag{5.21}$$

In Eqn. 5.21 Ω is a non dimensional reaction rate parameter:

$$\Omega = \left[(\rho/\tau)^{-1}(S/V)W_{H_2}^{1-b}(\bar{W}/RT)^b P_0^{-n} A exp(-E/RT)\right] P^{b+n} Y_{H_2,IN}^{b-1} \tag{5.22}$$

The dependence of Z on equivalence ratio (or $Y_{H_2,IN}$) and pressure can be deduced from Eqns. 5.21 and 5.22. The bracketed term in the right side of Eqn. 5.22 is constant since the ratios (ρ/τ) and (S/V) as well as the temperature T of the SPSR are fixed in the simulations (the mean molecular weight $\bar{W}$ and density ρ are practically constant for the investigated very low H_2/air equivalence ratios ϕ = 0.10-0.28). For any hydrogen reaction order b>0, Z is a monotonically increasing function of Ω (see Fig. 5.4a, for $\Omega_1 > \Omega_2$, $Z_1[\Omega_1] > Z_2[\Omega_2]$). Further restricting the analysis to b>1, Ω becomes a monotonically increasing function of $Y_{H_2,IN}$ ($Y_{H_2,IN}^{b-1}$ dependence of Ω in Eqn. 5.22) and thus Z is a monotonically increasing function of $Y_{H_2,IN}$. Similarly, for b+n>0, Ω is a monotonically increasing function of pressure (P^{b+n} dependence of Ω in Eqn. 5.22) and hence Z is also a monotonically increasing function of pressure. It will be shown next that values b>1 and b+n>0 pertain to hydrogen catalytic kinetics above the ignition temperature. It is also worth noting that, although not relevant to fuel lean hydrogen catalytic kinetics, a first order b = 1 leads to a conversion Z independent of $Y_{H_2,IN}$, while $0 \leq b < 1$ leads to Z monotonically decreasing with $Y_{H_2,IN}$. Below the catalytic ignition temperature, hydrogen inhibits its catalytic reactivity and this requires b<0 in Eqn. 5.19. Plots of Z versus Ω for b<0 are shown in Fig. 5.4b. Such plots are nonetheless not valid for large conversions, since as $Z \rightarrow 1$, $Y_{H_2,OUT} \rightarrow 0$ and hence $\dot{s} \rightarrow \infty$ in Eqn. 5.19. This in turn leads to an infinitely large right side in Eqn. 5.18 that cannot be balanced by the finite left side in Eqn. 5.18 unless the reaction rate coefficient becomes vanishingly small, $A(P/P_0)^n exp(-E/RT) \rightarrow 0$. At low to moderate conversions, Z is a monotonically increasing function of Ω (see

Fig 5.4b) and since Ω is a monotonically decreasing function of $Y_{H_2,IN}$ ($Y_{H_2,IN}^{b-1}$ dependence in Eqn. 5.22), Z is also a monotonically decreasing function of $Y_{H_2,IN}$. The dependence of Z on pressure is determined by the sign of b+n; for b+n>0 the conversion Z increases with rising pressure while for b+n<0, Z decreases with rising pressure.

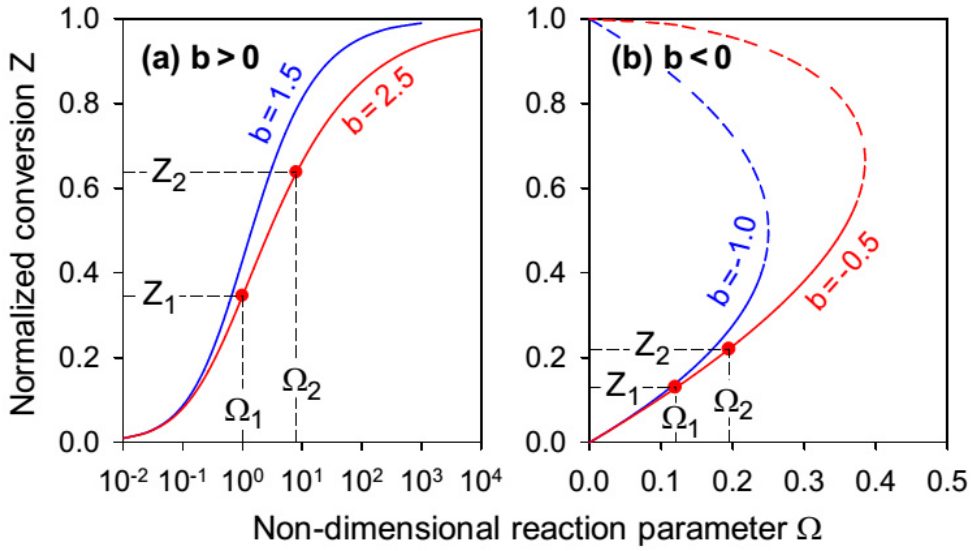

Figure 5.4: *Dependence of normalized conversion Z on the non-dimensional reaction rate parameter Ω in an SPSR (Eqn. 5.21): (a) reaction order b>0 in Eqn. 5.19, (b) reaction order b<0 in Eq. 5.19.*

Figure 5 provides hydrogen conversions Z (in %) as a function of the constant SPSR temperature, computed with the detailed catalytic reaction mechanism from Deutschmann et al. [31], for equivalence ratios ϕ = 0.10 and 0.28, and pressures P = 1, 3 and 5 bar. The residence times at P = 1, 3 and 5 bar are τ = 10, 30 and 50 μs, respectively, thus maintaining constant ratios (ρ/τ). The catalytic ignition temperatures in Fig. 5.5 (see the vertical arrows marked T_{ign} in Fig. 5.5 as well as in the insets of Fig. 5.5) are the temperatures where hydrogen conversion sharply increases from nearly zero to appreciably high values. Ignition is accompanied by an abrupt change of the surface coverage from dominant H(s) (for $T<T_{ign}$) to dominant Pt(s) and O(s) (for $T>T_{ign}$), as discussed in [39]. By comparing Figs. 5.5a and 5.5b, the well known hydrogen self inhibition of catalytic ignition [39, 40] becomes evident: for a given pressure, the ignition temperature T_{ign} is always higher at ϕ = 0.28 compared to ϕ = 0.10. The very weak conversions Z at $T<T_{ign}$ are (for a given pressure and temperature) larger at ϕ = 0.10 than ϕ = 0.28, as shown by comparing the two insets of Fig. 5.5. Likewise, for a given equivalence ratio

and temperature ($T<T_{ign}$) an increase in pressure reduces the conversion Z and increases the ignition temperature. The above dependence of Z on pressure and equivalence ratio suggests that for $T<T_{ign}$ the detailed catalytic reaction mechanism shows the same qualitative behaviour as the single step rate of Eqn. 5.19 with b<0 and b+n<0. Figure 5.6 summarizes the ignition temperatures T_{ign} at three pressures over the extended equivalence ratio range $0.10< \phi <0.40$. The inhibition of catalytic ignition with rising equivalence ratio and rising pressure is clearly seen in Fig. 5.6. Over the range $0.10< \phi <0.28$, which is of interest in the present study, catalytic ignition temperatures vary from 302 to 398 K. Key in the operation of practical channel or honeycomb reactors is not only the dependence of T_{ign} on equivalence ratio and pressure, which was discussed before, but also the dependence of the catalytic reactivity on these two key parameters after catalytic ignition ($T>T_{ign}$). For a given pressure and temperature ($T>T_{ign}$), an increase in equivalence ratio enhances the conversion Z (compare Figs. 5.5a and Fig. 5.5b). Moreover, for a given equivalence ratio and temperature ($T>T_{ign}$), a rise in pressure leads to higher hydrogen conversions Z (see either Figs. 5.5a or Fig. 5.5b). This suggests that the detailed catalytic reaction mechanism at $T>T_{ign}$ displays qualitatively the same behaviour as the single step rate of Eqn. 5.19 with b>1 and b+n>0.

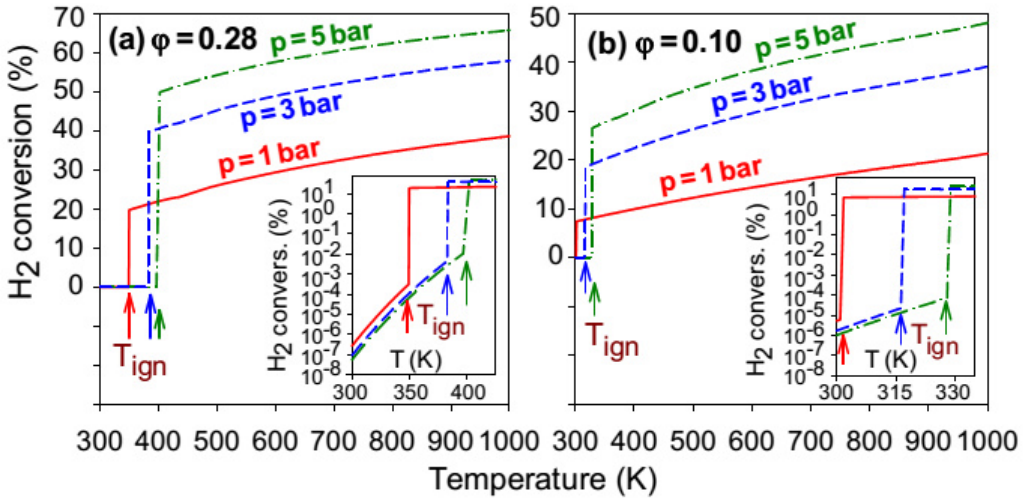

Figure 5.5: *Computed hydrogen percentage conversion at three pressures as a function of temperature in an isothermal Pt-coated SPSR with surface-to-volume ratio S/V = 20 cm^{-1}: (a) ϕ = 0.10 and (b) ϕ = 0.28. The vertical arrows marked T_{ign} in denote the catalytic ignition temperatures while the inset figures show details close to T_{ign}. The SPSR residence times are 10, 30 and 50 µs at 1, 3 and 5 bar, respectively.*

To determine the pressure dependence of the catalytic reactivity at $T>T_{ign}$, the following kinetic parameters for the global catalytic step $2H_2+O_2 \rightarrow 2H_2O$ have been fitted to the rate expression of Eqn. 5.19 in order to reproduce the detailed chemistry results in Fig. 5.5: A = 3.2x106 $\text{mol}^{-0.5} cm^{2.5} s^{-1}$, n = -0.53, b = 1.5 and E = 8 kJ/mol. The negative pressure exponent n = -0.53 is necessary to restrain the rate of increase of the catalytic reactivity with rising pressure in Eqn. 5.19: in the absence of the $(P/P_0)^n$ term, the pressure dependence of the catalytic reactivity would have been unrealistically high (determined by the hydrogen concentration exponent b = 1.5). Such negative pressure exponents n were also found necessary to correctly describe with global steps the oxidation of light hydrocarbons over platinum at elevated pressures. For example, experimentally fitted exponents n in methane [64] and propane [106] oxidation over Pt are -0.52 and -0.40, respectively. The overall pressure dependence of the hydrogen catalytic reactivity in Eqn. 5.19 is thus P^{n+b} with n+b = 0.97. On the other hand, for a given pressure the dependence of the catalytic reactivity on hydrogen concentration is C_{H2}^b with b = 1.5. The global step in Eqn. 5.19 with the aforementioned kinetic parameters reproduces the detailed catalytic chemistry predictions in Fig. 5.5 with accuracy better than 24% over the ranges $0.10< \phi <0.28$, 1 bar$< P <5$ bar, and 400 K$< T <$1000 K (i.e. $T>T_{ign}$). Interestingly, while hydrogen inhibits its own catalytic ignition and hence its catalytic reactivity at $T<T_{ign}$, it promotes its catalytic reactivity at $T>T_{ign}$ as manifested by the exponent b = 1.5. Similarly, while pressure inhibits the hydrogen catalytic reactivity and its catalytic ignition at $T<T_{ign}$, it promotes the hydrogen catalytic reactivity at $T>T_{ign}$ due to the positive exponent n+b = 0.97. These dependencies have not been elaborated in the past and crucially affect the start up of practical reactors, as will be elaborated next.

5.3.2 Channel simulations with only heterogeneous chemistry

Simulation results are first presented in the channel geometry of Fig. 5.1 with the inclusion of detailed heterogeneous chemistry alone (no gas phase chemistry). Predicted streamwise profiles of channel wall temperatures (FeCr-alloy wall material) and for the two extreme equivalence ratios ϕ = 0.10 and 0.28 are depicted in Fig. 5.7 (P =1 bar) and Fig. 5.8 (P = 5 bar) at selected times during the reactor start up. Time integration is carried out for at least 5 sec, to ensure accurate evaluation of the steady state (the latter is also verified by a steady version of the same numerical code [107, 4]). The longest provided times in Figs. 5.7 and 5.8, marked as $t_{st,T}$, correspond to the times where the wall temperatures have reached (at any axial position) at least 99.9% of their steady state values. Moreover, the horizontal dashed lines marked T_{ad} indicate the adiabatic equilibrium temperatures based on the inlet equivalence ratios and the inlet temperatures of each case.

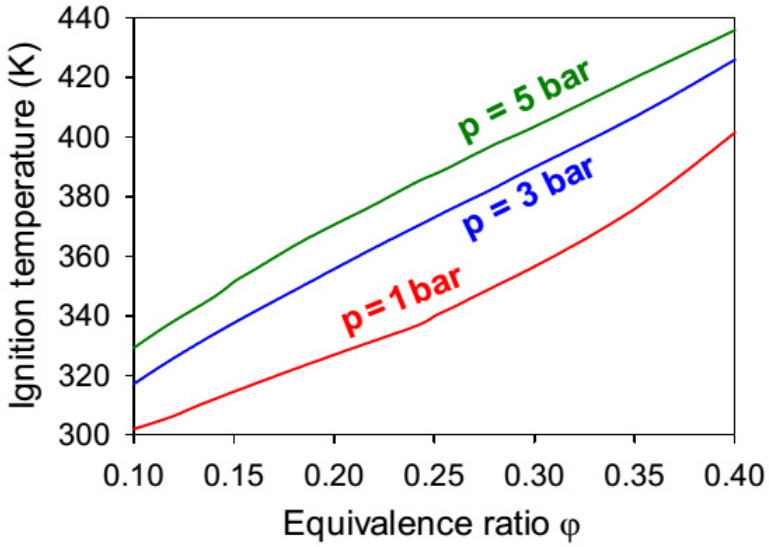

Figure 5.6: *Computed catalytic ignition temperatures for fuel-lean H2/air mixtures as a function of equivalence ratio at three different pressures. SPSR isothermal calculations, residence times and surface-to-volume ratio as in Fig. 5.5.*

Catalytic ignition

For a given pressure, the initial channel heat up occurs faster at the lower equivalence ratio $\phi = 0.10$ as seen by comparing the temperature profiles at early times in Figs. 5.7a 5.7b and Figs. 5.8a 5.8b.

For example, for $\phi = 0.10$ and P = 1 bar the maximum wall temperature at the end of the first time step (15 ms) is 434 K (Fig. 5.7a), while for $\phi = 0.28$ and P = 1 bar the maximum wall temperature is only 404 K after 315 ms (Fig. 5.7b). The faster ignition for the leaner mixture is also attested from the streamwise profiles of hydrogen catalytic conversion rates in Fig. 5.9, pertaining to P = 1 bar. For $\phi = 0.10$ (Fig. 5.9a), the hydrogen catalytic conversion rate is already high after the first time step (15 ms), while for $\phi = 0.28$ the conversion rate attains appreciable values only after 330 ms. Moreover, for $\phi = 0.10$ ignition is achieved at the reactor front since the catalytic conversion in Fig. 5.9a peaks at x≈0 already after 15 ms. On the other hand, for $\phi = 0.28$ ignition is achieved at the reactor rear (the conversion peaks close to x≈10 mm at times as long as 315 ms). This start up behavior is in contrast to methane catalytic ignition [68], where there is always a rear end ignition followed by a slow upstream propagation of the reaction front. The faster ignition at $\phi = 0.10$ shown in Figs. 5.7 and 5.8 is a result of the inhibition of catalytic ignition with rising hydrogen concentration, as discussed in the foregoing Section 2.1. Surface coverage profiles for P = 1 bar are provided in

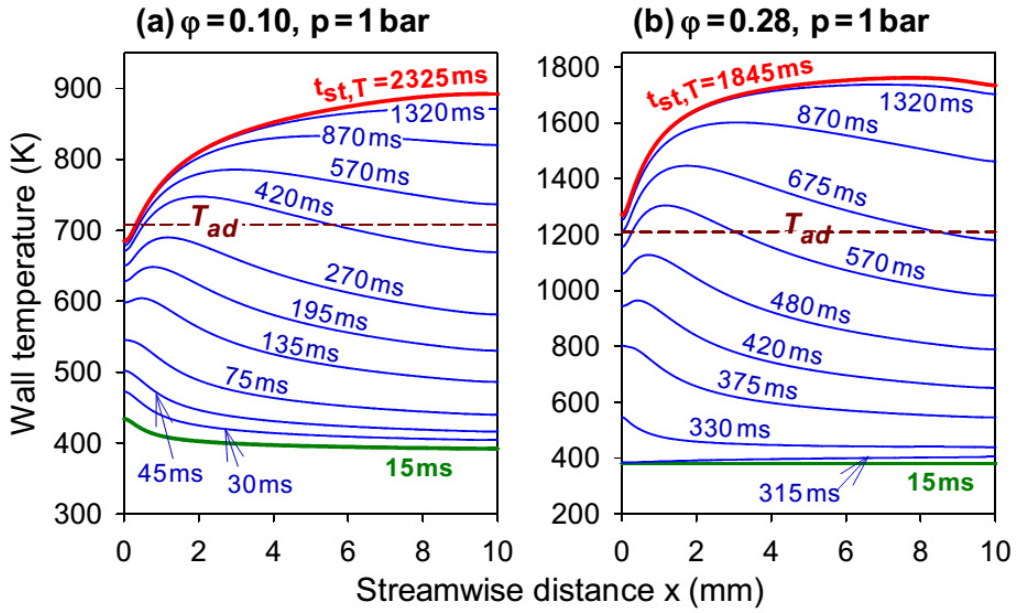

Figure 5.7: *Streamwise profiles of wall temperatures at various times: (a) P = 1 bar, T_{IN} = 380 K, U_{IN} = 50 m/s, ϕ = 0.10, and (b) P = 1 bar, T_{IN} = 380 K, U_{IN} = 50 m/s, ϕ = 0.28. Thick solid lines denote the first time step (15 ms) and the times where the wall temperatures have reached 99.9% of the corresponding steady-state values (2325 ms and 1845 ms in (a) and (b), respectively). The horizontal dashed lines marked T_{ad} indicate the adiabatic equilibrium temperatures for the two cases.*

Fig. 5.10. For the ϕ = 0.10 case in Fig.5.10a, catalytic ignition has already been achieved at the first step (15 ms) as manifested by the very low H(S) coverage ($\theta_H < 10^{-6}$). On the other hand, for ϕ = 0.28 the surface is blocked by H(S) at the first time step ($\theta_H \approx 0.987$ in Fig. 5.10b at 15 ms). It is clarified that the catalytic ignition processes at the two different pressures (Figs. 5.7 and 5.8) cannot be directly compared as the initial temperatures are different (380 K and 400 K at P = 1 and 5 bar, respectively).

Channel heat up to steady state

Upon catalytic ignition, the wall temperatures peak close to the channel entry (Figs. 5.7 and 5.8), while later on the corresponding maxima shift farther downstream. The wall temperatures eventually attain superadiabatic values (see the dashed lines marked T_{ad} in Figs. 5.7 and 5.8) due to the diffusional imbalance of hydrogen (Lewis number of hydrogen in fuel lean H_2/air mixtures is $Le_{H_2} \approx$

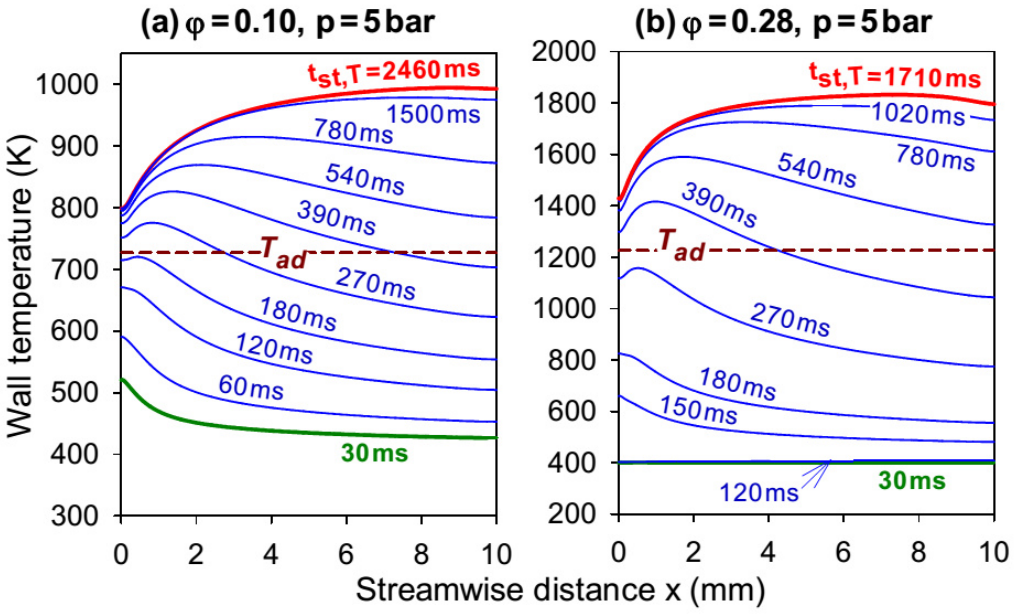

Figure 5.8: *Streamwise profiles of wall temperatures at various times: (a) P = 5 bar, T_{IN} = 400 K, U_{IN} = 10 m/s, ϕ = 0.10, and (b) P = 5 bar, T_{IN} = 400 K, U_{IN} = 10 m/s, ϕ = 0.28. Thick solid lines denote the first time step (30 ms) and the times where the wall temperatures have reached 99.9% of the corresponding steady-state values (2460 ms and 1710 ms in (a) and (b), respectively). The horizontal dashed lines marked Tad indicate the adiabatic equilibrium temperatures for the two cases.*

0.32). At fuel lean H_2/air stoichiometries, the less than unity Lewis number of hydrogen leads to a surface equivalence ratio ϕ_{surf} about twice that of the bulk gas phase ϕ_{bulk} [30, 31]. However, the aforementioned relation $\phi_{surf} \approx 2\phi_{bulk}$ holds only for transport limited hydrogen conversion and for a catalytic flat plate. For the confined channel flow configuration, and still for transport limited hydrogen conversion, the effective ϕ_{surf} drops from the maximum of $\approx 2\phi_{bulk}$ at the channel entry to ϕ_{bulk} farther downstream when complete hydrogen conversion is achieved [43, 108]. The theoretical maximum wall temperature for an adiabatic channel with transport limited hydrogen conversion is attained at the channel entry (x = 0) and is given by the relation $T_{w,max} = T_{IN} + Le_{H_2}^{-2/3}(T_{ad} - T_{IN})$ [43]. This leads to $T_{w,max}$ = 1081 K (Fig. 5.7a), 2153 K (Fig. 5.7b), 1099 K (Fig. 5.8a) and 2168 K (Fig. 5.8b). However, the maximum superadiabatic surface temperatures in Figs. 5.7 and 5.8 are lower than the theoretical $T_{w,max}$ for two reasons: the hydrogen conversion is not transport controlled but mixed transport/kinetically controlled and the reactor is non adiabatic due to radiation heat losses from the hotter chan-

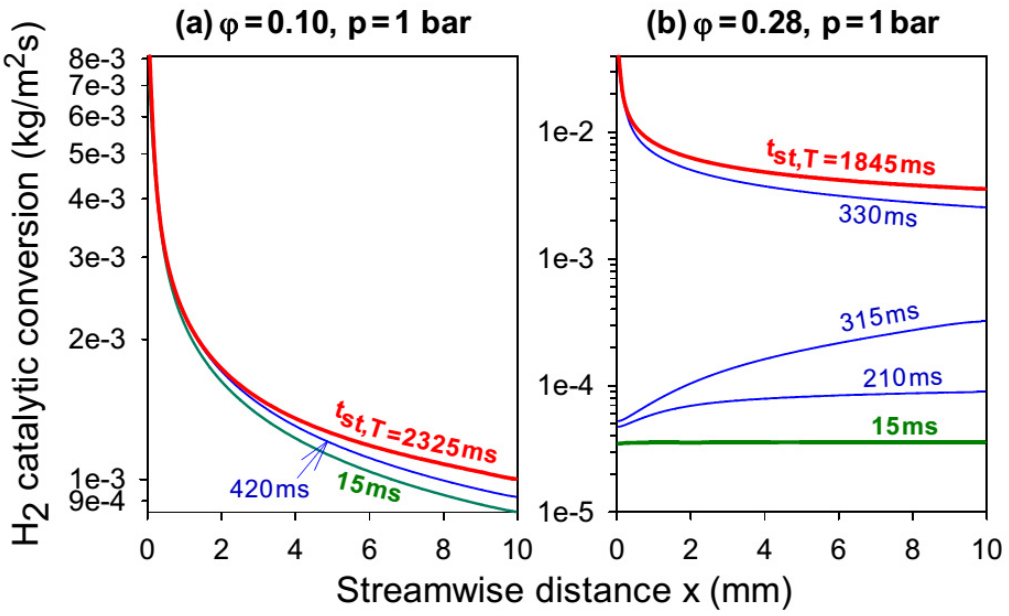

Figure 5.9: *Streamwise profiles of hydrogen catalytic conversion rates in the channel of Fig. 5.1 (FeCr-alloy wall, simulations with inclusion of catalytic chemistry only) at various times for the two cases in Fig. 5.7: (a) P = 1 bar, T_{IN} = 380 K, U_{IN} = 50 m/s, ϕ = 0.10, and (b) P = 1 bar,T_{IN} = 380 K, U_{IN} = 50 m/s, ϕ = 0.28. Thick lines denote $t_{st,T}$ (the times where the wall temperatures have reached 99.9% of their corresponding steady-state values).*

nel surface elements towards the colder inlet section.

The mixed transport/kinetically controlled hydrogen conversion is demonstrated in Fig. 5.11, providing transverse profiles of hydrogen mass fractions for the four investigated cases in Figs. 5.7 and 5.8 at three selected axial locations and two times. The longer times shown in Fig. 5.11 (dashed lines) correspond to the steady state wall temperature times $t_{st,T}$. It is evident that even at these longer times (where steady state wall temperatures have been practically achieved) the catalytic conversion is not transport limited since the ratio Y_{H_2}(y = 0.5 mm)/Y_{H_2}(y = 0) can be appreciably higher than zero: for example, it is greater than 20% in Fig. 5.11a, 8% in Fig. 5.11b, 6% in Fig. 5.11c and 2% in Fig. 5.11d. Finite rate chemistry effects are only mildly reduced with increasing time for ϕ = 0.10 (see Figs. 5.11a and 5.11c) and this leads to hydrogen catalytic conversion rates only weakly dependent on time as seen in Fig. 5.9a. On the other hand, for ϕ = 0.28 the strong finite rate chemistry at times 315 ms (Fig. 5.11b) and 120 ms (Fig. 5.11d) are substantially reduced afterwards, leading to hydrogen catalytic

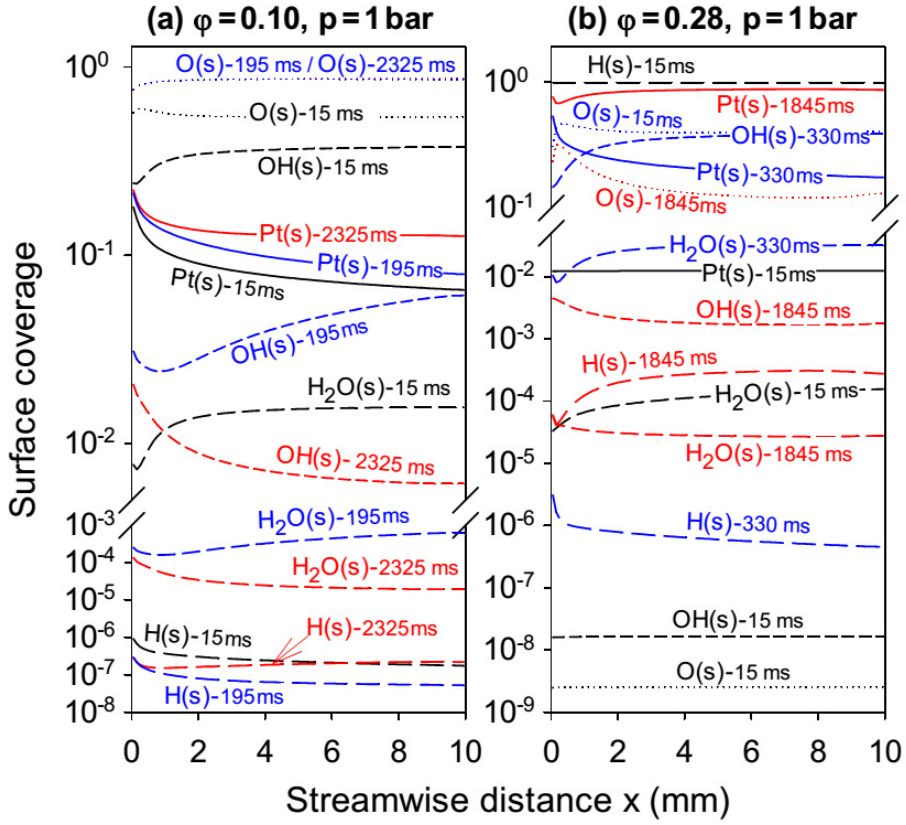

Figure 5.10: *Streamwise profiles of surface coverages for the two cases in Fig. 5.7 (FeCr-alloy wall, simulations with inclusion of catalytic chemistry only) at three different times. The longer times (2325 ms and 1845 ms in (a) and (b), respectively) correspond to $t_{st,T}$ (the times where the wall temperatures have reached 99.9% of their corresponding steady-state values)*

conversion rates strongly time dependent (Fig. 5.9b). The elapsed times required to reach 99.9% of the steady state wall temperatures $t_{st,T}$ range from 1710 to 2460 ms (see Figs. 5.7 and 5.8). Such long time integrations are not easily tractable by DNS, as discussed in [91] and clearly show the advantages of the QSS model. The $t_{st,T}$ times are, for a given pressure, longer for ϕ= 0.10 than for ϕ= 0.28. At P = 1 bar, the $t_{st,T}$ times for ϕ = 0.10 and 0.28 are 2325 ms and 1845 ms (Fig. 5.7), while at P = 5 bar the corresponding values are 2460 ms and 1810 ms (Fig. 5.8). The longer $t_{st,T}$ at ϕ = 0.10 compared to ϕ = 0.28 occurs despite the longer initial ignition process at ϕ = 0.28, which was discussed in the previous section. The reason for the shorter $t_{st,T}$ times at ϕ = 0.28 can be explained by the approximate kinetic expression in Eqn. 5.19. After catalytic ignition ($T>T_{ign}$), the $C_{H2}^{1.5}$

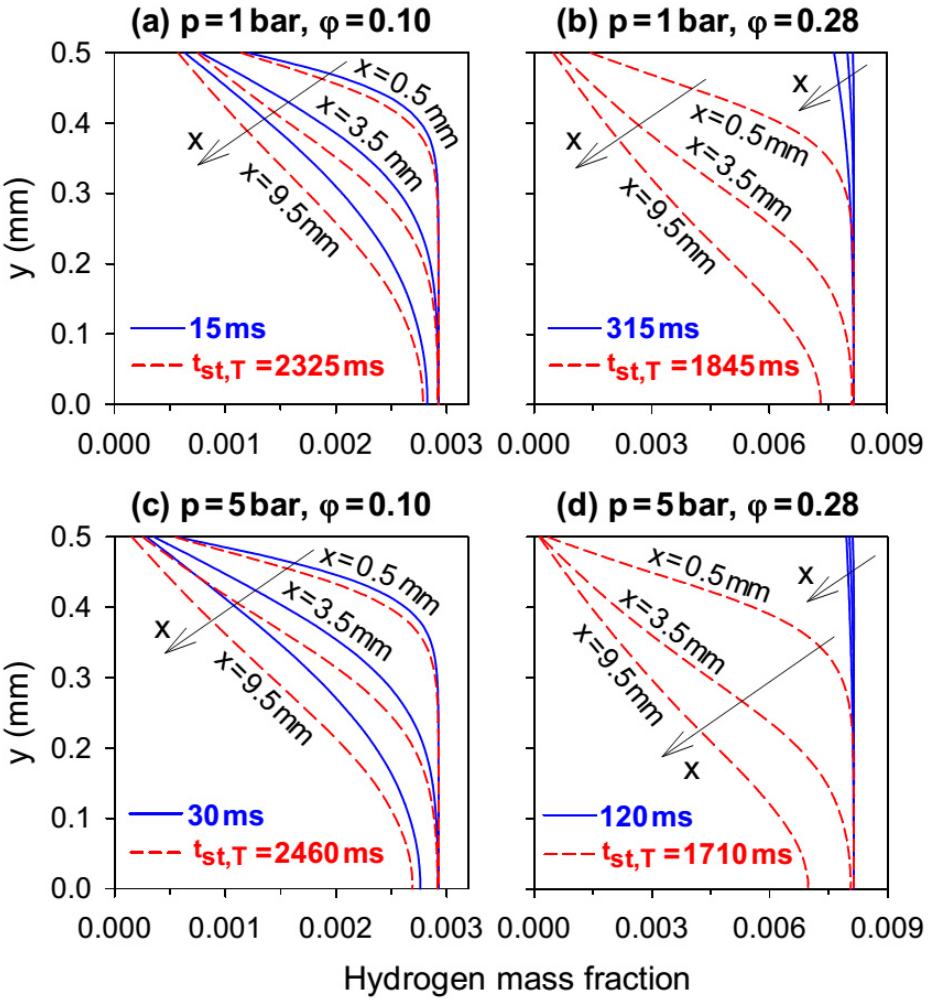

Figure 5.11: *Transverse profiles of hydrogen in the channel of Fig. 5.1 (FeCr-alloy wall, simulations with inclusion of catalytic chemistry only) for the four cases in Figs. 5.7 and 5.8 at three axial positions x = 0.5, 3.5 and 9.5 mm and two times; y = 0 is the channel symmetry plane and y = 0.5 mm the gas-wall interface. The longer times (dashed lines) correspond to $t_{st,T}$ (the times where the wall temperatures have reached 99.9% of their corresponding steady-state values)*

dependence in Eqn. 5.19 promotes the hydrogen catalytic conversion at higher equivalence ratios, and this effect overtakes the initial inhibition ($T<T_{ign}$) at ϕ = 0.28. It is nonetheless clarified that, for the chemical promoting effect at $T>T_{ign}$ to impact the hydrogen conversion in the channel, key requirement is a reactor operation in the kinetically controlled (or mixed kinetically/transport controlled) and not in the purely transport controlled regime. This requirement is satisfied for

the operating conditions in Figs. 5.7 and 5.8, as has been discussed in the context of Fig. 5.11.

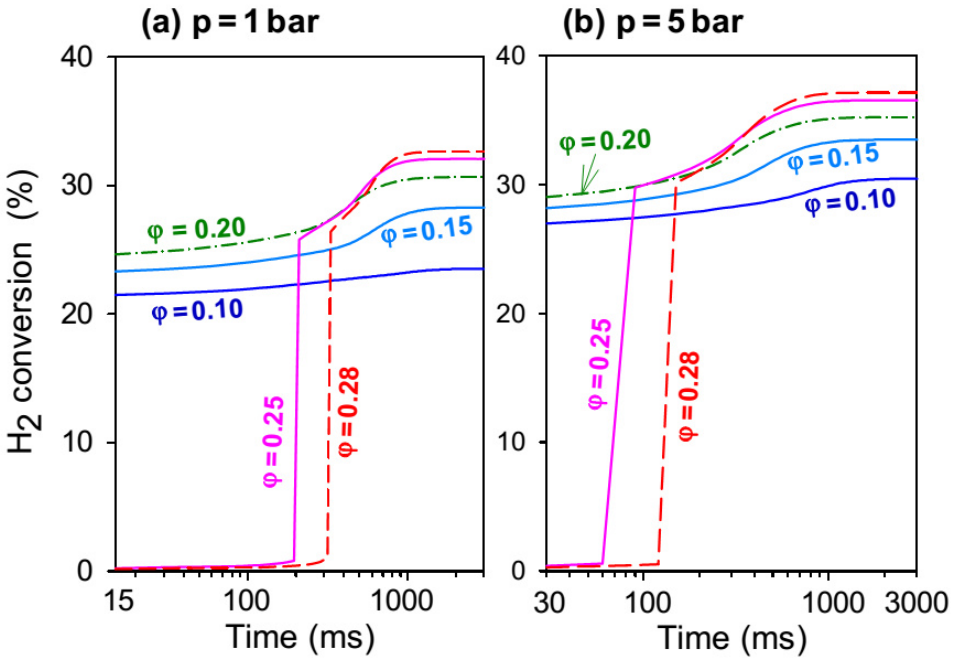

Figure 5.12: *Time histories of hydrogen conversion in the channel of Fig. 5.1 (FeCr-alloy wall, simulations with inclusion of catalytic chemistry only) for different equivalence ratios: (a) P = 1 bar, T_{IN} = 380 K, U_{IN} = 50 m/s, and (b) P = 5 bar, T_{IN} = 400 K, U_{IN} = 10 m/s.*

Time histories of total hydrogen percentage conversions (over the entire length of the channel) are provided in Fig. 5.12 for two pressures and various equivalence ratios. Concentrating on the steady state results, the conversions are appreciably larger at 5 bar: for example, at ϕ = 0.10 the hydrogen conversion at steady state is 23.5% (P = 1 bar) and 30.4% (P = 5 bar), while at ϕ = 0.28 the conversion is 32.6% (P = 1 bar) and 37.3% (P = 5 bar). Since the mass flux throughput $\rho_{IN}U_{IN}$ is, for a given equivalence ratio, practically the same at different pressures (notwithstanding the small differences in T_{IN} at P = 1 and 5 bar) and hence the inlet Reynolds number ($\rho_{IN}U_{IN}b/\mu_{IN}$) is nearly the same, mass transfer considerations dictate the same hydrogen conversion under transport limited reactor operation [19]. The observed differences in hydrogen conversions are due to finite rate surface chemistry, which is more pronounced at P = 1 bar due to the reduced catalytic reactivity at lower pressures (see the $P^{0.97}$ dependence of the catalytic reaction rate in Eqn. 5.19 for $T>T_{ign}$). The reduced catalytic reactivity at P = 1 bar also leads to lower maximum wall temperatures. For example, when ϕ = 0.10 the

maximum wall temperature at $t_{st,T}$ is 892.3 K for P = 1 bar (Fig. 5.7a) and 994.4 K for P = 5 bar (Fig. 5.8a). The difference of 102.1 K is much larger than the 20 K difference in inlet temperatures (380 K versus 400 K) and is a clear indication of the promoting effects of pressure on the catalytic reaction rate. Similarly, for ϕ = 0.28 the maximum wall temperature at steady state is 1761.7 K at P = 1 bar (Fig. 5.7b) and 1832.3 K at P = 5 bar (Fig. 5.8b), i.e. a difference of 70.6 K. Figure 5.13 provides the $t_{st,T}$ times as well as the elapsed times required to achieve 99.9% of the steady state hydrogen conversion (marked $t_{st,H2}$) as a function of equivalence ratio, for the two investigated pressures. It is evident that $t_{st,H2}$ are shorter than $t_{st,T}$ due to the weak increase of hydrogen conversion above a certain level of wall temperatures (see Fig. 5.9). For a given pressure, the computed $t_{st,T}$ and $t_{st,H2}$ times in Fig. 5.13 become shorter with increasing equivalence ratio. Alternately, for a given equivalence ratio the computed $t_{st,T}$ and $t_{st,H2}$ times are shorter for the higher pressure, with an exception at ϕ = 0.10.

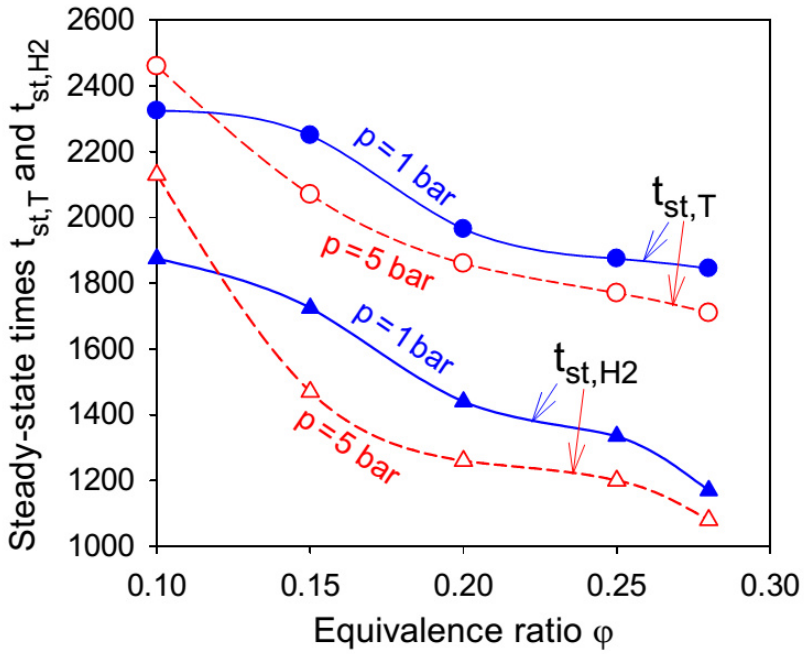

Figure 5.13: *Times need to reach 99.9% of steady-state wall temperatures ($t_{st,T}$) and 99.9% of steady-state hydrogen conversions ($t_{st,H2}$) in the channel of Fig. 5.1 (FeCr-alloy wall, simulations with inclusion of catalytic chemistry only) as a function of equivalence ratio for two different pressures.*

The reason is that for ϕ = 0.10, the steady state solution at P = 1 bar settles to appreciably lower wall temperatures compared to P = 5 bar (as discussed in the

previous paragraph); this in turn leads to a shorter time necessary to reach steady state at P = 1 bar, despite the lower catalytic reactivity at P = 1 bar for any time between 15 ms (first time step) and steady state. It is noted that steady state times based on the fuel conversion are at least an order of magnitude longer in methane fueled Pt coated channels of the same geometry and FeCr-alloy walls (42 s and 28 s at P = 1 bar and 5 bar, respectively [68]) compared to the corresponding hydrogen times $t_{st,H2}$ in Fig. 5.13. In summary, for a given pressure, the shorter steady state times ($t_{st,T}$ or $t_{st,H2}$) at larger equivalence ratios bear two distinct effects: a) chemical effects due to the enhanced catalytic reactivity at larger equivalence ratios when $T>T_{ign}$, and b) thermal effects due to the higher exothermicity and thus higher wall temperatures at larger equivalence ratios that in turn accelerate the catalytic reaction rates. The shorter $t_{st,T}$ and $t_{st,H2}$ times at higher pressures (for a given equivalence ratio ϕ >0.10) are a result of the positive pressure dependence of the catalytic reactivity at $T>T_{ign}$. The above analysis has thus shown a very rich behavior in the start up of hydrogen fueled catalytic reactors.

Comparison between FeCr alloy and cordierite wall materials

During the heat up process, the solid thermal conductivity k_s as well as its heat capacity $\rho_s c_s$ are important; in particular, materials with a higher heat capacity require larger energy input to raise their temperature. On the other hand, at steady state operation the solid heat capacity $\rho_s c_s$ becomes irrelevant (see Eqn. 5.11) and only the thermal conductivity of the solid affects the solution. Figure 5.14 provides wall temperature profiles at P = 1 bar, for cordierite walls. By comparing Figs. 5.14 and 5.7, it is seen that the cases with cordierite walls heat up faster than the corresponding ones with FeCr-alloy walls. For $t\leq$135 ms at ϕ = 0.10, and for t $\leq$ 420 ms at ϕ = 0.28, the cordierite wall temperatures are always higher than the corresponding FeCr-alloy wall temperatures at any axial position (compare Figs. 5.14a 5.7a and Figs. 5.14b 5.7b). In particular, the catalytic ignition at ϕ = 0.28 is appreciably shortened: while catalytic ignition for FeCr-alloy occurs between 315 ms and 330 ms (see Fig. 5.7b and Fig. 5.9b), catalytic ignition is achieved between 240 ms and 255 ms for cordierite (Fig. 5.14b). This is primarily a result of the cordierite heat capacity (≈16% lower than that of FeCr-alloy, see $\rho_s c_s$ values in Table 5.1). The times required to reach the steady state times $t_{st,T}$ are 21.3% shorter (ϕ = 0.10) and 23.5% shorter (ϕ = 0.28) for cordierite compared to FeCr-alloy (see Figs. 5.14 and 5.7).

With increasing time, the axial locations of the wall temperature maxima ($x_{T,max}$) shift farther downstream. For t>135 ms and ϕ = 0.10 (or t>420 ms and ϕ = 0.28), over the length $x_{T,max}\leq x\leq L$ the cordierite wall temperatures are, at a given time, always higher than those of FeCr-alloy wall. For example, at t = 570 ms and ϕ = 0.10, the maximum wall temperature is 821.3 K for cordierite (Fig.

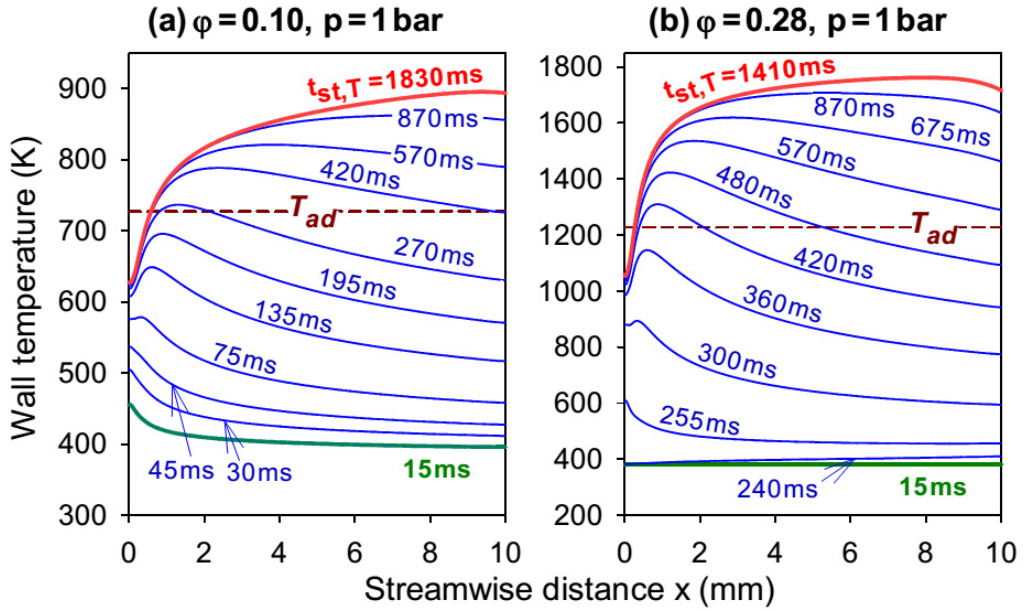

Figure 5.14: *Streamwise profiles of wall temperatures in the channel of Fig. 5.1 (cordierite wall, simulations with inclusion of catalytic chemistry only) at various times: (a) P = 1 bar, T_{IN} = 380 K, U_{IN} = 50 m/s, ϕ = 0.10, and (b) P = 1 bar, T_{IN} = 380 K, U_{IN} = 50 m/s, ϕ = 0.28. Thick lines denote the first time step (15 ms) and $t_{st,T}$ (the times where the wall temperatures have reached 99.9% of their corresponding steady-state values: 1830 ms and 1410 ms in (a) and (b), respectively). The horizontal dashed lines marked T_{ad} indicate the adiabatic equilibrium temperatures.*

5.14a) and 785.8 K for FeCr-alloy (Fig. 5.7a); the corresponding maximum values at ϕ = 0.28 are 1536.2 K for cordierite (Fig. 5.14b) and 1304.7 K for FeCr-alloy (Fig. 5.7b). At $t_{st,T}$ the maximum wall temperatures are only slightly higher for cordierite material: 895.5 K for cordierite and 892.4 K for FeCr-alloy at ϕ = 0.10, 1762.2 K for cordierite and 1761.6 K for FeCr-alloy at ϕ = 0.28. Conversely, for t>135 ms at ϕ = 0.10 (or t>420 ms at ϕ = 0.28) and x<$x_{T,max}$, the cordierite wall temperatures can become lower than those of the FeCr-alloy wall. For example, at $t_{st,T}$ and ϕ = 0.10 the front-end temperatures (x = 0) are 627.8 K for cordierite and 685.4 K for FeCr-alloy (Figs. 5.14a and 5.7a), while for ϕ = 0.28 the corresponding temperatures are 1058.6 K and 1272.2 K (Figs. 5.14b and 5.7b). The higher wall temperatures at the channel entry for the FeCr-alloy are due to its substantially higher thermal conductivity k_s compared to that of cordierite (see Table 5.1), which facilitates heat conduction from the hotter downstream parts of

the channel to the colder upstream sections. Qualitative similar results to those in Figs. 5.14 (P = 1 bar) are also obtained for P = 5 bar (not shown here). In conclusion, cordierite walls (when compare to FeCr-alloy walls) shorten the times required to reach steady state, while leading to only slightly higher maximum wall temperatures and to appreciably lower entry wall temperatures. Depending on the particular application, cordierite can be used when faster ignition and shorter steady state times $t_{st,T}$ are needed (i.e. gas turbine catalytic reactors), while FeCr-alloy is preferable when higher spatial homogeneity of the surface temperatures is required (e.g. coupling of reactor to thermoelectric modules).

5.3.3 Channel simulations with heterogeneous and homogeneous chemistry

Catalytic ignition and hetero-/homogeneous combustion

Streamwise profiles of wall temperatures are depicted in Fig. 5.15 for P = 5 bar, ϕ = 0.20 and ϕ = 0.28, at various times during the reactor startup (solid lines); dashed lines are predictions with only catalytic chemistry (no gas phase chemistry included). For the ϕ = 0.20 case in Fig. 5.15a, the wall temperature profiles at t $\leq$ 600 ms coincide in both type of simulations (catalytic chemistry alone or combined catalytic and gas phase chemistry); similarly, for ϕ = 0.28 in Fig. 5.15b the wall temperature profiles of both simulations coincide at t $\leq$ 390 ms. It is obvious that the catalytic ignition and early reactor heat up are not affected by gas phase chemistry. It has been shown [104] that gas phase chemistry is initiated at wall temperatures above ≈1350 K for P = 5 bar, fuel lean H_2/air stoichiometries, and planar channels with 1 mm height. For P = 5 bar, gaseous combustion is significant only when $\phi \geq$0.20. On the other hand, at P = 1 bar gaseous combustion has a modest contribution only at the highest ϕ = 0.28, and hence this pressure will not be further discussed. The diminishing contribution of gaseous chemistry at P = 1 bar, is not attributed to the modestly lower inlet temperature at P = 1 bar (T_{IN} = 380 K) compared to P = 5 bar (T_{IN} = 400 K), but mainly to the increasing gaseous reactivity with rising pressure. Even though the pressure dependence of hydrogen gas phase kinetics is intricate, over the range $1 \leq P \leq 5$ bar the gaseous reactivity of fuel lean H_2/air mixtures increases monotonically with rising pressure for temperatures greater than 1200 K [104, 35].

Streamwise profiles of catalytic (C) and gas phase (G) hydrogen conversion rates are shown in Fig. 5.16 at selected times from the onset of gaseous combustion to the steady state $t_{st,T}$ times. The volumetric gas phase conversions G in Fig. 5.16 have been integrated over the channel half height in order to be directly comparable to the surface catalytic conversion rates C. Catalytic conversion rate profiles at $t_{st,T}$ obtained with only catalytic chemistry simulations are also shown

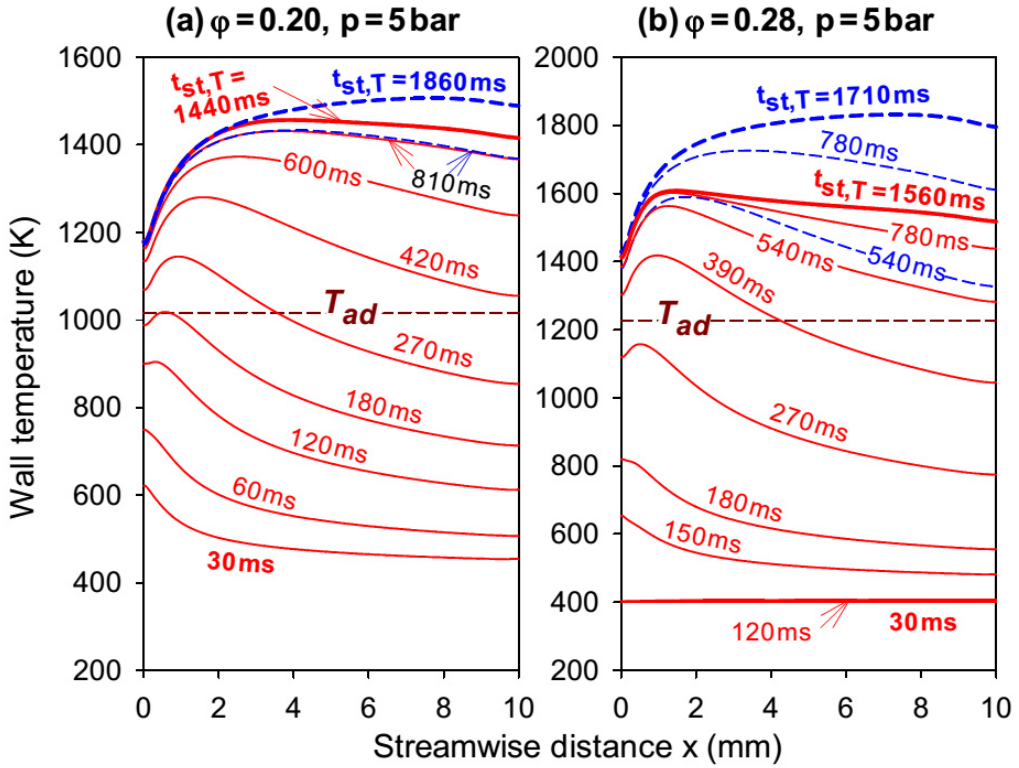

Figure 5.15: *Streamwise profiles of wall temperatures in the channel of Fig. 5.1 (FeCr-alloy wall) at various times. Solid lines are simulations with inclusion of both catalytic and gaseous chemistry and dashed lines are simulations with catalytic chemistry only: (a) P = 5 bar, T_{IN} = 400 K, U_{IN} = 10 m/s, ϕ = 0.20, and (b) P = 5 bar, T_{IN} = 400 K, U_{IN} = 10 m/s, ϕ = 0.28. Thick lines denote $t_{st,T}$ (the times where the wall temperatures have reached 99.9% of their corresponding steady-state values). The horizontal dashed lines marked T_{ad} indicate the adiabatic equilibrium temperatures.*

in Fig. 5.16 (thick dashed dotted lines). The plots in Fig. 5.16 indicate that following homogeneous ignition, the G rates increase with increasing time at the expense of the C rates. At the steady state time $t_{st,T}$ = 1560 ms in Fig. 5.16b (ϕ = 0.28), the C rate practically ceases at x>3 mm and the G rate dominates. On the other hand, for ϕ = 0.20 in Fig. 5.16a, at $t_{st,T}$ = 1440 ms there is always a non zero contribution of the C conversion rate over the entire channel length, leading to parallel conversion of hydrogen by both catalytic and gas phase pathways. Combined catalytic and gas phase conversion at a given axial location implies that hydrogen leaks through the gaseous combustion zone to be subsequently converted catalytically on the platinum surface.

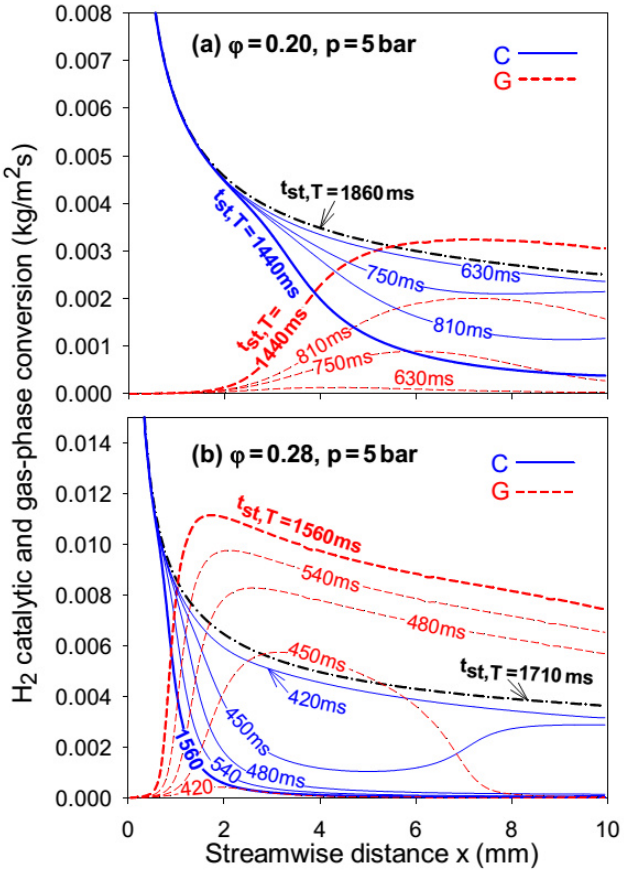

Figure 5.16: *Streamwise profiles of wall temperatures in the channel of Fig. 5.1 (FeCr-alloy wall) at various times. Solid lines are simulations with inclusion of both catalytic and gaseous chemistry and dashed lines are simulations with catalytic chemistry only: (a) P = 5 bar, T_{IN} = 400 K, U_{IN} = 10 m/s, ϕ = 0.20, and (b) P = 5 bar, T_{IN} = 400 K, U_{IN} = 10 m/s, ϕ = 0.28. Thick lines denote $t_{st,T}$ (the times where the wall temperatures have reached 99.9% of their corresponding steady-state values). The thick dashed-dotted lines provide the corresponding catalytic conversion rates C computed using only heterogeneous chemistry.*

5.3.4 Channel heat up to steady state

An important finding in Fig. 5.15 is that the maximum wall temperatures at $t_{st,T}$ obtained with heterogeneous and homogeneous chemistry simulations can be substantially lower than the corresponding maximum wall temperatures at $t_{st,T}$ computed with only catalytic chemistry. For example, in Fig. 5.15b (ϕ = 0.28) the maximum wall temperature is 1832.3 K with hetero-/homogeneous chemistry

simulations ($t_{st,T}$ = 1710 ms) and 1608.4 K with only heterogeneous chemistry simulations ($t_{st,T}$ = 1560 ms); corresponding values for ϕ = 0.20 in Fig. 5.15a are 1506.9 K and 1456.9 K. This suppression of the highly superadiabatic wall temperatures due to the presence of gas phase combustion was initially observed experimentally in [34] and then verified with 2-D steady simulations [4, 109]. Reason for this suppression is that gaseous combustion occurs close to and nearly parallel to the catalyst surface and thus "shields" the catalyst surface from the hydrogen rich channel core; this in turn deprives hydrogen from the heterogeneous reaction pathway and eventually moderates the catalytic combustion induced superadiabatic surface temperatures.

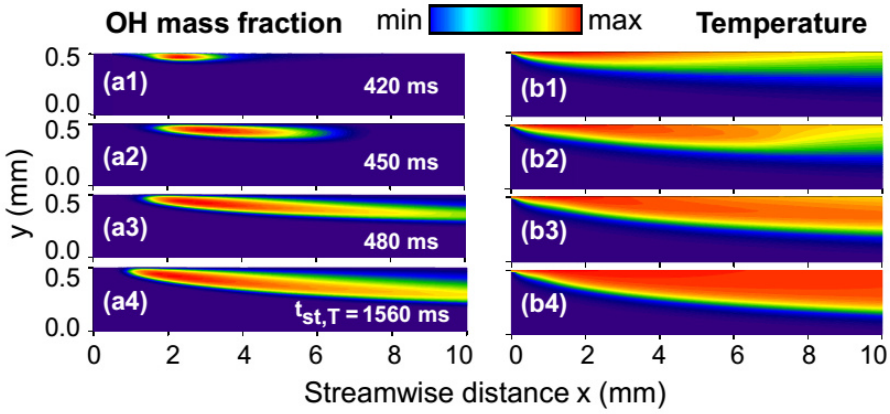

Figure 5.17: *Two-dimensional distributions of OH mass fraction (a1-a4) and temperature (b1-b4) at selected times from the onset of homogeneous ignition to the steady-state time $t_{st,T}$: P = 5 bar, T_{IN} = 400 K, U_{IN} = 10 m/s, ϕ = 0.28 (same as in Figs. 5.15b and 5.16b). Simulations for FeCr-alloy wall material in the channel of Fig. 5.1 with inclusion of catalytic and gas-phase chemistry (y = 0 is the channel plane of symmetry and y = 0.5 mm the gas-wall interface). OH mass fractions range from 0 to 3.5x10^{-5} (a1), 5.1x10^{-4} (a2), 8.5x10^{-4} (a3), and 1.3x10^{-3} (a4). Temperatures range from 400 K to 1462.7 K (a1), 1500.2 K (a2), 1528.9 K (a3), and 1608.4 K (a4).*

This shielding action is illustrated in Fig. 5.17, providing 2-D distributions of the OH mass fraction and temperature for the two P = 5 bar cases of Figs. 5.15 and 5.16. As manifested by the OH distributions, the flame zones are at all times nearly parallel to the x-axis (for this, note also the difference between x and y scales in Fig. 5.17) and furthermore they never extend to the channel core (y = 0). The OH maps in Fig. 5.17(a1) attest the onset of homogeneous ignition at t≈420 ms. Subsequently, gaseous combustion propagates slowly upstream and at a faster rate downstream such that at $t_{st,T}$ (Fig. 5.17(a4)) gaseous combustion extends over

$1 \leq x \leq 10$ mm. Similarly, the gas in the channel heats up appreciably at $t_{st,T}$ (Fig. 5.17(b4)) due to the presence of homogeneous combustion. The implications of the aforementioned hetero-/homogeneous chemistry coupling (which is specific to the diffusionally imbalanced hydrogen fuel) for the reactor heat up and steady state performance are profound as will be discussed next. The steady state times $t_{st,T}$ can be substantially shorter in combined heterogeneous and homogeneous chemistry simulations compared to only heterogeneous chemistry; for example, in Fig. 5.15b $t_{st,T}$ = 1560 ms for the former simulations and $t_{st,T}$ = 1710 ms for the latter (corresponding values in Fig. 5.15a are $t_{st,T}$ = 1440 ms and $t_{st,T}$ = 1860 ms). The shorter $t_{st,T}$ are clearly a result of the lower final wall temperatures in the case of combined heterogeneous and homogeneous chemistry, as explained in the previous paragraph. The time history of the percentage hydrogen conversions are illustrated in Fig. 5.18 for P = 5 bar and for the three stoichiometries $\phi \geq 0.20$ wherein gaseous combustion plays a role; solid lines are predictions with both catalytic and gas phase chemistry, while dashed lines are predictions with only catalytic chemistry (the latter are also shown in Fig. 5.12). Both types of predictions coincide down to the times of homogeneous ignition (marked with the vertical arrows $t_{ign,hom}$ in Fig. 5.18), whereas afterwards the combined catalytic and gas phase chemistry simulations lead to substantially higher conversions.

For ϕ = 0.28, the final hydrogen conversions are 63.2% (catalytic and gas phase chemistry) and 37.1% (only catalytic chemistry); corresponding numbers for ϕ = 0.20 are 40.8% and 35.2%. The higher hydrogen conversions in the combined hetero-/homogeneous chemistry simulations are due to the fact that the gaseous reaction pathway does not exhibit the strong transport limitations of the catalytic pathway. This is demonstrated as follows. In an ideal planar adiabatic laminar flame, the mass burning rate for ϕ = 0.20, P = 5 bar and a characteristic fresh mixture temperature of 673 K is $\dot{m}_0$ = 0.1 kg/m^{2}s [104]. As the flame in the channel is aligned nearly parallel to the x-axis (see Fig. 5.17), it can consume about 0.4 kg of hydrogen per unit channel wall area when further neglecting flame stretch effects. On the other hand, the local catalytic mass flux, for P = 5 bar and ϕ = 0.20, has a much lower average value of about 0.005 kg/m^{2}s as seen in Fig. 5.16a (see the dashed dotted line for the catalytic conversion at $t_{st,T}$ = 1860 ms) Computed steady state times $t_{st,T}$ and $t_{st,H2}$ are plotted in Fig. 5.19 for various equivalence ratios at P = 5 bar using combined catalytic and gas phase chemistry or catalytic chemistry alone. The inclusion of gaseous chemistry reduces $t_{st,T}$ for $\phi \geq 0.20$, as discussed previsouly. On the other hand, the steady state times for hydrogen conversion $t_{st,H2}$ increase in the presence of gaseous combustion. The elongated $t_{st,H2}$ with addition of gas phase chemistry was also observed in previous studies of a methane fueled catalytic reactor startup [68] and was attributed to the less effective heat transfer from the reacting gas to the channel wall (the thermal conductivity of the hot reacting gases is about two orders of magnitude

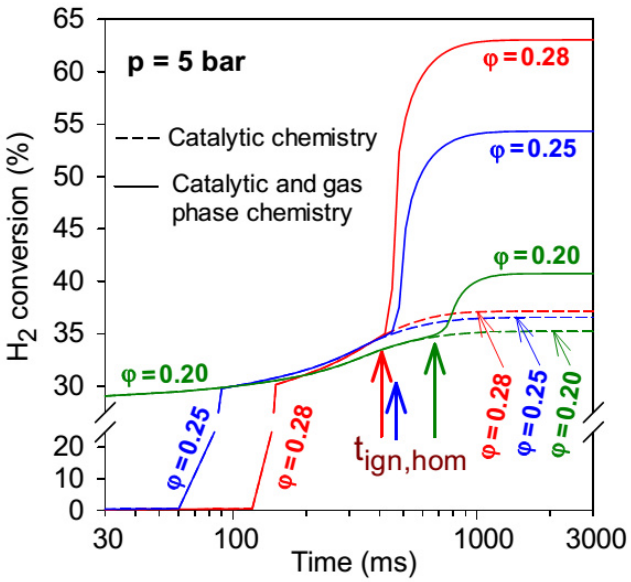

Figure 5.18: *Time histories of hydrogen conversion in the channel of Fig. 5.1 (FeCr-alloy wall), for p = 5 bar and three different equivalence ratios. Solid lines are predictions with inclusion of catalytic and gas-phase chemistry and dashed lines are predictions with only catalytic chemistry.*

lower than the thermal conductivity of the solid wall). Nonetheless, considering for a practical system as steady state time the maximum among $t_{st,T}$ and $t_{st,H2}$, it becomes evident from Fig. 5.19 that $t_{st,T}$ is always longer irrespective of the simulation type (catalytic and gas phase chemistry or catalytic chemistry only). It is therefore deduced that the presence of gaseous chemistry reduces the time required to reach steady state in catalytic channel reactors fed with fuel lean H_2/air mixtures.

For practical hydrogen fueled power generation catalytic systems, gas phase combustion has the benefits of shorter steady state times, larger hydrogen conversions and lower wall temperatures that ensure long term thermal stability of the catalyst and the reactor. Methods for promoting or inhibiting the onset of gas phase combustion in catalytic channels (e.g. by changing the channel hydraulic diameter) have been discussed elsewhere [109]. Conversely, gaseous combustion is detrimental in applications where high wall temperatures are needed (such as catalytic reactors coupled with thermoelectric systems or catalytic reactors used as heat exchangers).

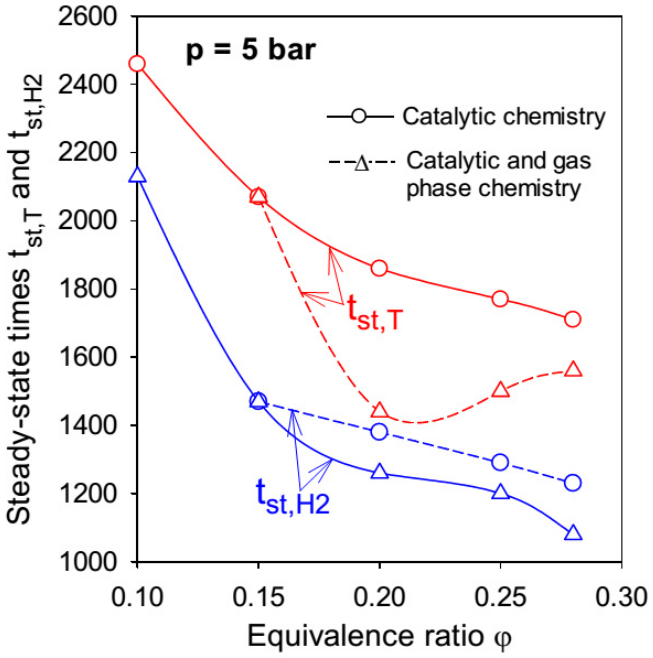

Figure 5.19: *Times need to reach 99.9% of steady-state wall temperatures ($t_{st,T}$) and 99.9% of steady-state hydrogen conversions ($t_{st,H2}$) in the channel of Fig. 5.1 (FeCr-alloy wall) as a function of equivalence ratio at P = 5 bar. Simulations with catalytic and gas-phase chemistry (circles, solid-lines) and catalytic chemistry only (triangles, dashed lines).*

5.4 Conclusions

The startup of platinum coated catalytic planar channels with heights of 1 mm and fed with fuel lean hydrogen/air mixtures (equivalence ratios 0.10 to 0.28) was investigated numerically at pressures of 1 and 5 bar and inlet temperatures 380-400 K, using a 2-D transient code with detailed hetero-/homogeneous chemistry, heat conduction in the solid wall and surface radiation heat transfer. The impact of catalytic and gas phase chemistry, pressure, equivalence ratio and solid material properties on the transient processes leading to ignition and finally to steady state operation was assessed. The following are the key conclusions of this study.

- Kinetic studies in a surface perfectly stirred reactor (SPSR) have shown that catalytic ignition of fuel lean hydrogen/air mixtures is inhibited with an increase in pressure or equivalence ratio. At temperatures above the catalytic ignition temperature T_{ign}, the above picture is reversed: catalytic reactivity exhibits positive order of ≈1.5 with respect to hydrogen concentration and

an overall pressure order of ≈0.97.

- Channel simulations with inclusion of only catalytic chemistry have shown that, for a given pressure, despite the initial longer ignition period at higher equivalence ratios (due to the inhibition discussed in point 1 above) the steady state times are shorter at larger equivalence ratios. This is due to chemical effects from the one side (enhanced catalytic reactivity at larger equivalence ratios when T>Tign) and thermal effects form the other side (higher exothermicity at larger equivalence ratios that in turn accelerate the catalytic reaction rates). Moreover, superadiabatic surface temperatures are eventually attained for all investigated equivalence ratios due to the diffusional imbalance of the hydrogen fuel.

- Steady state times defined on the hydrogen conversion, $t_{st,H2}$, are appreciably shorter than the corresponding steady state times based on the channel wall temperature, $t_{st,T}$, due to high reactivity of hydrogen on platinum that leads to catalytic hydrogen conversions changing only mildly above a certain wall temperature.

- The impact of gas phase chemistry on the startup process is profound at P = 5 bar. Homogeneous chemistry moderates substantially the surface temperatures. In particular, the steady state temperatures are lower by as much as 224 K (ϕ = 0.28) when gas phase chemistry is included in the simulations. This is because the gaseous combustion zone extends nearly parallel to the wall and hence shields the catalyst surface from the hydrogen rich channel core. This in turn leads to a reduction of the hydrogen catalytic conversion and hence to a drop of the catalytically induced surface superadiabaticity. Contrary to the significant impact of gas phase chemistry at P = 5 bar, at P = 1 bar it becomes modestly important and only for ϕ = 0.28. This is due to the acceleration of the gas phase hydrogen reactivity with rising pressure over the operating temperatures of the channel reactor.

- Gas phase chemistry substantially enhances the hydrogen conversion (by as much as 70% at ϕ = 0.28). This is because the homogeneous reaction pathway does not have the strong transport limitations of the catalytic pathway. Moreover, gas phase chemistry shortens the times required to reach steady state wall temperatures, $t_{st,T}$. For power generation systems, whereby catalyst thermal stability as well as reactor integrity, increased fuel conversion and faster startup are all issues of prime interest, the presence of gaseous chemistry is a clear advantage.

- Cordierite walls shorten the times required to reach steady state when compared to FeCr-alloy walls due to their lower heat capacity. Moreover, at

steady state the cordierite walls result in only slightly higher maximum wall temperatures and to appreciably lower entry wall temperatures due to their lower thermal conductivity. Depending on the particular application, cordierite can be used when faster ignition and shorter steady state times are needed (i.e. gas turbine catalytic reactors), while FeCr-alloy is preferable when higher spatial homogeneity of the surface temperatures is required (e.g. coupling of reactor to thermoelectric modules).

Chapter 6

H_2 production by steam reforming of natural gas

In this Chapter we discuss the most relevant process of H_2 production, its thermodynamics, the kinetics and we present an original set-up built to investigate the processes and its kinetics on commercial and novel catalysts, under pressure.

The great advancing in hydrogen based technologies has significantly increased the hydrogen world demand during the last decades [2]. Natural gas reforming is currently the most efficient, economical and widely used process for large scale hydrogen production. Despite the groth of new technologies, primarily validated for small-scale application, like membrane reforming [110], Steam Methane Reforming (SMR) is still the standard method on the large scale. Compact, small-scale, reformers have been also proposed in the past as an option [111], but they are still quite far from being reality.

The upstream desulphurisation is the major factor affecting fixed cost of a large-scale steam methane reformer. But the operative costs are determined by the amount of steam used. The main goal of SMR processes is maximising the H_2 yield and methane conversion, preventing the formation of elemental carbon and keeping it from fouling the catalyst. To this aim, the reformer is operated with steam-to-carbon ratio in excess of the stoichiometric. Operative costs such as pumping, steam production, reactor heating and products cooling for water separation are strongly increased by the large amount of steam required to prevent coking. Platinum Group Metals (PGM) catalyst successfully resist coking, but are extremely expensive and most PG elements are critical materials. The search for new catalysts is constantly progressing, with the aim of increasing the activity, while extending the catalyst lifetime and resistance to carbon deposition.

Here we undertake a theoretical and experimental study on catalysts for H_2 production by SMR, trying to lower the steam-to-carbon ratio, approaching S/C = 1), with the aim of determining critical operative conditions at which carbon

deposition is minimized.

Aiming at identifying suitable operative conditions, industrially meaningful, we first review the thermodynamics constraints. Then, we will analyse the kinetic models available for the most common, Ni-based catalysts, with special attention to detailed surface chemistry models, which is the main focus of this Thesis. Subsequently, the design of a laboratory testing rig for high pressure kinetic studies on commercial and novel catalysts will be described. One built, a comparative study on several catalyst is presented.

6.1 SMR thermodynamics

The methane steam reforming reaction 6.1 is a strongly endothermic reaction. It always occurs associated with water-gas shift reaction 6.2, mildly exothermic; also the total carbon oxidation can occur, reaction 6.3, also endothermic.

$$CH_4 + H_2O \rightleftharpoons CO + 3H_2 \quad \Delta H_{298K} = 206.1 kJ/mol \tag{6.1}$$

$$CO + H_2O \rightleftharpoons CO_2 + H_2 \quad \Delta H_{298K} = -41.15 kJ/mol \tag{6.2}$$

$$CH_4 + 2H_2O \rightleftharpoons CO_2 + 4H_2 \quad \Delta H_{298K} = 163.5 kJ/mol \tag{6.3}$$

Note that reactions 6.1 and 6.3 significantly increase the number of moles. Accordingly, thermodynamics suggests that low pressure and high temperature are optimal conditions for maximum methane conversion and H_2 production.

A thorough thermodynamic analysis has been carried out to evaluate the effect of varying temperature, pressure and steam/carbon ratio, in a range of industrial relevance. We considering a multiphase reactive system composed by an ideal gas mixture and a pure solid phase, made of carbon as graphite. Thermodynamic equilibrium has been calculated at different conditions by the *equilibrate* function of Cantera [67], suitably modified to account for the possible coexistence of two phases.

For industrial purposes, real operative conditions are usually forced to high pressure both because of the natural gas is available at approximately at 5 bar, and because of the pressure drop in the packed bed reactor and in possible downstream units. Reference pressure of 10 bar was assumed in all the calculations and will be used for the experiments as well.

The present study is mainly focused on low steam-to-carbon operative conditions for SMR process, however further complication is related to the higher hydrocarbons which strongly promote carbon deposition. Being the natural gas a mixture, we must account for the presence of higher hydrocarbons. Moreover, part of the hydrogen produced in the reforming process is usually recycled in the reforming reactor to favor catalyst's metal reduction, relevant for its activity.

Table 6.1: *Reference conditions for thermodynamic analysis. CH_4, H_2, C_2H_6 mole fractions refer to the dry mixture.*

P	T	S/C	$\mathbf{x}_{CH_4}$	$\mathbf{x}_{H_2}$	$\mathbf{x}_{C_2H_6}$
[bar]	[K]		[%]	[%]	[%]
10	923	1.4	85.5	5	9.5

The steam-to-carbon ratio, S/C, is frequently used above 2. Here we assume 1.4 as a first target. We will explore also values above and below it.

It has to be specified that reforming reactors are usually packed beds, arranged as pipes in a furnace. There will be a widely varying temperature profile along the bed (and across it, as well). The colder region is the inlet, where higher HCs, mainly responsible for coking, are more abundant. Often different catalyst layers are used, with a progressively higher activity and lower resistance to carbon deposition, from the inlet to the outlet, respectively. In the present study, the first catalyst layer, more exposed to carbon deposition because of the relatively low temperature ($\approx$ 920 K) and high hydrocarbons content, has been considered. Given this industrial consistency, we set the reference conditions for the thermodynamic analysis as summarized in Tab. 6.1.

According to the reference values reported in Tab. 6.1, pressure, temperature and steam-to-carbon values have been individually studied, by keeping the other variables constant. Methane conversion and selectivity to hydrogen/carbon were calculated with the following definitions:

$$X_{CH_4} = 1 - \frac{mol_{CH_4,OUT}}{mol_{CH_4,IN}} \tag{6.4}$$

$$Y_{H_2,C} = \frac{mol_{CH_4/C,OUT} - mol_{CH_4/C,IN}}{\sum_{i=H_2,CO,CO2,C}(mol_{i,OUT} - mol_{i,IN})} \tag{6.5}$$

Pressure effects

As previously discussed, the SMR reaction is not favored at high pressure. Mole fraction profiles at thermodynamic equilibrium reported in Figs. 6.1, clearly confirm that at the lower operative pressure H_2 and carbon monoxide are higher. H_2 mole fraction of 0.6 was calculated at 1 bar while at 20 bar was halved to 0.3. Similarly the CO molar fraction decreased from 0.13 to 0.03. A broad maximum has been noticed in the carbon dioxide production approximately at S/C = 5. Lower pressure (<1 bar) could be even more favorable for H_2 and CO production, however the explosion hazard due to air infiltration requires to guarantee a pressure

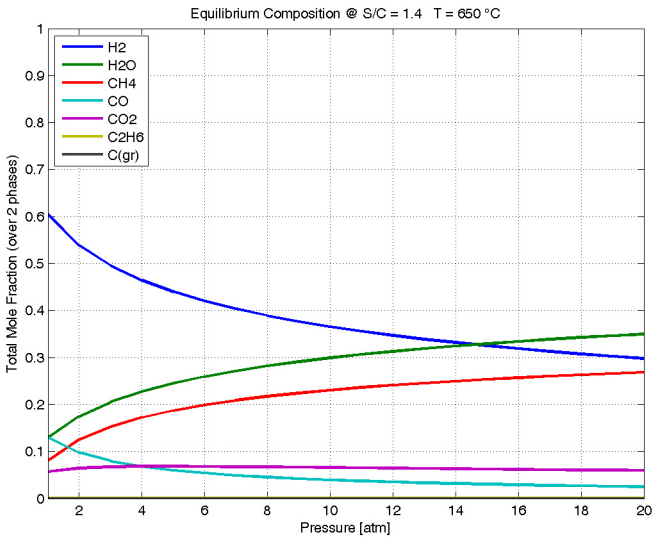

Figure 6.1: *Species mole fractions at thermodynamic equilibrium, pressure effects. T = 923 K and S/C = 1.4*

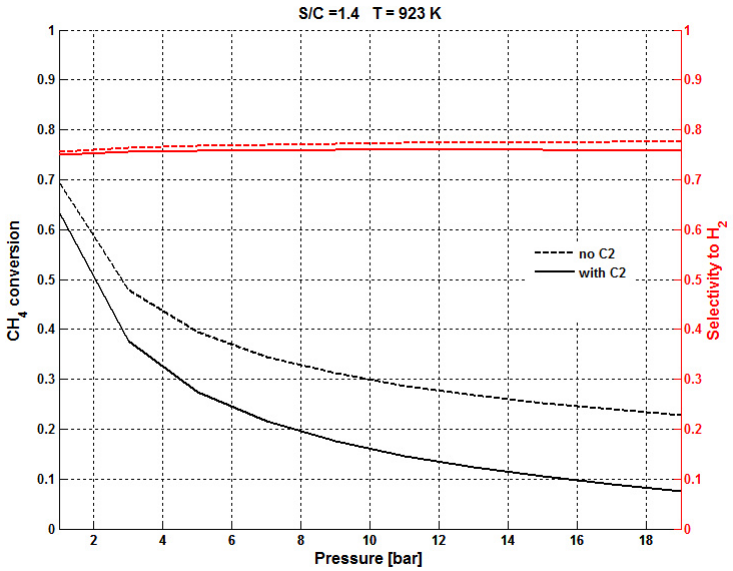

Figure 6.2: *Methane conversion and selectivity to hydrogen, with (solid lines) and without (dashed lines) ethane, at varying pressure. T = 923 K and S/C = 1.4.*

at least greater than the ambient one. Unfortunately, at low pressure also graphite formation is favored, as apparent from Fig. 6.1. Interestingly, also thermodynamics support operation at higher P to prevent coking.

Comparison of the two cases, with and without ethane (solid and dashed lines respectively), is shown in Fig. 6.2 in terms of methane conversion and selectivity to hydrogen. Methane conversion is reduced, with ethane both because of the lower available steam, also involved in the reforming with the ethane and for the C_2H_6 cracking that produce CH_4. A slight increment of selectivity to H_2 is shown without ethane; however it was nearly constant at 80% for the overall pressure range.

Temperature effects

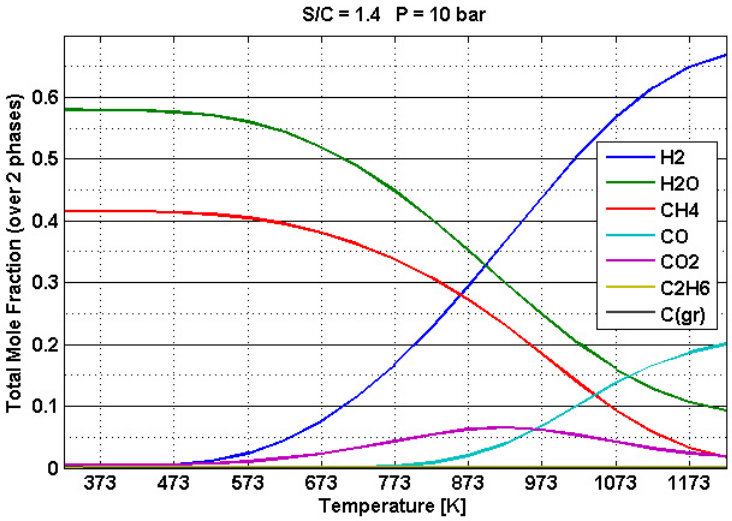

Figure 6.3: *Species mole fractions at thermodynamic equilibrium, temperature effects. P = 10 bar and S/C = 1.4*

Because of the strong endothermicity of the SMR process, shifting of the reaction equilibrium towards products is observed at higher temperature, Fig. 6.3. Consequently, the higher H_2 production has been evidenced at higher temperatures, 0.1 H_2 mole fraction at 700 K against the 0.6 at 1100 K. The effects of WGS reaction is evident: until 933 K CO and H_2O were successfully converted to H_2 and CO_2 but for T > 923 K, as highlighted by the maximum in CO_2 mole fraction profile, WGS reaction was progressively inhibited.

However Fig. 6.4 underlines significant differences for the case with and without ethane. In absence of C_2H_6, dashed lines in Fig. 6.3, selectivity to hydrogen

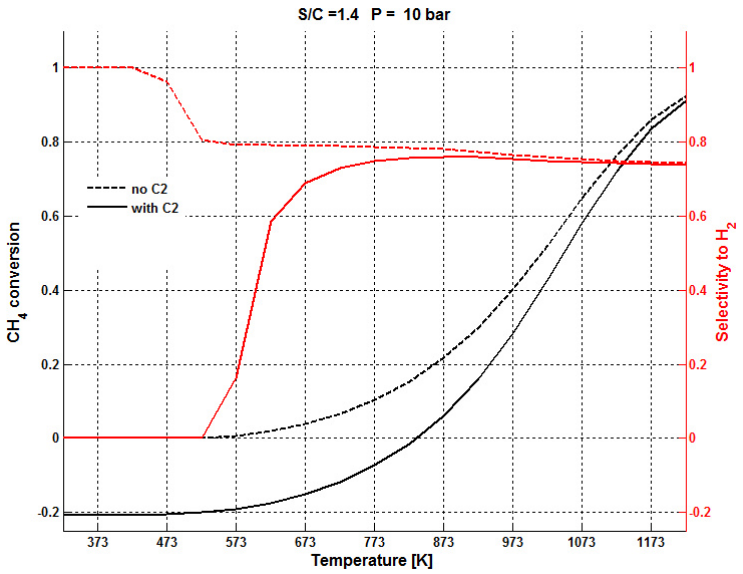

Figure 6.4: *Methane conversion and selectivity to hydrogen, with (solid lines) and without (dashed lines) ethane, at varying temperature. P = 10 bar and S/C = 1.4.*

show a decreasing trend, most probably related to the Water Gas Shift (WGS) reaction 6.2. Including ethane, as denoted by the negative CH_4 conversion in the range 298 < T < 873 K, solid lines in Fig. 6.4, methane was produced by ethane cracking and ethane hydrogenation according to Eqn. 6.6.

$$C_2H_6 + H_2 \rightarrow 2CH_4 \tag{6.6}$$

At temperature T > 873 K steam methane reforming was prevalent and hydrogen selectivity achieved the performance of the case without ethane. Temperature-promoted selectivity to hydrogen was evidenced for the case that included ethane. Carbon monoxide conversion to hydrogen is thermodynamically limited at higher temperature thus leading to significantly higher CO mole fractions Although the relatively low steam-to-carbon ratio, no carbon deposition was noticed. Despite the evident promoting effects at high temperature, real operative conditions are limited by material integrity hazard, both of the reactor and of the catalyst support. Considering the pressure of 10 bar, the presence of water and the high temperature, reactor material can fail. Moreover, high temperatures can endanger the catalyst support matrix leading to the collapse of the pellet structure, leading to reactor clogging.

Steam effects

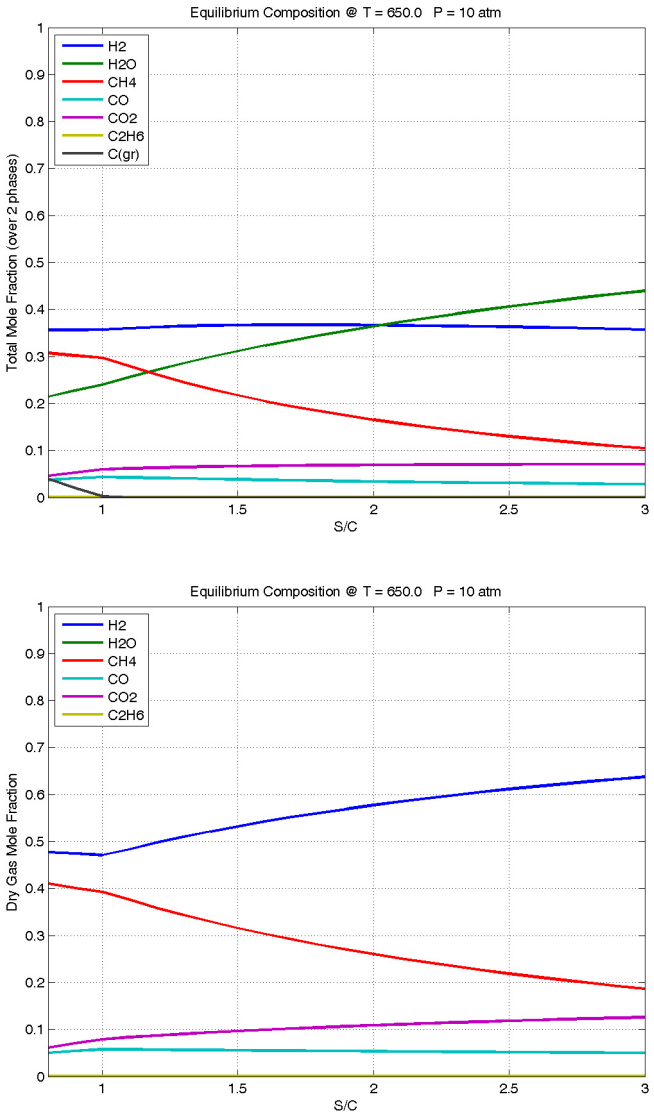

Figure 6.5: *Species mole fractions (total, above, and dry-basis, below) at thermodynamic equilibrium, S/C effects. T = 923 K and P = 10 bar*

The positive effects of steam excess have been previously discussed, mainly a limitation of coking. However it is quite interesting to observe carefully the equilibrium profiles reported in Fig. 6.5. To correctly explain the S/C effects, also dry gas mixture composition has been considered. The total mole fraction recall that coking has to be expected at S/C close and below the stoichiometric.

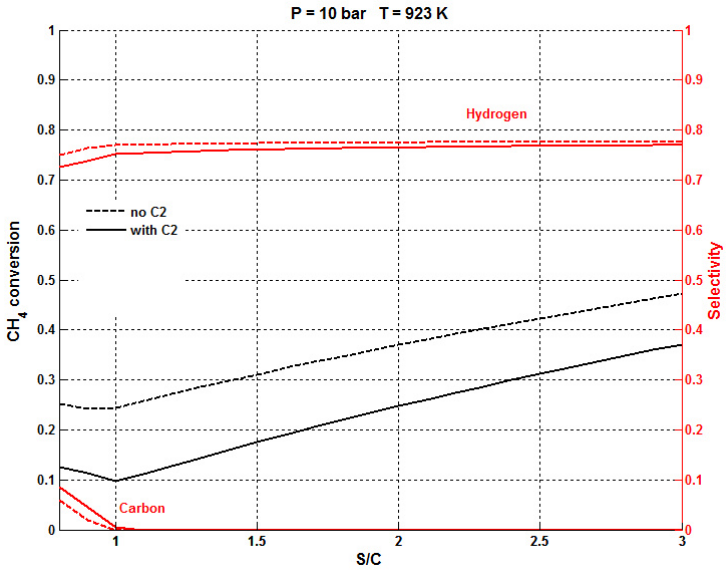

Figure 6.6: *Methane conversion and selectivity both to hydrogen and to solid carbon, with (solid lines) and without (dashed lines) ethane, at varying steam-to-carbon. T = 923 K and P = 10 bar.*

As soon as graphite does not form anymore, the conversion of methane increases rapidly, with a discontinuity that reflects on the H_2 production, as clear from the dry composition

In the range S/C = 0-1, reforming reaction was not favored because of the lack of H_2O. However, some methane conversion already occurred because of the cracking reaction which led to carbon deposition, as described by selectivity to carbon and hydrogen in Fig. 6.6. For S/C greater than one, steam methane reaction was significantly promoted and the high H_2O excess also favors the water gas shift reaction 6.2. Indeed, slight and progressive decrease in CO mole fraction was noticed Fig. 6.6, thus evidencing that WGS equilibrium supports hydrogen and carbon dioxide production. A nearly constant gap of 10% was observed in methane conversion, with and without ethane. Excess steam has a secondary role as thermal carrier, because of the highly endothermic reaction.

6.2 Kinetics

Steam methane (SMR), and partly dry (when CO_2 replaces H_2O) reforming is the most studied and industrially accepted technology for syn-gas production on the large scale [112].

Already studied in several aspects which range from operative conditions op-

timisation, catalyst metals activity, metal-support and additive interaction, with particular focus on the carbon deposition phenomena, an unique commonly accepted kinetic model has not been proposed.

Metal dispersion and support effects on CH_4-reforming rate on Platinum Group Metals (PGM) have been already demonstrated [118] , however, despite the lower activity and the higher attitude to deactivation by carbon deposition or metal oxidation, nickel-based catalyst are actually the most widely used. They have significantly lower raw material costs ($\approx$ two order of magnitudes). Moreover, catalyst support and metal dispersion have confirmed their fundamental role to extend catalyst resistance to carbon deposition which allow the nickel-based catalysts to compete with the noble-metal based ones. The industrial interest on nickel-based catalyst justify the great efforts to design and quantitatively defined a detailed kinetic mechanism.

In one of the earlier study [113], the carbon intermediates and adsorbed oxygen interactions were assumed rate determining, thus suggesting a kinetic strongly controlled by the oxygen availability on the catalyst surface. The kinetic was designed on the basis of the experimental investigation on $Ni/MgAl_2O_4$ catalyst with particle size of 0.18-0.25 mm. Kinetic model discrimination allowed to reduce the elementary chemistry from 21 to 16 reactive steps.

Subsequently, Aparicio [114] defined a mechanism of 13 reversible Arrhenius-based kinetic steps, whose parameters have been tuned considering the experimental data from Xu et al [113] combined with Trasitional State Theory analysis. The mechanism is summarized in Fig. 6.7. Order of magnitude of the Turn Over Frequency was defined for the methanation reactive step, with respect to the previous collected in the Literature.

Similarly, a detailed kinetic model has been developed by Hou et al. [115], mainly based on the assumption that both methane and steam are dissociatively adsorbed on the catalyst, with methane dissociated into CH_2 and H_2, or adsorbed H, and the suggestion that surface reactions between adsorbed species are rate controlling. The catalyst used was Ni/α-Al_2O_3 powder with particle sizes of 0.12-0.18 mm. It has to be noticed that the experimental campaign reported in [113, 115], were carried out at operative conditions particularly favorable to the reaction equilibrium, both for the low pressure, 1 and 5 bar for Xu et al. [113] and Hou et al. [115] respectively, and the extremely high steam-to-carbon ratio, S/C = 5 [113] and S/C = 4-7 [115].

The study of methane activation in methane-hydrogen mixtures carried out by Nielsen et al. [116] and the extensive numerical support by DFT analysis in [117], further investigated the relation between nickel surface structure and activity for different atom dispositions. Stepped surface of Ni(211) was found to be sensibly more active than the close-packed Ni(111).

Dissociative methane adsorption was further investigated showing that it is not

$$CH_4 + 2* = *CH_3 + *H$$
$$*CH_3 + * = *CH_2 + *H$$
$$*CH_2 + * = *CH + *H$$
$$*CH + * = *C + *H$$
$$H_2O + * = *H_2O$$
$$*H_2O + * = *OH + *H$$
$$*C + *OH = **CHO$$
$$CO_2 + 2* = **CO_2$$
$$**CO_2 + *H = **COOH + *$$
$$**COOH + H + 2* = **CHO + *OH + 2*$$
$$**CHO + 3* = **CO + *H + 2*$$
$$**CO = CO + 2*$$
$$2*H = H_2 + 2*$$

Figure 6.7: *SMR kinetic mechanism for Ni-based catalyst proposed by Aparicio [114].*

promoted by adsorbed precursors state, thus highlighting the inconsistency of the mechanism proposed by Xu et al. [125]

CH_4 steam and dry reforming on nickel and rhodium based catalysts was further investigated by Wei et al. [118, 119, 120]. Their experimental analysis concluded that reaction rates are proportional to the CH_4 partial pressure, and independent on co-reactants. C-H bond activation steps were found to be irreversible and kinetically crucial, a parameter to define catalyst reactivity. On the opposite, co-reactant activation was defined a fast step therefore metals surfaces are basically uncovered by intermediate species. Methane adsorption rate-determining was thus commonly accepted in the Literature.

Kinetic mechanism including carbon deposition elementary steps were proposed in [121], in which different metal loadings over gadolinia-doped ceria (GDC) were tested. For Ni contents above 5 wt% yield in hydrogen did not increased and the surplus of metal active sites contributed to C deposition and catalyst deactivation. It has been also underlined the importance of metal-support interaction: de-coking capability was achieved by ceria based support which, despite the impossibility of H_2O dissociative adsorption thus the production of adsorbed O(S) because of catalyst surface wasting by carbon, shares the oxygen from the solid-matrix for C(S)+O(S)→CO(S) reaction. Higher activity towards carbon de-coking was experimentally observed for the smaller ni particles than the large one.

Nickel-based catalysts were also compared with innovative rhodium-

perovskite structured catalysts by Zeppier et al. [122] who extend the operative condition range to a critical steam to carbon ration emphasising intrinsic kinetic far from thermodynamic equilibrium.

Indeed, despite the extensive studies previously discussed [113, 115], the experimental operative conditions at steam-to-carbon ratios S/C = 3-7 and the high hydrogen inlet compositions H_2/CH_4 = 1-1.25, which strongly inhibits carbon deposition, led to reactive performances very close to the thermodynamic equilibrium; fitted kinetic mechanisms can not be representative of the elementary chemistry.

Extensive experimental and numerical (DFT) investigations on nickel-coated honeycomb reactors, at also critical steam to carbon ratios S/C = 1-4, led to 42 elementary steps, summarised in Fig. 6.8, in which carbon deposition was also included [123]. Such high number of reactive steps make the kinetic mechanism prohibitive for detailed 2-D simulations. Moreover, the mechanisms has been validated only at high steam-to-carbon ratios, S/C = 2-4, and thermodynamics consistency is not always respected.

Summarizing, the Literature review highlights the strong relation between catalyst structure and activity towards SMR and carbon de-coking. The metal dispersion, particle sizes and the interplay between catalyst support matrix and metal active particles are crucial to evaluate the real reaction kinetic which cannot be deduced from simplified studies on bulk metals.

6.3 Laboratory high-pressure testing unit

In this section the experimental campaign carried out to test the commercial an novel nickel-based catalysts is presented. The aim of this testing sets is finding a catalyst that do not suffer of deactivation in conditions of low temperature (923 K) and S/C as close as possible to the unit. Laboratory scale plant and experimental methodology are first introduced. Particular attention has been focused on the scaling down from typical industrial conditions to the lab-scale set-up on the basis of two main parameters: W/F ratio, where W is the total weight of the catalyst (regardless of the concentration of active principle) and F is the total molar flow rate of the mixture, and local space velocity. Insights about the impossibility of contemporary scaling both the total molar carbon inflow and the flow regime are discussed. Catalyst pretreatment and ageing have been defined on the basis of Temperature Programmed Reduction (TPR) and on the guideline of the catalyst producer. Finally, experimental results and conclusion are discussed.

Subsequently to a ambient pressure experimental campaign, whose details are reported in [124], an high pressure laboratory scale plant has been designed for steam methane reforming. A P&ID diagram of the experimental set-up is shown

	Reaction	A (cm, mol, s)	E_a (kJ/mol)	β (–)
R1	$H_2 + 2Ni(s) \rightarrow 2H(s)$	1.000×10^{-02}	s.c.	0.0
R2	$2H(s) \rightarrow 2Ni(s) + H_2$	$2.545 \times 10^{+19}$	81.21	0.0
R3	$O_2 + 2\,Ni(s) \rightarrow 2O(s)$	1.000×10^{-02}	s.c.	0.0
R4	$2O(s) \rightarrow 2Ni(s) + O_2$	$4.283 \times 10^{+23}$	474.95	0.0
R5	$CH_4 + Ni(s) \rightarrow CH_4(s)$	8.000×10^{-03}	s.c.	0.0
R6	$CH_4(s) \rightarrow CH_4 + Ni(s)$	$8.705 \times 10^{+15}$	37.55	0.0
R7	$H_2O + Ni(s) \rightarrow H_2O(s)$	1.000×10^{-01}	s.c.	0.0
R8	$H_2O(s) \rightarrow H_2O + Ni(s)$	$3.732 \times 10^{+12}$	60.79	0.0
R9	$CO_2 + Ni(s) \rightarrow CO_2(s)$	1.000×10^{-05}	s.c.	0.0
R10	$CO_2(s) \rightarrow CO_2 + Ni(s)$	$6.447 \times 10^{+07}$	25.98	0.0
R11	$CO + Ni(s) \rightarrow CO(s)$	5.000×10^{-01}	s.c.	0.0
R12	$CO(s) \rightarrow CO + Ni(s)$	$3.563 \times 10^{+11}$	$111.27 - 50\theta_{CO(s)}$	0.0
R13	$CH_4(s) + Ni(s) \rightarrow CH_3(s) + H(s)$	$3.700 \times 10^{+21}$	57.7	0.0
R14	$CH_3(s) + H(s) \rightarrow CH_4(s) + Ni(s)$	$6.034 \times 10^{+21}$	61.58	0.0
R15	$CH_3(s) + Ni(s) \rightarrow CH_2(s) + H(s)$	$3.700 \times 10^{+24}$	100.0	0.0
R16	$CH_2(s) + H(s) \rightarrow CH_3(s) + Ni(s)$	$1.293 \times 10^{+23}$	55.33	0.0
R17	$CH_2(s) + Ni(s) \rightarrow CH(s) + H(s)$	$3.700 \times 10^{+24}$	97.10	0.0
R18	$CH(s) + H(s) \rightarrow CH_2(s) + Ni(s)$	$4.089 \times 10^{+24}$	79.18	0.0
R19	$CH(s) + Ni(s) \rightarrow C(s) + H(s)$	$3.700 \times 10^{+21}$	18.8	0.0
R20	$C(s) + H(s) \rightarrow CH(s) + Ni(s)$	$4.562 \times 10^{+22}$	161.11	0.0
R21	$CH_4(s) + O(s) \rightarrow CH_3(s) + OH(s)$	$1.700 \times 10^{+24}$	88.3	0.0
R22	$CH_3(s) + OH(s) \rightarrow CH_4(s) + O(s)$	$9.876 \times 10^{+22}$	30.37	0.0
R23	$CH_3(s) + O(s) \rightarrow CH_2(s) + OH(s)$	$3.700 \times 10^{+24}$	130.1	0.0
R24	$CH_2(s) + OH(s) \rightarrow CH_3(s) + O(s)$	$4.607 \times 10^{+21}$	23.62	0.0
R25	$CH_2(s) + O(s) \rightarrow CH(s) + OH(s)$	$3.700 \times 10^{+24}$	126.8	0.0
R26	$CH(s) + OH(s) \rightarrow CH_2(s) + O(s)$	$1.457 \times 10^{+23}$	47.07	0.0
R27	$CH(s) + O(s) \rightarrow C(s) + OH(s)$	$3.700 \times 10^{+21}$	48.1	0.0
R28	$C(s) + OH(s) \rightarrow CH(s) + O(s)$	$1.625 \times 10^{+21}$	128.61	0.0
R29	$H(s) + O(s) \rightarrow OH(s) + Ni(s)$	$5.000 \times 10^{+22}$	97.9	0.0
R30	$OH(s) + Ni(s) \rightarrow H(s) + O(s)$	$1.781 \times 10^{+21}$	36.09	0.0
R31	$H(s) + OH(s) \rightarrow H_2O(s) + Ni(s)$	$3.000 \times 10^{+20}$	42.7	0.0
R32	$H_2O(s) + Ni(s) \rightarrow H(s) + OH(s)$	$2.271 \times 10^{+21}$	91.76	0.0
R33	$OH(s) + OH(s) \rightarrow H_2O(s) + O(s)$	$3.000 \times 10^{+21}$	100.0	0.0
R34	$H_2O(s) + O(s) \rightarrow OH(s) + OH(s)$	$6.373 \times 10^{+23}$	210.86	0.0
R35	$C(s) + O(s) \rightarrow CO(s) + Ni(s)$	$5.200 \times 10^{+23}$	148.1	0.0
R36	$CO(s) + Ni(s) \rightarrow C(s) + O(s)$	$1.354 \times 10^{+22}$	$116.12 - 50\theta_{CO(s)}$	−3.0
R37	$CO(s) + O(s) \rightarrow CO_2(s) + Ni(s)$	$2.000 \times 10^{+19}$	$123.6 - 50\theta_{CO(s)}$	0.0
R38	$CO_2(s) + Ni(s) \rightarrow CO(s) + O(s)$	$4.653 \times 10^{+23}$	89.32	−1.0
R39	$CO(s) + H(s) \rightarrow HCO(s) + Ni(s)$	$4.019 \times 10^{+20}$	132.23	−1.0
R40	$HCO(s) + Ni(s) \rightarrow CO(s) + H(s)$	$3.700 \times 10^{+21}$	$0.0 + 50\theta_{CO(s)}$	0.0
R41	$HCO(s) + Ni(s) \rightarrow CH(s) + O(s)$	$3.700 \times 10^{+24}$	95.8	−3.0
R42	$CH(s) + O(s) \rightarrow HCO(s) + Ni(s)$	$4.604 \times 10^{+20}$	109.97	0.0

Figure 6.8: *Maier et al. SMR elementary chemistry from Ni-coated channel [114].*

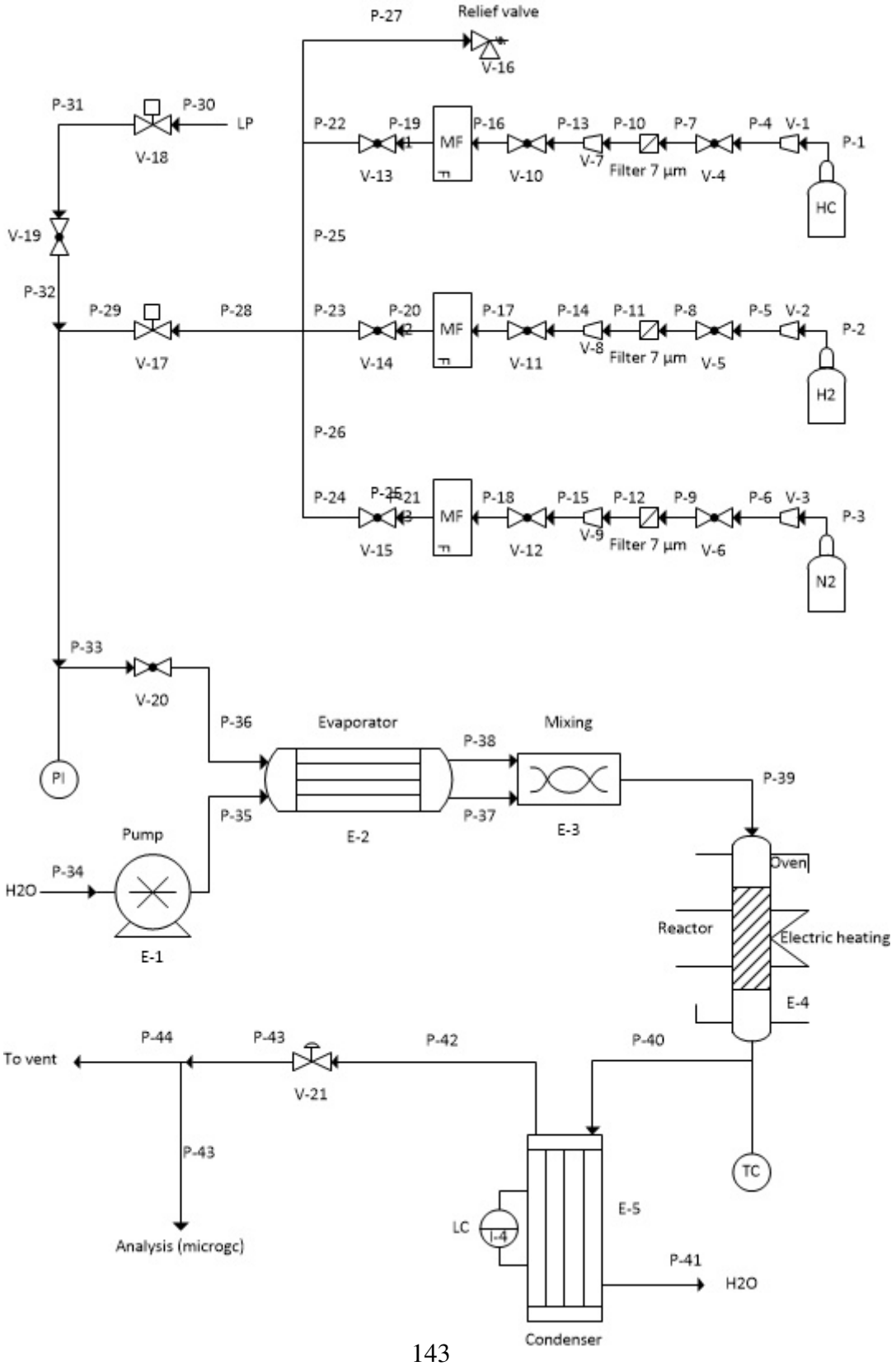

Figure 6.9: *Diagram of the experimental laboratory scale plant adopted to catalyst's activity tests.*

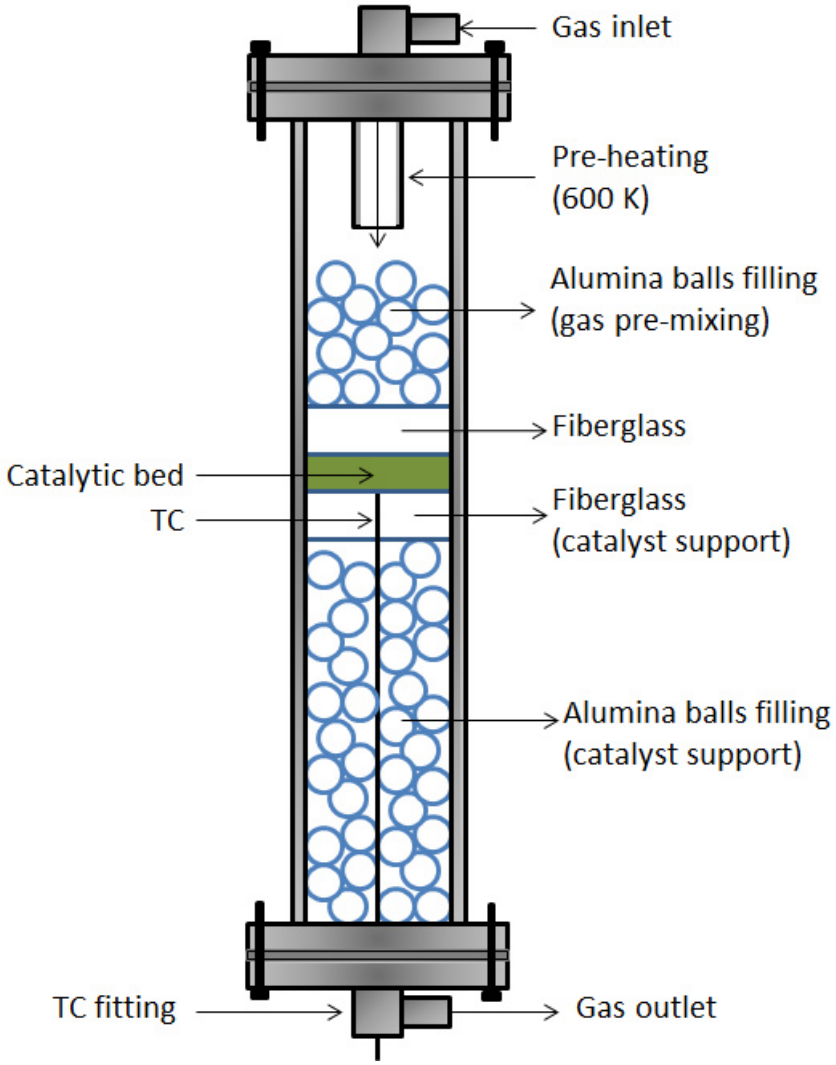

Figure 6.10: *High pressure Inconel reactor and filling.*

Table 6.2: *Target operative conditions for industrial application. CH_4, H_2, C_2H_6 mole fractions refer to dry mixture.*

Gas	Flow rate
	[NmL/min]
HCs mix	0-2000
H_2	0-50
N_2	0-10

Table 6.3: *Details and operative conditions used for gas-chromatography.*

Column	Temperature	Pressure	Gases
	[K]	[kPa]	
PPU	373	200	CO_2, C_2H_6
Molsieve	310	100	H_2, N_2, CH_4, CO

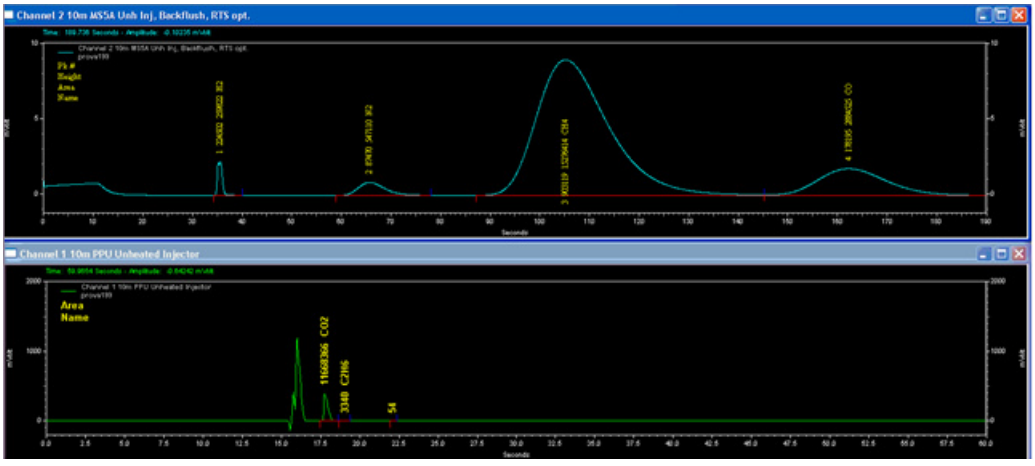

Figure 6.11: *Typical chromatograms analysis.*

in Fig. 6.9. The gas supply lines and the water feed through the high pressure pump are shown, water is first evaporated and then mixed with the dry gases. In the reactor outlet a total condenser, and the discharge line, has been set to minimise water content to the downstream analytic set-up. The high pressure gas lines are three: the hydrocarbons mixture (90% CH_4 and 10% C_2H_6), the hydrogen and the inert (N_2), used as tracer to calculate the total flow rate in the outlet, required to formulate mass balances, yields and conversions calculation. The massive flowmeters adopted (Bronkhorst), were chosen according to the flow range of each gas species, are reported in Tab. 6.2. Between the cylinders and the flowmeters a a two-step pressure reduction has been set: the first bring the pressure from the cylinder's pressure to 30 bars; the second reduces further to 15 bars. This allows a more effective and accurate regulation of the flow. Between the two reduction stages there is a sintered steel filter, with a pore diameter of 7 micron, to safeguard the following flowmeters. The gas streams after the flowmeters are mixed in a simple cross connector, then the mixture pass through a pneumatically operated valve, normally closed, for safety. The compressed air line required to activate the main valve on the reacting mixture is controlled by a solenoid valve, remotely operated by the controlling computer. A second pneumatic valve, equal to the previous, controls the parallel low pressure feed line, possibly used for inertisation, catalyst reduction, carbon oxidation, and atmospheric tests. For safety, a relief valve (Swagelok SS-4R3A) has been installed upstream of the reactor; it vents the gas under the hood. A pressure transducer (Sensor technics, model CTE9020GN0) has been placed on the gas feed line, before the heated sections. Given that the pressure is controlled on the tail of the reaction line, after the reactor, the upstream transducer provides a measure of the pressure upstream of the reactor, i.e. it quantifies the pressure drop across the reactor. This is essentially determined by the catalytic bed and carbon deposition. The dry gas mixture then pass through the evaporator, where it is pre-heated co-currently (no mixing yet) with the water vapor line. Given that the boiling temperature of water at 10 bars is about 450 K, the temperature in the evaporator is kept at 620 K to prevent any condensation, by an independent, local temperature control loop. The mixture then reaches the reactor through an insulated line, maintained at 620 K by a heating band. As schematically represented in Fig. 6.10, the reactor is an Inconel tube (Alloy 600), 0.3 m long, with an internal diameter of 12.5 mm, heated with a two-shells furnace. Notwithstanding its material, the possibility that the reaction tube interfere with the catalytic activity must be verified. For this purpose, periodic checks are carried out, without any catalyst, at reference reaction conditions: T = 923 K, P = 10 bar, $1.2 < S/C < 2.8$, W/F = 13 kg_{cat}/(mol/s). To ensure the chemical inertia of the reactor materials, two strategies have been used. One involves passivating treatments, consisting in a 50%/50% steam and inert, at 1220 K, for 24 hours. A surface layer of chromium oxide is expected to build up, inert for the

reaction. Alternatively, an internal coating obtained with a spray of Al_2O_3 powder has been applied. The type of passivating strategy before the several experimental campaigns is specified below. The effectiveness of the inerting treatments is checked with the standard test mentioned in the following chapter. The catalyst is loaded in the form of granules, with a nominal size between 700 to 1000 microns. Starting from the bottom, reactor was filled up with alumina balls in order to minimise gas residence time without significantly increasing pressure drops, catalytic bed was supported on a fibreglass layer and a second fibreglass layer was adopted to separate the catalytic bed from the gas pre-mixing area, again obtained with alumina balls. Reactor temperature control is provided by an Omron E5CC controller, remotely operated by the controlling computer (CX-Thermo). The two half-cylinders of the furnace are held together by a metal band. The two reactor ends are connected with 5/8" Swagelok connectors. The thermocouple that drives the reactor temperature control is placed between the reactor and refractory, while a second thermocouple is inside the reactor, exactly at the center of the catalytic bed (in radial direction), to monitor the actual bed temperature. The reactor outlet goes through a condenser first. It is insulated with a sheath, where the water is condensed by a cooling fluid, ethylene glycol, kept at 278 K by an external chiller (Lauda RC20 CP). After condensation, a manual back pressure controller (Swagelok, model KBP 1J0A4A5A20000) determines the operating pressure in the reactor; the pressure was always initially set at 10 bar, as indicated by the transducer upstream of the reactor. The dry gas is fed to the analysis, achieved by a microGC (Varian CP-4900), where two columns are installed, one to separate the condensible gases (PPU) and one for non condensible (Molsieve). Helium was used as carrier. It was created a method, reported in Tab. 6.3, with which it was possible to detect and quantify very effectively the following substances: CH_4 C_2H_6 H_2 CO N_2 CO_2. The Fig. 6.11 shows a typical chromatogram of the analysis. At the top it can be seen the chromatogram of Molsieve column, where the peaks are, in order, H_2, N_2, CH_4, CO. At the bottom there is the chromatogram of PPU column, in which CO and C_2H_6 are separated from the other gases.

6.3.1 Scaling rules

Scaling down from an industrial scale to a laboratory reactor is a controversial process, particularly for heterogeneous systems in which the interplay between heat and mass transfer is crucial. In the specific case of gas-solid systems, transport restrictions over the gas film is the most serious problem in scaling down [125]. Typical Reynolds numbers for industrial reactor are in the range Re = 1000 - 10000, whereas laboratory reactors usually operate in the laminar flow range with possible effects on the film restrictions. As already argued in [125], the SMR process scale down cannot not always contemporary respect all scale parameters

Table 6.4: *Gas Space Hour Velocity for typical industrial operative conditions and laboratory reactor inlet flow rate.*

GHSV [1/h]	V_{cat} [m^3]	$\dot{V}$ [Nm^3/min]
1537	1.61E-6	45E-6

and this aspect has been considered in the scaling down methodologies discussed next. Subsequently, experimental methodologies and final results are discussed.

The scale down to laboratory reactors involves a suitable evaluation of the scale rules which have to be adopted in order to correctly reproduce the physics of the industrial plant on a smaller scale. The first approach, considered in the preliminary test campaign at ambient pressure, was based on the Gas Hour Space Velocity (GHSV) parameter, who is defined as the ratio between the total inlet flow rate (Nm^3/h) on the catalyst solid volume (m^3):

$$GHSV = \frac{\dot{V}}{V_{cat}\epsilon} \tag{6.7}$$

Typical GHSV for large scale plant has been reported in Tab. 6.4. By assuming an arbitrary packed bed volume of the lab-scale reactor, calculating the catalyst solid volume with Eqn. 6.8 and keeping the same GHSV of the industrial plant, dry gas inlet flow rate of the small scale reactor, considering the industrial value S/C = 2.8, has been defined as in Eqn. 6.8. Values are reported in Tab. 6.4

$$V_{cat} = \frac{m_{cat,loaded}}{\rho_{cat}} \tag{6.8}$$

$$\dot{V} = \frac{GHSV * V_{cat}}{S/C + 1} \tag{6.9}$$

It is evident that the GHSV parameter is temperature/pressure dependent, thus it is irrespective of the total molar flow rate when increasing the pressure from 1 to 10 bar. In order to define a parameter which is independent from the operative conditions, the ratio between the weight of the catalyst and the total molar flow rate of the mixture has been considered. It means that, for constant W_{cat} = 4 g, the lower W/F ratio, the higher is the total inlet molar flow rate of the mixture.

$$W/F = \frac{\text{total weight of catalyst}}{\text{total molar flow rate of the mixture}} \tag{6.10}$$

All tests were carried out at W/F = 13 kg_{cat}/(mol/s), which is a conservative value respect the usual industrial conditions W/F_{ind} = 26 kg_{cat}/(mol/s), which

Table 6.5: *Scaling factor from industrial to laboratory scales and mass of catalyst adopted in the lab-scale reactor.*

$\mathbf{W/F}_{ind}$ [kg_{cat}/(mol/s)]	$\mathbf{W/F}_{lab}$ [kg_{cat}/(mol/s)]	$\mathbf{W}_{cat}$ [g]
26	13	4

means that twice the amount catalyst per unit of flow rate has been adopted. The value has been selected to operate sufficiently far from the equilibrium, where kinetics is expected to control the reactor yield. Before getting in deep on the experimental methodology, it is quite interesting to compare the flow regime and the heat transfer in the gas phase between the large and the small-scale plants, by the following equations. W/F = 13 kg_{cat}/(mol/s) and W_{cat} = 4g have been considered.

Gas density (ideal gas law):

$$\rho_{gas} = \frac{PV(MW_{mix})}{RT} \tag{6.11}$$

Gas velocity in the catalytic packed bed:

$$v_{gas} = \frac{\dot{V}}{S\,\epsilon} \tag{6.12}$$

Catalyst volume:

$$V_{cat} = \frac{m_{cat}}{\rho_{cat}} \tag{6.13}$$

Fluid volume in the catalytic bed:

$$V_{gas} = \epsilon V_{cat} \tag{6.14}$$

Volume of a single catalyst grain approximated to a spherical shape with a diameter of d_{grain} = 850 μm (corresponding to the mean value respect to the size range 700-1000 μm):

$$V_{grain} = \frac{\pi d_{grain}^3}{6} \tag{6.15}$$

Number of grains for W_{cat} = 4g:

$$n_{grain} = \frac{V_{cat}}{V_{grain}} \tag{6.16}$$

Catalyst surface area:

$$S_{cat} = n_{grain}\pi d_{grain}^2 \tag{6.17}$$

Equivalent hydraulic diameter:

$$d_{h,eq} = 4\frac{V_{gas}}{S_{cat}} \tag{6.18}$$

Reynolds number:

$$Re_{gas} = \frac{\rho_{gas} v_{gas} d_{eq}}{\mu_{gas}} \tag{6.19}$$

Nusselt number for laminar flow regime:

$$Nu = 1.86\left(4Pr\frac{d_{eq}}{h_{cat}}\right)^{0.33} \tag{6.20}$$

Nusselt number for turbulent flow regime:

$$Nu = 0.023Re^{0.8}Pr^{0.33} \tag{6.21}$$

Prandtl number:

$$Pr = \frac{Cp_{gas}\mu_{gas}}{k_{gas}} \tag{6.22}$$

Convective heat transfer coefficient:

$$h_T = \frac{Nuk_{gas}}{d_{eq}} \tag{6.23}$$

Biot number:

$$Bi = \frac{h_T d_{eq}}{k_s} \tag{6.24}$$

Results for the default mixture with 81%/9%/5%/5% respectively to $CH_4/C_2H_6/H_2/N_2$ and the industrial steam-to-carbon ratio S/C = 2.6, are reported in Tab. 6.6. Comparison with data evidenced by Rostrup-Nielsen et al. (RN) [125] have been also proposed.

Results clearly evidence, in agreement with the conclusions in [125], that despite the equivalent W/F, fluid flow regime cannot be conserved and that is mainly related to the difference in the catalyst particle sizes. The Re value in the lab-scale reactor has be found three order of magnitude lower than the industrial plant, also in agreement with the results evidenced by Rostrup-Nielsen et al. for a microreactor: laminar flow regime was estimated for the small scale reactor whereas turbulent flow regime for the large scale one. Minor disagreement were evidenced for the Biot number and for the convective heat transfer coefficient, an order of magnitude for the first case and approximately the same order for the second one.

Table 6.6: *Comparison of Re, Bi numbers and convective heat transfer coefficient of the laboratory scale plant and the industrial one. Value from [125] are also reported.*

	Lab-scale	**Industrial scale**
Re	1	2210
Re_{RN}	12	9500
Bi	0.002	0.029
Nu	0.47	8.74
h_T	218395	142033
$h_{T,RN}$	15000	73000

6.3.2 Experimental methods

Operative conditions and methodologies have been determined on the basis of typical industrial conditions, specifically representative of the first catalyst layer, of the packed bed reactor, which is more exposed to carbon deposition. A set of three commercial catalysts has been tested with a standard procedures in order to identify the two most promising that will be subsequently adopted for more detailed kinetic studies. Nickel-based catalysts classification has been limited to Ni-A, which has been used as reference to compare activity of the other two, Ni-B and Ni-C. The catalyst considered in the present study differ in the amount of Ni loaded which determines the catalytic activity. In particular the Ni-C, with the highest content in nickel, is the more active, while the Ni-C, with the lower nickel content, is the less active. Moreover Ni-B and Ni-C have also carbon resistance promoters. For these reasons, the commercial catalyst (Ni-B and Ni-C) proposed in this study require a dedicate designed kinetic, especially to accurately define the carbon deposition dynamic. Average activity was declared for Ni-A, with no additional promoters.

The following methodology is the result of a preliminary campaign at ambient pressure in which Ni-A catalyst has been extensively tested [124]. Catalyst pre-reduction time and aging were found to be crucial for correctly representing the steady operative conditions of the industrial catalyst. Each charge of the catalyst was pre-treated at ambient pressure according to the following procedure:

1. Preheating with inert (N_2) up to 923 K
2. Pre-reduction at 923 K, 3h, with 50% H_2/N_2 (total flow rate 50 sccm)
3. Further heating until reactive temperature (T_{react}), in inert atmosphere
4. Aging for 12h at S/C = 2.8

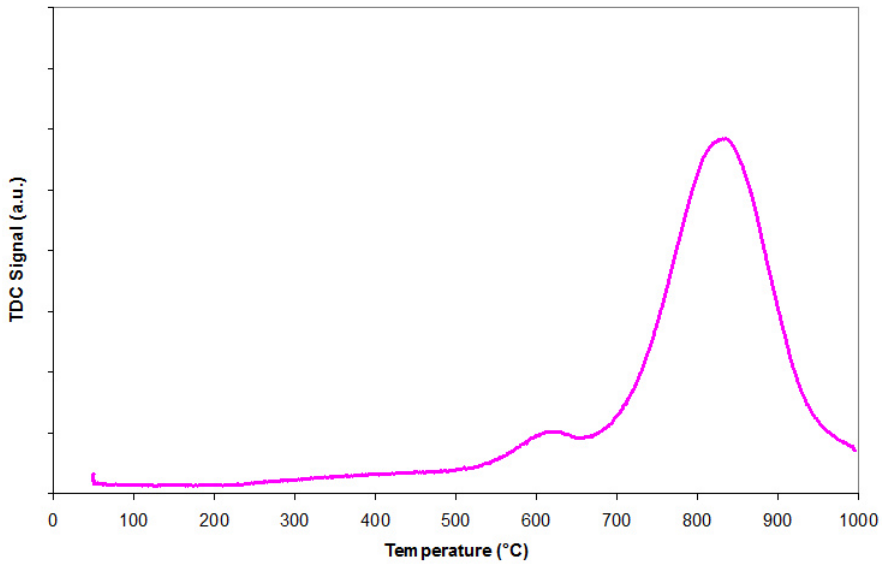

Figure 6.12: *Example of TPR analysis on Ni-B catalyst.*

The S/C ratio is determined as the molar ratio $H_2O/(CH_4 + 2\ C_2H_6)$. Catalyst pretreatment operative conditions have been suitable defined on the basis of TPR analysis, which has been carried out in collaboration with prof. Trovarelli from University of Udine. Example of the TPR profile measured for the Ni-B catalyst is reported in Fig. 6.12. It is evident that the catalyst reduction is strongly promoted at higher temperatures, however stability of active metal dispersion on support can be endangered for reductive pretreatment above the 970 K. Operative temperature of 920 K have been assumed for catalyst pre-reduction in order to avoid solid matrix rearrangement, three hour pretreatment were found to be sufficient to overcome the lower reduction rate obtained at 920 K, as evidenced by the TPR in Fig. 6.12, respect to higher temperatures.
After pre-treatment, the activities test took place in a sequence, with the following order:

- for tests at fixed temperature T = 923 K, P = 10 bar, W/F = W/F = 13 kg_{cat}/(mol/s) and different S/C ratio:

    6. test at S/C = 2
    7. test at S/C = 1.8
    8. test at S/C = 1.6
    9. test at S/C = 1.4

10. test at S/C = 1.2

- for tests at fixed S/C = 2.6, P = 10 bar, W/F = 13 kg_{cat}/(mol/s) and variable temperature:

    6. test at 1120 K
    7. test at 1070 K
    8. test at 1020 K
    9. test at 970 K
    10. test at 920 K

- for stable activity tests lasting 10 hours (only on Ni-B and Ni-C catalysts) at T = 923 K, P = 10 bar, W/F = 13 kg_{cat}/(mol/s) and S/C = 1.2:

    6. activity test
    7. catalyst oxidation at T = 870 K, with 5% of O_2 in N_2
    8. activity test
    9. catalyst oxidation at T = 870 K, with 5% of O_2 in N_2

- for tests at fixed temperature T = 923 K, S/C = 2, P = 10 bar and variable W/F:

    6. test at W/F = 13 kg_{cat}/(mol/s)
    7. test at W/F = 10 kg_{cat}/(mol/s)
    8. test at W/F = 8 kg_{cat}/(mol/s)
    9. test at W/F = 5 kg_{cat}/(mol/s)

At the end the reactor was shut down according to the following procedure:

11. cooling to ambient temperature under inert
12. possible oxidation with 5% of O_2 in N_2

In all phases from 5 to 9 the following conditions are maintained:

- P = 10 bar;
- 81%/9%/5%/5% respectively to CH_4/C_2H_6/H_2/N_2.

Each activity verification phase (i.e steps 5 to 9) has a minimum duration of 4 h, except for the stability test lasting 10 hours. Periodically the GC analysis has been disconnected to allow columns conditioning between one test and another, but the catalyst remained in operation and the reactor set at the given conditions, up the end of the designed phase. During all the test duration, temperature in the centre of the catalytic bed, at the external wall, and the pressure upstream of the reactor were continuously monitored and registered. In the case of a significant increase (> 2 bar), the test was stopped to directly proceed to the phase 10. If surface characterisation was required (tested catalyst were sent to University of Udine), catalyst oxidation was not carried out, otherwise in-situ carbon deposition evaluation, corresponding to the phase 11, was included.

6.4 Experimental results and discussion

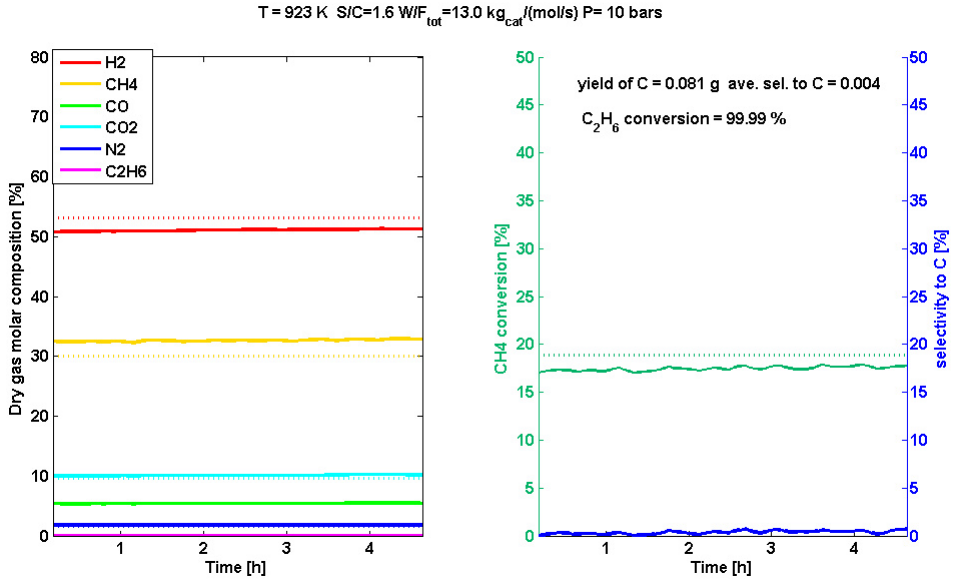

Figure 6.13: *Example of measured profiles for 4 hours activity test. Dry gas molar composition on the left and CH_4 conversion plus calculated selectivity to carbon on the right.*

On the basis of the methodologies previously discussed, approximately eighty tests, including replicas for reproducibility analysis, were carried out in the laboratory scale plant at University of Padua. Results have been organised as follows. Experimental data have been post processed in order to directly compare the activity performances of the catalyst. In order to introduce how molar composition

profiles looked when measured during reactivity test, ans example for T = 923 K, P = 10 bar, W/F = 13 kg_{cat}/(mol/s) and S/C = 1.6 is reported in Fig. 6.13: on the left, dry gas molar composition profiles during 4 hours test are evidenced. Solid lines are the measured values while the dashed line propose the relative thermodynamic equilibrium. It has to be remarked that nitrogen was used in traces to calibrate mass balances thus it assumed to not affect the overall reaction. On the right side, methane conversion, both measured and equilibrium values, are plotted together with the selectivity to carbon, which was deduced from mass balances. Calculated selectivity to carbon was usually compared to the measured value obtained from the final controlled oxidative step.

6.4.1 Preliminary tests on Ni-A catalyst at varying temperatures

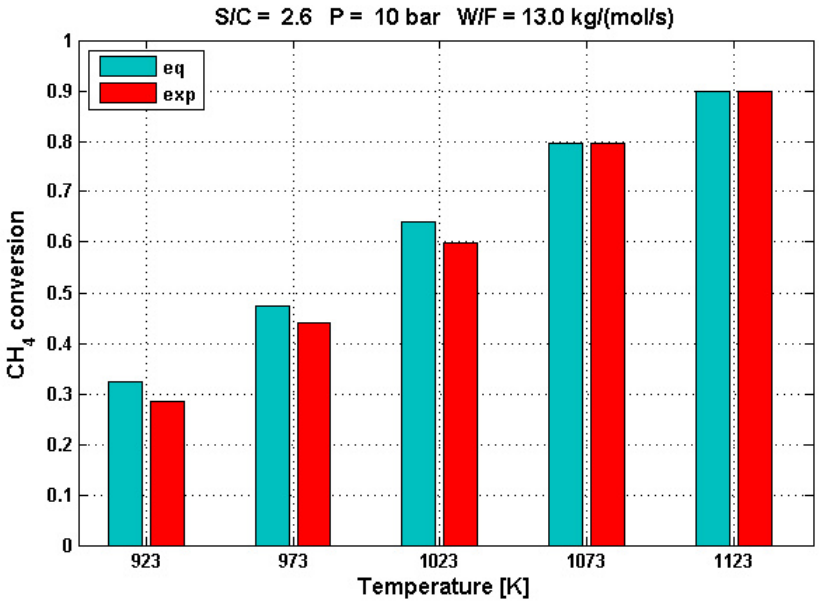

Figure 6.14: *CH_4 conversion at different temperature for SMR with Ni-A catalyst (red). Comparison with equilibrium is proposed (light blue).*

Preliminary test campaign on the commercial Ni-A catalyst was carried out considering the standard operative conditions P = 10 bar, S/C = 2.6 and W/F = 13 kg_{cat}/(mol/s), temperature was varied in the range 923-1123 K. The aim o this experimental temperature effects screening was mainly focused on the validation of the lab scale set-up and analytic sensibility to catalyst activity. Moreover, the

comparison with calculated thermodynamic equilibrium confirmed that at the reference industrial operative condition, thus T = 923 K, steady performances were still in the kinetic regime, slightly below the equilibrium. As reported in Fig. 6.10, for T = 1073-1123 K experimental conversions were equal to the correspondent equilibrium whereas at T = 923-1023 K experimental methane conversion was 5% lower than the equilibrium value.

6.4.2 SMR at decreasing steam-to-carbon ratios

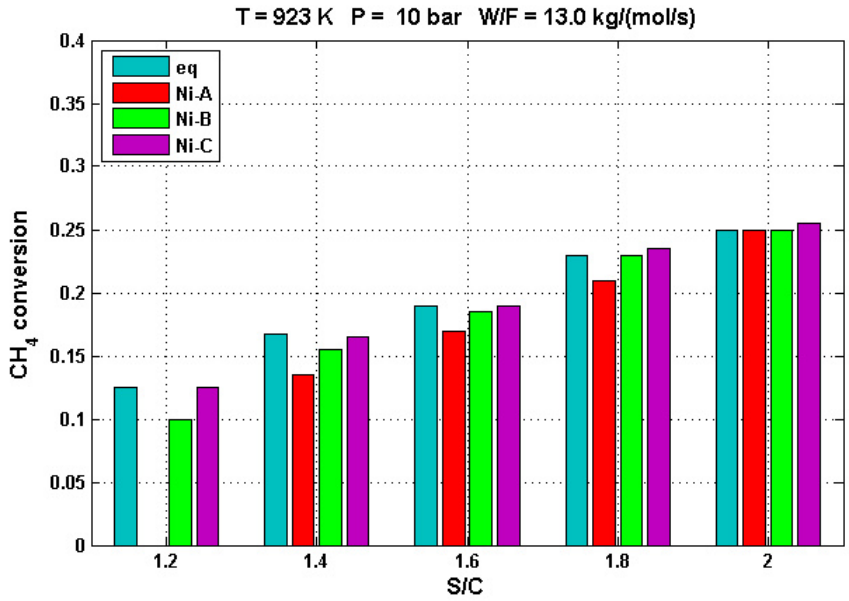

Figure 6.15: *CH_4 conversion at different S/C ratios for catalyst Ni-A (red), Ni-B (green) and Ni-C (purple). Comparison with equilibrium is proposed (light blue).*

Directly focusing on the aim of the present study, which consist in evaluating the best catalyst able to tolerate critical operative condition at which carbon deposition could significantly compromise the catalytic activity, catalyst testing at decreasing S/C ratios was carried out. S/C ratio, accordingly with the procedure described in the previous Section, was progressively decreased from 2 to 1.2 (below the possible first target S/C = 1.4) after four hours test at steady operative conditions. Other operative variables were set as follows: T = 923 K, P = 10 bar, W/F = 13 kg_{cat}/(mol/s). Results reported in Fig. 6.15 represent the average value of the measures in case of steady conditions, particular dynamic are discussed next. For S/C = 2, all the catalyst reached the reaction equilibrium consisting in 25% of methane conversion. Slight over-estimation was noticed for the Ni-C

which reached the 25.% but that is representative of the very small experimental error in the product analysis. At lower steam-to-carbon-ratios the overall trend confirmed a classification by which the Ni-C and Ni-C catalyst are respectively the more and the less active.

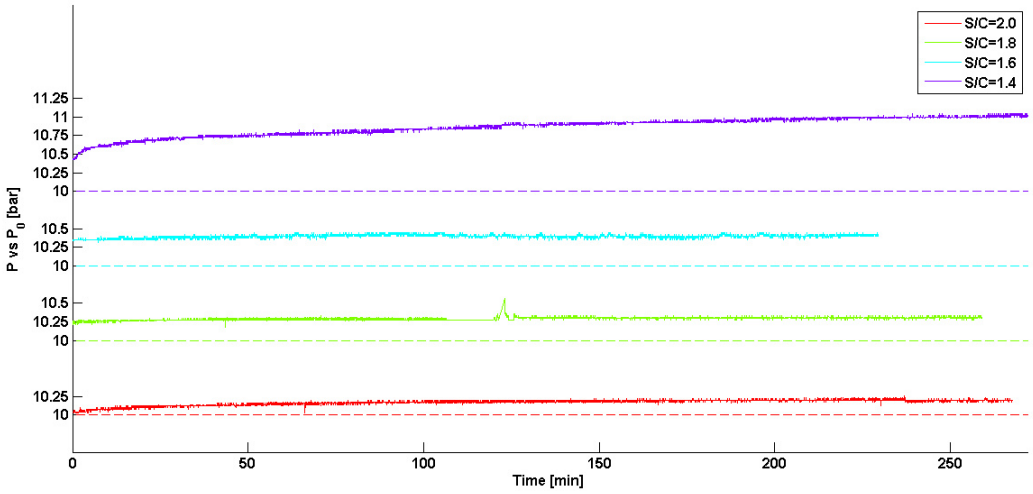

Figure 6.16: *Measured pressure profiles for decreasing S/C ratios during activity test with Ni-A catalyst.* P_0 *= 10 bar and measured P, dashed and solid lines respectively.*

At S/C = 1.4 average methane conversion were 16.5%/15%/14% respectively to Ni-C/Ni-B/Ni-A catalysts, thus confirming that Ni-C was able to reach the reaction equilibrium even at low S/C ratio. However, critical operative conditions were evidenced for catalyst Ni-A which did not tolerate the carbon deposition rate. On the contrary of the pressure profiles measured during activity tests for Ni-B and Ni-C catalysts, which were stable at 10 bar, overpressure was measured for the Ni-A catalyst. As summarised by the measured pressure profiles at increasing S/C ratio reported in Fig. 6.16, stable pressure was confirmed down to S/C = 1.6 while at S/C = 1.4 it progressively decreased up to 11 bar also suggesting a constant increasing trend. Catalyst Ni-B and Ni-C were further tested at S/C = 1.2. Results in Fig. 6.15 again confirmed a higher activity for Ni-C catalyst with a 12.5% of methane conversion, equal to the equilibrium, against the 10% measured with Ni-B. Results were found quite exciting for the industrial purpose but stability investigation was required to confirmed the possibility of catalysts Ni-B and Ni-C to tolerate very low steam-to-carbon ratios. Despite the first target was S/C = 1.4 and considering the promising performances of the catalyst Ni-B and Ni-C, stability tests lasting 10 hours were carried out.

6.4.3 Performance stability for Ni-B and Ni-C catalysts

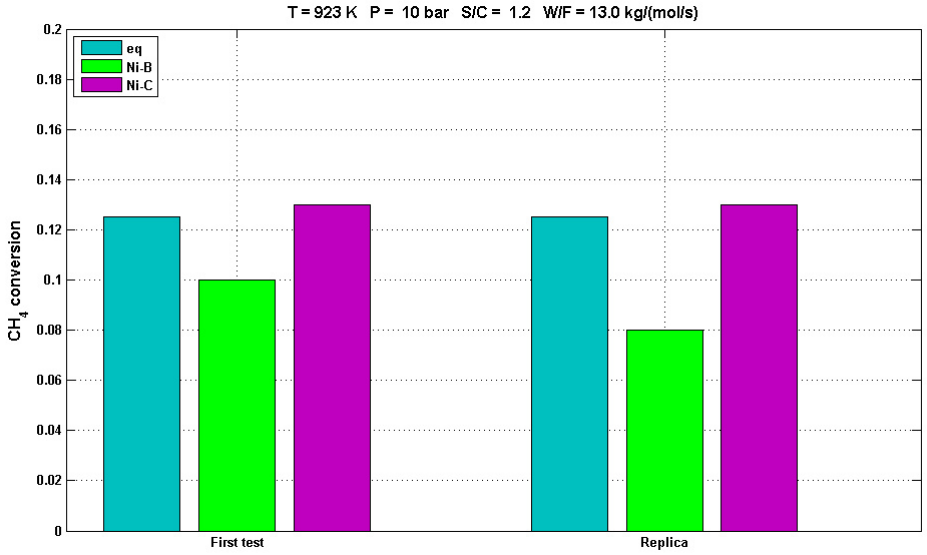

Figure 6.17: *Average methane conversion at S/C = 1.2 with Ni-B (green) and Ni-C (purple). Comparison with thermodynamic equilibrium (light blue) is proposed.*

Catalysts Ni-B and Ni-C were further compared with a activity measures organised in 10 hours SMR reaction test, catalyst oxidation, SMR reaction and final catalyst oxidation. The aim of the oxidative steps consist both in evaluating the carbon deposition rate and to highlight possible instability of the solid matrix after catalyst regeneration. Operative conditions during catalysts oxidation were T = 870 K, x_{O_2} = 5% in N_2.

Methane conversion reported in Fig. 6.17 confirmed the higher activity of the catalyst Ni-C which achieved the reaction equilibrium while the 10% was not exceeded with the Ni-B. After the first catalyst oxidation, SMR reaction was performed again and for 10 hours. Despite the steady performances observed during the ten hours reactive tests for each catalyst, the replica for Ni-B highlighted lower catalytic activity, 8% instead of 10% of methane conversion. On the opposite, Ni-C did not suffer of the oxidative step thus again confirming methane conversion as high as 12.5%. An example of the measures carried out during catalyst oxidation is showed in Fig. 6.18, CO_2 mass fraction profile was used to calculate the total mass of CO_2 produced thus the mass of C.

Total mass of carbon deposited after the first and the second reactivity tests are reported in Tab. 6.7. Lower carbon deposition was evidenced for the Ni-B, around 0.010 g for both cases, while approximately four time higher value was noticed after the first test with Ni-C. The results are in good agreement with the

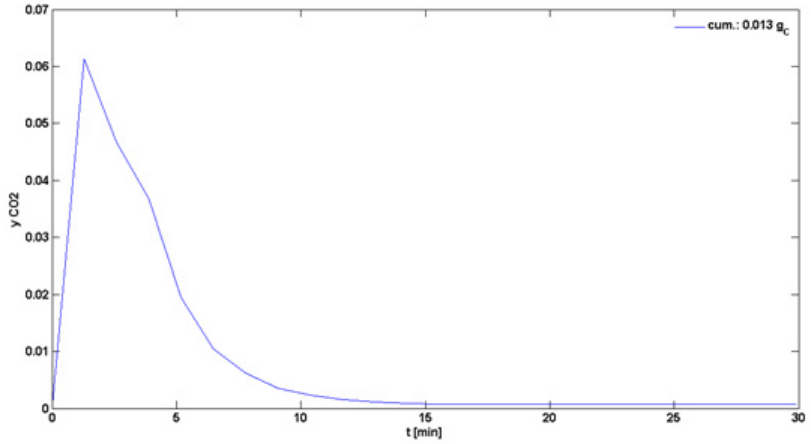

Figure 6.18: *Measured CO_2 mass fractions profiles during Ni-C catalyst oxidation. Mass carbon deposited is calculated by integrating the y_{CO_2} profile.*

Table 6.7: *Total of carbon deposited during catalyst oxidation. Results are in grams [g].*

	First oxidation	**Second oxidation**
Ni-B	0.010	0.011
Ni-C	0.038	0.013

confidential information about catalyst compositions, by which the Ni-B should be more carbon resistant but less active, because of the lower amount of nickel loaded, and Ni-C should be more active and more prone to carbon deposition, thanks to the higher nickel loading. To get in deep about the relation between catalyst composition and catalytic activity as well as carbon deposition resistance, further comparisons were carried out at S/C = 2 in order to include the Ni-A catalyst. Being the measured conversion mostly close to the equilibrium, especially for Ni-C, W/F was also adjusted in order to move to a more kinetically controlled regime.

6.4.4 Activity test in the kinetically controlled regime

In order to better understand how catalysts can be rightly compared, also considering their different loading in nickel content, parallel to the aim of moving to more kinetically controlled regime operative conditions, total inlet flow rate was adjusted by keeping the mass of catalyst loaded in the reactor constant to 4 g. With this logic, reactive tests were carried out at progressively decreasing W/F

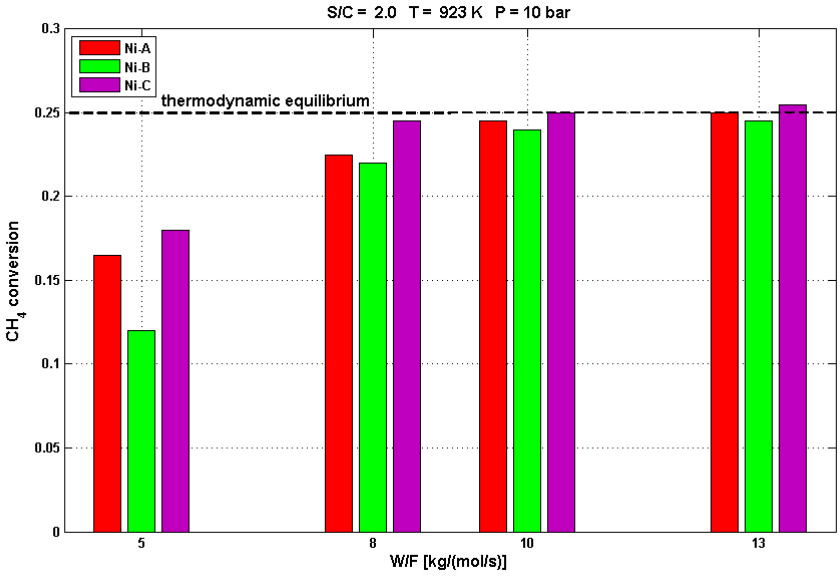

Figure 6.19: *Measured methane conversion at different W/F values.*

values, spacing from 13 down to 5 kg_{cat}/(mol/s). Other operative variables were set to the default values as follows: T = 923 K, P = 10 bar, S/C = 2. The high steam-to-carbon ratio allowed to reconsider the Ni-A, which suffered from carbon deposition at S/C = 1.4, for a full comparison with the other two catalyst. For all the following results, at the operative condition previously mentioned, methane conversion at thermodynamic equilibrium is 25%.

Results for W/F in the range 5-13 kg_{cat}/(mol/s) have been summarised in Fig. 6.19. The catalyst with the higher loading in nickel, Ni-C, was again confirmed the most active by achieving the equilibrium still at W/F = 10 kg_{cat}/(mol/s). At W/F = 5 kg_{cat}/(mol/s) Thanks to the relatively high S/C ratio, carbon deposition was negligible thus minimising possible effects on catalyst performances. Indeed, in agreement with the catalyst compositions, Ni-B, with the lower nickel content, was found to be always the less active whereas Ni-A lead to average performances at each W/F. Despite the standard comparison in terms of measured methane conversion, which do not take in consideration any information about catalyst compositions as well as metal loading, further comparisons have been elaborated. The first is based on the commonly accepted definition [118, 119, 120]:

$$\frac{X_{CH_4}}{W_{Ni}} = \frac{\text{moles of methane converted per time unit}}{\text{grams of Ni loaded in the catalytic packed bed}} \tag{6.25}$$

With this new definition, the amount of active metal is taken in consideration and the trends of Fig. 6.19 are completely overturned: the average amount of

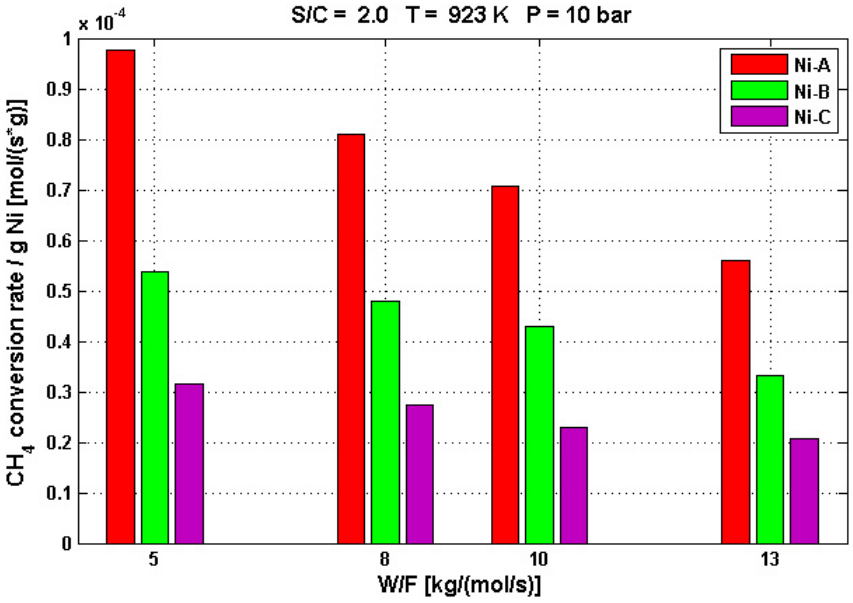

Figure 6.20: *Moles of methane converted per time unit normalised on the total weight of Ni loaded, at different W/F values.*

nickel (respect to the other catalysts) contained in Ni-A, makes it becoming the most active catalyst. Furthermore, despite the lower activity previously evidenced and thanks to the very low nickel loading, Ni-B overcome the performances of Ni-C. However this definition (X_{CH_4}/W_{Ni}) could be misleading because it does not take in consideration the real active area of the metal particles, which also depends on the nickel particle sizes. Il collaboration with prof. Trovarelli from University of Udine, specific surface active areas were measured for each catalyst by nitrogen adsorption/desorption isotherms at 77 K (BET analysis). Results from BET analysis for the three catalysts are reported in Tab. 6.8. The new definition, as reported in Eqn. 6.26, aim to weight the methane conversion rate on the surface active area per unit of nickel mass.

$$\frac{X_{CH_4}}{A_{Ni,N}} = \frac{\text{moles of methane converted per time unit}}{\text{surface active area normalised on the total Ni weight}} \tag{6.26}$$

The results reported in Fig. 6.21, based on $X_{CH_4}/A_{Ni,N}$, again proposed a completely different overview of the catalyst activities, strongly enhancing the Ni-B performances. Similar results, but opposite respect to Ni-A and Ni-C, have been found with the definition reported in Eqn. 6.27, by which methane conversion has been normalised on the measured surface active area. That is because the activity of the catalyst is strongly related to metal dispersion which must be appositely

Table 6.8: *Catalyst surface active area from BET analysis [m^2/g].*

Ni-A	Ni-B	Ni-C
0.5605	0.1427	1.3152

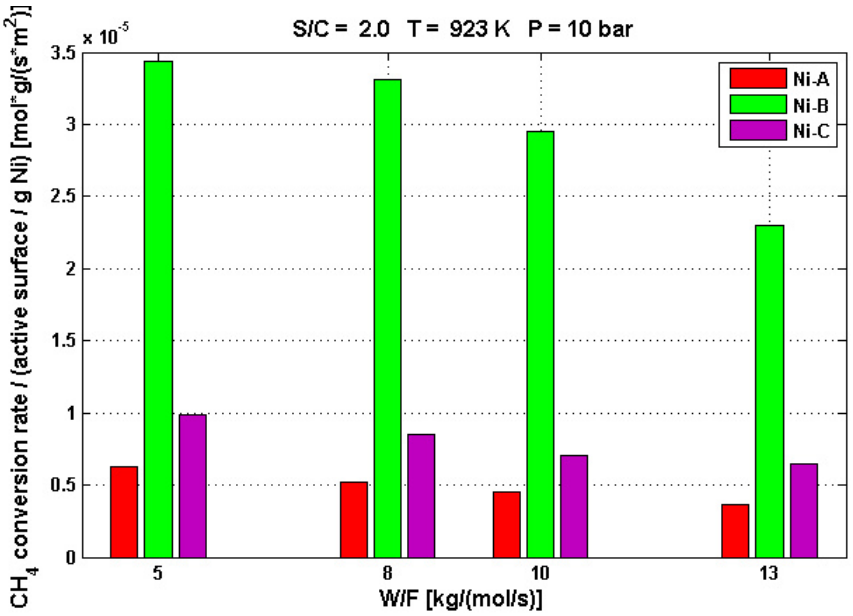

Figure 6.21: *Measured methane conversion normalised on $X_{CH_4}/A_{Ni,N}$ at different W/F values.*

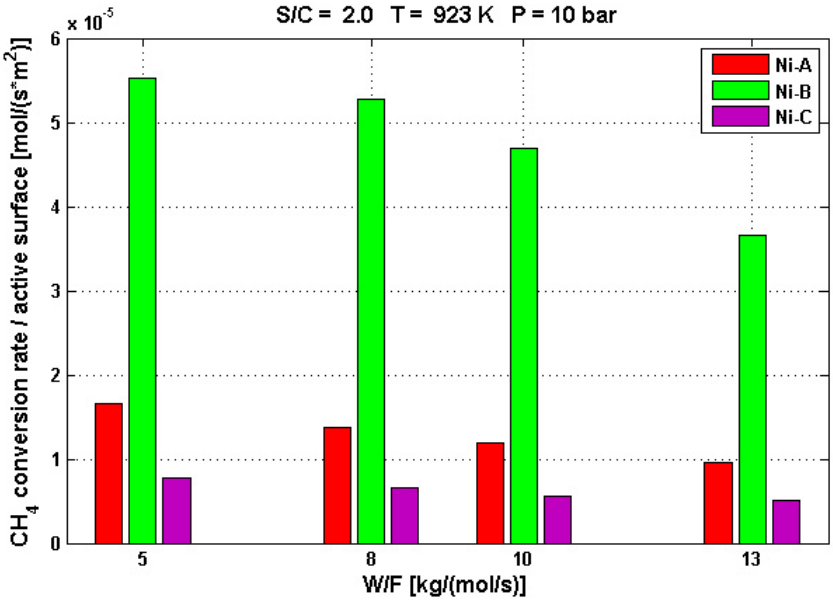

Figure 6.22: *Measured methane conversion normalised respect to the surface active area, at different W/F values.*

defined in order to prevent metal particles clustering on the support surface. The results reported in Figs. 6.21 and 6.22 are significantly important for industrial purpose. Despite the lower activity measured in the previous test and considering the importance of the catalyst resistance at critical steam-to-carbon ratio, thus the ability of tolerate carbon deposition, the Ni-B, which has a very lower active metal content, is very promising. In fact, the importance of balancing catalytic activity and carbon resistance promotion has been also experimentally observed when lowering the S/C to 1.4: Ni-A, which is more active than Ni-B, was not able to tolerate that critical conditions thus leading the pressure to increase because of carbon production. Better activities were evidenced in the case Ni-C, but catalyst controlled oxidation revealed higher carbon content, 0.038 g and 0.010 g respectively to Ni-C and Ni-B, which can affect the overall activity for long time exposure at reactive conditions.

$$\frac{X_{CH_4}}{A_{Ni}} = \frac{\text{moles of methane converted per time unit}}{\text{surface active area}} \tag{6.27}$$

The comparisons of the methane conversion and selectivity to hydrogen respect to the measured surface active area of the catalysts, at T = 923 K, P = 10 bar, S/C = 2, W/F = 5 kg_{cat}/(mol/s), are reported in Fig. 6.23. Despite the increasing trend of methane conversion respect to the surface active area, Ni-C>Ni-A>Ni-B, the selectivity to hydrogen production was the same for each catalyst. The results

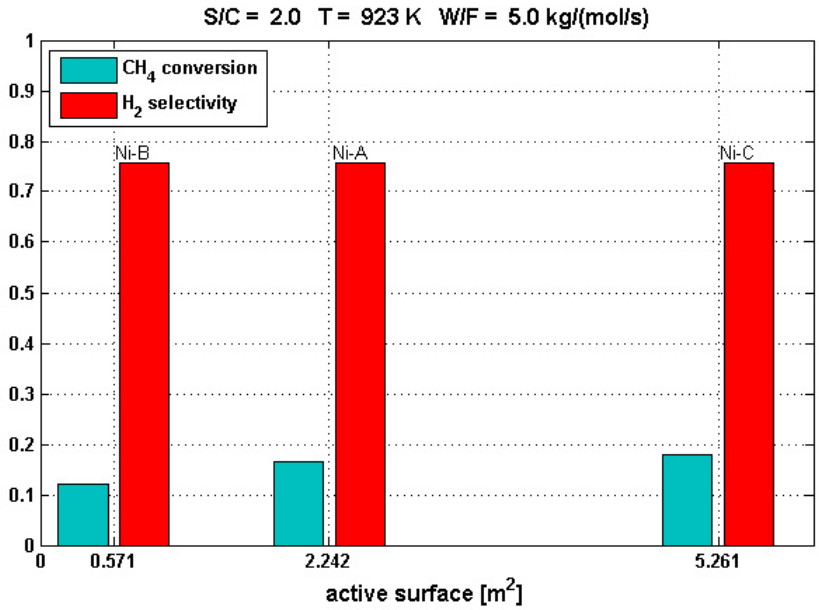

Figure 6.23: *Measured methane conversion and selectivity to hydrogen for the different catalyst surface active areas.*

suggest that the an unique kinetic, at negligible carbon deposition rates, could be adopted to describe the activities of the tested catalysts. At critical steam-to-carbon conditions, suitable kinetic should be adopted in order to reproduce the different carbon deposition rates.

6.5 Conclusions

Steam methane reforming reaction has been experimentally studied in a high pressure laboratory scale reactor, suitable designed to operate at typical industrial conditions: P = 10 bar, T = 923 K, and inlet compositions 81%/9%/5%/5% respectively to $CH_4/C_2H_6/H_2/N_2$. Total inlet flow rate was adjusted according to the W/F scaling factor defined as the ratio between the catalyst weight and the total molar inlet flow rate. The aim was to reproduce the same carbon inflow of large scale reactors in order to focus on carbon deposition rate, particularly at very low steam-to-carbon ratio. Reynold, Nusselt and Biot based similitude analysis was discussed in Section 6.2, thus evidencing that, mainly because of the large differences in the catalyst solid particle sizes, flow regime cannot be respect when scaling down from large scale plant, which are typically in the turbulent regime, to the small scale, usually in the laminar regime. However, heat transfer from the fluid and the solid was nearly reproduced. Three commercial catalysts, differing

in the nickel loading and type of carbon resistance promoters, have been considered. The impact of temperature, steam-to-carbon ratio, exposure time at reactive conditions and W/F were assessed. The following are the key conclusions of this study.

- Steam-to-carbon ratio effects were extensively studied in the range S/C = 1.2-2. Critical conditions were observed at S/C = 1.4 for Ni-A, carbon deposition rate led to progressively increasing the reactor pressure up to 11. On the other hand, S/C = 1.2 was possible for the catalysts Ni-B and Ni-C, the last also achieving the thermodynamic equilibrium;

- 10 hours stability tests, on Ni-B and Ni-C, confirmed the higher activity of the catalyst Ni-C towards methane conversion. Slight detrimental activity evolution was observed for the Ni-B after the intermediate oxidative step, methane conversion decreased from 10% to 8%. On the opposite, temperature controlled oxidation, adopted for total carbon deposition evaluation, confirmed the higher carbon resistance of Ni-B in which 0.010 g of adsorbed carbon were estimated, whereas 0.038 g for Ni-C, which is expected to be more active thanks to the higher nickel loading, but less resistant to carbon deposition;

- Catalytic performances were further investigated in kinetically regime by adjusting the W/F in the range 5-13 kg_{cat}/(mol/s), thus keeping constant the catalyst mass loaded in the reactor and changing the total molar inlet flow rate. Other operative variables were set as follows: T = 923 K, P = 10 bar and S/C = 2, sufficiently high for testing the Ni-A catalyst at negligible carbon deposition rate. The lower nickel content of Ni-B significantly affected the methane conversion respect to the performances evidenced for the other catalysts: 12%/16%/18% CH_4 conversion for Ni-B/Ni-A/Ni-C respectively.

- Considered the different metal dispersion and active particle sizes of the three catalysts tested, and reprocessing the experimental data on the basis of the weight of active metal contents, also related to the measured surface active areas, catalysts performances have been revisited. At S/C = 2, T = 923 K, P = 10 bar and different W/F, catalyst Ni-B was the most promising in terms of methane conversion rate normalised on the surface active area $X_{CH_4}A_{Ni}$ thus meaning that the despite the low nickel loading, the specific conversion was significantly higher than the other catalysts. Moreover, these results suggest that the real surface active area at low steam-to-carbon ratio may be affected by carbon deposition thus significantly reducing when not protected by promoters as strong as in Ni-B. The higher activity of Ni-C may be overcame by carbon deposition which can endanger the effective catalytic activity;

- Further comparison of the performances at S/C = 2, T = 923 K, P = 10 and W/F = 5 k_{cat}/(mol/s), thus in the kinetically regime, expressed in terms of methane conversion and selectivity to hydrogen respect to the surface active area (relatively to 4 g of catalyst) has been proposed. The different CH_4 combined with the same selectivity to H_2 suggest that, at relatively high S/C = 2, the promoters do not affect the overall kinetic that can be simply reduced to a common nickel-based catalyst, whose activity depends on the its surface active area. Comparison of catalytic performances on the basis of the mass of nickel loaded can lead to misleading.

Chapter 7

Conclusions

In this thesis two main reactions that involves hydrogen have been extensively studied, platinum catalysed oxidation and steam methane reforming on nickel-based catalysts for hydrogen production.

Detailed mean field based elementary chemistries of hydrogen Pt-catalysed oxidation have been published. They speculate about the elementary surface chemistry and their quantitative treatment, in terms of reaction rates. A quantitative comparison, with particular attention on hydrogen and oxygen competitive adsorption kinetics, highlighted significant discrepancies among mechanisms. Deutschmann and Forsth kinetics, who proposed two different surface coverage corrective functions, predict quite different O_2 adsorption rates. Further comparison of the Deutschmann kinetic with the Kasemo and Schmidt ones, has confirmed the higher reactivity predicted by the Deutschmann's kinetics, apparently determined by the higher oxygen adsorption rate. An isothermal heterogeneous reactor model, in the form of a closed-vessel with a well-stirred gas phase has been implemented to compare Literature mechanisms in terms of light-off, at different reactant compositions. The numeric comparison has highlighted incongruities in reaction light-off profiles, especially at high hydrogen partial pressure at which catalytic activity inhibition by H(S) prevails. For x_{H_2} = 28%, reaction ignition, determined at 20% of reactant conversion, has been calculated to vary from 360 K to 460 K. Further investigation of the experimental ignition temperature collected in the Literature, by which kinetic parameters have been tuned, have been reported thus evidencing particular discrepancies at low hydrogen concentration relative to O_2. Being the elementary chemistries mainly obtained from a collage of single kinetic step studies which underlines the importance of the catalyst surface structure, evidences of platinum surface rearrangement have been reported from the Literature. SEM analysis on platinum foils exposed to hydrogen or ammonia oxidation confirmed that the catalyst is not a static phase and surface evolves quite easily, affecting the gas-solid interaction both in terms of specific surface area

as well as in the local activation energy barrier. Considering the discrepancies previously evidenced, an experimental campaign of hydrogen Pt-catalysed oxidation has been planned to evaluate both ignition temperatures at varying hydrogen partial pressure and catalyst pre-treatment effects on kinetics.

Catalytic combustion of hydrogen has been reproduced in a suitable designed Stagnation Point Flow Reactor, purposely built, on the basis of a CFD analysis, to for testing disc-shaped model catalysts, typically amenable to surface science studies. Catalyst activity has been found to be sensitive to surface history: pretreatments in H_2-rich mixtures develop a higher reactivity of the surface which is also related to a surface rearrangement, as confirmed by SEM and XRD analysis. Surface structure rearrangements were observed after intensive H_2 pretreatment and reaction, confirming that the catalyst has a living structure, also in the case of bulk metals. After catalyst pretreatment in H_2 at high temperature, almost complete H_2 consumption by O_2 can be achieved. Resetting the catalyst activity by lapping, we could prove that H_2 has an activating role, that was explained in terms of a shift of platinum surface crystalline structure, from a preferential Pt(111) to a more stable and evidently more reactive Pt(200).

Catalyst exposure to O_2 alone leads to an extremely high activity that gradually drops to an asymptotic value, independent of the previous history. The same asymptote is achieved after thermal or H_2 pretreatments. The very high initial activity after O_2 pretreatment was connected to the competition of O_2 and H_2 for active sites. The larger affinity of Pt for H_2 leads to the H_2-inhibition effect, which is very detrimental to the surface activity. Exposing the surface to O_2 can artificially unbalance a competition where H_2 is favoured, resulting in a transient of very high activity, that vanishes as H_2 regain control of the surface. Catalytic reaction light-off studies summarize all these observations. Reducing enough the H_2 concentration leads to a much higher activity, that results in a very low, apparently unique ignition temperature. As H_2 increases, reaction becomes progressively inhibited, passing through a bifurcation region, where 2-steps ignition appears to occur. That provides enough explanation to the discrepancies between our experimental ignition temperatures and the ones collected from the Literature, and among them. Modern microkinetics mechanisms must be developed to account for these surface rearrangements that have been experimentally proved to dramatically affect the reactivity, especially in the range of operative conditions at which only catalytic reaction are active.

The competition between hydrogen self-inhibition on platinum and heat of reaction thermal promotion is not so obvious. Referring to possible real operative conditions of micro power generator or to a single channel of honeycomb catalysts, the startup of platinum coated catalytic planar channels with heights of 1 mm and fed with fuel lean hydrogen/air mixtures (equivalence ratios 0.10 to 0.28) was investigated numerically at pressures of 1 and 5 bar and inlet temper-

atures 380-400 K, using a 2-D transient code with detailed hetero-/homogeneous chemistry, heat conduction in the solid wall and surface radiation heat transfer. The impact of catalytic and gas phase chemistry, pressure, equivalence ratio and solid material properties on the transient processes leading to ignition and finally to steady state operation was assessed. The kinetic studies in a surface perfectly stirred reactor (SPSR) have shown that catalytic ignition of fuel lean hydrogen/air mixtures is inhibited with an increase in pressure or equivalence ratio. At temperatures above the catalytic ignition temperature T_{ign}, the above picture is reversed: catalytic reactivity exhibits positive order of ≈1.5 with respect to hydrogen concentration and an overall pressure order of ≈0.97. Channel simulations with inclusion of only catalytic chemistry have shown that, for a given pressure, despite the initial longer ignition period at higher equivalence ratios (due to the inhibition discussed in point 1 above) the steady state times are shorter at larger equivalence ratios. This is due to chemical effects from one side (enhanced catalytic reactivity at larger equivalence ratios when T>Tign) and thermal effects form the other side (higher exothermicity at larger equivalence ratios that in turn accelerate the catalytic reaction rates). Moreover, superadiabatic surface temperatures are eventually attained for all investigated equivalence ratios due to the diffusional imbalance of the hydrogen fuel. Steady state times defined on the hydrogen conversion, $t_{st,H2}$, are appreciably shorter than the corresponding steady state times based on the channel wall temperature, $t_{st,T}$, due to high reactivity of hydrogen on platinum that leads to catalytic hydrogen conversions changing only mildly above a certain wall temperature.The impact of gas phase chemistry on the startup process is profound at P = 5 bar. Homogeneous chemistry moderates substantially the surface temperatures. In particular, the steady state temperatures are lower by as much as 224 K (ϕ = 0.28) when gas phase chemistry is included in the simulations. This is because the gaseous combustion zone extends nearly parallel to the wall and hence shields the catalyst surface from the hydrogen rich channel core. This in turn leads to a reduction of the hydrogen catalytic conversion and hence to a drop of the catalytically induced surface superadiabaticity. Contrary to the significant impact of gas phase chemistry at P = 5 bar, at P = 1 bar it becomes modestly important and only for ϕ = 0.28. This is due to the acceleration of the gas phase hydrogen reactivity with rising pressure over the operating temperatures of the channel reactor. Gas phase chemistry substantially enhances the hydrogen conversion (by as much as 70% at ϕ = 0.28). This is because the homogeneous reaction pathway does not have the strong transport limitations of the catalytic pathway. Moreover, gas phase chemistry shortens the times required to reach steady state wall temperatures, $t_{st,T}$. For power generation systems, whereby catalyst thermal stability as well as reactor integrity, increased fuel conversion and faster startup are all issues of prime interest, the presence of gaseous chemistry is a clear advantage. Cordierite walls shorten the times required to reach steady

state when compared to FeCr-alloy walls due to their lower heat capacity. Moreover, at steady state the cordierite walls result in only slightly higher maximum wall temperatures and to appreciably lower entry wall temperatures due to their lower thermal conductivity. Depending on the particular application, cordierite can be used when faster ignition and shorter steady state times are needed (i.e. gas turbine catalytic reactors), while FeCr-alloy is preferable when higher spatial homogeneity of the surface temperatures is required (e.g. coupling of reactor to thermoelectric modules). All the above consideration are of practical interest for reactor start up and designed, particularly in the effects of the support material properties.

The complexity of steam methane reforming reaction and the role of the catalyst as well as its composition, require a dedicate study to assess the specific kinetic of the gas-solid system. Indeed, as evidenced in the Literature overview, there is not a uniquely accepted kinetic of steam methane reforming with nickel-based catalysts. Steam methane reforming reaction has been experimentally studied in a high pressure laboratory scale reactor, suitably designed to operate at typical industrial conditions: P = 10 bar, T = 923 K, and inlet compositions 81%/9%/5%/5% respectively to $CH_4/C_2H_6/H_2/N_2$. Total inlet flow rate was adjusted according to the W/F scaling factor defined as the ratio between the catalyst weight and the total molar inlet flow rate. The aim was to reproduce the same carbon inflow of large scale reactors in order to focus on carbon deposition rate, particularly at very low steam-to-carbon ratio. Reynolds, Nusselt and Biot based similitude analysis was discussed in Section 6.2, evidencing that, mainly because of the large differences in the catalyst solid particle sizes, flow regime cannot be respected when scaling down from large scale plant, which are typically in the turbulent regime, to the small scale, usually in the laminar regime. However, heat transfer from the fluid and the solid was closely reproduced. Three catalysts, differing in the nickel loading and type of carbon resistance promoters, have been considered. The impact of temperature, steam-to-carbon ratio, exposure time at reactive conditions and W/F were assessed. Steam-to-carbon ratio effects were extensively studied in the range S/C = 1.2-2. Critical conditions were observed at S/C = 1.4 for Ni-A, carbon deposition rate led to a progressively increase of the reactor pressure up to 11. On the other hand, S/C = 1.2 was possible for the catalysts Ni-B and Ni-C, the last also achieving the thermodynamic equilibrium. 10 hours stability tests, on Ni-B and Ni-C, confirmed the higher activity of the catalyst Ni-C towards methane conversion. Slight detrimental activity evolution was observed for the Ni-B after the intermediate oxidative step, methane conversion decreased from 10% to 8%. On the opposite, temperature controlled oxidation, adopted for total carbon deposition evaluation, confirmed the higher carbon resistance of Ni-B in which 0.010 g of adsorbed carbon were estimated, whereas 0.038 g for Ni-C, which is expected to be more active thanks to the higher nickel loading,

but less resistant to carbon deposition. Catalytic performances were further investigated in kinetically regime by adjusting the W/F in the range 5-13 kg_{cat}/(mol/s), thus keeping constant the catalyst mass loaded in the reactor and changing the total molar inlet flow rate. Other operative variables were set as follows: T = 923 K, P = 10 bar and S/C = 2, sufficiently high for testing the Ni-A catalyst at negligible carbon deposition rate. The lower nickel content of Ni-B significantly affected the methane conversion with respect to the performances evidenced for the other catalysts: 12%/16%/18% CH_4 conversion for Ni-B/Ni-A/Ni-C respectively. Considered the different metal dispersion and active particle sizes of the three catalysts tested, and reprocessing the experimental data on the basis of the weight of active metal contents, also related to the measured surface active areas, catalysts performances have been revisited. At S/C = 2, T = 923 K, P = 10 bar and different W/F, catalyst Ni-B was the most promising in terms of methane conversion rate normalised on the surface active area $X_{CH_4}A_{Ni}$, meaning that the despite the low nickel loading, the specific conversion was significantly higher than the other catalysts. These results suggest that the real surface active area at low steam-to-carbon ratio may be affected by carbon deposition, reducing significantly when not protected by promoters as strong as in Ni-B. The higher activity of Ni-C may be overcome by carbon deposition which can endanger the effective catalytic activity. Further comparisons of the performances at S/C = 2, T = 923 K, P = 10 and W/F = 5 k_{cat}/(mol/s), then in the kinetically controlled regime, expressed in terms of methane conversion and selectivity to hydrogen with respect to the surface active area has been proposed. The different CH_4 conversions combined with the same selectivity to H_2 suggest that, at relatively high S/C = 2, the promoters do not affect the overall kinetic that can be simply reduced to a common nickel-based catalyst, whose activity depends on its surface active area. Comparison of catalytic performances on the basis of the mass of nickel loaded can be misleading. Future works will be focused on the interpretation of the large amount of experimental data collected on methane steam reforming reaction, on NI-based catalysts, aiming at developing a representative surface kinetics model, in the presence of appreciable carbon deposition rate.

Chapter 8

List of Symbols

A, A_l	reaction rate pre exponentials, Eqns. 5.8, 5.19
b	channel half height, Fig. 5.1
C_k	concentration of k th species, Eqns. 5.7, 5.19
c_p, c_s	specific heat of gas at constant pressure, specific heat of solid
D_{km}	mixture average species diffusion coefficient, Eqn. 5.9
D_k^T	species thermal diffusion coefficient, Eqn. 5.9
n E, E_l	activation energies, Eqns. 5.8, 5.19
F_{k-j}	configuration factor between surface elements k and j, Eqn. 5.12
h, h_0	total enthalpy, chemical enthalpy of k th gaseous species, Eqns. 5.4, 5.10
k, m	indices for gas phase and surface species
K_g, K_s	number of gaseous species, number of surface species
k_s	thermal conductivity of solid, Eqn. 5.11
k, m	indices for gas-phase and surface species
λ	index for surface reactions
L	channel length, Fig. 5.1
N_s	number of surface reactions
n	pressure exponent in 5.19
P	pressure
q_{rad}, q_k	radiative flux, radiative flux on k th surface element, Eqns. 5.11, 5.12
R	universal gas constant
$\dot{s}_k$	heterogeneous molar production rate of k th species, Eqns. 5.6, 5.7
S/V	surface to volume ratio, Eqns. 5.16, 5.18
t	time
T, T_o	temperature and reference temperature, Eqn. 5.10
u, U_{IN}	streamwise velocity component, inlet streamwise velocity
v	transverse velocity component
$\vec{V}_k$	species diffusion velocity vector, Eqn. 5.9

W_k, $\bar{W}$	gas phase species molecular weight, mixture average molecular weight
X_k, Y_k	mole fraction and mass fraction of k th gaseous species
x, y	streamwise and transverse coordinates, Fig. 5.1
Z	normalized hydrogen conversion in an SPSR, Eqn. **??**

Greek Symbols

Subscripts

Γ	surface site density, Eqn. 5.6
δ	channel wall thickness, Fig. 5.1
ϵ	surface emissivity, Eqns. 5.12, 5.14
ϵ_{i_l}	parameter in surface reaction rate coefficient, Eqn. 5.8
θ_m	coverage of surface species m, Eqns. 5.8, 5.16
λ_g	thermal conductivity of gas, Eqns. 5.4, 5.11
μ	viscosity
μ_{i_l}	parameter in surface reaction rate coefficient, Eqn. 5.8
ρ, rho_s	density of gas, density of solid
σ	Stefan Boltzmann constant, Eqns. 5.12, 5.14
σ_m	surface species site occupancy, Eqn. 5.6
τ	residence time in surface perfectly stirred reactor, Eqn. 5.18
$\tau_{chem,k}$	characteristic chemical times of k th species, Eqn. 5.17
$\dot{\omega}_k$	homogeneous molar production rate of k^{th} gaseous species, Eqn. 5.5
Ω	non dimensional reaction rate parameter, Eqn. 5.22

Subscripts

IN, OUT	inlet, outlet
in	catalytic ignition
ign,hom	homogeneous ignition
w	wall
st	steady state

Acronyms

CFD	comutational fluid dynamics
CST	catalytically stabilized thermal combustion
DFT	density functional theory
DNS	direct numerical simulation
QSS	quasi-steady state
SEM	Scanning Electron Microscopy
XRD	X-Ray Diffraction

Bibliography

[1] The University of York. No TitleThe essential chemical industry, 2013.

[2] Freedonia. World hydrogen. Technical report, Cleveland - USA.

[3] L O Nord, R Anantharaman, and O Bolland. Design and off-design analyses of a pre-combustion CO2 capture process in a natural gas combined cycle power plant. *Int. J. Greenh. Gas Con.*, 3(4):385–392, 2009.

[4] Yohannes Ghermay, John Mantzaras, and Rolf Bombach. Effects of hydrogen preconversion on the homogeneous ignition of fuel-lean H2/O2/N2/CO2 mixtures over platinum at moderate pressures. *Combustion and Flame*, 157(10):1942–1958, October 2010.

[5] G Di Lorenzo, P Barbera, and G Ruggieri. Pre-combustion carbon-capture technologies for power generation: an engineering-economic assessment. *Int. J. Energ. Res.*, 37:389–402, 2013.

[6] M Reinke, Mantzaras, R Bombach, S Schenker, N Tylli, and K Boulouchos. Effects of H2O and CO2 dilution on the catalytic and gas phase combustion of methane over platinum at elevated pressures. *Combust. Sci. Technol.*, 179:553–600, 2007.

[7] B Belaissaoui, G Cabot, M S Cabot, D Willson, and E Favre. An energetic analysis of CO2 capture on a gas turbine combining flue gas recirculation and membrane separation. *Energy*, 38:167–175, 2012.

[8] D Winkler, P Mueller, S Reimer, T Griffin, A Burdet, J Mantzaras, and Y Ghermay. Improvement of gas turbine combustion reactivity under flue gas recirculation condition with in situ hydrogen addition, 2009.

[9] D G Norton, E D Wetzel, and D G Vlachos. Fabrication of single-channel catalytic microburners: effect of confinement on the oxidation of hydrogen/air mixtures. *Ind. Eng. Chem. Res.*, 43:4833–4840, 2004.

[10] V Seshadri and N S Kaisare. Simulation of hydrogen and hydrogen-assisted propane ignition in pt catalyzed microchannel. *Combust. Flame*, 157:2051–2062, 2010.

[11] S Karagiannidis and J Mantzaras. Numerical investigation on the hydrogen-assisted start-up of methane-fueled, catalytic microreactors. *Flow Turbul. Combust.*, 89:215–230, 2012.

[12] G D Stefanidis and D G Vlachos. High vs. low temperature reforming for hydrogen production via microtechnology. *Chem. Eng. Sci.*, 64:4856–4865, 2009.

[13] G D Stefanidis, D G Vlachos, N S Kaisare, and M Maestri. Methane steam reforming at microscales: operation strategies for variable power output at millisecond contact times. *AIChE J.*, 55(1):180–191, 2009.

[14] C Diehm and O Deutschmann. Hydrogen production by catalytic partial oxidation of methane over staged Pd/Rh coated monoliths: Spatially resolved concentration and temperature profiles. *Int. J. Hydrogen Energ*, 39:17998–18004, 2014.

[15] J D Holladay, Y Wang, and E Jones. Review of developments in portable hydrogen production using microreactor technology. *Chem. Rev.*, 104:4767–4789, 2004.

[16] M Hartmann, L Maier, H D Minh, and O Deutschmann. Catalytic partial oxidation of iso-octane over rhodium catalysts: an experimental, modeling, and simulation study. *Combust. Flame*, 157:1771–1782, 2010.

[17] A Schlegel, P Benz, T Griffin, W Weisenstein, and H Bockhorn. Catalytic stabilization of lean premixed combustion: method for improving NOx emissions. *Combust. Flame*, 105:332–340, 1996.

[18] Richard Carroni and Timothy Griffin. Catalytic hybrid lean combustion for gas turbines. *Catal. Today*, 155(1-2):2–12, 2010.

[19] J Mantzaras and P Benz. An asymptotic and numerical investigation of homogeneous ignition in catalytically stabilized channel flow combustion. *Combust. Flame*, 119:455–472, 1999.

[20] W C Pfefferle and L D Pfefferle. Catalytically stabilized combustion. *Prog. Energy Combust. Sci.*, 12:25–41, 1986.

[21] G Pizza, C E Frouzakis, J Mantzaras, A G Tomboulides, and K Boulouchos. Dynamics of premixed hydrogen/air flames in microchannels. *Combust. Flame*, 152(3):433–450, 2008.

[22] C J Evans and D C Kyritsis. Operational regimes of rich methane and propane/oxygen flames in mesoscale non-adiabatic ducts. *Proc. Combust. Inst.*, 32:3107–3114, 2009.

[23] G Pizza, C E Frouzakis, J Mantzaras, A G Tomboulides, and K Boulouchos. Three-dimensional simulations of premixed hydrogen/air flames in microtubes. *J. Fluid Mech.*, 658:463–491, 2010.

[24] A W Fan, J L Wan, K Maruta, H Nakamura, H Yao, and W Liu. Flame dynamics in a heated meso-scale radial channel. *Proc. Combust. Inst.*, 34:3351–3359, 2013.

[25] Andrea Brambilla, Marco Schultze, Christos E. Frouzakis, John Mantzaras, Rolf Bombach, and Konstantinos Boulouchos. An experimental and numerical investigation of premixed syngas combustion dynamics in mesoscale channels with controlled wall temperature profiles. *Proceedings of the Combustion Institute*, July 2014.

[26] Gianmarco Pizza, John Mantzaras, Christos E. Frouzakis, Ananias G. Tomboulides, and Konstantinos Boulouchos. Suppression of combustion instabilities of premixed hydrogen/air flames in microchannels using heterogeneous reactions. *Proceedings of the Combustion Institute*, 32(2):3051–3058, 2009.

[27] Gianmarco Pizza, John Mantzaras, and Christos E Frouzakis. Flame dynamics in catalytic and non-catalytic mesoscale microreactors. *Catal. Today*, 155(1-2):123–130, 2010.

[28] B Hellsing, B Kasemo, and V P Zhdanov. Kinetics of the hydrogen oxygen reaction on platinum . *J. Catal.*, 132(1):210–228, 1991.

[29] O. Deutschmann, R. Schmidt, F. Behrendt, J Warnatz, and J. Warnat. Numerical modeling of catalytic ignition. *Proceedings of the Combustion Institute*, 26(1):1747–1754, 1996.

[30] M. Rinnemo, O. Deutschmann, F. Behrendt, and B. Kasemo. Experimental and numerical investigation of the catalytic ignition of mixtures of hydrogen and oxygen on platinum. *Combustion and Flame*, 111(4):312–326, December 1997.

[31] O Deutschmann, L.I I Maier, U Riedel, a.H H Stroemman, and R.W W Dibble. Hydrogen assisted catalytic combustion of methane on platinum. *Catal. Today*, 59(1-2):141–150, 2000.

[32] Matteo Maestri, Alessandra Beretta, Tiziano Faravelli, Gianpiero Groppi, Enrico Tronconi, and Dionisios G. Vlachos. Two-dimensional detailed modeling of fuel-rich H2 combustion over Rh/Al2O3 catalyst. *Chemical Engineering Science*, 63(10):2657–2669, May 2008.

[33] P A Bui, D G Vlachos, and P R Westmoreland. Homogeneous ignition of hydrogen/air mixtures over platinum. *Proc. Combust. Inst.*, 26:1763–1770, 1996.

[34] Christoph Appel, John Mantzaras, Rolf Schaeren, Rolf Bombach, Andreas Inauen, Beat Kaeppeli, Bernd Hemmerling, and Anna Stampanoni. An experimental and numerical investigation of homogeneous ignition in catalytically stabilized combustion of hydrogen/air mixtures over platinum. *Combustion and Flame*, 128(4):340–368, 2002.

[35] John Mantzaras, Rolf Bombach, and Rolf Schaeren. Hetero-/homogeneous combustion of hydrogen/air mixtures over platinum at pressures up to 10 bar. *Proceedings of the Combustion Institute*, 32(2):1937–1945, 2009.

[36] Y Ghermay, J Mantzaras, and R Bombach. Experimental and numerical investigation of hetero-/homogeneous combustion of CO/H2/O2/N2 mixtures over platinum at pressures up to 5 bar. *Proc. Combust. Inst.*, 33:1827–1835, 2011.

[37] M Schultze, J Mantzaras, R Bombach, and K Boulouchos. An experimental and numerical investigation of the hetero-/homogeneous combustion of fuel-rich hydrogen/air mixtures over platinum. *Proc. Combust. Inst.*, 34:2269–2277, 2013.

[38] X Zheng, J Mantzaras, and R Bombach. Homogeneous combustion of fuel-lean syngas mixtures over platinum at elevated pressures and preheats. *Combust. Flame*, 160:155–169, 2013.

[39] F Behrendt, O Deutschmann, R Schmidt, and J Warnatz. Ignition and extinction of hydrogen-air and methane-air mixtures over platinum and palladium. In B Warren, editor, *Heterogeneous Hydrocarbon Oxidation*. ACS Symposium Series, Washington DC, 1996.

[40] D G Vlachos and P A Bui. Catalytic ignition and extinction of hydrogen: comparison of simulations and experiments. *Surf. Sci.*, 364:1625–1630, 1996.

[41] a B Mhadeshwar and D G Vlachos. Hierarchical, multiscale surface reaction mechanism development: CO and H2 oxidation, water-gas shift, and preferential oxidation of CO on Rh. *Journal of Catalysis*, 234(1):48–63, August 2005.

[42] Julian N. Bär, Canan Karakaya, and Olaf Deutschmann. Catalytic ignition of light hydrocarbons over Rh/Al2O3 studied in a stagnation-point flow reactor. *Proceedings of the Combustion Institute*, 34(2):2313–2320, January 2013.

[43] Xin Zheng and John Mantzaras. An analytical and numerical investigation of hetero-/homogeneous combustion with deficient reactants having larger than unity Lewis numbers. *Combustion and Flame*, 161(7):1911–1922, July 2014.

[44] R. Kraehnert and M. Baerns. Morphology changes of Pt-foil catalyst induced by temperature-controlled ammonia oxidation near atmospheric pressure. *Applied Catalysis A: General*, 327(1):73–81, July 2007.

[45] N.E. Fernandes, Y.K. Park, and D.G. Vlachos. The autothermal behavior of platinum catalyzed hydrogen oxidation: experiments and modeling. *Combustion and Flame*, 118(1-2):164–178, July 1999.

[46] K A Petersen, I Dybkjaer, C V Ovesen, N C Schjodt, J Sehested, and S G Thomsen. Natural gas to synthesis gas - Catalysts and catalytic processes. *Journal of Natural Gas Science and Engineering*, 3:423–459, 2011.

[47] Jiahui Xu, Connie M.Y. Yeung, Jun Ni, Frederic Meunier, Nadia Acerbi, Martin Fowles, and Shik Chi Tsang. Methane steam reforming for hydrogen production using low water-ratios without carbon formation over ceria coated Ni catalysts. *Applied Catalysis A: General*, 345(2):119–127, August 2008.

[48] N. de Miguel, J. Manzanedo, and P. L. Arias. Testing of a ni-al2o3 catalyst for methane steam reforming using different reaction systems. *Chemical Engineering and Technology*, 35(4):720–728, 2012.

[49] Metal Prices, 2015.

[50] T. Melchiori. *Study of non catalytic gas-solid reactions: development of a single particle model*. PhD thesis, 2014.

[51] R Kissel-Osterrieder, F Behrendt, J Warnatz, U Metka, H R Volpp, and J Wolfrum. Experimental and theoretical investigation of the CO-oxidation on platinum: bridging the pressure and the materials gap. *Proc. Combust. Inst.*, 28:1341–1348, 2000.

[52] D G Vlachos and P R Westmoreland. Homogeneous ignition of hydrogen-air mixtures over platinum. pages 1763–1770, 1996.

[53] Kyle Brady, Chih Jen Sung, and James T'Ien. Ignition propensity of hydrogen/air mixtures impinging on a platinum stagnation surface. *International Journal of Hydrogen Energy*, 35(20):11412–11423, October 2010.

[54] M Rinnemo, M Fassihi, and B Kasemo. The critical condition for catalytic ignition . Hz / O2 on Pt. 2(1):60–64, 1993.

[55] H. Ikeda, J. Sato, and F.a. Williams. Surface kinetics for catalytic combustion of hydrogen-air mixtures on platinum at atmospheric pressure in stagnation flows. *Surface Science*, 326(1-2):11–26, March 1995.

[56] Michael Forsth, Frank Eisert, Fredrik Gudmundson, John Persson, and Arne Rosen. Analysis of the kinetics for the H2 + 1/2 O2 < − > H2O reaction on a hot Pt surface in the pressure range 0.10 - 10 Torr. *Catalysis Letters*, 66(1-2):63–69, 2000.

[57] W R Williams, C M Marks, and L D Schmidt. Steps in the reaction H2+O2=H2O on Pt - OH desorption at high-temperatures. *J. Phys. Chem.*, 96(14):5922–5931, 1992.

[58] T Wahnstrom, E Fridell, S Ljungstrom, B Hellsing, B Kasemo, and A Rosén. Determination of the activation energy for OH desorption in the H2 + O2 reaction on polycrystalline platinum. *Surface Science Letters*, 223:L905 – L912, 1989.

[59] Erik Fridell, Arne Rosn, Bengt Kasemo, and A Rosen. A laser-induced fluorescence study of OH desorption from Pt in H2O/O2 and H2O/H2 mixtures. *Langmuir*, 10:699–708, 1994.

[60] C. Appel, J. Mantzaras, R Schoren, R. Bombach, A. Inauen, and R. Schaeren. Catalytic Combustion of Hydrogen-Air Mixtures Over Platinum: Validation of Hetero/Homogeneous Chemical Reaction Schemes. *Clean Air: International Journal on Energy for a Clean Environment*, 5(1):21–44, 2004.

[61] Sigrídur Gudmundsdóttir, Egill Skúlason, Kees-Jan Weststrate, Ludo Juurlink, and Hannes Jónsson. Hydrogen adsorption and desorption at the Pt(110)-(1×2) surface: experimental and theoretical study. *Physical chemistry chemical physics : PCCP*, 00(17):1–10, May 2013.

[62] E. M. Shustorovich and a. V. Zeigarnik. The UBI-QEP method: Basic formalism and applications to chemisorption phenomena on transition metal surfaces. Chemisorption energetics. *Russian Journal of Physical Chemistry*, 80(1):4–30, January 2006.

[63] Harrell Sellers. The generalized UBI-QEP method for modeling the energetics of reactions on transition metal surfaces. *Surface Science*, 524(1-3):29–39, February 2003.

[64] Michael Forsth. Sensitivity Analysis of the Reaction Mechanism for Gas-Phase Chemistry of H2+O2 Mixtures Induced by a Hot Pt Surface. *Combustion and flame*, 130:241–260, 2002.

[65] D. a. Hickman and L. D. Schmidt. Steps in CH4 oxidation on Pt and Rh surfaces: high-temperature reactor simulations. *AIChE Journal*, 39(7):1164–1177, July 1993.

[66] Young K Park, Preeti Aghalayam, and Dionisios G Vlachos. A generalized approach for predicting coverage-dependent reaction parameters of complex surface reactions: application to H2 oxidation over platinum. *J. Phys. Chem. A*, 103:8101–8107, 1999.

[67] David G. Goodwin, Harry K. Moffat, and Raymond L. Speth. Cantera: An object-oriented software toolkit for chemical kinetics, thermodynamics, and transport processes, 2014.

[68] Symeon Karagiannidis and John Mantzaras. Numerical investigation on the start-up of methane-fueled catalytic microreactors. *Combustion and Flame*, 157(7):1400–1413, July 2010.

[69] John Mantzaras. *Catalytic Combustion of Hydrogen, Challenges, and Opportunities*, volume 45 of *Advances in Chemical Engineering*. Elsevier, 1 edition, 2014.

[70] P.-a. Bui, D. G. Vlachos, and P. R. Westmoreland. Modeling Ignition of Catalytic Reactors with Detailed Surface Kinetics and Transport: Oxidation of H2/Air Mixtures over Platinum Surfaces. *Industrial & Engineering Chemistry Research*, 36(7):2558–2567, July 1997.

[71] Zhongwei Zhu, Franklin Feng Tao, Fan Zheng, Rui Chang, Yimin Li, Lars Heinke, Zhi Liu, Miquel Salmeron, and Gabor a Somorjai. Formation of nanometer-sized surface platinum oxide clusters on a stepped Pt(557) single crystal surface induced by oxygen: a high-pressure STM and ambient-pressure XPS study. *Nano letters*, 12(3):1491–7, March 2012.

[72] M Baerns, R Imbihl, V Kondratenko, R Kraehnert, W Offermans, R Vansanten, and a Scheibe. Bridging the pressure and material gap in the catalytic ammonia oxidation: structural and catalytic properties of different platinum catalysts. *Journal of Catalysis*, 232(1):226–238, May 2005.

[73] R Imbihl, a Scheibe, Y F Zeng, S Günther, R Kraehnert, V a Kondratenko, M Baerns, W K Offermans, a P J Jansen, and R a van Santen. Catalytic ammonia oxidation on platinum: mechanism and catalyst restructuring at high and low pressure. *Physical chemistry chemical physics : PCCP*, 9(27):3522–40, July 2007.

[74] S. Horch, H. T. Lorensen, S. Helveg, E. Laegsgaard, I. Stensgaard, K. W. Jacobsen, and J. K. Norskov. Enhancement of surface self-diffusion of platinum atoms by adsorbed hydrogen. *Nature*, 398:134–136, 1999.

[75] Ola Nilsen, Arne Kjekshus, and Helmer Fjellvå g. Reconstruction and loss of platinum catalyst during oxidation of ammonia. *Applied Catalysis A: General*, 207(1-2):43–54, February 2001.

[76] R J Kee, M E Coltrin, and P Glaborg. *Chemically Reacting Flow, Theory and Practice*. Wiley, Hoboken, USA, 2003.

[77] M E Coltrin, R J Kee, G H Evans, E Meeks, F M Rupley, and J F Grcar. SPIN (Version 3.83): A FORTRAN program for modeling one-dimensional rotating-disk/stagnation-flow chemical vapor deposition reactors. Technical report, 1991.

[78] Robert J. Kee a Huayang Zhu a James A. Nabity b Jeffrey R. Engel David T. Wickham Michael J. Kaufman Nicholas E. McGuire, Neal P. Sullivan. Catalytic steam reforming of methane using rh supported on sr-substituted hexaaluminate. *Chemical Engineering Science*, 64:5231–5239, 2009.

[79] R Imbihl and G Ertl. Oscillatory kinetics in heterogeneous catalysis. *Chem. Reviews*, 95:697–733, 1995.

[80] Victor W Dean and Michael Frenklach. Catalytic Etchlng. *The Journal of Physical Chemistry*, 1(14):5731–5738, 1988.

[81] Calvin H Bartholomew. Mechanisms of catalyst deactivation. *Applied Catalysis A: General*, 212(1-2):17–60, April 2001.

[82] Jochen Bandlow, Payam Kaghazchi, Timo Jacob, C. Papp, B. Tränkenschuh, R. Streber, M. P. a. Lorenz, T. Fuhrmann, R. Denecke, and H.-P. Steinrück. Oxidation of stepped Pt(111) studied by x-ray photoelectron spectroscopy and density functional theory. *Physical Review B*, 83(17):174107, May 2011.

[83] F. Eisert, a. P. Elg, and a. Rosï¿½n. Adsorption of oxygen and hydrogen on Pt(111) studied with second-harmonic generation. *Applied Physics A Materials Science and Processing*, 60(2):209–215, February 1995.

[84] A Schneider, J Mantzaras, and S Eriksson. Ignition and extinction in catalytic partial oxidation of methane-oxygen mixtures with large H2O and CO2 dilution. *Combust. Sci. Technol.*, 180:89–126, 2008.

[85] J S Tien. Transient catalytic combustor model. *Combust. Sci. Technol.*, 26(1-2):65–75, 1981.

[86] T Ahn, W V Pinczewski, and D L Trimm. Transient performance of catalytic combustors for gas-turbine applications. *Chem. Eng. Sci.*, 41(1):55–64, 1986.

[87] P.M. M Struk, J S Tien, F.J. J Miller, D.L. L Dietrich, and J.S. Tien. Transient numerical modeling of catalytic channels using a quasi-steady gas phase. *Chemical Engineering Science*, 119:158–173, November 2014.

[88] Xin Zheng, John Mantzaras, and Rolf Bombach. Kinetic interactions between hydrogen and carbon monoxide oxidation over platinum. *Combustion and Flame*, 161(1):332–346, January 2014.

[89] J Mantzaras and C Appel. Effects of finite rate heterogeneous kinetics on homogeneous ignition in catalytically stabilized channel-flow combustion. *Combust. Flame*, 130:336–351, 2002.

[90] G Groppi, A Belloli, E Tronconi, and P Forzatti. A Comparison of lumped and distributed models of monolith catalytic combustors. *Chem. Eng. Sci.*, 50(17):2705–2715, 1995.

[91] Andrea Brambilla, Christos E. Frouzakis, John Mantzaras, Ananias Tomboulides, Stefan Kerkemeier, and Konstantinos Boulouchos. Detailed transient numerical simulation of H2/air hetero-/homogeneous combustion in platinum-coated channels with conjugate heat transfer. *Combustion and Flame*, 161(10):2692–2707, October 2014.

[92] R Carroni, T Griffin, J Mantzaras, and M Reinke. High-pressure experiments and modeling of methane/air catalytic combustion for power generation applications. *Catal. Today*, 83:157–170, 2003.

[93] B Schneider, S Karagiannidis, M Bruderer, D Dyntar, C Zwyssig, Q Guangchun, M Diener, K Boulouchos, R S Abhari, L Guzzella, and J W Kolar. Ultra-high-energy-density converter for portable power. In *PowerMEMS 2005*, Tokyo, Japan, November 28-30, 2005.

[94] N Sinha, C Bruno, and F V Bracco. Two-dimensional, transient catalytic combustion of CO-air on platinum. *Physicochem. Hydrod.*, 6:373–391, 1985.

[95] Y S Touloukian, R W Powell, C Y Ho, and P G Klemens. Thermal conductivity: metallic elements and alloys. In Y S Touloukian and C Y Ho, editors, *Thermophysical properties of matter*, volume 1. the TPRC Data Series, Plenum, New York, 1970.

[96] R. Siegel and J. R. Howell. *Thermal radiation heat transfer*. New York, 1981.

[97] Juan Li, Zhenwei Zhao, Andrei Kazakov, and Frederick L. Dryer. An updated comprehensive kinetic model of hydrogen combustion. *International Journal of Chemical Kinetics*, 36(10):566–575, October 2004.

[98] Y Ghermay, J Mantzaras, R Bombach, and K Boulouchos. Homogeneous combustion of fuel lean H2/O2/N2 mixtures over platinum at elevated pressures and preheats. *Combust. Flame*, 158:1491–1506, 2011.

[99] M. E. Coltrin, R. J. Kee, F. M. Rupley, and E. Meeks. Surface Chemkin: a Fortran package for analyzing heterogeneous chemical kinetics at solid surface/gas-phase interface, Report No. SAND96-8217. Technical report, Sandia National Laboratories, 1996.

[100] R J Kee, F M Rupley, and J A Miller. Chemkin II: A Fortran chemical kinetics package for the analysis of gas-phase chemical kinetics, 1996.

[101] R. J. Kee, G. Dixon-Lewis, J. Warnatz, M. E. Coltrin, and J. A. Miller. A Fortran Computer Code Package for the Evaluation of Gas-phase Multicomponent Transport Properties, Report No. SAND86-8246. Technical report, Sandia National Laboratories, 1996.

[102] J. H. Ferziger and M. Petric. *Computational methods for fluid Dynamics*. New York, springer v edition, 1999.

[103] R J Kee, F M Rupley, and J A Miller. The Chemkin thermodynamic data base, 1996.

[104] Yohannes Ghermay, John Mantzaras, Rolf Bombach, and Konstantinos Boulouchos. Homogeneous combustion of fuel-lean H2/O2/N2 mixtures over platinum at elevated pressures and preheats. *Combustion and Flame*, 158(8):1491–1506, August 2011.

[105] H K Moffat, R J Kee, J F Grcar, and J A Miller. Surface PSR: A Fortran program for modeling well-stirred reactors with gas and surface reactions. Technical report, 1993.

[106] S Karagiannidis, J Mantzaras, R Bombach, S Schenker, and K Boulouchos. Experimental and numerical investigation of the hetero-/homogeneous combustion of lean propane/air mixtures over platinum. *Proc. Combust. Inst.*, 32:1947–1955, 2009.

[107] S Karagiannidis, J Mantzaras, and K Boulouchos. Stability of hetero-/homogeneous combustion in propane and methane fueled catalytic microreactors: channel confinement and molecular transport effects. *Proc. Combust. Inst.*, 33:3241–3249, 2011.

[108] Marco Schultze and John Mantzaras. Hetero-/homogeneous combustion of hydrogen/air mixtures over platinum: Fuel-lean versus fuel-rich combustion modes. *International Journal of Hydrogen Energy*, 38(25):10654–10670, August 2013.

[109] John Mantzaras. Catalytic Combustion of Syngas. *Combustion Science and Technology*, 180(6):1137–1168, May 2008.

[110] Y. Shirasaki, T. Tsuneki, Y. Ota, I. Yasuda, S. Tachibana, H. Nakajima, and K. Kobayashi. Development of membrane reformer system for highly efficient hydrogen production from natural gas. *International Journal of Hydrogen Energy*, 34(10):4482 – 4487, 2009. 2nd World Hydrogen Technologies Convention 2nd World Hydrogen Technologies Convention.

[111] J M Ogden. Review of small stationary reformers for hydrogen production. Technical report, Princeton University - USA, 2001.

[112] J.R. Rostrup-Nielsen. Production of synthesis gas. *Catalysis Today*, 18(4):305 – 324, 1993.

[113] Jianguo Xu and Gilbert F. Froment. Methane steam reforming, methanation and water-gas shift: I. Intrinsic kinetics. *AIChE Journal*, 35(1):88–96, January 1989.

[114] L.M. Aparicio. Transient isotopic studies and microkinetic modeling of methane reforming over nickel catalysts. *Journal of Catalysis*, 165(2):262 – 274, 1997.

[115] Kaihu Hou and Ronald Hughes. The kinetics of methane steam reforming over a ni /α-al$_2$o catalyst. 82(May 2000):311–328, 2001.

[116] Jens R. Rostrup-Nielsen, Jens Sehested, and Jens K. Norskov. Hydrogen and synthesis gas by steam- and {C02} reforming. volume 47 of *Advances in Catalysis*, pages 65 – 139. Academic Press, 2002.

[117] H.S. Bengaard, J.K. NÃ¸rskov, J. Sehested, B.S. Clausen, L.P. Nielsen, A.M. Molenbroek, and J.R. Rostrup-Nielsen. Steam reforming and graphite formation on ni catalysts. *Journal of Catalysis*, 209(2):365 – 384, 2002.

[118] Junmei Wei and Enrique Iglesia. Isotopic and kinetic assessment of the mechanism of reactions of {CH4} with {CO2} or {H2O} to form synthesis gas and carbon on nickel catalysts. *Journal of Catalysis*, 224(2):370 – 383, 2004.

[119] Junmei Wei and Enrique Iglesia. Reaction pathways and site requirements for the activation and chemical conversion of methane on ru-based catalysts. *The Journal of Physical Chemistry B*, 108(22):7253–7262, 2004.

[120] Junmei Wei and Enrique Iglesia. Structural requirements and reaction pathways in methane activation and chemical conversion catalyzed by rhodium. *Journal of Catalysis*, 225(1):116 – 127, 2004.

[121] Ta-Jen Huang and Meng-Chin Huang. Effect of ni content on hydrogen production via steam reforming of methane over ni/gdc catalysts. *Chemical Engineering Journal*, 145(1):149 – 153, 2008.

[122] M. Zeppieri, P.L. Villa, N. Verdone, M. Scarsella, and P. De Filippis. Kinetic of methane steam reforming reaction over nickel- and rhodium-based catalysts. *Applied Catalysis A General*, 387(1-2):147 – 154, 2010.

[123] L. Maier, B. Schadel, K. Herrera Delgado, S. Tischer, and O. Deutschmann. Steam reforming of methane over nickel: Development of a multi-step surface reaction mechanism. *Topics in Catalysis*, 54(13-15):845–858, 2011.

[124] M Gregoris. *Sviluppo di un impianto sperimental per studiare lo steam reforming di metano a bassirapporti steam to carbon*. PhD thesis, 2014.

[125] J.R. Rostrup-Nielsen, L.J. Christiansen, and J.-H. Bak Hansen. Activity of steam reforming catalysts role and assessment. *Applied Catalysis*, 43(2):287 – 303, 1988.

Appendix A

Surface kinetics mechanisms

In the following the elementary surface chemistry and thermodynamic data of the H/O system on Pt are reported, in Cantera format. When ”stick” has been specify, parameter refer to sticking coefficient and reaction rate coefficient is calculated as follows:

$$k = \frac{\gamma_i^0}{\Gamma^\tau} \sqrt{\frac{RT}{2\pi M_i}} \tag{A.1}$$

where τ is calculate with the following equation:

$$\tau = \sum_{j=1}^{N_s} \nu'_{jk} \tag{A.2}$$

with γ_i^0 = initial (uncovered surface) sticking coefficient, N_s = surface species, Γ = surface active site density, M_i = molecular weigh and ν = stoichiometric coefficient.

Schmidt, 1993

```
#*************************************************************
#****     H2-O2 SURFACE MECHANISM  ON PT
#****     Version 1   November  1993
#****     Schmidt, Univ. Minnesota, Minneapolis
#****
#****     Kinetic data:
#****     k = A * T**b * exp (-Ea/RT)
#****         A b Ea: (cm,mol,s)  -  kJ/mol *
#****
#*************************************************************
#  Ref: D. A. Hickmann, L. D. Schmidt, AIChE Journal 1993, 39-7
#-------------------------------------------------------------

units(length = "cm", time = "s", quantity = "mol", act_energy = "kJ/mol")

# Define a gas mixture with species imported from GRI-Mech.
# Transport properties will be computed using a mixture- averaged model.


ideal_gas(name = "gas",
          elements = "H O N",
          species = """gri30: H2 H O O2 OH H2O HO2 H2O2 N2""",
           transport = 'Mix',
           reactions = 'all',
           options = ['skip_undeclared_elements',
                      'skip_undeclared_species',
                      'skip_undeclared_third_bodies'],
           initial_state = state(
           temperature = 300.0,
           pressure = OneAtm,
           mole_fractions = 'O2:0.21, N2:0.79'))

ideal_interface(name = "Pt_surf",
                elements = "Pt H O",
                species = """PT(S) H(S) H2O(S) OH(S) O(S)""",
                phases = "gas",
                site_density = 2.7063e-9,
                reactions = "all",
                initial_state = state(
                temperature = 900.0,
                coverages = 'O(S):0.0, PT(S):1, H(S):0.0'))

#-------------------------------------------------------------
#  Species data
#-------------------------------------------------------------
```

```
species(name = "PT(S)",
    atoms = " Pt:1 ",
    thermo = (
       NASA( [  300.00,  1000.00], [  0.000000000E+00,
0.000000000E+00,
                0.000000000E+00,   0.000000000E+00,
0.000000000E+00,
                0.000000000E+00,   0.000000000E+00] ),
       NASA( [ 1000.00,  3000.00], [  0.000000000E+00,
0.000000000E+00,
                0.000000000E+00,   0.000000000E+00,
0.000000000E+00,
                0.000000000E+00,   0.000000000E+00] )))

species(name = "H(S)",
    atoms = " H:1  Pt:1 ",
    thermo = (
       NASA( [  300.00,  1000.00], [ -1.302987700E+00,
5.417319900E-03,
                3.127797200E-07,  -3.232853300E-09,
1.136282000E-12,
               -4.227707500E+03,   5.874323800E+00] ),
       NASA( [ 1000.00,  3000.00], [  1.069699600E+00,
1.543223000E-03,
               -1.550092200E-07,  -1.657316500E-10,
3.835934700E-14,
               -5.054612800E+03,  -7.155523800E+00] )))

species(name = "H2O(S)",
    atoms = " O:1  H:2  Pt:1 ",
    thermo = (
       NASA( [  300.00,  1000.00], [ -2.765155300E+00,
1.331511500E-02,
                1.012769500E-06,  -7.182008300E-09,
2.281377600E-12,
               -3.639805500E+04,   1.209814500E+01] ),
       NASA( [ 1000.00,  3000.00], [  2.580305100E+00,
4.957082700E-03,
               -4.689405600E-07,  -5.263313700E-10,
1.199832200E-13,
               -3.830223400E+04,  -1.740632200E+01] )))

species(name = "OH(S)",
    atoms = " O:1  H:1  Pt:1 ",
    thermo = (
       NASA( [  300.00,  1000.00], [ -2.034088100E+00,
9.366268300E-03,
                6.627521400E-07,  -5.207488700E-09,
```

```
1.708873500E-12,
               -2.531994900E+04,   8.986318600E+00] ),
       NASA( [ 1000.00,  3000.00], [  1.824997300E+00,
3.250156500E-03,
               -3.119754100E-07,  -3.460320600E-10,
7.917147200E-14,
               -2.668549200E+04,  -1.228089100E+01] )))

species(name = "O(S)",
    atoms = " O:1  Pt:1 ",
    thermo = (
       NASA( [  300.00,  1000.00], [ -9.498690400E-01,
7.404230500E-03,
               -1.045142400E-06,  -6.112042000E-09,
3.378799200E-12,
               -1.320991200E+04,   3.613790500E+00] ),
       NASA( [ 1000.00,  3000.00], [  1.945418000E+00,
9.176164700E-04,
               -1.122671900E-07,  -9.909962400E-11,
2.430769900E-14,
               -1.400518700E+04,  -1.153166300E+01] )))

#-----------------------------------------------------------------
#  Reaction data
#-----------------------------------------------------------------

# adsorption
#-----------

#  Reaction 1
surface_reaction("H2 + 2 PT(S) => 2 H(S)",
stick(0.05, 0, 0),order = "PT(S):1")

#  Reaction 2
surface_reaction( "H + PT(S) => H(S)",
stick(1, 0, 0))

#  Reaction 3
surface_reaction( "O2 + 2 PT(S) => 2 O(S)",
stick(0.003, 0, 0),order = "PT(S):1")

#  Reaction 4
surface_reaction( "O + PT(S) => O(S)",
stick(1, 0, 0))

#  Reaction 5
surface_reaction( "H2O + PT(S) => H2O(S)",
stick(0.1, 0, 0))
```

```
#  Reaction 6
surface_reaction( "OH + PT(S) => OH(S)",
stick(1, 0, 0))

# surface reaction
#-----------------

#  Reaction 7
surface_reaction( "H(S) + O(S) => OH(S) + PT(S)",
[3.7E+23, 0, 10.5])

#  Reaction 8
surface_reaction( "OH(S) + PT(S) => H(S) + O(S)",
[3.7E+16, 0, 21])

#  Reaction 9
surface_reaction( "H(S) + OH(S) => H2O(S) + PT(S)",
[3.3E+25, 0, 62.8])

#  Reaction 10
surface_reaction( "H2O(S) + PT(S) => H(S) + OH(S)",
[6.7E+21, 0, 155])

#  Reaction 11
surface_reaction( "OH(S) + OH(S) => H2O(S) + O(S)",
[3.7E+23, 0, 51.5])

# desorption
#-----------

#  Reaction 12
surface_reaction( "2 H(S) => H2 + 2 PT(S)",
[1.9E+21, 0, 75.4])

#  Reaction 13
surface_reaction( "2 O(S) => O2 + 2 PT(S)",
[1.9E+21, 0, 218])

#  Reaction 14
surface_reaction( "H2O(S) => H2O + PT(S)",
[1E+13, 0, 45.2])

#  Reaction 15
surface_reaction( "OH(S) => OH + PT(S)",
[1.5E+13, 0, 201.1])
```

Kasemo, 1994

```
#*************************************************************
#****     H2-O2 SURFACE MECHANISM  ON PT
#****     Version 1   November  1994
#****     Kasemo, Univ. Technology & Univ. of Goteborg, Sweden
#****
#****     Kinetic data:
#****     k = A * T**b * exp (-Ea/RT)
#****         A b Ea: (cm,mol,s)  -  kJ/mol *
#****
#*************************************************************
#  Ref: E. Fridell, A. Rosen, B. Kasemo, Langmuir 1994, 10, 699-708
#-------------------------------------------------------------
units(length = "cm", time = "s", quantity = "mol", act_energy = "kJ/mol")

# Define a gas mixture with species imported from GRI-Mech.
# Transport properties will be computed using a mixture- averaged model.

ideal_gas(name = "gas",
         elements = "H O N",
         species = """gri30: H2 H O O2 OH H2O HO2 H2O2 N2""",
          transport = 'Mix',
          reactions = 'gri30: all',
          options = ['skip_undeclared_elements',
                     'skip_undeclared_species',
                     'skip_undeclared_third_bodies'],
          initial_state = state(
          temperature = 300.0,
          pressure = OneAtm,
          mole_fractions = 'O2:0.21, N2:0.79'))

ideal_interface(name = "Pt_surf",
                elements = "Pt H O",
                species = """PT(S) H(S) H2O(S) OH(S) O(S)""",
                phases = "gas",
                site_density = 2.7063e-9,
                reactions = "all",
                initial_state = state(
                temperature = 900.0,
                coverages = 'O(S):0.0, PT(S):1, H(S):0.0'))

#-------------------------------------------------------------
#  Species data
#-------------------------------------------------------------

species(name = "PT(S)",
```

```
    atoms = " Pt:1 ",
    thermo = (
       NASA( [  300.00,  1000.00], [  0.000000000E+00,
0.000000000E+00,
                0.000000000E+00,   0.000000000E+00,
0.000000000E+00,
                0.000000000E+00,   0.000000000E+00] ),
       NASA( [ 1000.00,  3000.00], [  0.000000000E+00,
0.000000000E+00,
                0.000000000E+00,   0.000000000E+00,
0.000000000E+00,
                0.000000000E+00,   0.000000000E+00] )))

species(name = "H(S)",
    atoms = " H:1  Pt:1 ",
    thermo = (
       NASA( [  300.00,  1000.00], [ -1.302987700E+00,
5.417319900E-03,
                3.127797200E-07,  -3.232853300E-09,
1.136282000E-12,
               -4.227707500E+03,   5.874323800E+00] ),
       NASA( [ 1000.00,  3000.00], [  1.069699600E+00,
1.543223000E-03,
               -1.550092200E-07,  -1.657316500E-10,
3.835934700E-14,
               -5.054612800E+03,  -7.155523800E+00] )))

species(name = "H2O(S)",
    atoms = " O:1  H:2  Pt:1 ",
    thermo = (
       NASA( [  300.00,  1000.00], [ -2.765155300E+00,
1.331511500E-02,
                1.012769500E-06,  -7.182008300E-09,
2.281377600E-12,
               -3.639805500E+04,   1.209814500E+01] ),
       NASA( [ 1000.00,  3000.00], [  2.580305100E+00,
4.957082700E-03,
               -4.689405600E-07,  -5.263313700E-10,
1.199832200E-13,
               -3.830223400E+04,  -1.740632200E+01] )))

species(name = "OH(S)",
    atoms = " O:1  H:1  Pt:1 ",
    thermo = (
       NASA( [  300.00,  1000.00], [ -2.034088100E+00,
9.366268300E-03,
                6.627521400E-07,  -5.207488700E-09,
1.708873500E-12,
               -2.531994900E+04,   8.986318600E+00] ),
```

```
       NASA( [ 1000.00,  3000.00], [  1.824997300E+00,
3.250156500E-03,
               -3.119754100E-07,  -3.460320600E-10,
7.917147200E-14,
               -2.668549200E+04,  -1.228089100E+01] )))

species(name = "O(S)",
    atoms = " O:1  Pt:1 ",
    thermo = (
       NASA( [  300.00,  1000.00], [ -9.498690400E-01,
7.404230500E-03,
               -1.045142400E-06,  -6.112042000E-09,
3.378799200E-12,
               -1.320991200E+04,   3.613790500E+00] ),
       NASA( [ 1000.00,  3000.00], [  1.945418000E+00,
9.176164700E-04,
               -1.122671900E-07,  -9.909962400E-11,
2.430769900E-14,
               -1.400518700E+04,  -1.153166300E+01] )))

#-----------------------------------------------------------------
#  Reaction data
#-----------------------------------------------------------------

# adsorption
#-----------

#  Reaction 1
surface_reaction("H2 + 2 PT(S) => 2 H(S)",
stick(0.046, 0, 0),order = "PT(S):1")

#  Reaction 2
surface_reaction( "H + PT(S) => H(S)",
stick(1, 0, 0))

#  Reaction 3
surface_reaction( "O2 + 2 PT(S) => 2 O(S)",
stick(0.023, 0, 0))

#  Reaction 4
surface_reaction( "O + PT(S) => O(S)",
stick(1, 0, 0))

#  Reaction 5
surface_reaction( "H2O + PT(S) => H2O(S)",
stick(0.7, 0, 0))

#  Reaction 6
surface_reaction( "OH + PT(S) => OH(S)",
```

```
stick(1, 0, 0))

# surface reaction
#-----------------

#  Reaction 7
surface_reaction( "H(S) + O(S) => OH(S) + PT(S)",
[3.7E+21, 0, 11.5])

#  Reaction 8
surface_reaction( "OH(S) + PT(S) => H(S) + O(S)",
[3.7E+21, 0, 24.5])

#  Reaction 9
surface_reaction( "H(S) + OH(S) => H2O(S) + PT(S)",
[3.3E+21, 0, 17.5])

#  Reaction 10
surface_reaction( "H2O(S) + PT(S) => H(S) + OH(S)",
[3.7E+21, 0,113.5])

#  Reaction 11
surface_reaction( "OH(S) + OH(S) => H2O(S) + O(S)",
[3.7E+21, 0, 48.2])

#  Reaction 12
surface_reaction( "H2O(S) + O(S) => OH(S) + OH(S)",
[3.7E+21, 0, 131.4])

# desorption
#-----------

#  Reaction 13
surface_reaction( "2 H(S) => H2 + 2 PT(S)",
[3.7E+21, 0, 67.4])

#  Reaction 14
surface_reaction( "2 O(S) => O2 + 2 PT(S)",
[3.7E+21, 0, 213.2])

#  Reaction 15
surface_reaction( "H2O(S) => H2O + PT(S)",
[1E+13, 0, 42.3])

#  Reaction 16
surface_reaction( "OH(S) => OH + PT(S)",
[1E+13, 0, 192.8])
```

Deutschmann, 1995

```
#*************************************************************
#****     H2-O2 SURFACE MECHANISM  ON PT
#****     Version 1.2   November  1995
#****     O. Deutschmann, IWR, Heidelberg University, Germany
#****     Kinetic data:
#****     k = A * T**b * exp (-Ea/RT)
#****        A b Ea: (cm,mol,s)  -  kJ/mol *
#*************************************************************
#  Ref:- 1.) Deutschman et al., 26th Symp. (Intl.) on
#  Combustion,1996. pp. 1747-1754
# see http://reaflow.iwr.uni-heidelberg.de/~Olaf.Deutschmann/
#-------------------------------------------------------------
units(length = "cm", time = "s", quantity = "mol", act_energy = "kJ/mol")

# Define a gas mixture with species imported from GRI-Mech.
# Transport properties will be computed using a mixture- averaged model.

ideal_gas(name = "gas",
         elements = "H O N",
         species = """gri30: H2 H O O2 OH H2O HO2 H2O2 N2""",
          transport = 'Mix',
          reactions = 'all',
          options = ['skip_undeclared_elements',
                     'skip_undeclared_species',
                     'skip_undeclared_third_bodies'],
          initial_state = state(
          temperature = 300.0,
          pressure = OneAtm,
          mole_fractions = 'O2:0.21, N2:0.79'))

ideal_interface(name = "Pt_surf",
                elements = "Pt H O",
                species = """PT(S) H(S) H2O(S) OH(S) O(S)""",
                phases = "gas",
                site_density = 2.7063e-9,
                reactions = "all",
                initial_state = state(
                temperature = 900.0,
                coverages = 'O(S):0.0, PT(S):1, H(S):0.0'))

#-------------------------------------------------------------
#  Species data
#-------------------------------------------------------------

species(name = "PT(S)",
```

```
    atoms = " Pt:1 ",
    thermo = (
       NASA( [  300.00,  1000.00], [  0.000000000E+00,
0.000000000E+00,
                0.000000000E+00,   0.000000000E+00,
0.000000000E+00,
                0.000000000E+00,   0.000000000E+00] ),
       NASA( [ 1000.00,  3000.00], [  0.000000000E+00,
0.000000000E+00,
                0.000000000E+00,   0.000000000E+00,
0.000000000E+00,
                0.000000000E+00,   0.000000000E+00] )))

species(name = "H(S)",
    atoms = " H:1  Pt:1 ",
    thermo = (
       NASA( [  300.00,  1000.00], [ -1.302987700E+00,
5.417319900E-03,
                3.127797200E-07,  -3.232853300E-09,
1.136282000E-12,
               -4.227707500E+03,   5.874323800E+00] ),
       NASA( [ 1000.00,  3000.00], [  1.069699600E+00,
1.543223000E-03,
               -1.550092200E-07,  -1.657316500E-10,
3.835934700E-14,
               -5.054612800E+03,  -7.155523800E+00] )))

species(name = "H2O(S)",
    atoms = " O:1  H:2  Pt:1 ",
    thermo = (
       NASA( [  300.00,  1000.00], [ -2.765155300E+00,
1.331511500E-02,
                1.012769500E-06,  -7.182008300E-09,
2.281377600E-12,
               -3.639805500E+04,   1.209814500E+01] ),
       NASA( [ 1000.00,  3000.00], [  2.580305100E+00,
4.957082700E-03,
               -4.689405600E-07,  -5.263313700E-10,
1.199832200E-13,
               -3.830223400E+04,  -1.740632200E+01] )))

species(name = "OH(S)",
    atoms = " O:1  H:1  Pt:1 ",
    thermo = (
       NASA( [  300.00,  1000.00], [ -2.034088100E+00,
9.366268300E-03,
                6.627521400E-07,  -5.207488700E-09,
1.708873500E-12,
               -2.531994900E+04,   8.986318600E+00] ),
```

```
       NASA( [ 1000.00,  3000.00], [  1.824997300E+00,
3.250156500E-03,
               -3.119754100E-07,  -3.460320600E-10,
7.917147200E-14,
               -2.668549200E+04,  -1.228089100E+01] )))

species(name = "O(S)",
    atoms = " O:1  Pt:1 ",
    thermo = (
       NASA( [  300.00,  1000.00], [ -9.498690400E-01,
7.404230500E-03,
               -1.045142400E-06,  -6.112042000E-09,
3.378799200E-12,
               -1.320991200E+04,   3.613790500E+00] ),
       NASA( [ 1000.00,  3000.00], [  1.945418000E+00,
9.176164700E-04,
               -1.122671900E-07,  -9.909962400E-11,
2.430769900E-14,
               -1.400518700E+04,  -1.153166300E+01] )))

#-----------------------------------------------------------------
#  Reaction data
#-----------------------------------------------------------------

#  Reaction 1
surface_reaction("H2 + 2 PT(S) => 2 H(S)",
[4.45790E+10, 0.5, 0],order = "PT(S):1")

#  Reaction 2
surface_reaction( "2 H(S) => H2 + 2 PT(S)",
Arrhenius(3.7E+21, 0, 67.4,
coverage = ['H(S)', 0.0, 0.0, -6.0]))

#  Reaction 3
surface_reaction( "H + PT(S) => H(S)",
stick(1, 0, 0))

#  Reaction 4
surface_reaction( "O2 + 2 PT(S) => 2 O(S)",
Arrhenius(1.8E+21, -0.5, 0),
options = 'duplicate')

#  Reaction 5
surface_reaction( "O2 + 2 PT(S) => 2 O(S)",
stick(2.3E-02, 0, 0),
options = 'duplicate')

#  Reaction 6
surface_reaction( "2 O(S) => O2 + 2 PT(S)",
```

```
Arrhenius(3.7E+21, 0, 213.2,
coverage = ['O(S)', 0.0, 0.0, -60]) )

#  Reaction 7
surface_reaction( "O + PT(S) => O(S)",
stick(1, 0, 0))

#  Reaction 8
surface_reaction( "H2O + PT(S) => H2O(S)",
stick(7.5E-01, 0, 0))

#  Reaction 9
surface_reaction( "H2O(S) => H2O + PT(S)",
[1E+13, 0, 40.3])

#  Reaction 10
surface_reaction( "OH + PT(S) => OH(S)",
stick(1, 0, 0))

#  Reaction 11
surface_reaction( "OH(S) => OH + PT(S)",
[1E+13, 0, 192.8])

#  Reaction 12
surface_reaction( "H(S) + O(S) <=> OH(S) + PT(S)",
[3.7E+21, 0, 11.500])

#  Reaction 13
surface_reaction( "H(S) + OH(S) <=> H2O(S) + PT(S)",
[3.7E+21, 0, 17.400])

#  Reaction 14
surface_reaction( "OH(S) + OH(S) <=> H2O(S) + O(S)",
[3.7E+21, 0, 48.200])
```

Vlachos, 1999

```
#*************************************************************
#****     CH4-O2 SURFACE MECHANISM  ON PT
#****     K.Park, P. Aghalayam, D.G. Vlachos, J. Phys Chem. A (1999)
#****     Kinetic data:
#****     k = A * T**b * exp (-Ea/RT)
#         A          b       Ea
#****    (cm,mol,S)    -    kcal/mol
#*************************************************************

units(length = "cm", time = "s", quantity = "mol", act_energy = "kcal/mol")

ideal_gas(name = "gas",
         elements = "O H N",
         species = """gri30: H2 H O O2 OH H2O HO2 H2O2 N2""",
          transport = 'Mix',
          reactions = 'gri30: all',
          options = ['skip_undeclared_elements',
                     'skip_undeclared_species',
                    'skip_undeclared_third_bodies'],
          initial_state = state(temperature = 300.0,
                                pressure = OneAtm,
                     mole_fractions = 'H2:0.3, O2:0.1, N2:0.6'))

ideal_interface(name = "Pt_surf",
                elements = " Pt  H  O ",
                species = """PT(S) H(S) H2O(S) OH(S) O(S)""",
                phases = "gas",
                site_density = 2.7063e-9,
                reactions = "all",
                initial_state = state(temperature = 900.0,
                coverages = 'O(S):0.4,PT(S):0.4, H(S):0.2'))

#-----------------------------------------------------------------
#  Species data
#-----------------------------------------------------------------

species(name = "PT(S)",
    atoms = " Pt:1 ",
    thermo = (
       NASA( [  300.00,  1000.00], [  0.000000000E+00,
0.000000000E+00,
                0.000000000E+00,   0.000000000E+00,
0.000000000E+00,
                0.000000000E+00,   0.000000000E+00] ),
       NASA( [ 1000.00,  3000.00], [  0.000000000E+00,
```

```
0.000000000E+00,
                0.000000000E+00,   0.000000000E+00,
0.000000000E+00,
                0.000000000E+00,   0.000000000E+00] )))

species(name = "H(S)",
    atoms = " H:1  Pt:1 ",
    thermo = (
       NASA( [  300.00,  1000.00], [ -1.302987700E+00,
5.417319900E-03,
                3.127797200E-07,  -3.232853300E-09,
1.136282000E-12,
               -4.227707500E+03,   5.874323800E+00] ),
       NASA( [ 1000.00,  3000.00], [  1.069699600E+00,
1.543223000E-03,
               -1.550092200E-07,  -1.657316500E-10,
3.835934700E-14,
               -5.054612800E+03,  -7.155523800E+00] )))

species(name = "H2O(S)",
    atoms = " O:1  H:2  Pt:1 ",
    thermo = (
       NASA( [  300.00,  1000.00], [ -2.765155300E+00,
1.331511500E-02,
                1.012769500E-06,  -7.182008300E-09,
2.281377600E-12,
               -3.639805500E+04,   1.209814500E+01] ),
       NASA( [ 1000.00,  3000.00], [  2.580305100E+00,
4.957082700E-03,
               -4.689405600E-07,  -5.263313700E-10,
1.199832200E-13,
               -3.830223400E+04,  -1.740632200E+01] )))

species(name = "OH(S)",
    atoms = " O:1  H:1  Pt:1 ",
    thermo = (
       NASA( [  300.00,  1000.00], [ -2.034088100E+00,
9.366268300E-03,
                6.627521400E-07,  -5.207488700E-09,
1.708873500E-12,
               -2.531994900E+04,   8.986318600E+00] ),
       NASA( [ 1000.00,  3000.00], [  1.824997300E+00,
3.250156500E-03,
               -3.119754100E-07,  -3.460320600E-10,
7.917147200E-14,
               -2.668549200E+04,  -1.228089100E+01] )))

species(name = "O(S)",
    atoms = " O:1  Pt:1 ",
```

```
    thermo = (
       NASA( [  300.00,  1000.00], [ -9.498690400E-01,
7.404230500E-03,
               -1.045142400E-06,  -6.112042000E-09,
3.378799200E-12,
               -1.320991200E+04,   3.613790500E+00] ),
       NASA( [ 1000.00,  3000.00], [  1.945418000E+00,
9.176164700E-04,
               -1.122671900E-07,  -9.909962400E-11,
2.430769900E-14,
               -1.400518700E+04,  -1.153166300E+01] )))

#-----------------------------------------------------------------
#  Reaction data
#-----------------------------------------------------------------

#  Reaction 1F
surface_reaction( "H2 + PT(S) + PT(S)=> H(S) + H(S) ",
stick(0.5,0,0),order = "PT(S):1")

#  Reaction 1B
surface_reaction( "H(S) + H(S) => H2 + PT(S) + PT(S)",
Arrhenius(3.7E+20, 0, 20,
coverage = ['H(S)', 0.0, 0.0, -6.0]))

#  Reaction 2F
surface_reaction( "O2 + 2 PT(S) => 2 O(S)",
stick(0.03, 0, 0))

#  Reaction 2B
surface_reaction( "2 O(S) => O2 + 2 PT(S)",
Arrhenius(3.7E+21, 0, 51,
coverage = ['O(S)', 0.0, 0.0, -32]))

#  Reaction 3F
surface_reaction( "H(S) + O(S) => OH(S) + PT(S)",
Arrhenius(3.7E+19, 0, 12.1,
coverage = [['H(S)', 0.0, 0.0, -3.3],['O(S)', 0.0, 0.0, +1.3]]))

#  Reaction 3B
surface_reaction( "OH(S) + PT(S) => H(S) + O(S)",
Arrhenius(3.7E+19, 0, 24.4,
coverage = [['H(S)', 0.0, 0.0, +1.1],['O(S)', 0.0, 0.0, -6 ]]))

#  Reaction 4F
surface_reaction( "H(S) + OH(S) => H2O(S) + PT(S)",
Arrhenius(3.7E+18, 0, 12.4,
coverage = [['H(S)', 0.0, 0.0, -3.1],['O(S)', 0.0, 0.0, -12.4]]))
```

```
#  Reaction 4B
surface_reaction( " H2O(S) + PT(S) => H(S) + OH(S)",
Arrhenius(3.7E+19, 0, 18.4,
coverage = [['H(S)', 0.0, 0.0, +1.8],['O(S)', 0.0, 0.0, +20.7]]))

#  Reaction 5F
surface_reaction( "OH(S) + OH(S) => H2O(S) + O(S)",
Arrhenius(3.7E+19, 0, 18.9,
coverage = ['O(S)', 0.0, 0.0, -18.9]) )

#  Reaction 5B
surface_reaction( " H2O(S) + O(S) => OH(S) + OH(S)",
Arrhenius(3.7E+19, 0, 12.6,
coverage = ['O(S)', 0.0, 0.0, +21.5]) )

#  Reaction 6F
surface_reaction( "OH + PT(S) => OH(S) ",
stick(1,0,0))

#  Reaction 6B
surface_reaction( "OH(S) => OH + PT(S)",
Arrhenius(5E+14, 0, 63,
coverage = ['O(S)', 0.0, 0.0, -33]))

#  Reaction 7F
surface_reaction( "H2O + PT(S) => H2O(S) ",
stick(0.7,0,0))

#  Reaction 7B
surface_reaction( "H2O(S) => H2O + PT(S)",
[1E+13, 0, 10])

#  Reaction 8F
surface_reaction( "H + PT(S) => H(S)",
stick(1, 0, 0))

#  Reaction 8B
surface_reaction( " H(S) => H + PT(S)",
Arrhenius(1E+13, 0, 60.2,
coverage = ['H(S)', 0.0, 0.0, -4.8]) )

#  Reaction 9F
surface_reaction( "O + PT(S) => O(S) ",
stick(1.0E+00, 0, 0))

#  Reaction 9B
surface_reaction( "O(S) => O + PT(S) ",
Arrhenius(1E+13, 0, 92.6,
coverage = ['O(S)', 0.0, 0.0, -25.6]) )
```

Vlachos modified, 1999

```
#*************************************************************
#****     H2 SURFACE MECHANISM  ON PT
#****     Vlachos modified(not published), NO double coverage dependency
#****     Kinetic data:
#****     k = A * T**b * exp (-Ea/RT)
#          A          b       Ea
#****   (cm,mol,S)    -    kcal/mol
#*************************************************************

units(length = "cm", time = "s", quantity = "mol", act_energy = "kcal/mol")

ideal_gas(name = "gas",
         elements = "O H N",
         species = """gri30: H2 H O O2 OH H2O HO2 H2O2 N2""",
          transport = 'Mix',
          reactions = 'gri30: all',
          options = ['skip_undeclared_elements',
                     'skip_undeclared_species',
                    'skip_undeclared_third_bodies'],
          initial_state = state(temperature = 300.0,
                                pressure = OneAtm,
                     mole_fractions = 'H2:0.3, O2:0.1, N2:0.6'))

ideal_interface(name = "Pt_surf",
                elements = " Pt  H  O ",
                species = """PT(S) H(S) H2O(S) OH(S) O(S)""",
                phases = "gas",
                site_density = 2.7063e-9,
                reactions = "all",
                initial_state = state(temperature = 900.0,
                coverages = 'O(S):0.4,PT(S):0.4, H(S):0.2'))

#-----------------------------------------------------------------
#  Species data
#-----------------------------------------------------------------

species(name = "PT(S)",
    atoms = " Pt:1 ",
    thermo = (
       NASA( [  300.00,  1000.00], [  0.000000000E+00,
0.000000000E+00,
                0.000000000E+00,   0.000000000E+00,
0.000000000E+00,
                0.000000000E+00,   0.000000000E+00] ),
       NASA( [ 1000.00,  3000.00], [  0.000000000E+00,
```

```
0.000000000E+00,
                0.000000000E+00,   0.000000000E+00,
0.000000000E+00,
                0.000000000E+00,   0.000000000E+00] )))

species(name = "H(S)",
    atoms = " H:1  Pt:1 ",
    thermo = (
       NASA( [  300.00,  1000.00], [ -1.302987700E+00,
5.417319900E-03,
                3.127797200E-07,  -3.232853300E-09,
1.136282000E-12,
               -4.227707500E+03,   5.874323800E+00] ),
       NASA( [ 1000.00,  3000.00], [  1.069699600E+00,
1.543223000E-03,
               -1.550092200E-07,  -1.657316500E-10,
3.835934700E-14,
               -5.054612800E+03,  -7.155523800E+00] )))

species(name = "H2O(S)",
    atoms = " O:1  H:2  Pt:1 ",
    thermo = (
       NASA( [  300.00,  1000.00], [ -2.765155300E+00,
1.331511500E-02,
                1.012769500E-06,  -7.182008300E-09,
2.281377600E-12,
               -3.639805500E+04,   1.209814500E+01] ),
       NASA( [ 1000.00,  3000.00], [  2.580305100E+00,
4.957082700E-03,
               -4.689405600E-07,  -5.263313700E-10,
1.199832200E-13,
               -3.830223400E+04,  -1.740632200E+01] )))

species(name = "OH(S)",
    atoms = " O:1  H:1  Pt:1 ",
    thermo = (
       NASA( [  300.00,  1000.00], [ -2.034088100E+00,
9.366268300E-03,
                6.627521400E-07,  -5.207488700E-09,
1.708873500E-12,
               -2.531994900E+04,   8.986318600E+00] ),
       NASA( [ 1000.00,  3000.00], [  1.824997300E+00,
3.250156500E-03,
               -3.119754100E-07,  -3.460320600E-10,
7.917147200E-14,
               -2.668549200E+04,  -1.228089100E+01] )))

species(name = "O(S)",
    atoms = " O:1  Pt:1 ",
```

```
    thermo = (
       NASA( [  300.00,  1000.00], [ -9.498690400E-01,
7.404230500E-03,
               -1.045142400E-06,  -6.112042000E-09,
3.378799200E-12,
               -1.320991200E+04,   3.613790500E+00] ),
       NASA( [ 1000.00,  3000.00], [  1.945418000E+00,
9.176164700E-04,
               -1.122671900E-07,  -9.909962400E-11,
2.430769900E-14,
               -1.400518700E+04,  -1.153166300E+01] )))

#-----------------------------------------------------------------
#  Reaction data
#-----------------------------------------------------------------

#  Reaction 1F
surface_reaction( "H2 + PT(S) + PT(S)=> H(S) + H(S) ",
stick(0.5,0,0),order = "PT(S):1")

#  Reaction 1B
surface_reaction( "H(S) + H(S) => H2 + 2 PT(S) ",
Arrhenius(3.7E+20, 0, 20,
coverage = ['H(S)', 0.0, 0.0, -8.0]))

#  Reaction 2F
surface_reaction( "O2 + 2 PT(S) => 2 O(S)",
stick(0.03, 0, 0))

#  Reaction 2B
surface_reaction( "2 O(S) => O2 + 2 PT(S)",
Arrhenius(3.7E+21, 0, 51,
coverage = ['O(S)', 0.0, 0.0, -32]))

#  Reaction 3F
surface_reaction( "H(S) + O(S) => OH(S) + PT(S)",
Arrhenius(3.7E+19, 0, 11.357))

#  Reaction 3B
surface_reaction( "OH(S) + PT(S) => H(S) + O(S)",
Arrhenius(3.7E+19, 0, 22.183))

#  Reaction 4F
surface_reaction( "H(S) + OH(S) => H2O(S) + PT(S)",
Arrhenius(3.7E+18, 0, 1.569))

#  Reaction 4B
surface_reaction( " H2O(S) + PT(S) => H(S) + OH(S)",
Arrhenius(3.7E+19, 0, 25.231))
```

```
#  Reaction 5F
surface_reaction( "OH(S) + OH(S) => H2O(S) + O(S)",
Arrhenius(3.7E+19, 0, 5.2338))

#  Reaction 5B
surface_reaction( " H2O(S) + O(S) => OH(S) + OH(S)",
Arrhenius(3.7E+19, 0,18.0698) )

#  Reaction 6F
surface_reaction( "OH + PT(S) => OH(S) ",
stick(1,0,0))

#  Reaction 6B
surface_reaction( "OH(S) => OH + PT(S)",
Arrhenius(5E+14, 0, 63,
coverage = ['O(S)', 0.0, 0.0, -33]))

#  Reaction 7F
surface_reaction( "H2O + PT(S) => H2O(S) ",
stick(0.7,0,0))

#  Reaction 7B
surface_reaction( "H2O(S) => H2O + PT(S)",
[1E+13, 0, 10])

#  Reaction 8F
surface_reaction( "H + PT(S) => H(S)",
stick(1, 0, 0))

#  Reaction 8B
surface_reaction( " H(S) => H + PT(S)",
Arrhenius(1E+13, 0, 60.24,
coverage = ['H(S)', 0.0, 0.0, -4.8]) )

#  Reaction 9F
surface_reaction( "O + PT(S) => O(S) ",
stick(1.0E+00, 0, 0))

#  Reaction 9B
surface_reaction( "O(S) => O + PT(S) ",
Arrhenius(1E+13, 0, 92.64,
coverage = ['O(S)', 0.0, 0.0, -25.6]) )
```

Forsth, 2002

```
#*****************************************************************
#****     Forsth 2002.
#****     Kinetic data:
#****     k = A * T**b * exp (-Ea/RT)
#         A          b       Ea
#****     (cm,mol,S)     -      kJ/mol
#*****************************************************************

units(length = "cm", time = "s", quantity = "mol", act_energy = "kJ/mol")

ideal_gas(name = "gas",
         elements = "O H  N Ar",
         species = """gri30: H2 H O O2 OH H2O HO2 H2O2 N2""",
          transport = 'Mix',
          reactions = 'gri30: all',
          options = ['skip_undeclared_elements',
                     'skip_undeclared_species',
                     'skip_undeclared_third_bodies'],
          initial_state = state(temperature = 300.0,
                       pressure = OneAtm,
                      mole_fractions = 'O2:0.21, N2:0.79'))

ideal_interface(name = "Pt_surf",
                elements = " Pt  H  O  ",
                species = """ PT(S) H(S) H2O(S) OH(S) O(S)""",
                phases = "gas",
                site_density = 2.7063e-9,
                reactions = "all",
                initial_state = state(temperature = 900.0,
                coverages = 'O(S):0.0, PT(S):1, H(S):0'))

#-----------------------------------------------------------------
#  Species data
#-----------------------------------------------------------------

species(name = "PT(S)",
    atoms = " Pt:1 ",
    thermo = (
       NASA( [  300.00,  1000.00], [  0.000000000E+00,
0.000000000E+00,
                0.000000000E+00,   0.000000000E+00,
0.000000000E+00,
                0.000000000E+00,   0.000000000E+00] ),
       NASA( [ 1000.00,  3000.00], [  0.000000000E+00,
0.000000000E+00,
```

```
                0.000000000E+00,   0.000000000E+00,
0.000000000E+00,
                0.000000000E+00,   0.000000000E+00] )))

species(name = "H(S)",
    atoms = " H:1  Pt:1 ",
    thermo = (
       NASA( [  300.00,  1000.00], [ -1.302987700E+00,
5.417319900E-03,
                3.127797200E-07,  -3.232853300E-09,
1.136282000E-12,
               -4.227707500E+03,   5.874323800E+00] ),
       NASA( [ 1000.00,  3000.00], [  1.069699600E+00,
1.543223000E-03,
               -1.550092200E-07,  -1.657316500E-10,
3.835934700E-14,
               -5.054612800E+03,  -7.155523800E+00] )))

species(name = "H2O(S)",
    atoms = " O:1  H:2  Pt:1 ",
    thermo = (
       NASA( [  300.00,  1000.00], [ -2.765155300E+00,
1.331511500E-02,
                1.012769500E-06,  -7.182008300E-09,
2.281377600E-12,
               -3.639805500E+04,   1.209814500E+01] ),
       NASA( [ 1000.00,  3000.00], [  2.580305100E+00,
4.957082700E-03,
               -4.689405600E-07,  -5.263313700E-10,
1.199832200E-13,
               -3.830223400E+04,  -1.740632200E+01] )))

species(name = "OH(S)",
    atoms = " O:1  H:1  Pt:1 ",
    thermo = (
       NASA( [  300.00,  1000.00], [ -2.034088100E+00,
9.366268300E-03,
                6.627521400E-07,  -5.207488700E-09,
1.708873500E-12,
               -2.531994900E+04,   8.986318600E+00] ),
       NASA( [ 1000.00,  3000.00], [  1.824997300E+00,
3.250156500E-03,
               -3.119754100E-07,  -3.460320600E-10,
7.917147200E-14,
               -2.668549200E+04,  -1.228089100E+01] )))

species(name = "O(S)",
    atoms = " O:1  Pt:1 ",
    thermo = (
```

```
       NASA( [  300.00,  1000.00], [ -9.498690400E-01,
7.404230500E-03,
               -1.045142400E-06,  -6.112042000E-09,
3.378799200E-12,
               -1.320991200E+04,   3.613790500E+00] ),
       NASA( [ 1000.00,  3000.00], [  1.945418000E+00,
9.176164700E-04,
               -1.122671900E-07,  -9.909962400E-11,
2.430769900E-14,
               -1.400518700E+04,  -1.153166300E+01] )))

#-------------------------------------------------------------
#  Adsorption/Desorption
#-------------------------------------------------------------
#  Reaction data
#  NOTE:  reactions 1,8,10,12,14 are coverages dependent *(1-\theta)
#  Rection 2 is coverages dependent *(1-theta)^2
#  Multiplier function has been used for kinetic correction
#-------------------------------------------------------------

#  Reaction S1
surface_reaction("H2 + 2 PT(S) => 2 H(S)",
stick(0.046, 0, 0))

#  Reaction S2
surface_reaction( "2 H(S) => H2 + 2 PT(S) ",
[3.7E+21, 0, 67])

#  Reaction S3
surface_reaction( "O2 + 2 PT(S) => 2 O(S) ",
stick(0.023, 0.0, 0.0))

#  Reaction S4
surface_reaction( "2 O(S) => O2 + 2 PT(S) ",
[3.7E+21, 0.0, 213.384])

#  Langmuir-Hinshelwood surface reactions
#-------------------------------------------------------------

#  Reaction S5
surface_reaction( "H(S) + O(S) <=> OH(S) + PT(S) ",
[3.7E+21, 0.0, 54.340])

#  Reaction S6
surface_reaction( "H(S) + OH(S) <=> H2O(S) + PT(S) ",
[3.7E+21, 0.0, 64.636])

#  Reaction S7
surface_reaction( "OH(S) + OH(S) => H2O(S) + O(S) ",
```

```
[3.7E+21, 0.0, 74.283])

#  Product/Intermediates adsorption and desorption
#-------------------------------------------------------------

#  Reaction S8
surface_reaction( "H2O + PT(S) => H2O(S) ",
stick(0.7, 0, 0))

#  Reaction S9
surface_reaction( "H2O(S) => H2O + PT(S) ",
[1.0E+13, 0.0, 65])

#  Reaction S10
surface_reaction( "OH + PT(S) => OH(S) ",
stick(1.0, 0, 0))

#  Reaction S11
surface_reaction( "OH(S) => OH + PT(S) ",
[1.0E+14, 0.0, 245.039])

#  Reaction S12
surface_reaction( "O + PT(S) => O(S) ",
stick(1.0, 0, 0))

#  Reaction S13
surface_reaction( "O(S) => O + PT(S)",
[1E+13, 0, 356])

#  Reaction S14
surface_reaction( " H + PT(S) => H(S)",
stick(1.0, 0, 0))

#  Reaction S15
surface_reaction( " H(S) => H + PT(S)",
[1E+13, 0, 249])
```

Aghalayam, 2003

```
#*************************************************************
#****     CH4-O2 SURFACE MECHANISM  ON PT
#****     P. Aghalayam, D.G. Vlachos et al., J. Catal. (2003)
#****     Kinetic data:
#****     k = A * T**b * exp (-Ea/RT)
#         A          b       Ea
#****          (cm,mol,S)    -    kcal/mol
#*************************************************************

units(length = "cm", time = "s", quantity = "mol", act_energy = "kcal/mol")
ideal_gas(name = "gas",
         elements = "O H N",
         species = """gri30: H2 H O O2 OH H2O HO2 H2O2 N2""",
          transport = 'Mix',
          reactions = 'gri30: all',
          options = ['skip_undeclared_elements',
                     'skip_undeclared_species',
                    'skip_undeclared_third_bodies'],
          initial_state = state(temperature = 300.0,
                          pressure = OneAtm,
                    mole_fractions = 'H2:0.3, O2:0.1, N2:0.6'))

ideal_interface(name = "Pt_surf",
                elements = " Pt  H  O ",
                species = """PT(S) H(S) H2O(S) OH(S) O(S)""",
                phases = "gas",
                site_density = 2.7063e-9,
                reactions = "all",
                initial_state = state(temperature = 900.0,
                coverages = 'O(S):0.4,PT(S):0.4, H(S):0.2'))

#-----------------------------------------------------------------
#  Species data
#-----------------------------------------------------------------

species(name = "PT(S)",
    atoms = " Pt:1 ",
    thermo = (
       NASA( [  300.00,  1000.00], [  0.000000000E+00,
0.000000000E+00,
                0.000000000E+00,   0.000000000E+00,
0.000000000E+00,
                0.000000000E+00,   0.000000000E+00] ),
       NASA( [ 1000.00,  3000.00], [  0.000000000E+00,
0.000000000E+00,
```

```
                0.000000000E+00,   0.000000000E+00,
0.000000000E+00,
                0.000000000E+00,   0.000000000E+00] )))

species(name = "H(S)",
    atoms = " H:1  Pt:1 ",
    thermo = (
       NASA( [  300.00,  1000.00], [ -1.302987700E+00,
5.417319900E-03,
                3.127797200E-07,  -3.232853300E-09,
1.136282000E-12,
               -4.227707500E+03,   5.874323800E+00] ),
       NASA( [ 1000.00,  3000.00], [  1.069699600E+00,
1.543223000E-03,
               -1.550092200E-07,  -1.657316500E-10,
3.835934700E-14,
               -5.054612800E+03,  -7.155523800E+00] )))

species(name = "H2O(S)",
    atoms = " O:1  H:2  Pt:1 ",
    thermo = (
       NASA( [  300.00,  1000.00], [ -2.765155300E+00,
1.331511500E-02,
                1.012769500E-06,  -7.182008300E-09,
2.281377600E-12,
               -3.639805500E+04,   1.209814500E+01] ),
       NASA( [ 1000.00,  3000.00], [  2.580305100E+00,
4.957082700E-03,
               -4.689405600E-07,  -5.263313700E-10,
1.199832200E-13,
               -3.830223400E+04,  -1.740632200E+01] )))

species(name = "OH(S)",
    atoms = " O:1  H:1  Pt:1 ",
    thermo = (
       NASA( [  300.00,  1000.00], [ -2.034088100E+00,
9.366268300E-03,
                6.627521400E-07,  -5.207488700E-09,
1.708873500E-12,
               -2.531994900E+04,   8.986318600E+00] ),
       NASA( [ 1000.00,  3000.00], [  1.824997300E+00,
3.250156500E-03,
               -3.119754100E-07,  -3.460320600E-10,
7.917147200E-14,
               -2.668549200E+04,  -1.228089100E+01] )))

species(name = "O(S)",
    atoms = " O:1  Pt:1 ",
    thermo = (
```

```
       NASA( [  300.00,  1000.00], [ -9.498690400E-01,
7.404230500E-03,
               -1.045142400E-06,  -6.112042000E-09,
3.378799200E-12,
               -1.320991200E+04,   3.613790500E+00] ),
       NASA( [ 1000.00,  3000.00], [  1.945418000E+00,
9.176164700E-04,
               -1.122671900E-07,  -9.909962400E-11,
2.430769900E-14,
               -1.400518700E+04,  -1.153166300E+01] )))

#-------------------------------------------------------------
#  Reaction data
#-------------------------------------------------------------

#  Reaction 1F
surface_reaction( "OH(S) + PT(S) => H(S) + O(S) ",
[2.0741e+20, 0.0, 18.3])

#  Reaction 1B
surface_reaction( "H(S) + O(S) => OH(S) + PT(S) ",
[6.2963e+18, 0.0, 13.4])

#  Reaction 2F
surface_reaction( "H2O(S) + PT(S) => H(S) + OH(S) ",
[4.4444e+18, 0.0, 39.1])

#  Reaction 2B
surface_reaction( "H(S) + OH(S) => H2O(S) + PT(S) ",
[1.2963e+20, 0.0, 0.0])

#  Reaction 3F
surface_reaction( "H2O(S) + O(S) => OH(S) + OH(S) ",
[3.7037e+19, 0.0, 34.1])

#  Reaction 3B
surface_reaction( "OH(S) + OH(S) => H2O(S) + O(S) ",
[3.7037e+19, 0.0, 0.0])

#  Reaction 4F
surface_reaction( "H2 + PT(S) + PT(S)=> H(S) + H(S) ",
stick(0.09E+00, 0, 0))

#  Reaction 4B
surface_reaction( "H(S) + H(S) => H2 + PT(S) + PT(S)",
[1.2333e+21, 0.0, 20.0])

#  Reaction 5F
surface_reaction( "O2 + PT(S) + PT(S)=> O(S) + O(S) ",
```

```
stick(0.03E+00, 0, 0))

#  Reaction 5B
surface_reaction( "O(S) + O(S) => O2 + PT(S) + PT(S)",
[3.7037e+21, 0.0, 19.0])

#  Reaction 6F
surface_reaction( "H2O + PT(S) => H2O(S) ",
stick(1.0E+00, 0, 0))

#  Reaction 6B
surface_reaction( "H2O(S) => H2O + PT(S) ",
[5.330E+12, 0.0, 10.0])

#  Reaction 7F
surface_reaction( "OH + PT(S) => OH(S) ",
stick(1.0E+00, 0, 0))

#  Reaction 7B
surface_reaction( "OH(S) => OH + PT(S) ",
[1.000E+13, 0.0, 30.0])

#  Reaction 8F
surface_reaction( "H + PT(S) => H(S) ",
stick(1.0E+00, 0, 0))

#  Reaction 8B
surface_reaction( "H(S) => H + PT(S) ",
[1.000E+13, 0.0, 60.2])

#  Reaction 9F
surface_reaction( "O + PT(S) => O(S) ",
stick(1.0E+00, 0, 0))

#  Reaction 9B
surface_reaction( "O(S) => O + PT(S) ",
[1.000E+13, 0.0, 67.0])
```

Appendix B

Thermodynamic equilibium calculation

```
function eqdrive
% variante per grafici al variare di T, P o S/C
% Gran parte del programma organizza i dati in modo da utilizzare
% la routine eqsub, che dà la composizione di equilibrio fissata T,P X0

clc,close all, clear all

gas = IdealGasMix('gri30.cti');              % fase gassosa
carbon = importPhase('graphite.cti');        % C solido

nspG = nSpecies(gas);                % Numero di specie fase gas
names = cell(1,nspG);                % Nomi delle specie in fase gas
names(1:nspG) = speciesNames(gas);
names(nspG+1)={'C(gr)'};             % Aggiunto C(gr) in coda

% find species indices
ich4 = speciesIndex(gas,'CH4');
io2  = speciesIndex(gas,'O2');
ih2o = speciesIndex(gas,'H2O');
ih2  = speciesIndex(gas,'H2');
ic2  = speciesIndex(gas,'C2H6');
in2  = speciesIndex(gas,'N2');

x = zeros(nspG,1);
x(ich4) = 85.5;           % uso portata e poi normalizzo
x(ih2) = 5;
x(ic2) = 9.5;
xeqG = []; xeqGd = []; xeqT = []; Xeq = [];
```

```
caso = 1;   % 1 = T variabile; 2 = P variabile; 3 = S/C variabile
switch caso
    case 1
        P = 10;              % atm
        sc = 1.4;           % S/C
        T = 50:50:950;     %°C
        x(ih2o) = (x(ich4)+2*x(ic2))*sc;
        x = x/sum(x);           % Normalizzazione
        for i = 1:length(T)
            [xeqGi,xeqGdi,xeqTi,Xeqi] = eqsub(T(i),P,x);
            xeqG  = [xeqG   xeqGi'];
            xeqGd = [xeqGd  xeqGdi'];
            xeqT  = [xeqT   xeqTi'];
            Xeq   = [Xeq    Xeqi'];
        end
        xl = 'Temperature [°C]';
        ti = sprintf('Equilibrium Composition @ S/C = %3.1f
P = %2.0f atm',sc,P);
        xvar = T;

    case 2
        sc = 1.4;           % S/C
        T = 650;            %°C
        P = 1:2:20;         % atm
        x(ih2o) = (x(ich4)+2*x(ic2))*sc;
        x = x/sum(x);           % Normalizzazione
        for i = 1:length(P)
            [xeqGi,xeqGdi,xeqTi,Xeqi] = eqsub(T,P(i),x);
            xeqG  = [xeqG   xeqGi'];
            xeqGd = [xeqGd  xeqGdi'];
            xeqT  = [xeqT   xeqTi'];
            Xeq   = [Xeq    Xeqi'];
        end
        xl = 'Pressure [atm]';
        ti = sprintf('Equilibrium Composition @ S/C = %3.1f
T = %2.0f °C',sc,T);
        xvar = P;
case 3
        sc = 0.8:.1:3;      % S/C
        T = 650;            %°C
        P = 10;              % atm
        for i = 1:length(sc)
            x(ih2o) = (x(ich4)+2*x(ic2))*sc(1,i);
            xi = x/sum(x);          % Normalizzazione
            [xeqGi,xeqGdi,xeqTi,Xeqi] = eqsub(T,P,xi);
            xeqG  = [xeqG   xeqGi'];
            xeqGd = [xeqGd  xeqGdi'];
            xeqT  = [xeqT   xeqTi'];
```

```
            Xeq    = [Xeq    Xeqi'];
        end
        xl = 'S/C';
        ti = sprintf('Equilibrium Composition @ T = %3.1f
P = %2.0f atm',T,P);
        xvar = sc;
end

% ------------------------------------------------------------------------
% make plots
sp_out = {'H2' 'H2O' 'CH4' 'CO' 'CO2' 'C2H6'};
% specie di cui interessa grafico
i_out =  speciesIndex(gas,sp_out);

% Gas Mole Fractions
figure (1)
plot(xvar,xeqG(i_out,:),'Linewidth',2);
legend(names(i_out),'Location','Best')

ylabel('Gas Mole Fraction');
title(ti);
xlabel(xl);
axis([min(xvar) max(xvar) 0 1]);
print('-dpng',['.\Eq_G'] )


% Dry Gas Mole Fractions
figure (2)
plot(xvar,xeqGd(i_out,:),'Linewidth',2);
legend(names(i_out),'Location','Best')

ylabel('Dry Gas Mole Fraction');
title(ti);
xlabel(xl);
axis([min(xvar) max(xvar) 0 1]);
print('-dpng','.\Eq_GD' )


% Total Mole Fractions
figure (3)
i_out =  [speciesIndex(gas,sp_out)  length(names)];
plot(xvar,xeqT(i_out,:),'Linewidth',2);
legend(names(i_out),'Location','Best')

ylabel('Total Mole Fraction (over 2 phases)');
title(ti);
xlabel(xl);
axis([min(xvar) max(xvar) 0 1]);
print('-dpng','.\Eq_T__SC')
```

```
% Methane conversion
figure (4)
plot(xvar,Xeq,'Linewidth',2);

ylabel('CH4 conversion');
title(ti);
xlabel(xl);
axis([min(xvar) max(xvar) 0 1]);
print('-dpng','.\Eq_X__SC')


save('caso1')
```

Appendix C

Closed vessel simulation code

```
function batchcov_espl_seq
% test of kinetic mechanisms with catalytic batch reactor
% time dependent gas/surface mass balances
% esplicit coverages balance implemented, no advanceCoverages

clc
clear all
close all
tic

nmech = 7; % #, number of mechanisms
test = 'kin_cmp_low';
diary(strcat(test,'.txt'))
diary on
savefig = 1;

% operative conditions
Temp = 293:10:493;
xh2 = [1 2 3 4 7 10 15]/100;
xo2 = (1-xh2).*0.21;
tauf = 2;
leg = [];
XT = zeros(length(Temp),length(xh2),nmech);
cols = jet(length(xh2));
dir = '../kinetic mechanism/'; % kinetic mechanism directory
for i = 1:nmech
    switch i
            case 1
                mech = 'deutschmann.cti';
            case 2
                mech = 'vlachos.cti';
            case 3
```

```
                mech = 'aghalayam.cti';
            case 4
                mech = 'forsth.cti';
            case 5
                mech = 'kasemo.cti';
            case 6
                mech = 'schmidt.cti';
            case 7
                mech = 'park.cti';

    end

    disp(sprintf('Kinetic mechanism uploaded: %s',mech(1:end-4)))

    for k = 1:length(xh2)
        for j = 1:length(Temp)
            XT(j,k,i) = batchcov_espl(Temp(j),xh2(k),xo2(k),tauf,mech,dir);
            clearvars -except test nmech Temp xh2 xo2 tauf i mech k j XT leg co
        end
        j = [];
        figure(i)
        plot(Temp,XT(:,k,i),'Linewidth',2.5,'Color',cols(k,:)), hold on

    end
    figure(i)
    xlabel('temperature [K]')
    ylabel('H_2 conversion')
    title(['batch reactor: h2 conversion @x,T - kinetic from ' mech(1:end-4)])
    legend([repmat(char('H2[%]: '),length(xh2),1) num2str(xh2'*100)])
    set(gca,'YGrid','on','GridLineStyle','-','XGrid','on','GridLineStyle','-','
    if savefig
        saveas(gcf,[mech(1:end-4) '_X_Tx'],'png')
        saveas(gcf,[mech(1:end-4) '_X_Tx'],'fig')
    end

    k = [];
    leg = [leg; {char(mech(1:end-4))}];
end

save([test '.mat'],'test','nmech','Temp','xh2','xo2','tauf','XT','leg','cols')

toc
diary off

% --------------------------------------------------------------------
function XH2 = batchcov_espl(T,xh2,xo2,tauf,mech,dir)
% batch reactor model with heterogeneous catalytic reaction
% gas phase and coverages balances are coupled and solved @f(t)
% inhert species balance are explicit
```

```
% Cantera advanceCoverages function is NOT adopted

% operative conditions
P = 101325; % [Pa], pressure
xh2o = 0;
xn2 = 1-xh2-xo2;
V = 1; % m^3, reactor volume

% geometry
AV = 33.3e+2; % [m^-1], area/volume ratio

% gas
gas = importPhase(strcat(dir,mech),'gas');
set(gas,'T',T,'P',P,'X',['H2:' num2str(xh2) ',O2:' num2str(xo2) ',H2O:' num2str(xh2o)
Yg0 = massFractions(gas);
m_in = density(gas)*V; % kg, total mass @t0
% surf
surf = importInterface(strcat(dir,mech),'Pt_surf',gas);
sd = 2.7e-9; % [mol/cm^2], platinum site density
sd = sd*1e4; % [mol/m^2], platinum site density
setTemperature(surf,T);
setCoverages(surf,'PT(S):1');
% setCoverages(surf,'PT(S):0,O(S):1,H(S):0,H2O(S):0,OH(S):0');
xs0 = coverages(surf);
reactionEqn(surf);

% initial conditions
gas_mol0 = P*V/gasconstant/T*1000.*moleFractions(gas);
surf_mol0 = AV*V*sd.*xs0;
surf2gas_mol0 = (surf_mol0.*[1 .5 1 1 .5]')./([1; gas_mol0([1,6,5,4])]+surf_mol0)*100;
ng = nSpecies(gas);
ns = nSpecies(surf);
Y0 = [Yg0;xs0];

abstol = 1e-25;
reltol = 1e-7;
options=odeset('AbsTol',abstol,'RelTol',reltol);
[tau,Y] = ode15s(@BMi,[0 tauf],Y0,options,gas,surf,sd,tauf,T,P,ng,ns,AV,mech);

% ODE output
Yg = Y(:,1:ng);
xs = Y(:,ng+1:ng+ns);
Yh2 = Yg(:,1);
t50=tau(find(Yh2/Yh2(1)<.5,1));
if isempty(t50)
    t50 = 1e10;
end

% post-processing
```

```
Xg = zeros(length(Yg),ng);
for j = 1:length(tau)
    set(gas,'T',T,'P',P,'Y',Yg(j,:));
    Xg(j,:) = moleFractions(gas);
    setTemperature(surf,T);
    setCoverages(surf,xs(j,:));
    rate_f(:,j) = rop_f(surf);
    rate_r(:,j) = rop_r(surf);
    prod_f(:,j) = creationRates(surf);
    prod_r(:,j) = destructionRates(surf);
end

% mass balance
m_out = density(gas)*V; % kg, total mass @tend
massbalance = abs(m_in-m_out)/m_in*100; % %, mass balance error
disp(sprintf('massbalance error %3.1f %:',massbalance))

% moles balance
gas_molEND = P*V/gasconstant/T*1000.*Xg(end,:)';
surf_molEND = AV*V*sd.*xs(end,:)';
surf2gas_molEND = (surf_molEND.*[1 .5 1 1 .5]')./([1; gas_molEND([1,6,5,4])]+su

% fraction balance
Xg_ck = sum(Xg,2);
xs_ck = sum(xs,2);

% hydrogen conversion
ih2 = speciesIndex(gas,'H2');
XH2 = 1-Y(end,ih2)/Y(1,ih2);

% ---------------------------------------------------------------------
function dYdt = BMi(tau,Y,gas,surf,sd,tauf,T,P,ng,ns,AV,mech)

Yg = Y(1:ng); % [adim], gas mass fractions
xs = Y(ng+1:ng+ns); % [adim], surface mole fractions
% disp(xs')
set(gas,'T',T,'P',P,'Y',Yg);
setCoverages(surf,xs);
setTemperature(surf,T);

rho = density(gas); % [kg/m^3], gas density
MW = molarMasses(gas)/1000; % [kg/mol], molar masses

if strcmp({mech},'forsth.cti')
    sdot = forsth_fcov(surf); % coverages dependent sticking coeff
else
    sdot = netProdRates(surf)*1000; % [mol/m^2/s]
end
```

```
rg = sdot(1:ng); % [mol/m2/s]
rs = sdot(ng+1:ng+ns); % [mol/m2/s]

dYgdt = AV*rg(1:ng).*MW(1:ng)/rho;
dxsdt = rs/sd;

% progress
% waitbar(tau/tauf)

dYdt = [dYgdt; dxsdt];

% ---------------------------------------------------------------------
function sdot_fcov = forsth_fcov(surf)
% update the activation energy of Forsth's kinetic mechanism
% as a function of the coverages

if nargin == 0
    disp('variabili in ingresso non sufficienti')
end

% species index
ihs = speciesIndex(surf,'H(S)');
ios = speciesIndex(surf,'O(S)');
ih2os = speciesIndex(surf,'H2O(S)');
iohs = speciesIndex(surf,'OH(S)');

xs = coverages(surf);
lin_cov = 1-xs;

% Multiplier setting

% raection 1 - linear
setMultiplier(surf,1,lin_cov(ihs));
% reaction 3 - non-linear
setMultiplier(surf,3,lin_cov(ios)*lin_cov(ios));
% reaction 8 - linear
setMultiplier(surf,8,lin_cov(ih2os));
% reaction 10 - linear
setMultiplier(surf,10,lin_cov(iohs));
% reaction 12 - linear
setMultiplier(surf,12,lin_cov(ios));
% reaction 14 - linear
setMultiplier(surf,14,lin_cov(ihs));


% Production rate
sdot_fcov = netProdRates(surf)*1000; % [mol/m^2/s]
```